REPORT DOCUMENTATION PAGE

Form Approved OMB No. 0704-0188

Public reporting burden for this collection of informaiion is estimated to average 1 hour per response, including the time for reviewing instructions, searching existing data sources, gathering and maintaining the data needed, and completing and reviewing the collection of information. Send comments regarding this burden estimate or any other aspect of this collection of information, including suggestions for reducing this burden to Washington Headquarters Services, Directorate for Information Operations and Reports, 1215 Jefferson Davis Highway, Suite 1204, Arlington, VA 22202-4302, and to the Office of Management and Budget, Paperwork Reduction Project (0704-0188), Washington, DC 20503.

1. AGENCY USE ONLY (Leave blank)	2. REPORT DATE 3 December 1996	3. REPORT TYPE AND DATES COVERED Final Report

4. TITLE AND SUBTITLE

Computational Damage Model for Layered Composite Materials (Numerical Modeling of Dynamical Deforming of Damageable Thermoviscoelastic Composite Shell in Internal Loading)

5. FUNDING NUMBERS

F6170896W0103

6. AUTHOR(S)

Prof. Nickolay Smirnov

7. PERFORMING ORGANIZATION NAME(S) AND ADDRESS(ES)

Moscow State University
Subdept of Gas and Wave Dynamics
Moscow 119899
Russia

8. PERFORMING ORGANIZATION REPORT NUMBER

N/A

9. SPONSORING/MONITORING AGENCY NAME(S) AND ADDRESS(ES)

EOARD
PSC 802 BOX 14
FPO 09499-0200

10. SPONSORING/MONITORING AGENCY REPORT NUMBER

SPC 96-4012

11. SUPPLEMENTARY NOTES

12a. DISTRIBUTION/AVAILABILITY STATEMENT

Approved for public release; distribution is unlimited.

12b. DISTRIBUTION CODE

A

13. ABSTRACT (Maximum 200 words)

This report results from a contract tasking Moscow State University as follows: The contractor will create a new mathematical model for dynamical deforming and failure of viscoelastic damageable unidirectional laminated composites as detailed in his proposal dated 28 Dec 95.

19970113 005

14. SUBJECT TERMS

Aircraft Subsystem

15. NUMBER OF PAGES

165

16. PRICE CODE

N/A

17. SECURITY CLASSIFICATION OF REPORT	18. SECURITY CLASSIFICATION OF THIS PAGE	19. SECURITY CLASSIFICATION OF ABSTRACT	20. LIMITATION OF ABSTRACT
UNCLASSIFIED	UNCLASSIFIED	UNCLASSIFIED	UL

DISCLAIMER NOTICE

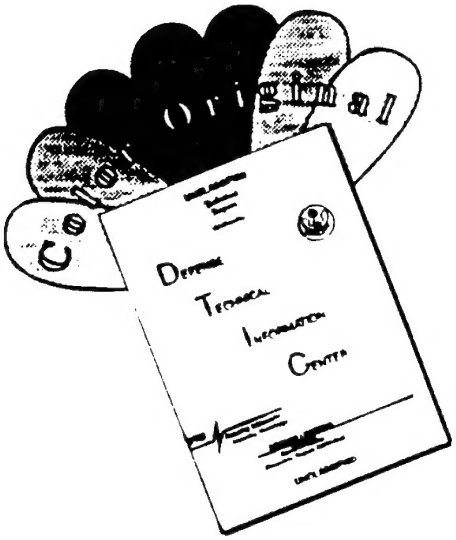

THIS DOCUMENT IS BEST QUALITY AVAILABLE. THE COPY FURNISHED TO DTIC CONTAINED A SIGNIFICANT NUMBER OF COLOR PAGES WHICH DO NOT REPRODUCE LEGIBLY ON BLACK AND WHITE MICROFICHE.

Final Report

on

SPC 96-4012

COMPUTATIONAL DAMAGE MODEL FOR LAMINATED COMPOSITE MATERIALS

Numerical Modelling of Dynamical Deforming of Damageable Thermoviscoelastic Composite Shell in Internal Loading.

Principal Investigator:

Prof.,Dr.Sc.(hab.) *N.N.Smirnov*

Investigators:

M.Sc. *V.F.Nikitin*
Prof.,Dr.Sc.(hab.) *A.B.Kiselev*
Dr. *I.D.Dimitrienko*
Dr. *V.R.Dushin*

19970113 005

BRUSSELS - 1996

DTIC QUALITY INSPECTED 1

Contents

Introduction 2

1 Part I. Mathematical model for damageable thermoviscoelastic laminated composite shell. 4

1.1 Foreword. 4

1.2 Governing system of equations for dynamical deforming of an axisymmetrical composite containment. 5

1.3 Numerical modelling. 11

2 Part II. Results of numerical modelling. 14

2.1 Foreword. 14

2.2 Determining the internal loading of a containment. 15

2.2.1 Mass balance equations in the gas phase. 15

2.2.2 Momentum equation for the gas phase. 16

2.2.3 Energy balance equation for the gas phase. 17

2.2.4 Fluxes modelling and closing the K-epsilon model. 18

2.2.5 Initial and boundary conditions. 19

2.2.6 Computational techniques. 19

2.2.7 Results of numerical modelling of internal loading. 21

2.3 Dynamical deforming of walls and accumulation of damages. . . 54

2.3.1 Evolution of the shell parameters in uniform dynamical loading. 54

2.3.2 Shell parameters in nonuniform dynamical loading. 113

References. 163

Conclusions 164

INTRODUCTION

The results of theoretical investigations undertaken within the frames of the present project brought to life a new approach to modelling of thermoviscoelastic damageable composite materials with laminated or fibrous structures. The mathematical models for dynamical deforming and failure of such composite materials is described in details in the interim reports[1,2]. The main results of the investigations are the following.

The structural breakup of composite materials has three characteristic stages:

1. Loading of the structure and accumulation of irreversible damages. 2. Fracture occuring in the zones where failure criterion is satisfied. 3. Post-fracture deformations, formation of cracks and fragments.

At the present phase of the Project the main attention was paid to the first two stages of the process. It was stated that failure generated from quasi-statically applied over-pressures differs significantly from dynamically applied over-pressures. Quasi-static matrix cracking may lead to "failure" in the form of a leak or, as a worst case, catastrophic failure involving matrix cracking and formation of segments attached to each other by the fibers. Pressures applied dynamically (with relatively high amplitudes and rates of loadings) force multiple fractures in all of the wall's constituent materials and result in the generation of many small particles.

A two-phase failure model was worked out for composite materials wherein irreversible work for damage production was used to determine the extent of damage accumulated in local regions of the structure. The model computes irreversible damage based on the growth of pores and the formation of dislocations and delaminations of layers. The characteristics of these processes are modeled as scalar quantities. The amount of damage that a material experiences is measured by the specific dissipation D. All of the individual damage processes are lumped together into the global quantity D. Failure of a material is determined by comparing D to an experimentally determined material property D^*. D^* represents the summation of all irrecoverable material motions upon failure of the laminate. D^* is presently a volummetric equivalent failure criterion analogous to a spherical failure envelope. The value of D^* remaines unknown in the equations [1,2] but experimental guidance describing one of the possible methods of determining the scalar value of D^* for spherical envelope was provided in the Third Quaterly Report [3].

The worked out failure model considers 3-D stresses. Specific dissipation D is being accumulated in each space element as the pressure loading continues. When $D = D^*$ is attained the element is assumed to have locally failed. The zones of the structure wherein the failure criterion $D = D^*$ is satisfied are considered to be damaged. A detailed fracture

progression model and methods of determining of fragments' characteristics have not been worked out yet for the thermoviscoelastic laminated composite materials.

To demonstrate the utility of the model a problem of dynamical deforming and formation of the failure zones in an axisymmetrical shell of the laminate under the influence of internal loading was regarded.

The governing system of equations for thermoviscoelastic laminates was written in the lagrangian variables to be applied for the description of behaviour of an axisymmetrical shell. The numerical model describing the dynamical deforming of the shell made use of a finite element approach. To determine the rates of internal wall loading the model was incorporated into a hydrocode enabling to solve the problems of shock waves propagation and reflections in gas in a closed vessel after internal explosion.

The Part I describes the mathematical model being used for the solution of the problem of dynamical deforming of an axisymmetrical laminated composite containment under the influence of internal loading in reflected shock waves. The model is based on the assumptions of the thin shell theory and enables to evaluate the accumulation of damges in the shell and the growth of spesific dissipation and damage parameters responsible for damages in tension, shear and delamination. The model incorporates three additional material constants characterizing the resistance of the laminate to accumulating the damages. The numerical method is also described briethly.

The Part II describes the results of numerical modelling of several problems characterised by different internal loading pattern. The numerical solution of those problems was undertaken to demonstrate the utility of the worked out model for damageable laminated composite material being incorporated into a hydrocode.

Chapter 1

Part I. Mathematical model for damageable thermoviscoelastic laminated composite shell.

1.1 Foreword.

The present Part describes the model for damageable thermoviscoelastic laminated composite material adapted for solving the problems of dynamical deforming and failure of axisymmetrical thin-walled containments in internal loading. Two possible cases of dynamical loading are regarded: uniform and nonuniform loading. In the last case the loads are determined with the help of a hydrocode modelling shock waves propagation in gas inside a closed vessel and reflections from the walls of the vessel. The shock waves inside the vessel originate due to a definite discontinuity in the initial conditions simulating an explosion. The initial zone of high pressure and density gas can be located in any place on the axis of symmetry and be of a variable volume.

The dynamical loads bring to an expansion of the walls of the containment and accumulations of damages. Since the actual criterion (the value of critical specific dissipation D^* for composites remains unknown the numerical programme continues working after the assumed critical values of dissipation are surpassed in some zones or even everywhere. To terminate the programme until the results loose the physical sence additional criteria are used making it possible to avoid overshoot in the damage parameters. That makes it

possible for us to follow the dynamics of the evolution of the zones in the shell wherein the values of the specific dissipation surpass the assumed critical values. In fact the numerical simulations based on the present model should be terminated as soon as D reaches critical value for anyone of the elements because the model does not take into account the changes in the stresses and strains of the neighbouring elements in case of a failure of one of the elements. The results of the present modelling are destined to demonstrate the applicability of the model and to serve the base for the further development of composite breakup modelling.

1.2 Governing system of equations for dynamical deforming of an axisymmetrical composite containment.

The system of equation derived in the present chapter was obtained making use of the model and notations described in details in [2]. Thus the general description of the model is not given here. If one applies results of our previous investigations (see reports [1-3]) to an axisymmetrical thick shell, one will obtain the following results.

Let x, r be the physical cylindrical coordinate system, and z, s - the lagrangian coordinates attached to the shell, so that the coordinate s changes along the generating line of the shell and z - across the shell. The equation $z = 0$ is satisfied on the surface generated by a set of points laying in the middle of the shell thickness. The part $z > 0$ faces the external side of the shell (see Fig.1.) The middle surface of the shell is represented by function $r = r_0(x)$ in the physical coordinate system, or the parametrical system of equations:

$$r = r_0(s),\ x = x_0(s).$$

It is assumed that the displacement of the shell is represented in the following terms:

$$u(z, s, t) = u^0(s, t) - z\Theta(s, t),\ w(z, s, t) = w^0(s, t),$$

where u is tangential displacement directed along the generating line, and w is the normal displacement directed collinear to the external normale to the shell.

With this assumption, the system of motion equations gets the following form:

$$\rho\frac{\partial^2 u^0}{\partial t^2} = \frac{1}{r_0}\frac{\partial(r_0 N_1)}{\partial s} - \frac{1}{r_0}\frac{\partial r_0}{\partial s}N_2 + QK_1$$

$$
\begin{aligned}
\rho\frac{\partial^2 w^0}{\partial t^2} &= \frac{1}{r_0}\frac{\partial(r_0 Q)}{\partial s} - N_1K_1 - N_2K_2 + \frac{1}{h}P_n(-h/2) \\
-\rho\frac{h^2}{12}\frac{\partial^2\Theta}{\partial t^2} &= \frac{1}{r_0}\frac{\partial(r_0 M_1)}{\partial s} - \frac{1}{r_0}\frac{\partial r_0}{\partial s}M_2 - Q
\end{aligned}
$$

Here $\rho =< \rho >= c\rho_1 + (1-c)\rho_2$ is the effective density of material and the other terms in the right side are the following:

K_1, K_2 are the physical main curvatures of the shell's middle surface, so that K_1 is inverse to the radius of curvature along the generating line, and K_2 is the curvature in the perpendicular direction. The curvatures are determined in terms of the physical coordinates $r^0(s,t)$, $x^0(s,t)$ of the middle surface:

$$
K_1 = \frac{\frac{\partial r_0}{\partial s}\frac{\partial^2 x_0}{\partial s^2} - \frac{\partial x_0}{\partial s}\frac{\partial^2 r_0}{\partial s^2}}{\left(\left(\frac{\partial r_0}{\partial s}\right)^2 + \left(\frac{\partial x_0}{\partial s}\right)^2\right)^{3/2}}, \quad K_2 = \frac{\frac{\partial x_0}{\partial s}}{r_0\left(\left(\frac{\partial r_0}{\partial s}\right)^2 + \left(\frac{\partial x_0}{\partial s}\right)^2\right)^{1/2}};
$$

N_1, N_2 are the shell tensions in the directions along the generating line and along the orthogonal geodesical line correspondingly:

$$
N_i = \frac{1}{h}\int_{-h/2}^{h/2} \sigma_{ii}\, dz,
$$

where h is the initial thickness of the shell;

Q is the rotational tension determined by:

$$
Q = \frac{1}{h}\int_{-h/2}^{h/2} \sigma_{1z}\, dz;
$$

M_1, M_2 are the bending moments along the generating line and perpendicular geodesical line correspondingly:

$$
M_i = \frac{1}{h}\int_{-h/2}^{h/2} z\sigma_{ii}\, dz.
$$

These tensions and moments are determined in terms of elastic deformations tensor components, enthropy and damadge parameters. But the elastic deformations themselves are determined by the values of full deformations tensor components.

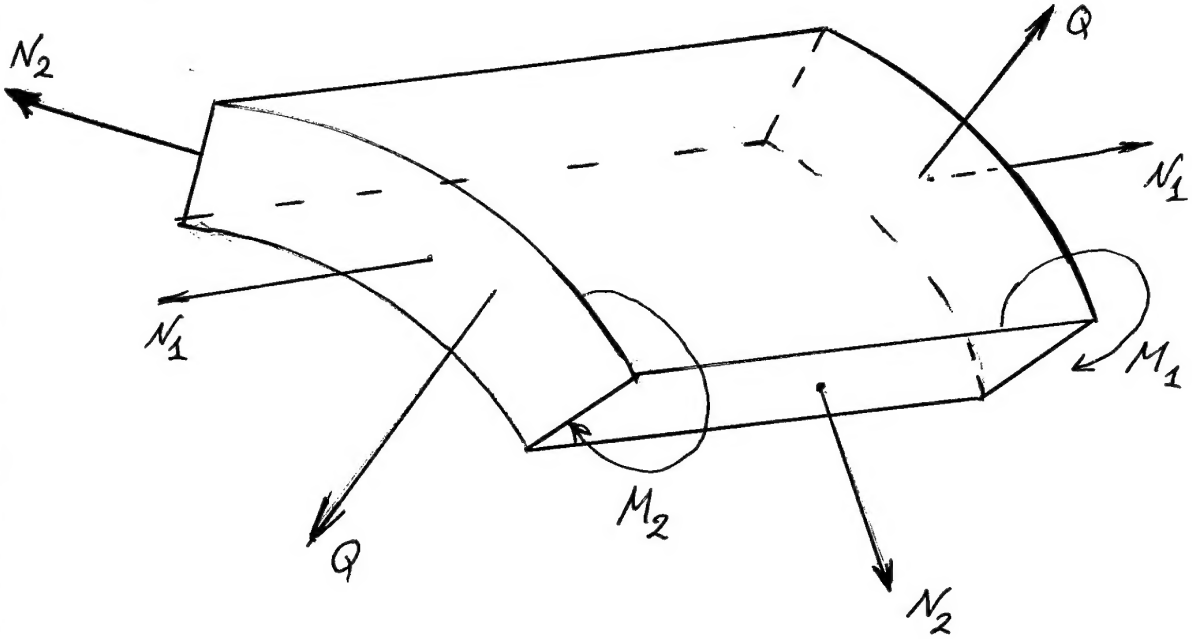

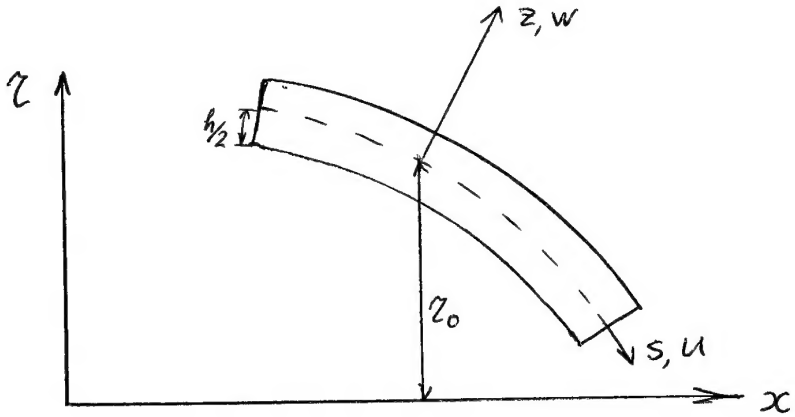

Fig. 1.

With our assumption of linear distribution of functions across the shell thickness, the components of the full deformations tensor velocities are represented in the following way:

$$\dot{\epsilon}_1(z,s,t) = \dot{\epsilon}_1^0(s,t) - z\dot{k}_1(s,t),\ \dot{\epsilon}_2(z,s,t) = \dot{\epsilon}_2^0(s,t) - z\dot{k}_2(s,t),\ \dot{\epsilon}_{1z} = \dot{\epsilon}_{1z}^0.$$

The linkage between the velocities of displacements and full deformations' velocities is the following:

$$\dot{\epsilon}_1^0 = \frac{\partial \dot{u}^0}{\partial s} + \dot{w}^0 K_1,\ \dot{\epsilon}_2^0 = \frac{\dot{u}^0}{r_0}\frac{\partial r_0}{\partial s} + \dot{w}^0 K_2,\ \dot{\epsilon}_{1z}^0 = \frac{\partial \dot{w}^0}{\partial s} - \dot{u}^0 K_1,$$

$$\dot{k}_1 = \frac{\partial \dot{\Theta}}{\partial s},\ \dot{k}_2 = \frac{\dot{\Theta}}{r_0}\frac{\partial r_0}{\partial s}.$$

The elastic deformations tensor components e_1, e_2, e_{1z} and the parameters Δ_+, Δ_- are also assumed to be distributed along the shell thickness like the components of the full deformations tensor. One obtains:

$$\dot{e}_1 = \dot{e}_1^0 - z\dot{\chi}_1,\ \dot{e}_2 = \dot{e}_2^0 - z\dot{\chi}_2,\ \dot{e}_{1z} = \dot{e}_{1z}^0,$$

$$\dot{\Delta}_+ = \dot{\Delta}_+^0 - z\dot{\chi}_+^{\Delta},\ \dot{\Delta}_- = \dot{\Delta}_-^0 - z\dot{\chi}_-^{\Delta}.$$

The tensions and moments are expressed in terms of elastic deformations components, enthropy and functions of damadge parameters.

$$N_1 = C_{22}e_1^0 + C_{23}e_2^0 - d_2(\eta - \overline{\eta_0}) - \frac{\Lambda\Omega}{1-\omega}\omega - \frac{AC}{1-\omega}\alpha\frac{2e_1^0 - e_2^0}{2e_u^0},$$

$$N_2 = C_{23}e_1^0 + C_{22}e_2^0 - d_2(\eta - \overline{\eta_0}) - \frac{\Lambda\Omega}{1-\omega}\omega - \frac{AC}{1-\omega}\alpha\frac{2e_2^0 - e_1^0}{2e_u^0},$$

$$Q = 2C_{66}e_{1z}^0 - 3\frac{AC}{1-\omega}\alpha\frac{e_{1z}^0}{e_u^0},$$

$$M_1 = -\frac{h^2}{12}\left(C_{22}\chi_1^0 + C_{23}\chi_2^0 - \frac{AC}{1-\omega}\alpha\frac{2\chi_1^0 - \chi_2^0}{2e_u^0}\right),$$

$$M_2 = -\frac{h^2}{12}\left(C_{23}\chi_1^0 + C_{22}\chi_2^0 - \frac{AC}{1-\omega}\alpha\frac{2\chi_2^0 - \chi_1^0}{2e_u^0}\right).$$

Here the following notations are used:

$$e_u^0 = \sqrt{(e_1^0)^2 + (e_2^0)^2 - e_1^0 e_2^0 + 3(e_{1z}^0)^2},\ \overline{\eta_0} = B_+\theta\Delta_+^0,$$

α, ω are damadge parameters and Ω, Λ, A, C are constants.

The damadge parameters, having zero values at initial state of undamadge material, are evaluated using the following differential kinetic equations.

$$\dot{\omega} = \Omega\left(\frac{e_1^0 + e_2^0}{1-\omega} - e_*\right) H\left(\frac{e_1^0 + e_2^0}{1-\omega} - e_*\right),$$

$$\dot{\alpha} = C\left(\frac{e_u^0}{1-\omega} - e_*^\tau\right) H\left(\frac{e_u^0}{1-\omega} - e_*^\tau\right),$$

$$\dot{\omega}_\Delta = D\left(\frac{\Delta^0}{1-\omega} - \Delta_*\right) H\left(\frac{\Delta^0}{1-\omega} - \Delta_*\right).$$

Here $H(x)$ is the Heavyside function, $D, e_*, e_*^\tau, \Delta_*$ are constants and

$$\Delta^0 = \sqrt{(\Delta_+^0)^2 + (\Delta_-^0)^2}.$$

The elastic deformations tensor terms and terms of Δ_+, Δ_- which were defined above, are evaluated by the following set of kinetic differential equations.

$$\dot{e}_1^0 = \dot{\epsilon}_1^0 - C_1^\alpha e_1^0 - C_2^\alpha e_2^0 + F\frac{\Lambda\Omega\omega}{1-\omega} + F\frac{AC\alpha}{1-\omega}\frac{e_1^0 + e_2^0}{2e_u^0} - \beta_2^+ q_+^0 - \beta_2^- q_-^0 + d_\alpha(\eta - \overline{\eta_0});$$

$$\dot{e}_2^0 = \dot{\epsilon}_2^0 - C_2^\alpha e_1^0 - C_1^\alpha e_2^0 + F\frac{\Lambda\Omega\omega}{1-\omega} + F\frac{AC\alpha}{1-\omega}\frac{e_1^0 + e_2^0}{2e_u^0} - \beta_2^+ q_+^0 + \beta_2^- q_-^0 + d_\alpha(\eta - \overline{\eta_0});$$

$$-\dot{\chi}_1 = -\dot{k}_1 + C_1^\alpha \chi_1 + C_2^\alpha \chi_2 - F\frac{AC\alpha}{1-\omega}\frac{\chi_1 + \chi_2}{2e_u^0} - \beta_2^+ q_+^\chi - \beta_2^- q_-^\chi + d_\alpha \overline{\eta_\chi};$$

$$-\dot{\chi}_2 = -\dot{k}_2 + C_2^\alpha \chi_1 + C_1^\alpha \chi_2 - F\frac{AC\alpha}{1-\omega}\frac{\chi_1 + \chi_2}{2e_u^0} - \beta_2^+ q_+^\chi + \beta_2^- q_-^\chi + d_\alpha \overline{\eta_\chi};$$

$$\dot{e}_{1z}^0 = \dot{\epsilon}_{1z}^0 - 2\alpha_{66} C_{66} e_{1z}^0 + 3\alpha_{66}\frac{AC\alpha}{1-\omega}\frac{e_{1z}^0}{e_u^0};$$

$$\dot{\Delta}_+^0 = -C_1^\beta(e_1^0 + e_2^0) + 2\beta_2^+\frac{\Lambda\Omega\omega}{1-\omega} + \beta_2^+\frac{AC\alpha}{1-\omega}\frac{e_1^0 + e_2^0}{2e_u^0} + \gamma q_+^0 + d_\beta(\eta - \overline{\eta_0});$$

$$-\dot{\chi}_+^\Delta = C_1^\beta(\chi_1 + \chi_2) - \beta_2^+\frac{AC\alpha}{1-\omega}\frac{\chi_1 + \chi_2}{2e_u^0} + \gamma q_+^\chi - d_\beta \overline{\eta_\chi};$$

$$\dot{\Delta}_-^0 = -C_2^\beta(e_1^0 - e_2^0) + 3\beta_2^+\frac{AC\alpha}{1-\omega}\frac{e_1^0 - e_2^0}{2e_u^0} + 3\gamma q_-^0;$$

$$-\dot{\chi}_-^\Delta = C_2^\beta(\chi_1 - \chi_2) - 3\beta_2^+\frac{AC\alpha}{1-\omega}\frac{\chi_1 - \chi_2}{2e_u^0} - 3\gamma q_-^\chi.$$

The expressions above use the following notations.

Constants:

$$C_1^\alpha = \alpha_{12}C_{12} + \alpha_{22}C_{22} + \alpha_{23}C_{23},\ C_2^\alpha = \alpha_{12}C_{12} + \alpha_{23}C_{22} + \alpha_{22}C_{23},$$

$$C_1^\beta = \beta_1^+ C_{12} + \beta_2^+ (C_{22} + C_{23}),\ C_2^\beta = C_{22} - C_{23},$$

$$F = \alpha_{22} + \alpha_{23},\ d_\alpha = \alpha_{12} d_1 + F d_2,\ d_\beta = \beta_1^+ d_1 + 2\beta_2^+ d_2.$$

Variables:

$$q_+^0 = B_+(\Delta_+^0 - \theta(T - T_0)) - \frac{\Lambda_\Delta D \omega_\Delta}{1-\omega}\frac{\Delta_+^0}{\Delta^0},\ q_-^0 = B_- \Delta_-^0 - \frac{\Lambda_\Delta D \omega_\Delta}{1-\omega}\frac{\Delta_-^0}{\Delta^0},$$

$$q_+^\chi = B_+(-\chi_+^\Delta) + \frac{\Lambda_\Delta D \omega_\Delta}{1-\omega}\frac{\chi_+^\Delta}{\Delta^0},\ q_-^\chi = B_-(-\chi_-^\Delta) + \frac{\Lambda_\Delta D \omega_\Delta}{1-\omega}\frac{\chi_-^\Delta}{\Delta^0},$$

$$\overline{\eta_0} = B_+ \theta \Delta_+^0,\ \overline{\eta_\chi} = B_+ \theta \chi_+^\Delta.$$

The enthropy η averaged by the thickness of the shell is evaluated from the following equation.

$$\dot{\eta} T = N_1(\dot{\epsilon}_1^0 - \dot{e}_1^0) + N_2(\dot{\epsilon}_2^0 - \dot{e}_2^0) + 2Q(\dot{\epsilon}_{1z}^0 - \dot{e}_{1z}^0) - \dot{\Delta}_+^0 q_+^0 - \dot{\Delta}_- q_-^0 + \Lambda \dot{\omega}^2 + A \dot{\alpha}^2 + \Lambda_\Delta \dot{\omega}_\Delta^2.$$

The temperature is evaluated by elastic deformations and enthropy:

$$T = T_0 - d_2(e_1^0 + e_2^0) + P(\eta - \overline{\eta_0}).$$

If we regard axisymmetrical closed shell, then there are at least 2 places of the shell laying on the axis. For the points belonging to the axis some expressions and equations change.

The expressions for curvatures K_1 and K_2 will be:

$$K_2 = K_1 = \frac{\frac{\partial^2 x_0}{\partial s^2}\frac{\partial r_0}{\partial s}}{\left|\frac{\partial r_0}{\partial s}\right|}.$$

The equations of motion change to:

$$\begin{aligned} u &= 0 \\ \rho \frac{\partial^2 w^0}{\partial t^2} &= 2\frac{\partial Q}{\partial s} - N_1 K_1 - N_2 K_2 + \frac{1}{h} P_n(-h/2) \\ \Theta &= 0 \end{aligned}$$

Linkage between the velocities of deformations and velocities of displacements changes to:

$$\dot{\epsilon}_1^0 = \frac{\partial \dot{u}^0}{\partial s} + \dot{w}^0 K_1,\ \dot{\epsilon}_2^0 = \frac{\partial \dot{u}^0}{\partial s} + \dot{w}^0 K_2,\ \dot{\epsilon}_{1z}^0 = 0,$$

$$\dot{k}_1 = \dot{k}_2 = \frac{\partial \dot{\Theta}}{\partial s}.$$

One can note that the following linkages must take place on the axis:

$$N_1 = N_2,\ Q = 0,\ M_1 = M_2,\ \epsilon_1 = \epsilon_2,\ \epsilon_{1z} = 0,\ k_1 = k_2.$$

The present mathematical model enables to determine the parameters of an axisymmetrical composite damageable shell under the influence of internal loading.

1.3 Numerical modelling.

The mathematical model described above was used to construct numerical model. This numerical model is based on finite elements approach, but since the equations contain time-derivative terms in significantely complex nonlinear form, the classical finite elements approaches using variational principles cannot be feasibly applied to the problem. We used the so-called semi-discrete Galiorkine's method [7] with some modifications. Details of calculations are listed below.

We have got the following vector of variables, changing with time and space:

$$W = (\dot{u}^0, \dot{w}^0, \dot{\Theta}, u^0, w^0, \Theta, \epsilon_1^0, \epsilon_2^0, \epsilon_{1z}^0, k_1, k_2,$$

$$e_1^0, e_2^0, e_{1z}^0, \chi_1, \chi_2, \Delta_+^0, \Delta_-^0, \chi_-^\Delta, \chi_+^\Delta, \omega, \alpha, \omega_\Delta, \eta).$$

Each member of the vector W has a governing differential equation evaluating it with time, so the whole set of differential equations can be expressed as:

$$\frac{\partial W}{\partial t} = dW(W).$$

The set of expressions $dW(W)$ uses some significant variables not beloning to W (no special differential equations for them). We can collect them in the vector V:

$$V = V(W, P) = (x^0, r^0, K_1, K_2, N_1, N_2, Q, M_1, M_2, T).$$

Note that P, i.e. loading on the wall, is obtained as an external parameter or taken from some external calculations (hydrocode application for example), and it is used to calculate the vector V.

The vector W consists of 2 sub-vectors: $W = (W_1, W_2)$ so that the first sub-vector W_1 contains variables, which governing equations contain space derivatives in the right side.

The equations for W_2 variables do not contain such derivatives explicitly. The sub-vector W_1 is the following:

$$W_1 = (\dot{u}^0, \dot{w}^0, \dot{\Theta}, \epsilon_1^0, \epsilon_2^0, \epsilon_{1z}^0, k_1, k_2).$$

The finite elements technique is used to evaluate expressions for dW_1.

The axisymmetrical shell is represented by a computational domain with Lagrangian coordinates (s, z). In our case, variables change only with the coordinate s. As we do not regard branches in this approach, then the domain is a segment $sin[0, S]$. The value of S is the length of the generating line from one pole of the shell to another. We cut the domain into elements, which are segments $[s_i, s_{i+1}]$, where $0 \leq i \leq N-2$, so obtaining $N-1$ elements bounded by N nodes.

Each variable is assumed to have linear distribution along each element, so that the internal values are expressed linearely by the values in the nodes:

$$v(s) = v_i + \frac{v_{i+1} - v_i}{s_{i+1} - s_i}(s - s_i),$$

where v is any one of the variables, $s \in [s_i, s_{i+1}]$, and v_i is value in the i-th node.

The equations evaluating vector W_1 can be represented in more detailed form:

$$C\frac{\partial W_1}{\partial t} = \frac{E}{r^0}\frac{\partial r^0}{\partial s} + \frac{\partial F}{\partial s} + G.$$

We regard any node i and the elements adjacent to it. In our case, there are generally 2 elements placed to the left and to the right except for the leftmost and rightmost nodes both laying on the axis. We integrate the equations on halves of each adjacent elements, and using our assumption of linear distribution, each integral can be evaluated analytically thus simplifying calculations. As there are no second-order derivatives in the right side of the equations, then the assumption of linear distribution is enough to obtain correct expressions. For the right side we obtain an expression depending on 3 successive nodal values of W and V as result of integrating. Integrating the left side and equating it to right, we obtain implicit set of linear equations with the same matrix evaluating dW_1. In our case matrices of all the equations are 3-diagonal, and this helps us to invert them with direct method of binary substitution.

The complete operation-of transfer from the time layer n to the next layer consists of following steps.

a. Determine the timestep value h_t according to the Courant criterion modified to avoid overshoots in evaluating kinetic equations.

b. Get the values of loading P^n at the current time moment.

c. Evaluate $V^n = V(W^n, P^n)$.

d. Evaluate dW^n consisting of dW_1^n and dW_2^n. For the first set of equations we apply finite elements technique, the second set is simply evaluated from expressions.

e. Predictor - preliminary evaluation of W to the next time layer:

$$\hat{W} = W^n + h_t \cdot dW^n.$$

f. Increase time counter and get the loading P^{n+1} on the next layer.

g. Evaluate $\hat{V} = V(\hat{W}, P^n)$.

h. Evaluate $d\hat{W}$ using the same technique as in the item d.

i. Corrector stage - obtain values of W on the next time layer:

$$W^{n+1} = W^n + \frac{h_t}{2}(d\hat{W} + dW^n).$$

j. Filtering the probable non-physical oscillations of velocities of displacements. This stage was suggested in [7].

Chapter 2

Part II. Results of numerical modelling.

2.1 Foreword.

The present Part contains the description of the results of numerical modelling of dynamical deforming of the walls of an axisymmetrical containment made of thermoviscoelastic laminated damageable composite material under the influence of internal loading. Two types of internal loading were regarded to demonstrate the utility of the composite model. The first one was characterised by a uniform increase of pressure in the containment that brought to an expansion of the shell and accumulation of damages wherein nonuniformity was introduced only by the initial difference of curvatures in different zones of the shell. In fact it was shown that for the case of uniform internal loading of a shell having the shape different from a spherical one there appeared nonuniformities in accumulation of damages and specific dissipation was maximal in the zones of maximal curvature gradients.

The second type of loading regarded was the one in reflected shock waves caused by internal explosion in a gas-filled containment. The rates of wall loading were determined having incorporated the present composite shell model into a hydrocode. To garantee the axisymmetrical loading pattern the centre of the explosion could be placed in any place of the axis of symmetry of the shell. A more detailed description of the model determining the wall loading and of the flow pattern in the gas inside the containment will be given below.

2.2 Determining the internal loading of a containment.

The internal nonuniform loading of the walls of the containment was determined within the frames of an assumption that the containment was filled in with an inert or chemically reacting gas mixture. The internal explosion was simulated by introducing discontinuity in the initial conditions: assigning high pressure and density values for the parameters inside a relatively small zone on the axis of symmetry. To describe the originating flow a gasdynamical model for turbulent flows in confined volumes was used.

2.2.1 Mass balance equations in the gas phase.

The mass balance of the k-th component is:

$$\partial_t(\rho_k) + \nabla \cdot (\rho_k \vec{u_k}) = \dot{\mathcal{M}}_k,$$

where ρ_k is the density of the component (mass per gas phase volume unit), $\vec{u_k}$ is the velocity vector of this component and $\dot{\mathcal{M}}_k$ is mass flux to the k-th component from the other components.

The following notations and definitions are introduced: $\rho = \sum_k \rho_k$ for gas phase density, $\rho u = \sum_k \rho_k u_k$ for gas phase general velocity vector, $\vec{w_k} = \vec{u_k} - \vec{u}$ for the velocity of k-th component diffusion, $I_k = \rho_k \vec{w_k}$ for the diffusive flux of k-th component, $Y_k = \rho_k/\rho$ for mass fraction of the k-th component so that:

$$\sum_k Y_k = 1, \ \sum_k I_k = 0.$$

With these definitions the mass balance equation for the k-th component in the gas phase can be transformed into:

$$\partial_t(\rho Y_k) + \nabla \cdot (\rho \vec{u} Y_k) = \dot{\mathcal{M}}_k - \nabla \cdot I_k. \tag{1}$$

After summing up the equations (1) for all the components the general mass balance equation for the gas phase is obtained:

$$\partial_t(\rho) + \nabla \cdot (\rho \vec{u}) = 0. \tag{2}$$

After Favre averaging of the equation (2) with the ρ weight the averaged mass balance equation for the gas phase is obtained:

$$\partial_t(\overline{\rho}) + \nabla \cdot (\overline{\rho}\tilde{u}) = 0. \tag{3}$$

By averaging (1) in the same way and using the notation $I_k^t = \overline{\rho}\widetilde{u"Y_k"}$ for the turbulent diffusion flux the averaged mass balance for the k-th component in the gas phase is obtained:

$$\partial_t(\overline{\rho}\tilde{Y}_k) + \nabla \cdot (\overline{\rho}\tilde{u}\tilde{Y}_k) = \overline{\dot{\mathcal{M}}_k} - \nabla \cdot (\overline{I_k} + I_k^t). \tag{4}$$

2.2.2 Momentum equation for the gas phase.

For the k-th component in the gas phase the momentum equation is:

$$\partial_t(\rho_k \vec{u_k}) + \nabla \cdot (\rho_k \vec{u_k} \otimes \vec{u_k}) = -\nabla p_k + \rho_k \vec{g} + \nabla \cdot \tau_k + \dot{\mathcal{K}}_k,$$

where p_k is the partial pressure in the component, τ_k is the partial viscous tensor, $\vec{g}$ is the gravity acceleration vector and $\dot{\mathcal{K}}_k$ is the momentum flux to the component from the other components.

Summing up these equations for all components, the following equation is obtained:

$$\partial_t(\rho \vec{u}) + \nabla \cdot (\rho \vec{u} \otimes \vec{u}) = -\nabla p + \rho \vec{g} + \nabla \cdot \tau, \tag{5}$$

where: $p = \sum_k p_k$ is the pressure in the gas phase according to Dalton's law,

$$\sum_k \dot{\mathcal{K}}_k = 0$$

is the condition of agreement for momentum fluxes from all the components. It is also assumed that the viscous stresses tensor for multicomponents flow is $\tau = \sum_k (\tau_k - \frac{1}{\rho_k} I_k \otimes I_k)$.

Following the Favre's techniques [4] the averaging of (5) yields:

$$\partial_t(\overline{\rho}\tilde{u}) + \nabla \cdot (\overline{\rho}\tilde{u} \otimes \tilde{u}) = \overline{\rho}g - \overline{\nabla p} + \nabla \cdot (\overline{\tau} + \tau^t), \tag{6}$$

where $\tau^t = -\overline{\rho}\widetilde{u" \otimes u"}$ is the Reynolds stress tensor.

2.2.3 Energy balance equation for the gas phase.

For each component in the gas phase it is possible to write the following energy balance equation:

$$\partial_t(\rho_k E_k) + \nabla \cdot (\rho_k \vec{u_k} E_k) = \rho_k \vec{u_k} \cdot \vec{g} - \nabla \cdot (p_k \vec{u_k}) - \nabla \cdot I_{qk} + \nabla \cdot (\tau_k \cdot \vec{u_k}) + \rho_k \theta_k + \dot{\mathcal{E}}_k,$$

where $E_k = e_k + \frac{1}{2}u_k^2$ is a sum of internal and kinematic energy for the k-th component, I_{qk} is conductive heat flux to the k-th component, θ_k is the radiation heat flux, $\dot{\mathcal{E}}_k$ is the heat flux from the other components. It is assumed that the gas phase is a mixture of perfect gases, so that:

$$e_k = c_{vk}T + h_{0k}, \qquad p_k = \frac{R_g}{W_k}\rho_k T,$$

where T is the temperature, c_{vk} is the heat capacity at constant volume, W_k is the molar mass and R_g is the gas constant,h_{0k} is the chemical energy of the k-th component.

The following notations for the mixture energy and generalized heat flux are used:

$$E = \sum_k Y_k E_k = \sum_k (Y_k e_k + \frac{I_k \cdot I_k}{2\rho_k^2}) + \frac{u \cdot u}{2},$$

$$I_q = \sum_k [I_{qk} + h_k I_k - (\tau_k - \frac{I_k \otimes I_k}{2\rho_k}) \cdot \frac{I_k}{\rho_k}] = J_q + \sum_k h_k I_k,$$

where $h_k = e_k + \frac{p_k}{\rho_k}$ is the enthalpy of k-th component. With these notations the summing up of the energy balance equations for all components leads to the following equation:

$$\partial_t(\rho E) + \nabla \cdot (\rho \vec{u} E) = \rho \vec{u} \cdot \vec{g} - \nabla \cdot (p\vec{u}) - \nabla \cdot I_q + \nabla \cdot (\tau \cdot \vec{u}) + \rho\theta, \tag{7}$$

where the condition of agreement for energy exchange between the components

$$\sum_k \dot{\mathcal{E}}_k = 0$$

is taken into account.

The terms of the second and higher orders of diffusion fluxes are neglected in the expression for the mixture energy. The equation of state for the gas phase and the expressions for the internal energy and enthalpy then take the form:

$$p = R_g \rho T \sum_k \frac{Y_k}{W_k}, \qquad e = \sum_k Y_k(c_{vk}T + h_{0k}), \qquad h = \sum_k Y_k(c_{pk}T + h_{0k}). \tag{8}$$

Averaging (7) by Favre's techniques allows to obtain:

$$\partial_t(\overline{\rho}\tilde{E}) + \nabla \cdot (\overline{\rho}\tilde{u}\tilde{E}) = \overline{\rho}\tilde{u} \cdot g - \nabla \cdot (\overline{\rho u} - \overline{\rho}\widetilde{u"E"}) - \nabla \cdot \overline{I_q} + \nabla \cdot (\overline{\tau \cdot u}) + \overline{\rho}\tilde{\theta}.$$

Assuming the expression (8) to be true also for the averaged values, brings the following assumptions:

$$\sum_k \frac{R_g}{W_k} \widetilde{T"Y_k"} \ll \frac{\overline{p}}{\rho}, \qquad \sum_k c_{vk} \widetilde{T"Y_k"} \ll \overline{e}, \qquad \sum_k c_{pk} \widetilde{T"Y_k"} \ll \overline{h}.$$

With these assumptions finally the averaged energy balance equation can be obtained:

$$\partial_t(\overline{\rho}\tilde{E}) + \nabla \cdot (\overline{\rho}\tilde{u}\tilde{E}) = \overline{\rho}\tilde{u} \cdot g - \nabla \cdot (\overline{p}\tilde{u}) - \nabla \cdot (\overline{I_q} + I_q^t) + \nabla \cdot (\overline{\tau \cdot u} + \tau^t \cdot \tilde{u}) + \overline{\rho}\tilde{\theta}. \quad (9)$$

The notation $I_q^t = \overline{\rho} \sum_k c_{pk} Y_k \widetilde{u"T"} + \sum_k (c_{pk}\tilde{T} + h_{0k}) I_k^t = J_q^t + \sum_k (c_{pk}\tilde{T} + h_{0k}) I_k^t$ is used for the generalized turbulent heat flux. The expression for the mixture energy $E = \sum_k Y_k(c_{vk}\tilde{T} + h_{0k}) + \frac{\tilde{u}\cdot\tilde{u}}{2} + k$, contains the averaged kinematic energy of turbulent pulsations k(the last term is usually neglected in calculations because it is assumed to be much smaller than the scalar product of the averaged gas velocity).

2.2.4 Fluxes modelling and closing the K-epsilon model.

According to the standard k-epsilon model for compressible gas flows, the following model for turbulent fluxes is introduced:

$$\overline{\tau} + \tau^t = \overline{\rho}(\nu + \nu^t)(\nabla\tilde{u} + \nabla\tilde{u}^T - \frac{2}{3}\nabla \cdot \tilde{u}I) - \frac{2}{3}\overline{\rho}kI,$$

$$\overline{I_k} + I_k^t = -\overline{\rho}(D + \frac{\nu^t}{\sigma_i})\nabla \cdot \tilde{Y}_k,$$

$$\overline{J_q} + J_q^t = -\sum_k c_{pk}\overline{\rho}(\lambda + \frac{\nu^t}{\sigma_t})\nabla \cdot \tilde{T}, \quad (10)$$

where I is the unit tensor of the second order. The energy dissipation term in the equation (9) can be transformed as:

$$\nabla \cdot (\overline{\tau \cdot u} + \tau^t \cdot \tilde{u}) = \nabla \cdot ((\overline{\tau} + \tau^t) \cdot \tilde{u}).$$

The turbulent kinematic viscosity ν^t is modelled according to k-epsilon model as:

$$\nu^t = C_\mu \frac{k^2}{\epsilon}. \quad (11)$$

The model is closed then by 2 equations for the kinematic energy of turbulent pulsations k and its decay due to dissipation ϵ:

$$\partial_t(\overline{\rho}k) + \nabla \cdot (\overline{\rho}\tilde{u}k) = \nabla \cdot (\rho(\nu + \frac{\nu^t}{\sigma_k})\nabla k) + \tau^t : \nabla\tilde{u} - \overline{\rho}\epsilon, \quad (12a)$$

$$\partial_t(\overline{\rho}\epsilon) + \nabla \cdot (\overline{\rho}\tilde{u}\epsilon) = \nabla \cdot (\rho(\nu + \frac{\nu^t}{\sigma_\epsilon})\nabla\epsilon) + \frac{\epsilon}{k}(C_{1\epsilon}\tau^t : \nabla\tilde{u} - C_{2\epsilon}\overline{\rho}\epsilon). \qquad (12b)$$

In this equations the Reynolds tensor τ^t can be modelled as:

$$\tau^t = \overline{\rho}\nu^t(\nabla\tilde{u} + \nabla\tilde{u}^T - \frac{2}{3}\nabla \cdot \tilde{u}I) - \frac{2}{3}\overline{\rho}kI.$$

The term containing k in the last expression is negligible as well as in the expression for the sum of viscous and Reynolds tensors.

The constants take the following values:

$$C_\mu = 0.09, \quad \sigma_k = 1, \quad \sigma_\epsilon = 1.3, \quad C_{1\epsilon} = 1.45, \quad C_{2\epsilon} = 1.92, \quad \sigma_i = \sigma_t = 1. \qquad (13)$$

The turbulent Prandtl and Schmidt numbers are assumed to be equal to 1 in (13).

2.2.5 Initial and boundary conditions.

The initial mean flow velocity in the air was supposed to be zero $\vec{u} = 0$, but the initial level of turbulence was introduced: $k(t = 0) = k_0; \epsilon(t = 0) = \epsilon_0$. A definite volume on the axis of symmetry $(0 \leq r \leq r_0)$, $X_1 \leq x \leq X_2$ was considered to be occupied by dense reaction products under high pressure. The rest of the containment was considered to be occupied by the gas of ambient pressure and density. At $t = 0$ the motion starts and the initial discontinuity in the pressure, density and temperature fields brings to formation of shock waves propagating inside the containment and being reflected by the walls.

The boundary conditions on the walls of the containment are the following:

$$\vec{u} = 0 - \text{the no-slip condition;}$$

$$\frac{\partial T}{\partial z} = \frac{\partial Y_k}{\partial z} = \frac{\partial k}{\partial z} = \frac{\partial \epsilon}{\partial z} = 0 - \text{the Neumann conditions.}$$

2.2.6 Computational techniques.

The calculations are carried out using two demi-steps to determine new parameters for the gaseous phase.

The value of the timestep is recalculated on the base of Courant criterion.

The system of gasdynamics equations can be rewritten in the following vector form:

$$\frac{\partial}{\partial t}\vec{U} + \frac{\partial}{\partial x}\vec{E} + \frac{\partial}{\partial r}\vec{F} + = \vec{H}, \tag{14}$$

where

$$\vec{U} = \begin{pmatrix} \dot{\rho} \\ \rho u \\ \rho v \\ \rho E \\ \rho k \\ \rho \epsilon \\ \rho Y_k \end{pmatrix}, \qquad \vec{E} = \vec{E}^H + \vec{E}^P = \begin{pmatrix} \rho u \\ \rho u^2 + p \\ \rho u v \\ \rho u E + u p \\ \rho u k \\ \rho u \epsilon \\ \rho u Y_k \end{pmatrix} + \begin{pmatrix} 0 \\ -\tau_{xx} \\ -\tau_{xz} \\ -u\tau_{xx} - v\tau_{xz} + J_{qx} \\ I_{kx} \\ I_{\epsilon x} \\ I_{kx} \end{pmatrix},$$

$$\vec{F} = \vec{F}^H + \vec{F}^P = \begin{pmatrix} \rho v \\ \rho u v \\ \rho v^2 + p \\ \rho v E + v p \\ \rho v k \\ \rho v \epsilon \\ \rho v Y_k \end{pmatrix} + \begin{pmatrix} 0 \\ -\tau_{xz} \\ -\tau_{zz} \\ -u\tau_{xz} - v\tau_{zz} + J_{qz} \\ I_{kz} \\ I_{\epsilon z} \\ I_{kz} \end{pmatrix},$$

$$\vec{H} = \vec{H}^H = \begin{pmatrix} 0 \\ 0 \\ 0 \\ 0 \\ P_k - \rho\epsilon \\ \frac{\epsilon}{k}(C_{1\epsilon}P_k - C_{2\epsilon}\rho\epsilon) \\ \dot{\mathcal{M}}_k \end{pmatrix}.$$

The formulae above contain the following notations: x, r - axial and radial coordinates respectively, u, v - mean velocity components in this coordinates, P_k is the turbulent energy production term (equation (12)). The superscript "H" means convection and production terms (hyperbolic part), "P" - generalized diffusive terms (including viscous, diffusive and thermoconductive terms, (parabolic part)). Note that the system (14) is mathematically overdefined, for $\sum_k Y_k = 1$, but in numerical calculations one more equation is kept for the control of precision and correction of results.

To solve the system (14) splitting by coordinates is used; it simplifies the solution and increases the possible timestep. The splitting is made according to MacCormack [5]. This

splitting represents the general operator $L(\Delta t)$ transferring U^n to the next timestep into U^{n+1}, in the form:

$$L(\Delta t) = L_x(\Delta t_x)L_r(\Delta t_r)L_r(\Delta t_r)L_x(\Delta t_x),$$
$$\text{or} \quad L(\Delta t) = L_r(\Delta t_r)L_x(\Delta t_x)L_x(\Delta t_x)L_r(\Delta t_r). \tag{15}$$

The sequence of operators in (15) yields the condition of symmetry. To yield the condition of timesteps, which together with the condition of symmetry ensures the second order of approximation, it is necessary to have:

$$\Delta t = 2\Delta t_x = 2\Delta t_r,$$

so that $\Delta t_x = \Delta t_r = \Delta t/2$. Both sequences of operators in (28) are able to represent the general operator $L(\Delta t)$; to avoid the accumulation of disagreements the sequences are changed at each timestep.

Each operator itself, L_x and L_r, is also split into two parts: one part is parabolic, L_x^P or L_r^P, the other is hyperbolico-parabolic, L_x^H or L_r^H, and contains terms, which are not present in L_x^P or L_r^P. This gives us the MacCormack rapid solver techniques [5]. The parabolic operator is solved using the implicit Laasonen scheme, the hyperbolico-parabolic operator is solved using FCT techniques[6]. This splitting removes viscosity from the timestep criterion and reduces it to the Courant criterion.

2.2.7 Results of numerical modelling of internal loading.

The results of numerical modelling of shock waves propagation and reflection inside the containment are shown in Figs. 2 - 3. The figures show the density and pressure fields inside the containment for different times. The length of the cylinder was $1m$, the radius - $0.5m$. The map of characteristic values of parameters is given in the upper right parts of the figures. The characteristic times are also given on the right screen. The black line segments on the figures reflect gas velocities.

The initial volume where the explosion takes place can be seen in Fig.2.a illustrating the initial density distribution at $t = 0$. Expansion of hot reaction products brings to a formation of a ball-shape zone of a compressed gas (Fig.2.b.) that after the reflection from a lower wall comes to a hemispherical shape (Figs.2.c, d.). The converging rarefaction waves bring to a decrease of density behind the diverging hemispherical shock wave (Figs.2.e, f). On reflecting the shock from the side walls of the containment density increases behind the reflected waves (Figs.2.g, h). The position of the reflected waves can be

easily tracked by the gradients of the velocity field. The reflected shock waves turn to be steeper and overtake the leading shock near the walls (Figs.2.h, i, k.) that finally brings to a formation of a Mach stem (Figs.2.l, m). The reflected shock waves are converging to the axis and bring to an increase of density after their collision (Figs.2.k, l, m).

The zone of high density originates near the upper wall after the reflection of the leading shock and the secondary shocks (Figs.2.m, n, o). The reflected shock wave propagates faster near the walls than in the center (Figs.2.p, q, r, s.) because it meets in the center a more dense gas with a large accumulated axial velocity.

The pressure field evolution shown in Figs.3.$a - n$ gives an idea of the internal loading of the shell of the containment. The ball-shape shock wave is formed at the very beginning (Fig.3.a). In reflection of the shock wave from the nearest lower wall the loading starts that spreads from the axis of symmetry (Figs.3.b, c, d, e). The converging rarefaction waves gradually decrease the pressure in the center (Figs.3.d, e.) and a high pressure zone is present only in the primary shock wave (Fig.3.e). The intensity of the primary shock wave decays but a new pressure increase takes place in the transverse shock waves reflected from the side walls (Figs.3.f, g). Converging shock waves bring to a pressure increase on the axis of symmetry (Figs.3.h, i). On reflecting the primary shock from the upper wall the pressure increases in the reflected shock wave (Figs.3.k, l, m.) and then gradually decreases due to the influence of rarefaction waves (Fig.3.n).

This typical example of wall loading in internal explosion gives wide possibilities to investigate the behaviour of the model for damageable composite shell in nonuniform loading.

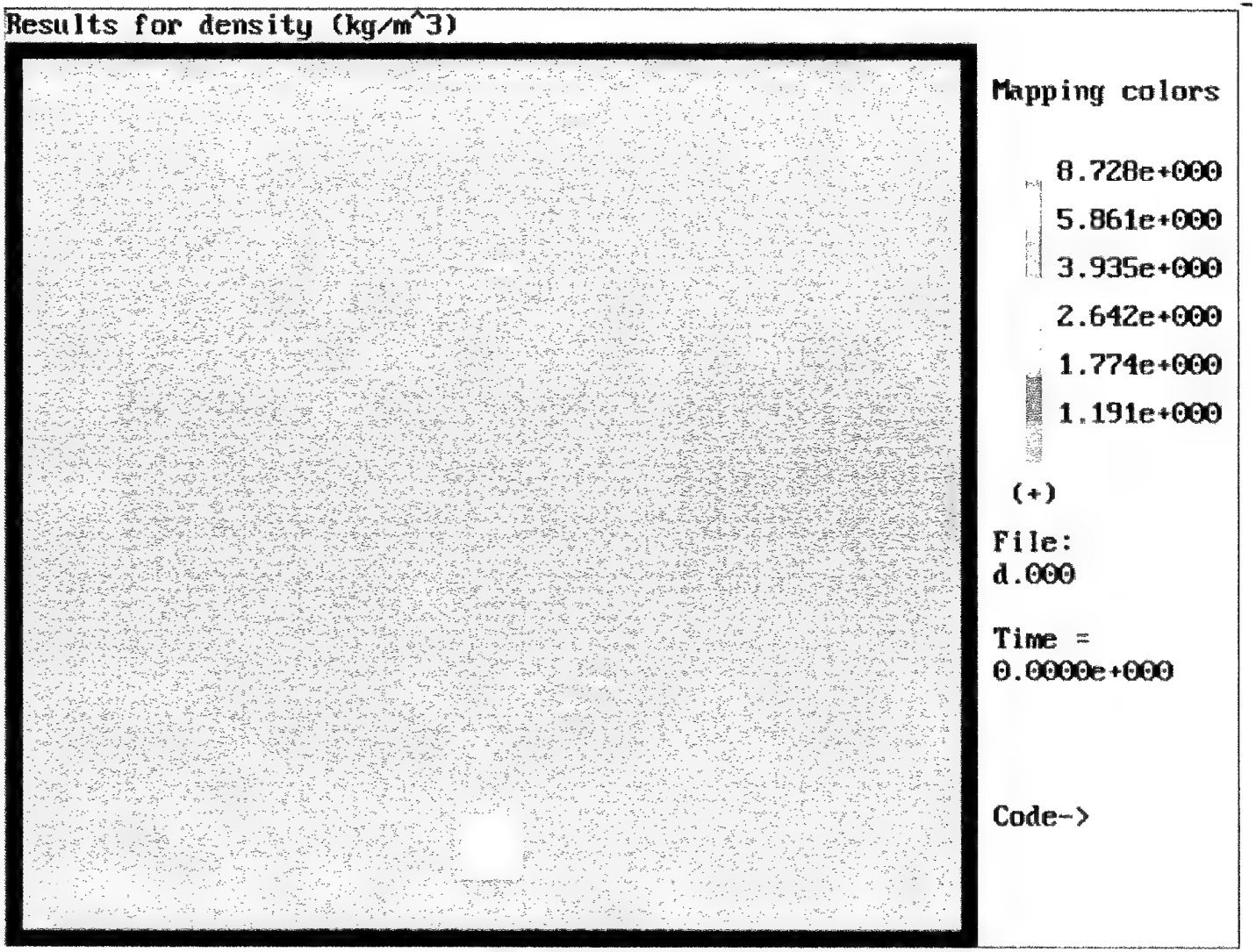
Results for density (kg/m^3)
Mapping colors
8.728e+000
5.861e+000
3.935e+000
2.642e+000
1.774e+000
1.191e+000
(+)
File:
d.000
Time =
0.0000e+000
Code->

Fig. 2.a.

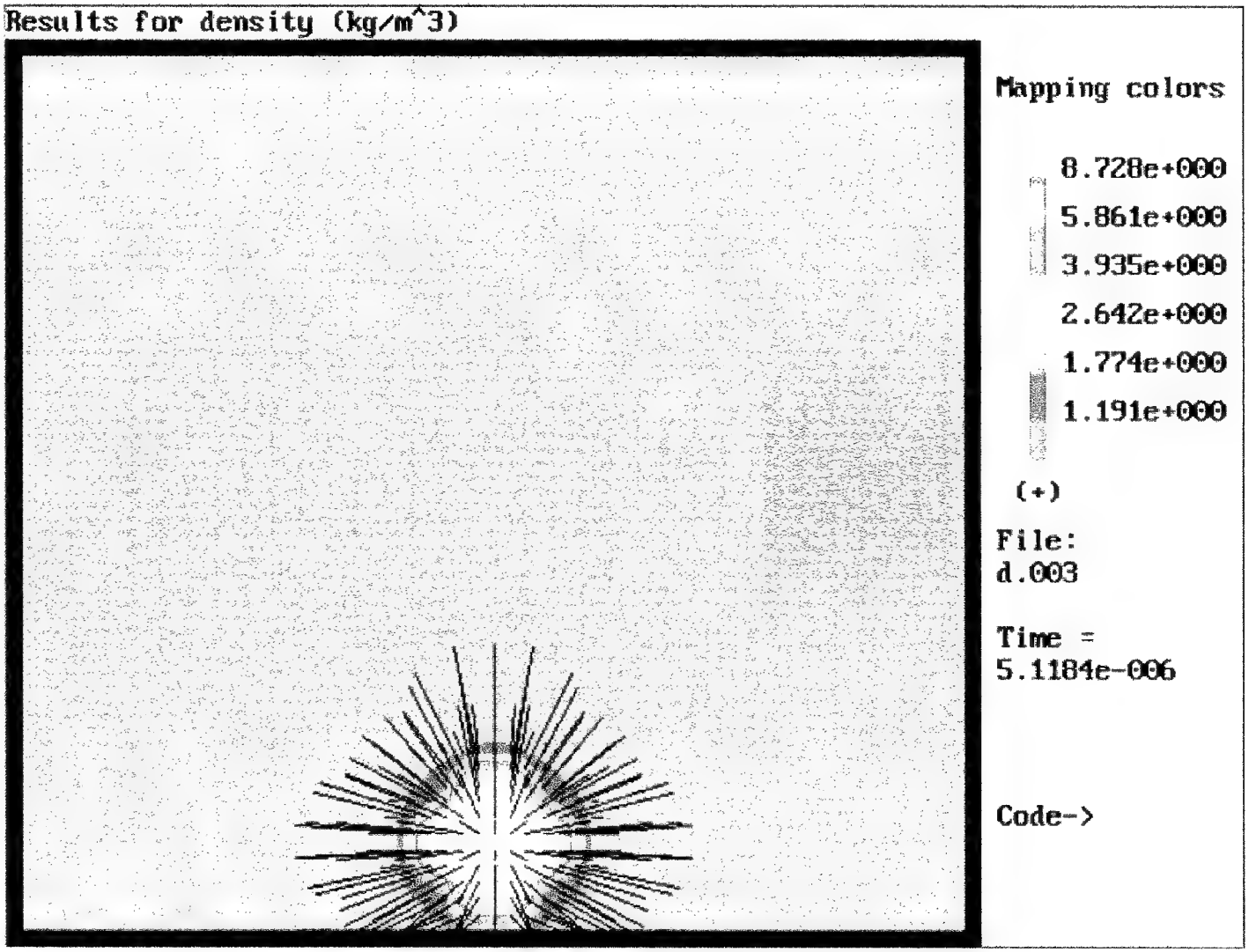
Results for density (kg/m^3)
Mapping colors
8.728e+000
5.861e+000
3.935e+000
2.642e+000
1.774e+000
1.191e+000
(+)
File:
d.003
Time =
5.1184e-006
Code->

Fig 2.6.

Results for density (kg/m^3)

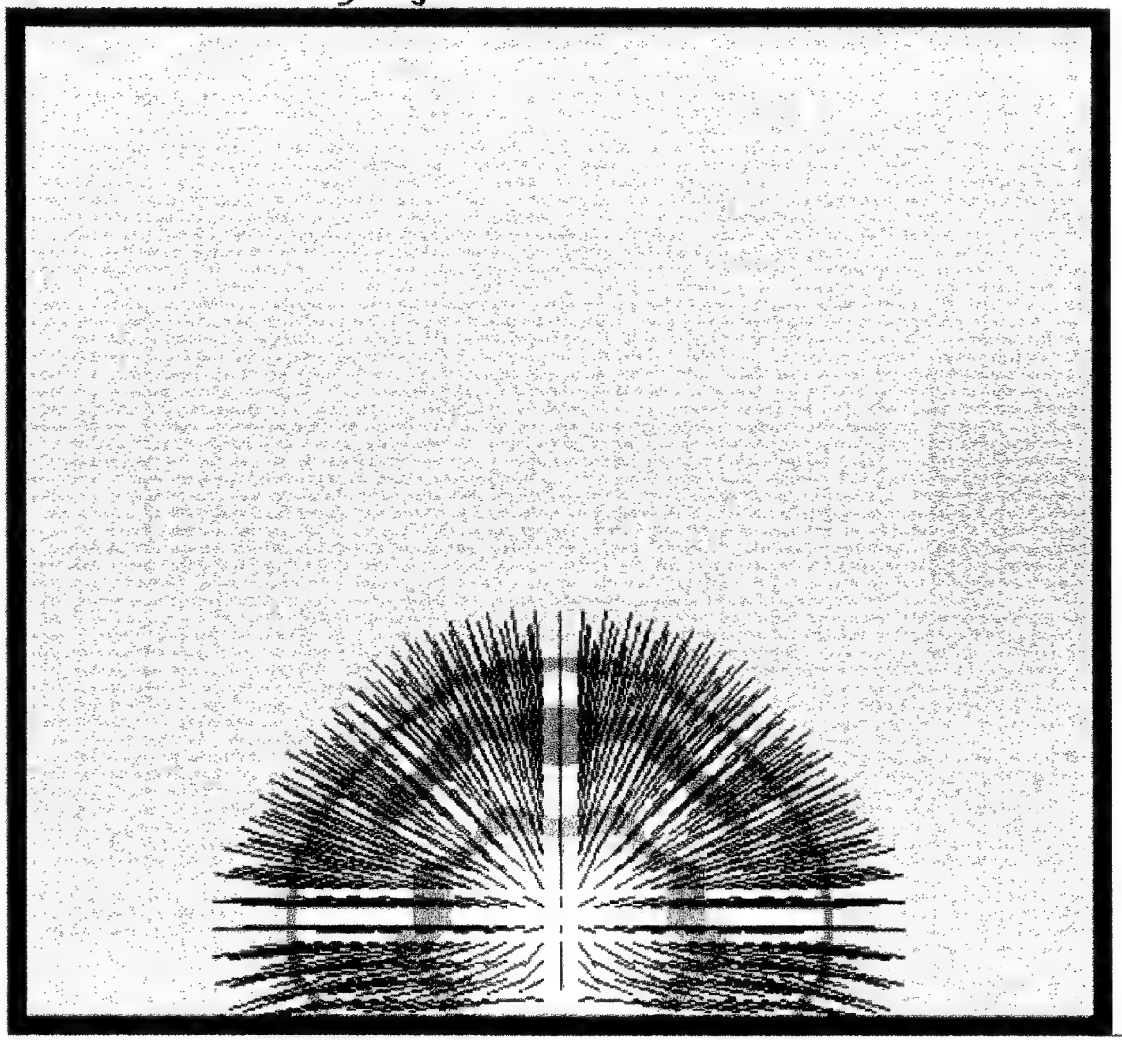

Mapping colors

8.728e+000
5.861e+000
3.935e+000
2.642e+000
1.774e+000
1.191e+000

(+)

File:
d.011

Time =
2.2551e-005

Code->

Fig. 2.c.
25

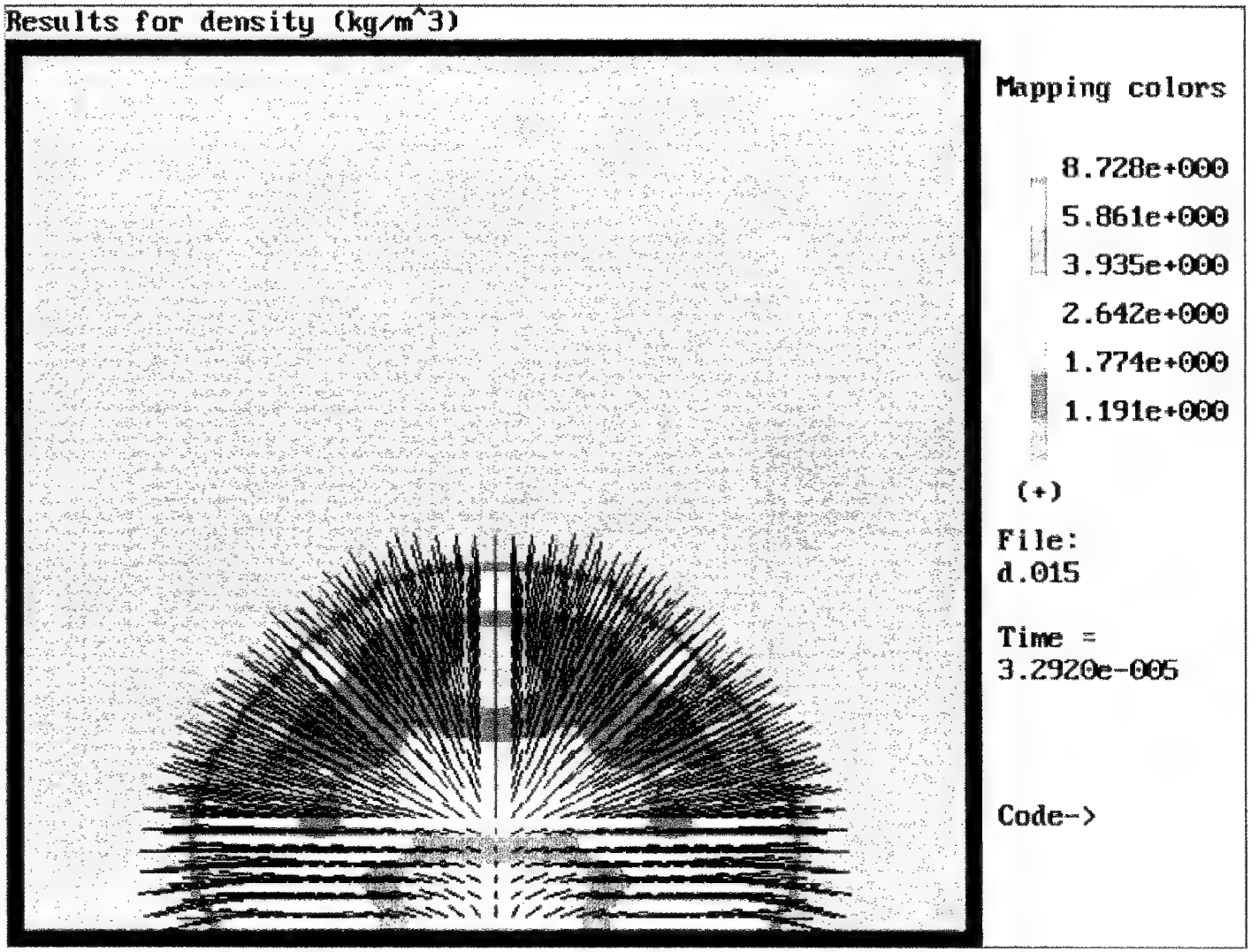
Results for density (kg/m^3)
Mapping colors
8.728e+000
5.861e+000
3.935e+000
2.642e+000
1.774e+000
1.191e+000
(+)
File:
d.015
Time =
3.2920e-005
Code->

Fig. 2.d

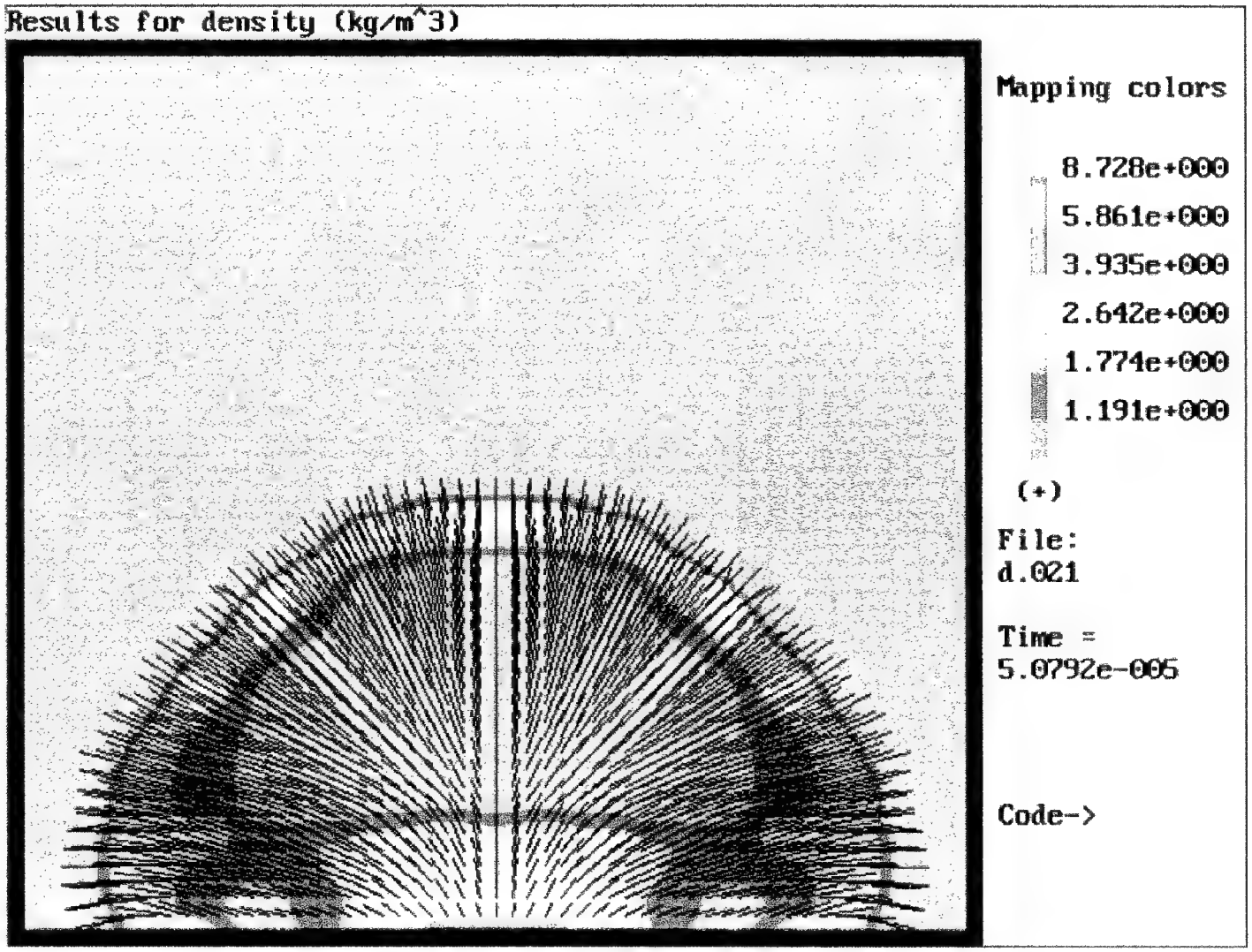
Results for density (kg/m^3)
Mapping colors
8.728e+000
5.861e+000
3.935e+000
2.642e+000
1.774e+000
1.191e+000
(+)
File:
d.021
Time =
5.0792e-005
Code->

Fig. 2.e

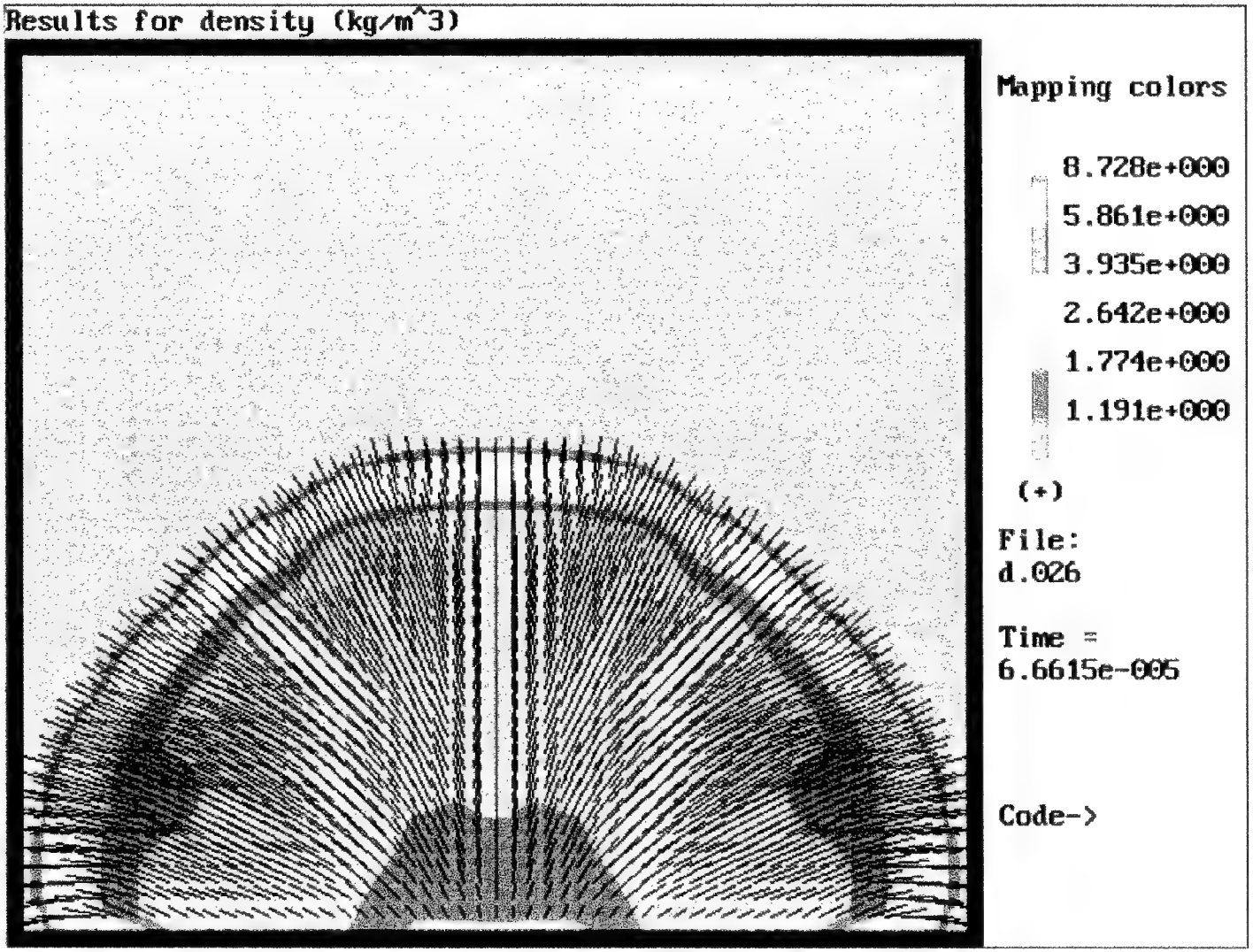
Results for density (kg/m^3)
Mapping colors
8.728e+000
5.861e+000
3.935e+000
2.642e+000
1.774e+000
1.191e+000
(+)
File:
d.026
Time =
6.6615e-005
Code->

Fig. 2.f.

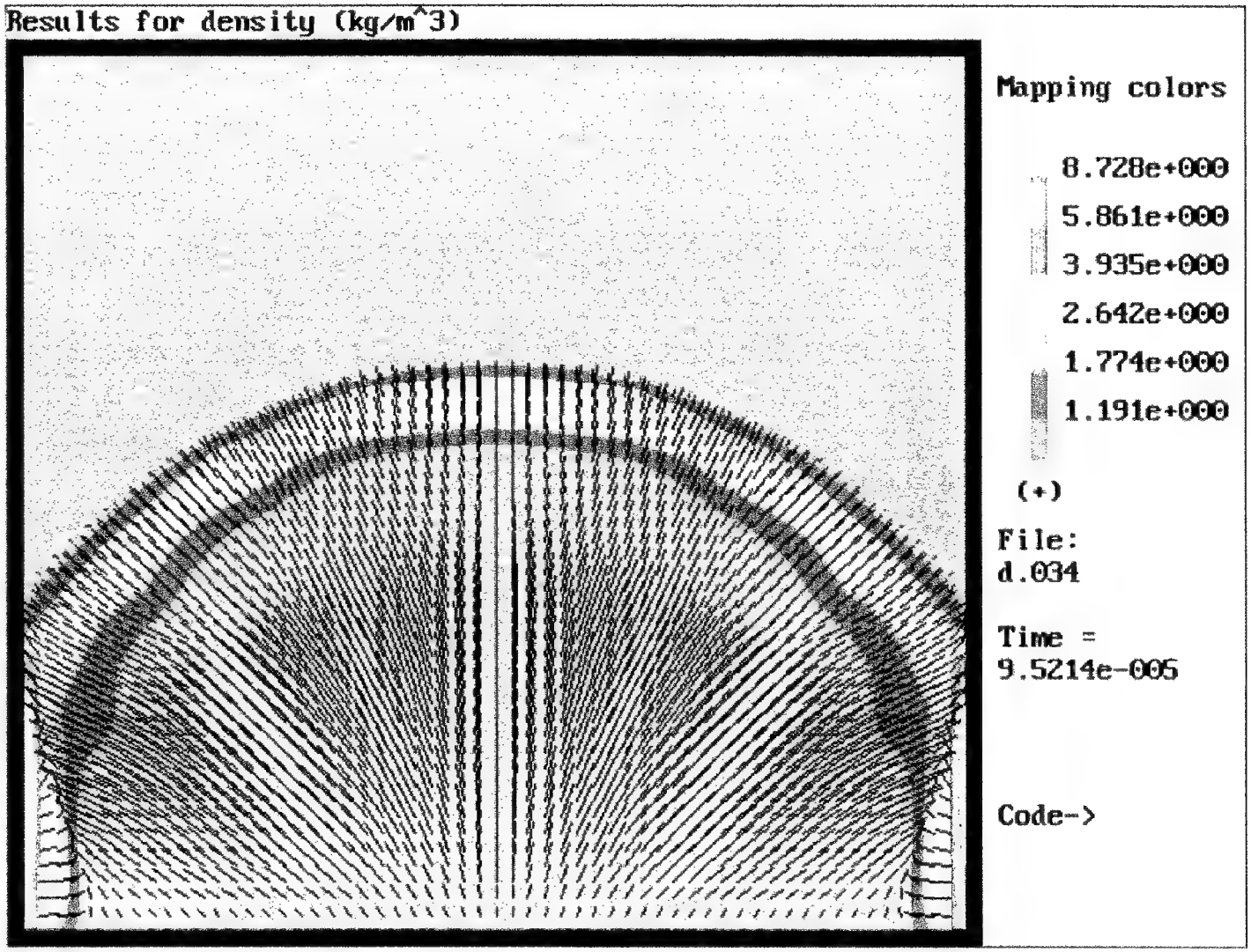
Results for density (kg/m^3)
Mapping colors
8.728e+000
5.861e+000
3.935e+000
2.642e+000
1.774e+000
1.191e+000
(+)
File:
d.034
Time =
9.5214e-005
Code->

Fig. 2.9.

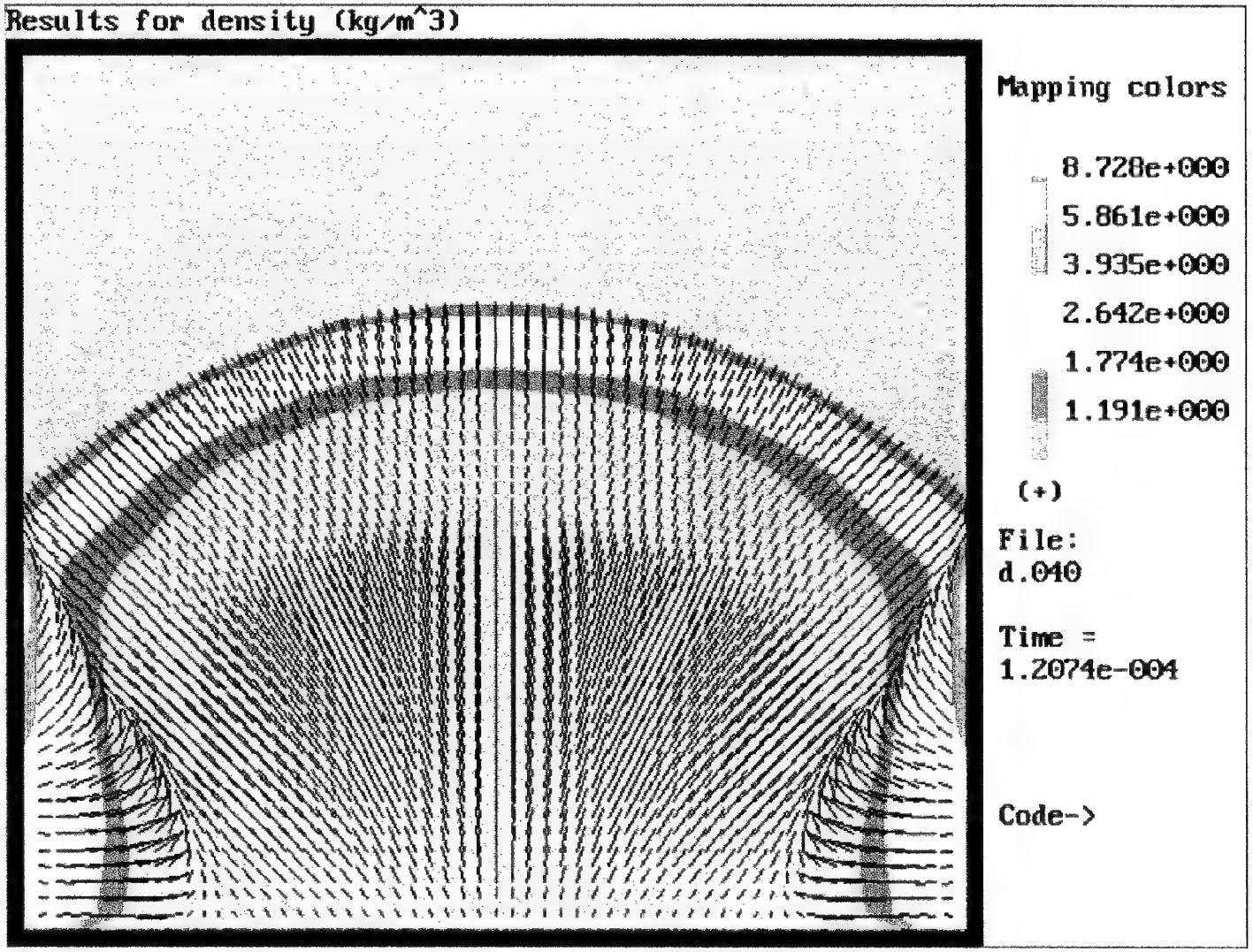
Results for density (kg/m^3)
Mapping colors
8.728e+000
5.861e+000
3.935e+000
2.642e+000
1.774e+000
1.191e+000
(+)
File:
d.040
Time =
1.2074e-004
Code->

Fig. 2.h.

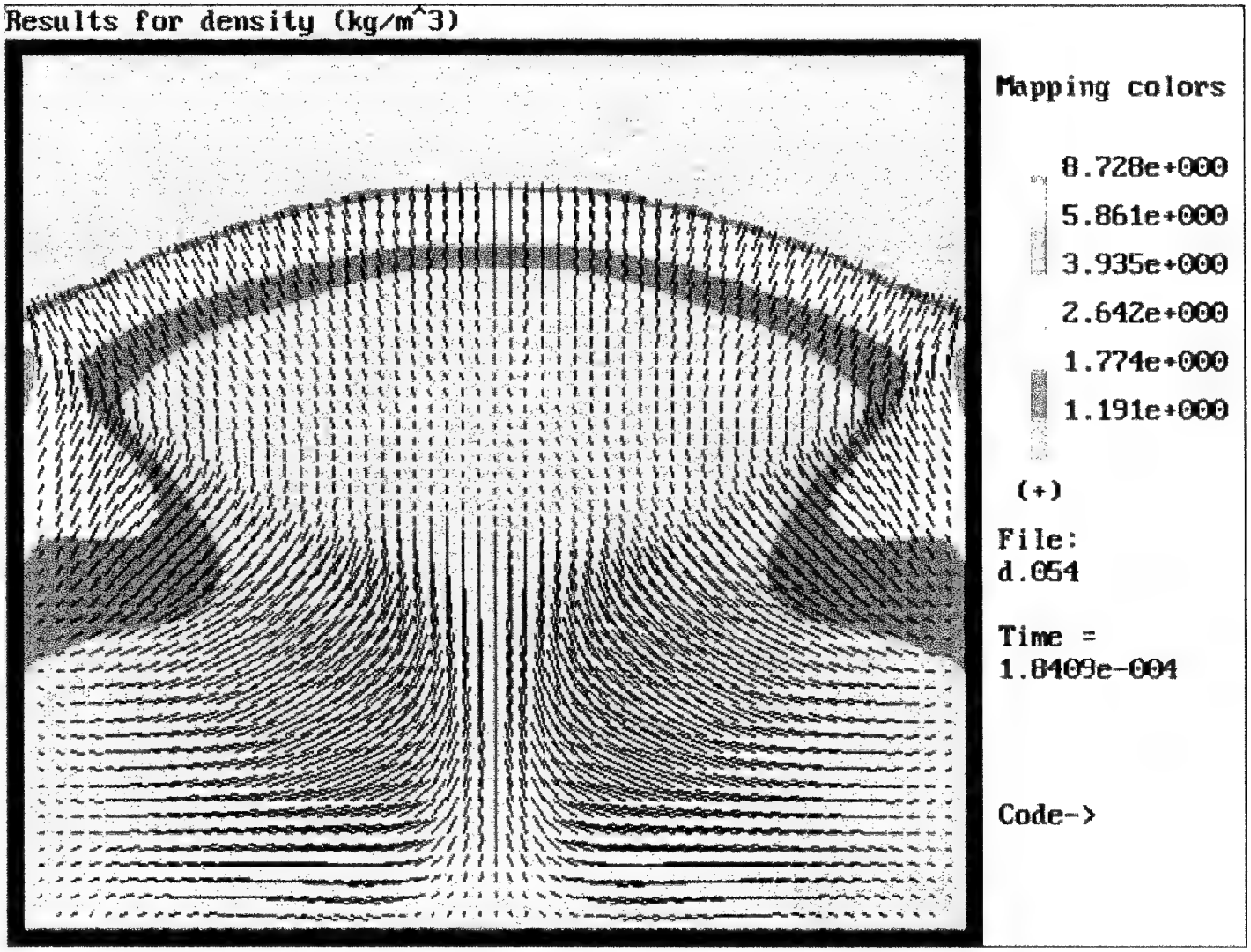
Results for density (kg/m^3)
Mapping colors
8.728e+000
5.861e+000
3.935e+000
2.642e+000
1.774e+000
1.191e+000
(+)
File:
d.054
Time =
1.8409e-004
Code->

Fig. 2.1.

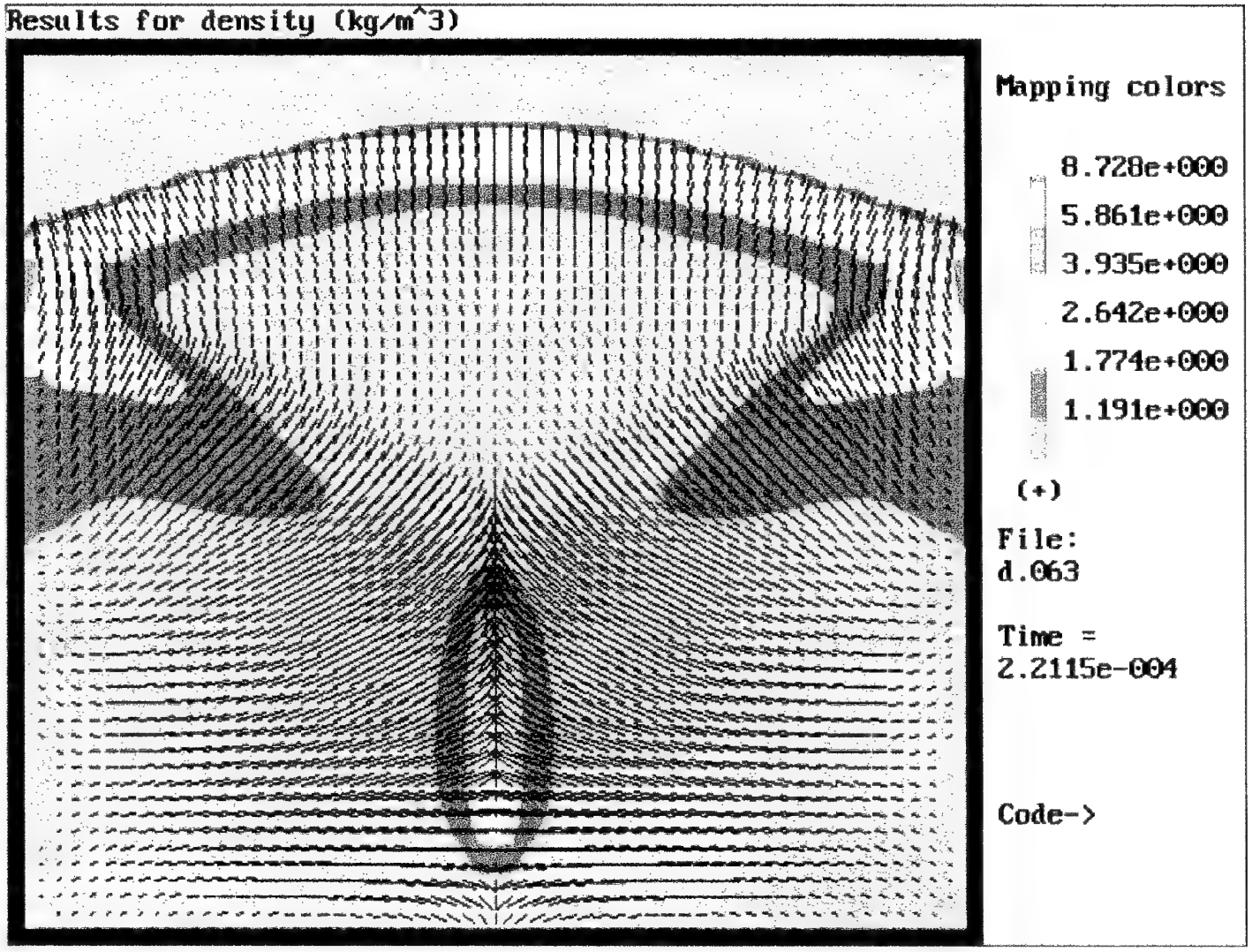
Results for density (kg/m^3)
Mapping colors
8.728e+000
5.861e+000
3.935e+000
2.642e+000
1.774e+000
1.191e+000
(+)
File:
d.063
Time =
2.2115e-004
Code->

Fig. 2.k.

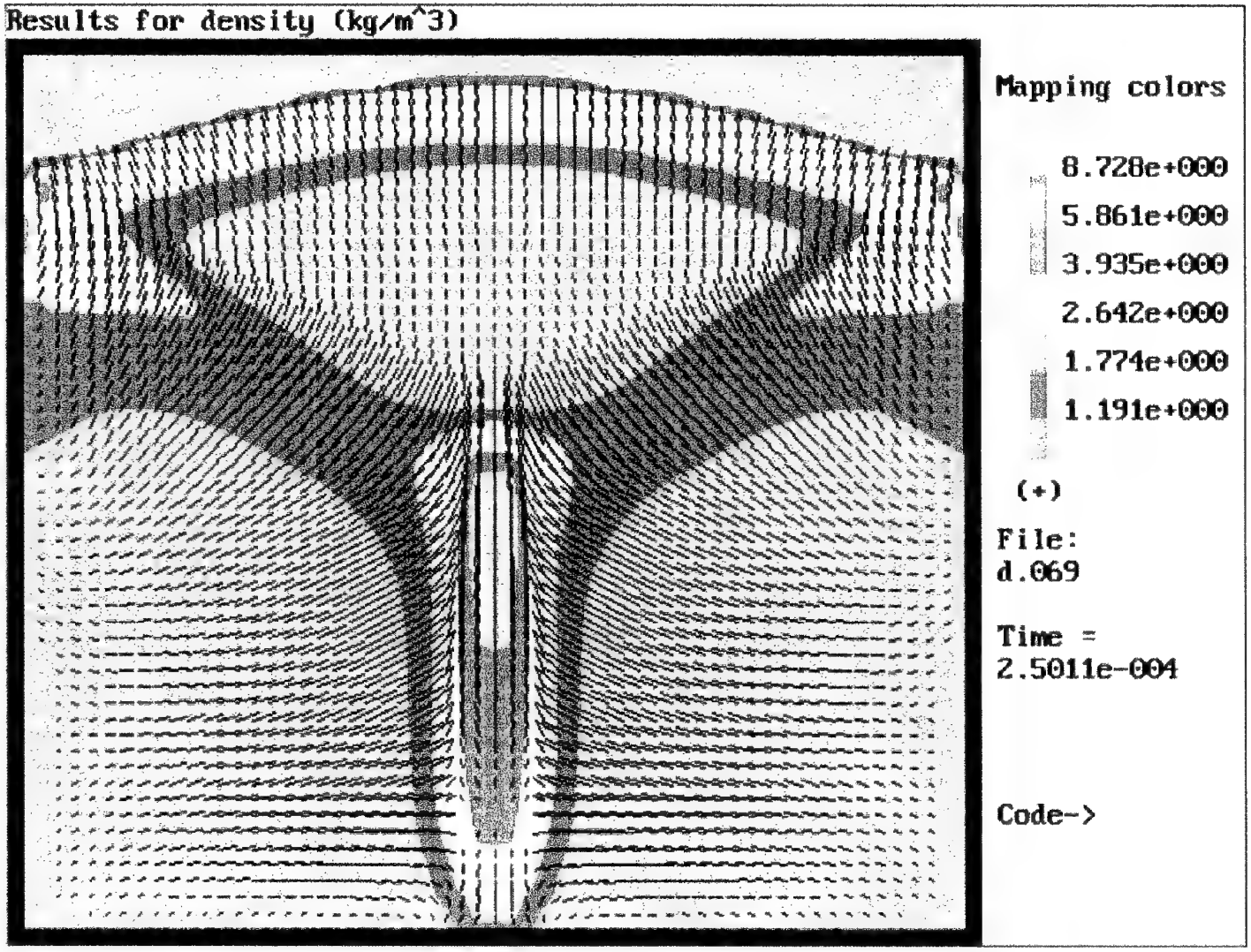
Results for density (kg/m^3)
Mapping colors
8.728e+000
5.861e+000
3.935e+000
2.642e+000
1.774e+000
1.191e+000
(+)
File:
d.069
Time =
2.5011e-004
Code->

Fig. 2.b.

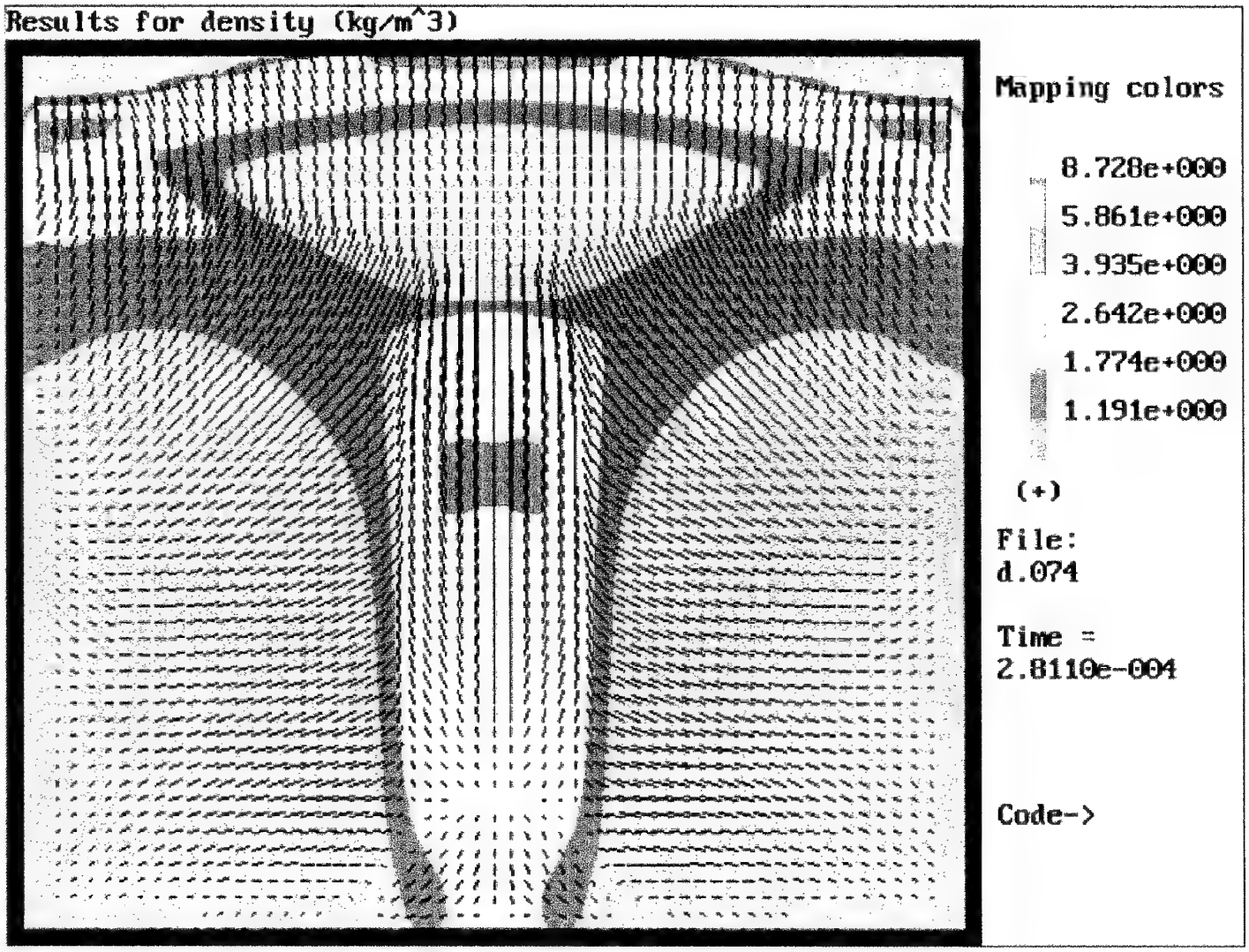
Results for density (kg/m^3)
Mapping colors
8.728e+000
5.861e+000
3.935e+000
2.642e+000
1.774e+000
1.191e+000
(+)
File:
d.074
Time =
2.8110e-004
Code->

Fig. 2.m.

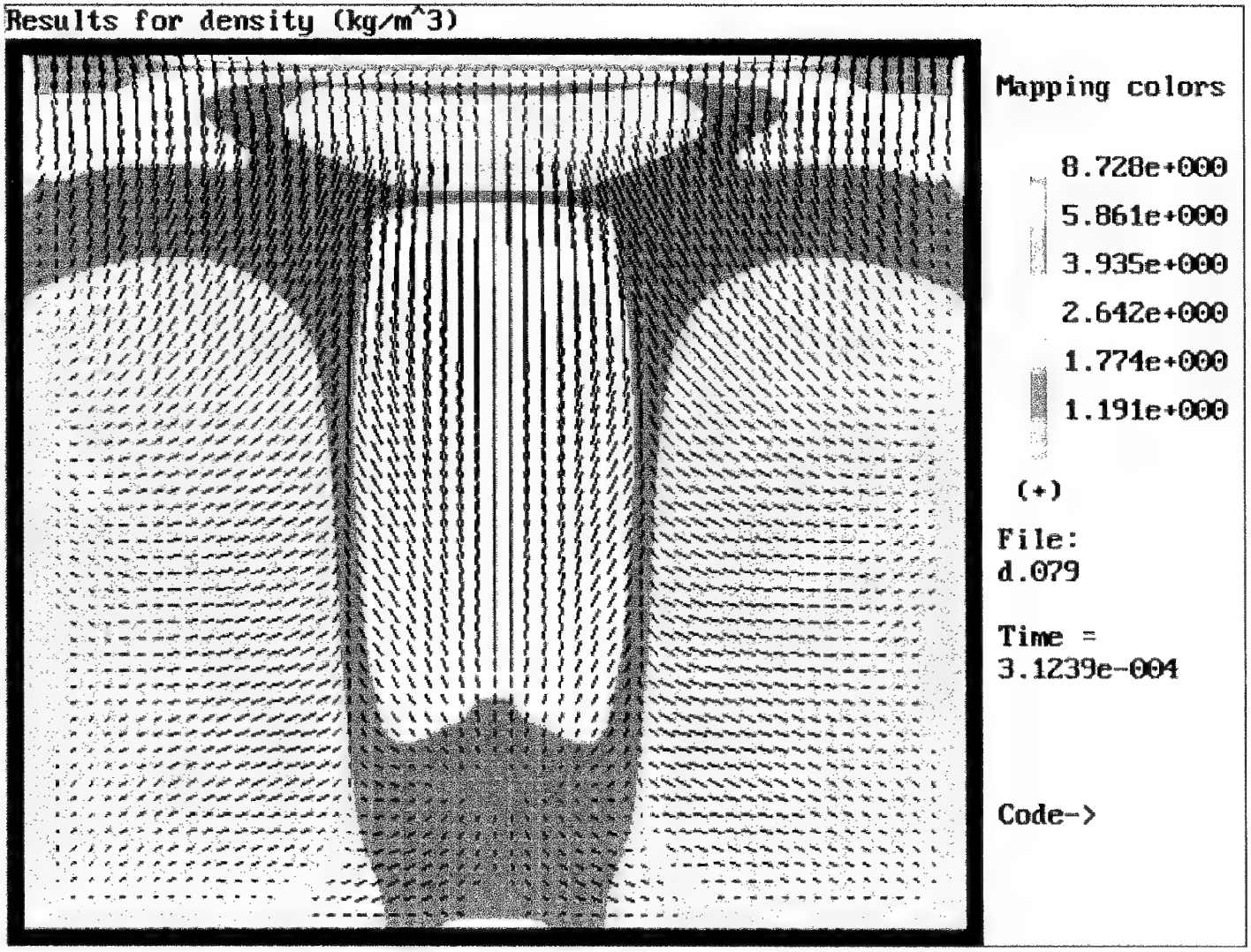
Results for density (kg/m^3)
Mapping colors
8.728e+000
5.861e+000
3.935e+000
2.642e+000
1.774e+000
1.191e+000
(+)
File:
d.079
Time =
3.1239e-004
Code->

Fig. 2. n.

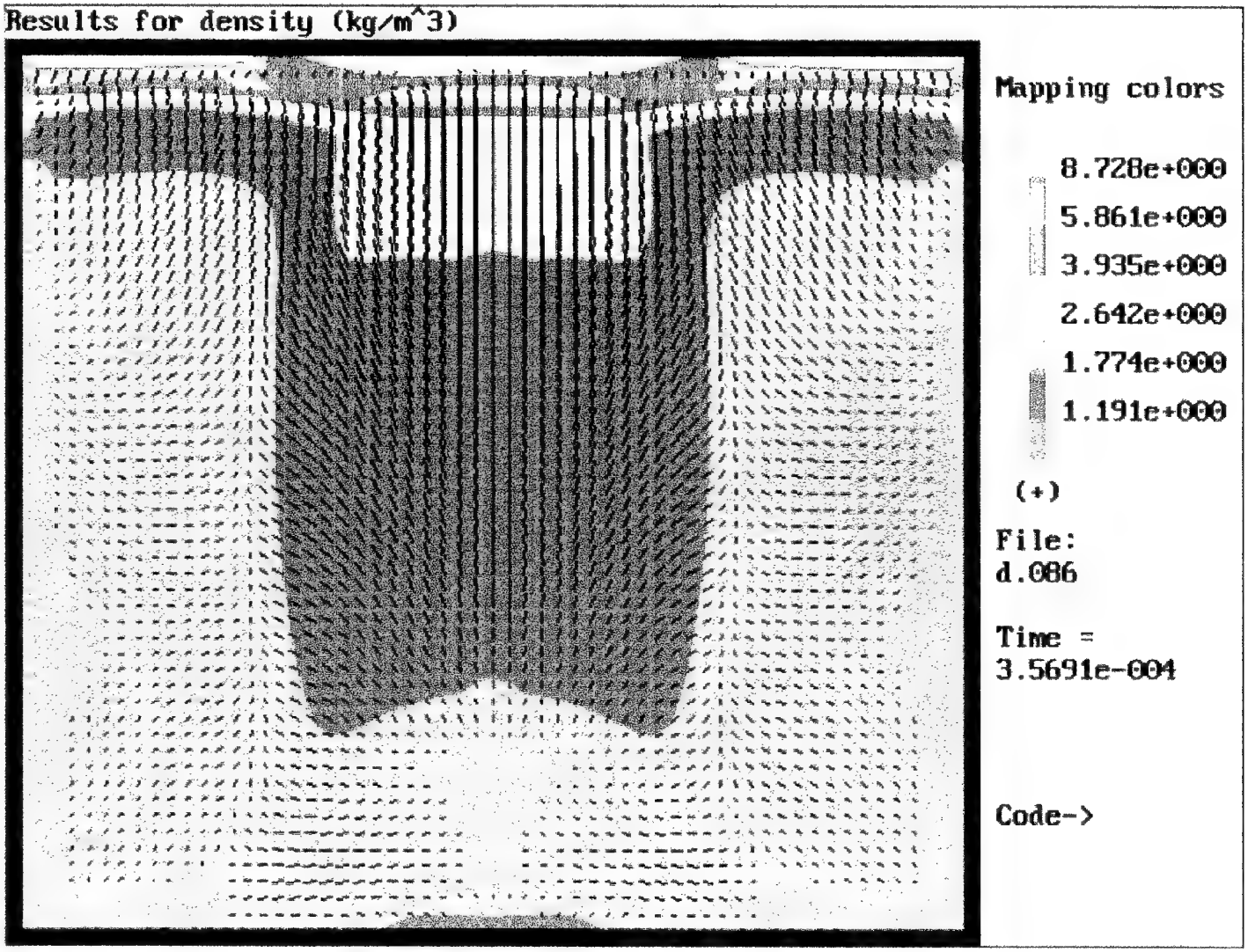
Results for density (kg/m^3)
Mapping colors
8.728e+000
5.861e+000
3.935e+000
2.642e+000
1.774e+000
1.191e+000
(+)
File:
d.086
Time =
3.5691e-004
Code->

Fig. 2.0.

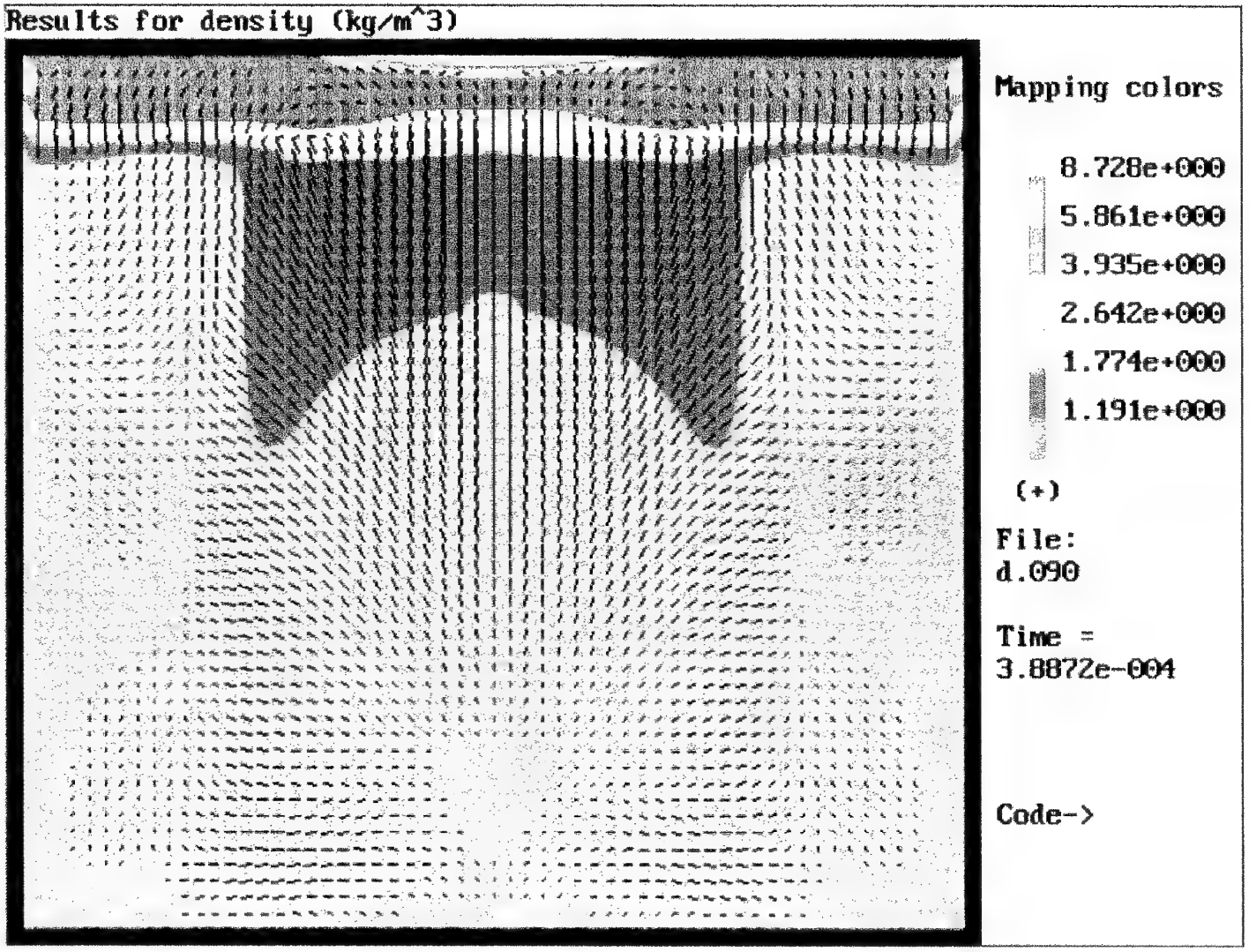
Results for density (kg/m^3)
Mapping colors
8.728e+000
5.861e+000
3.935e+000
2.642e+000
1.774e+000
1.191e+000
(+)
File:
d.090
Time =
3.8872e-004
Code->

Fig. 2, p. 37

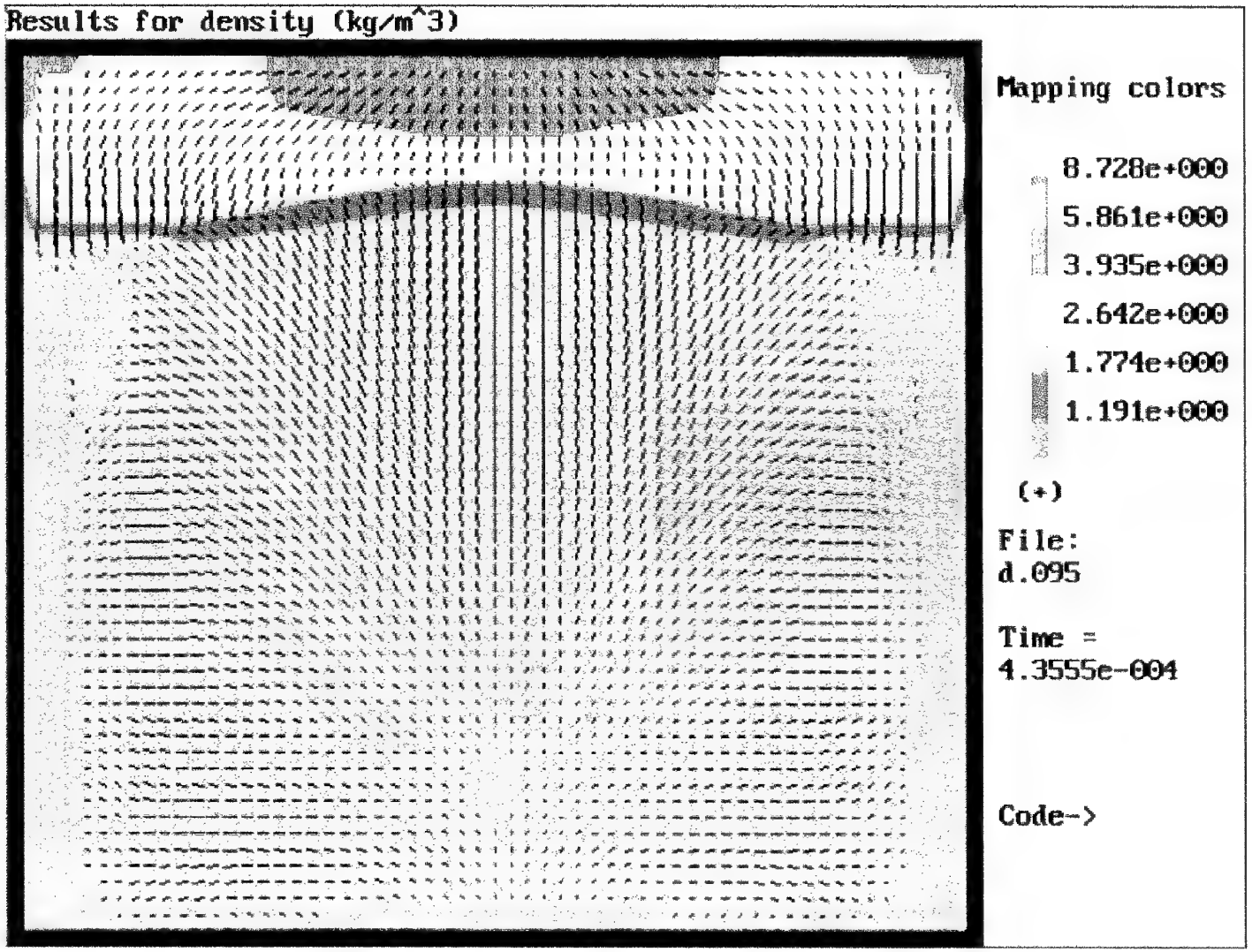
Results for density (kg/m^3)
Mapping colors
8.728e+000
5.861e+000
3.935e+000
2.642e+000
1.774e+000
1.191e+000
(+)
File:
d.095
Time =
4.3555e-004
Code->
Fig. 2.4.

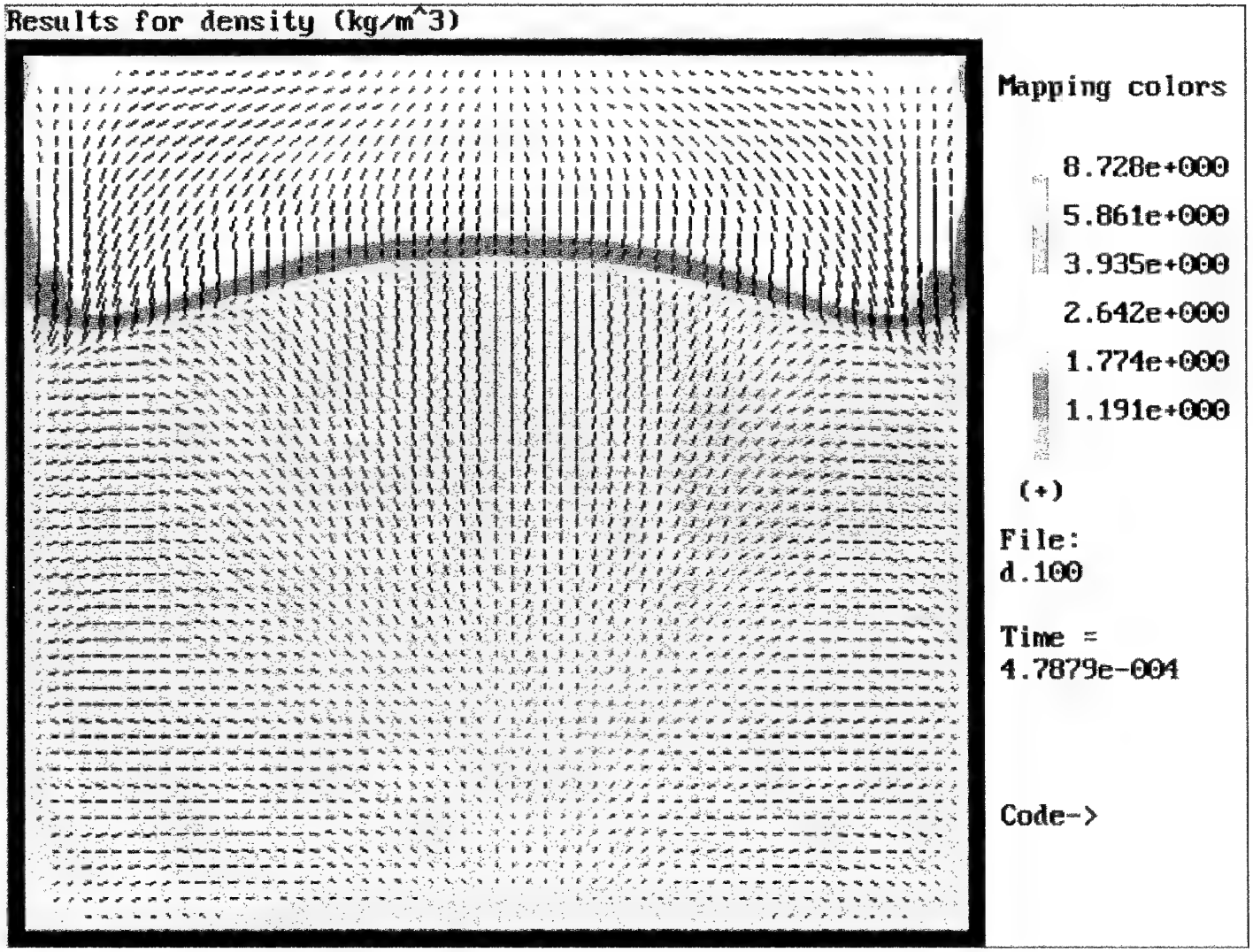
Results for density (kg/m^3)
Mapping colors
8.728e+000
5.861e+000
3.935e+000
2.642e+000
1.774e+000
1.191e+000
(+)
File:
d.100
Time =
4.7879e-004
Code->

Fig. 2.P.

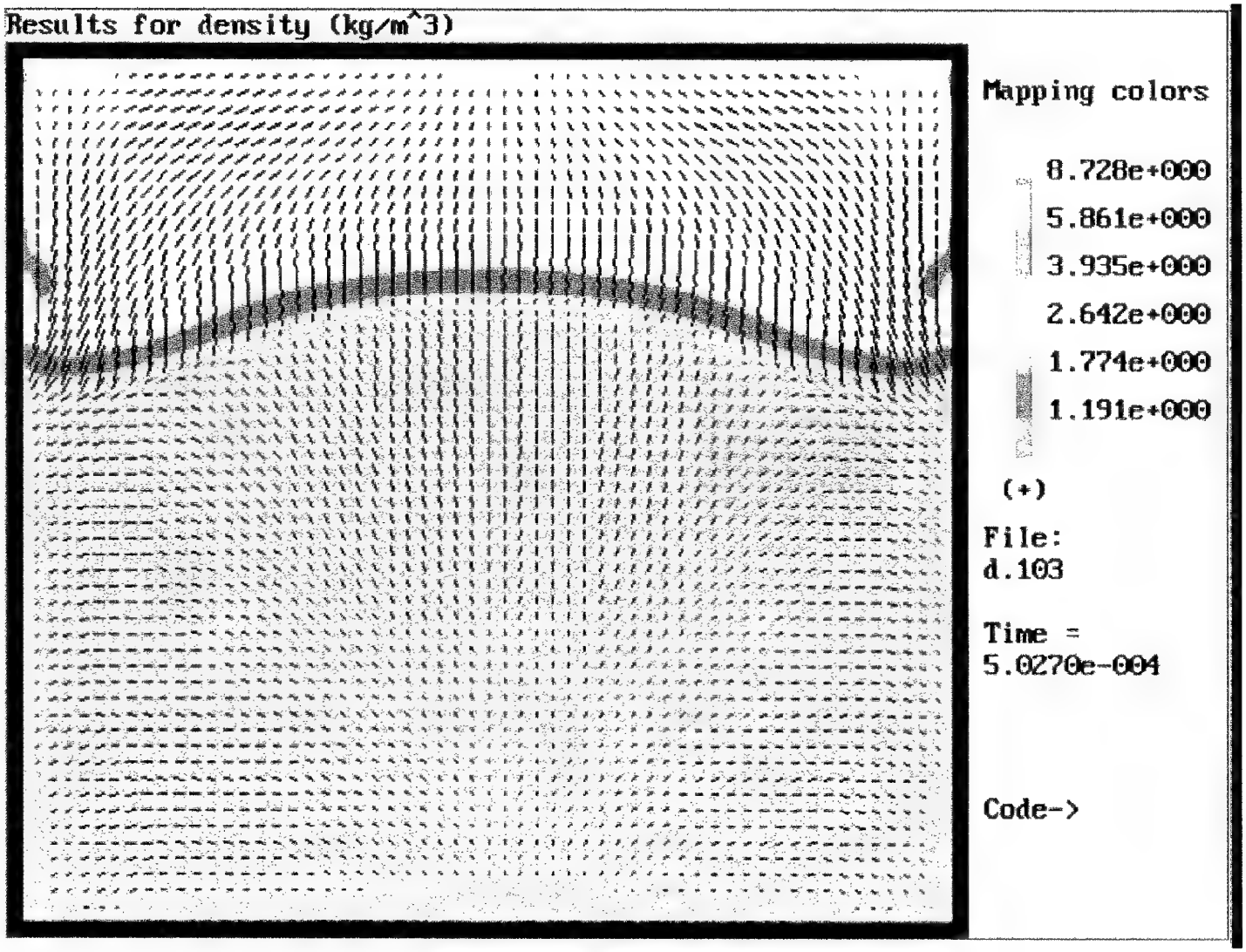
Results for density (kg/m^3)
Mapping colors
8.728e+000
5.861e+000
3.935e+000
2.642e+000
1.774e+000
1.191e+000
(+)
File:
d.103
Time =
5.0270e-004
Code->

Fig. 2.5.

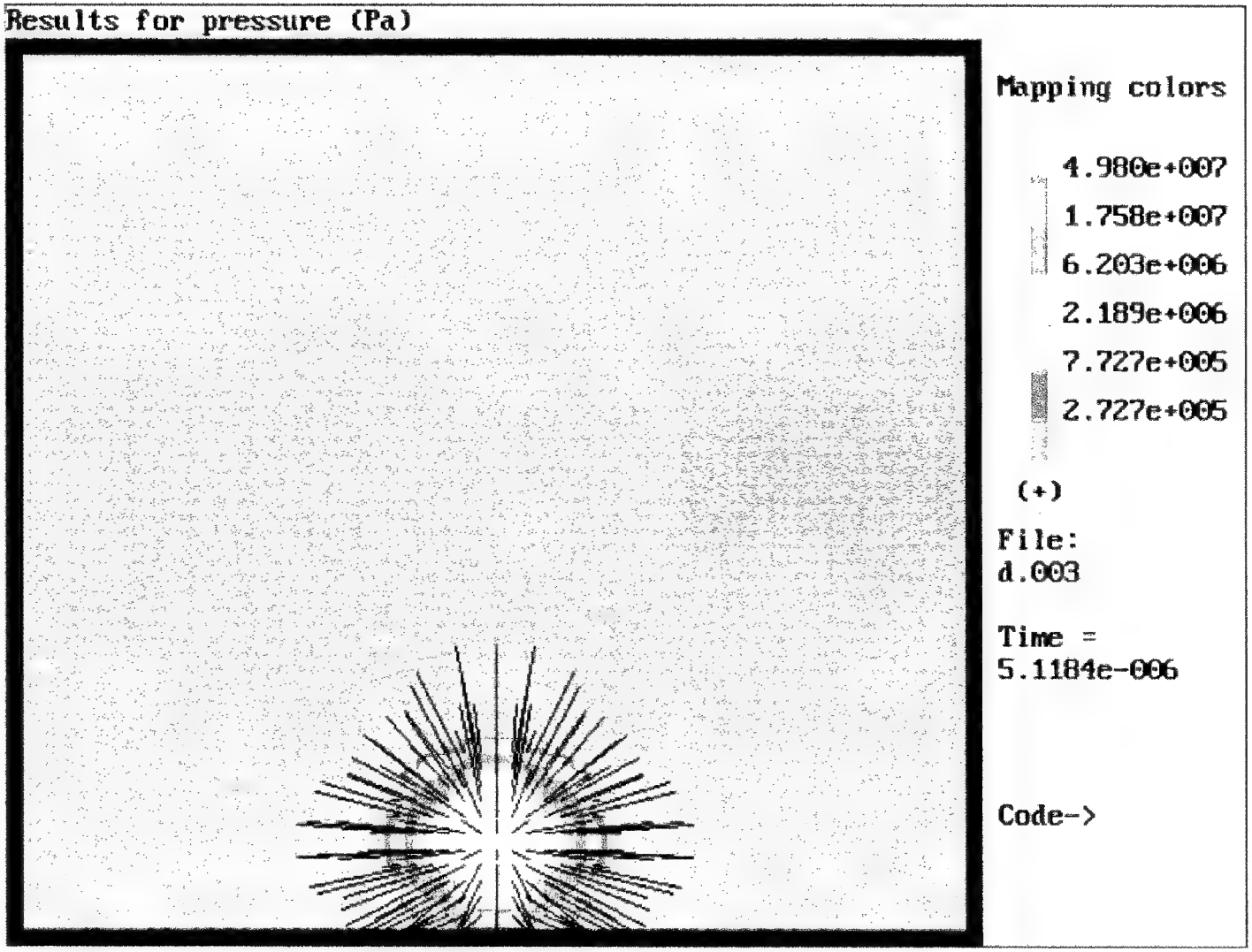
Results for pressure (Pa)
Mapping colors
4.980e+007
1.758e+007
6.203e+006
2.189e+006
7.727e+005
2.727e+005
(+)
File:
d.003
Time =
5.1184e-006
Code->

Fig. 3.a.

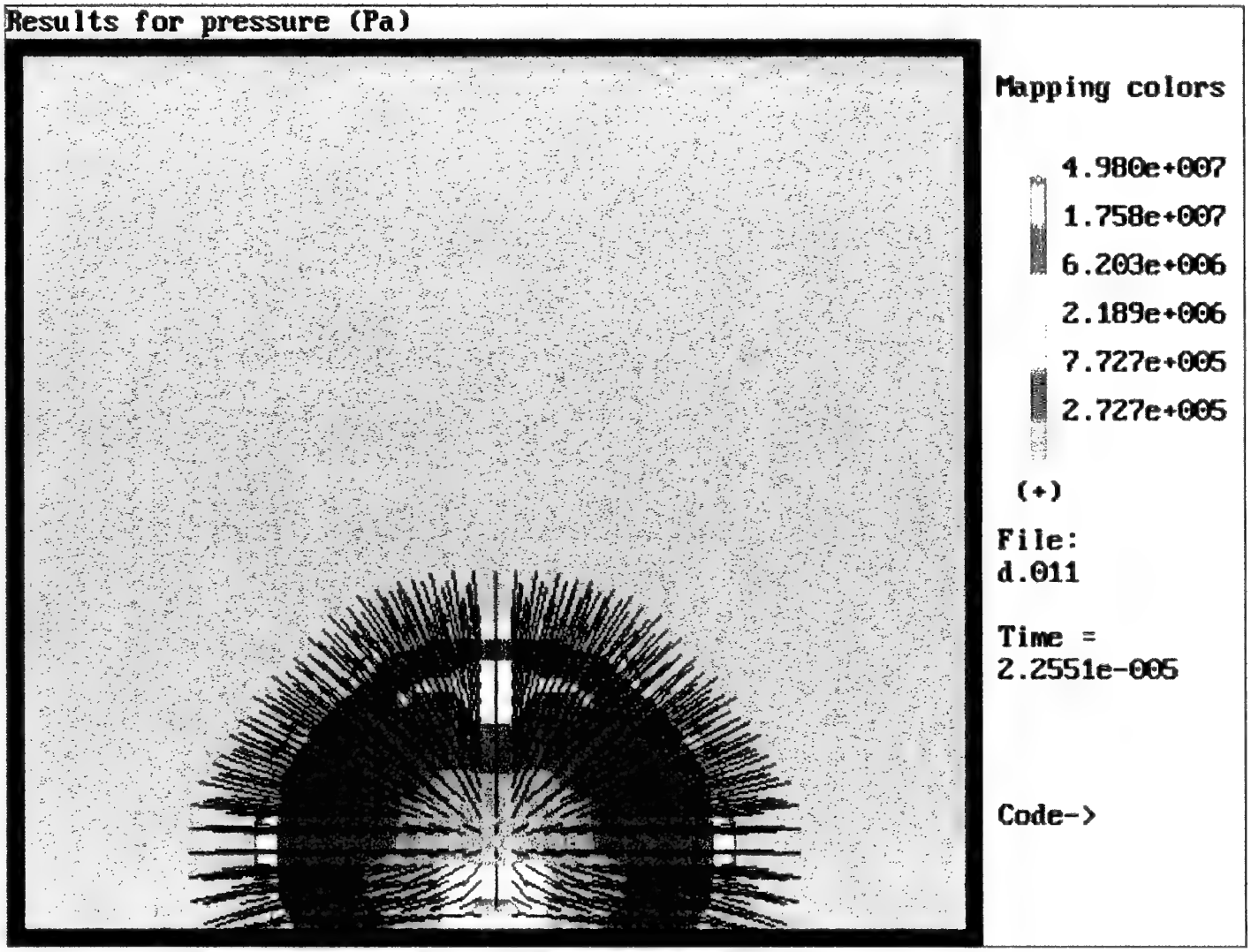
Results for pressure (Pa)
Mapping colors
4.980e+007
1.758e+007
6.203e+006
2.189e+006
7.727e+005
2.727e+005
(+)
File:
d.011
Time =
2.2551e-005
Code->

Fig. 3.6.

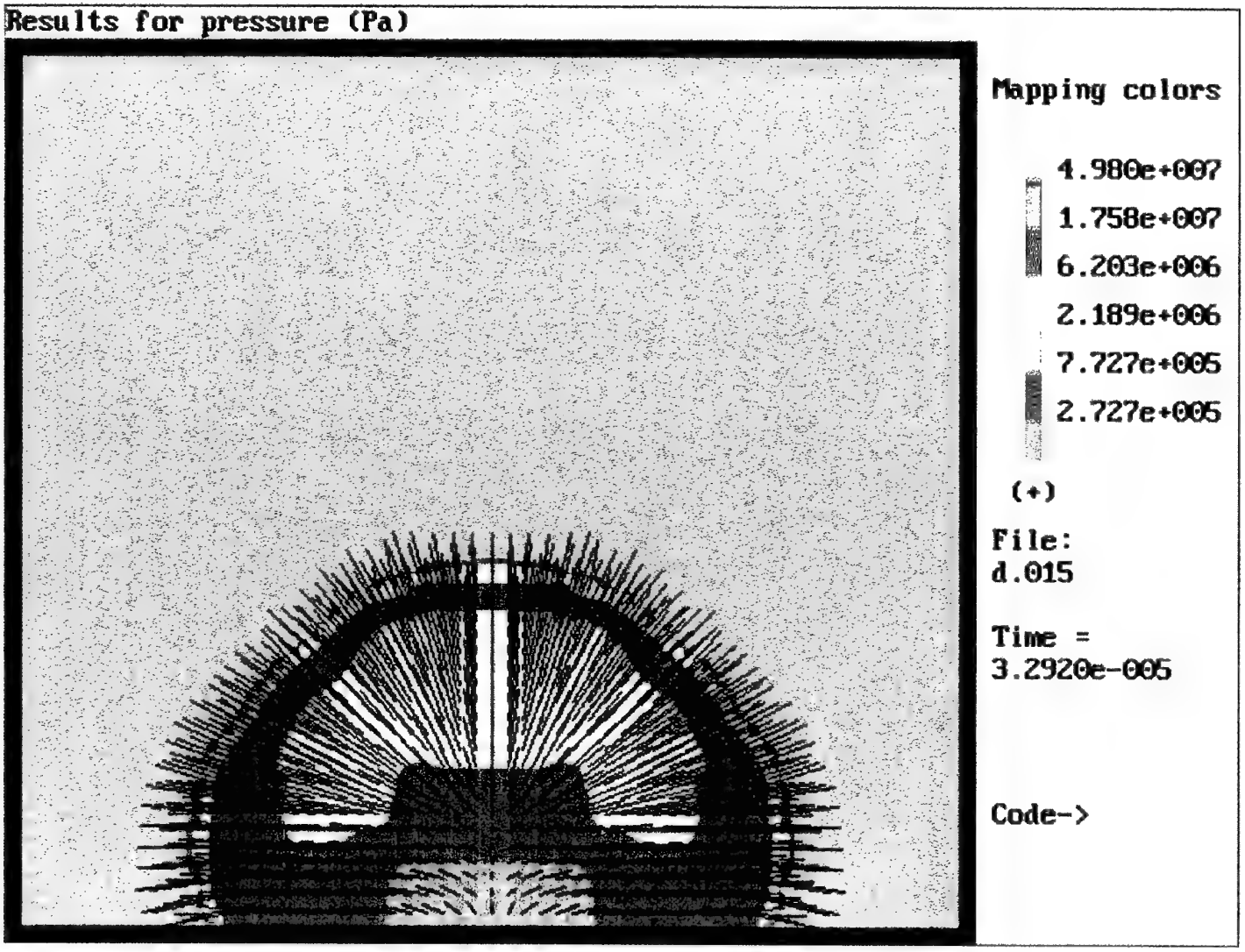
Results for pressure (Pa)
Mapping colors
4.980e+007
1.758e+007
6.203e+006
2.189e+006
7.727e+005
2.727e+005
(+)
File:
d.015
Time =
3.2920e-005
Code->

Fig. 3.c.

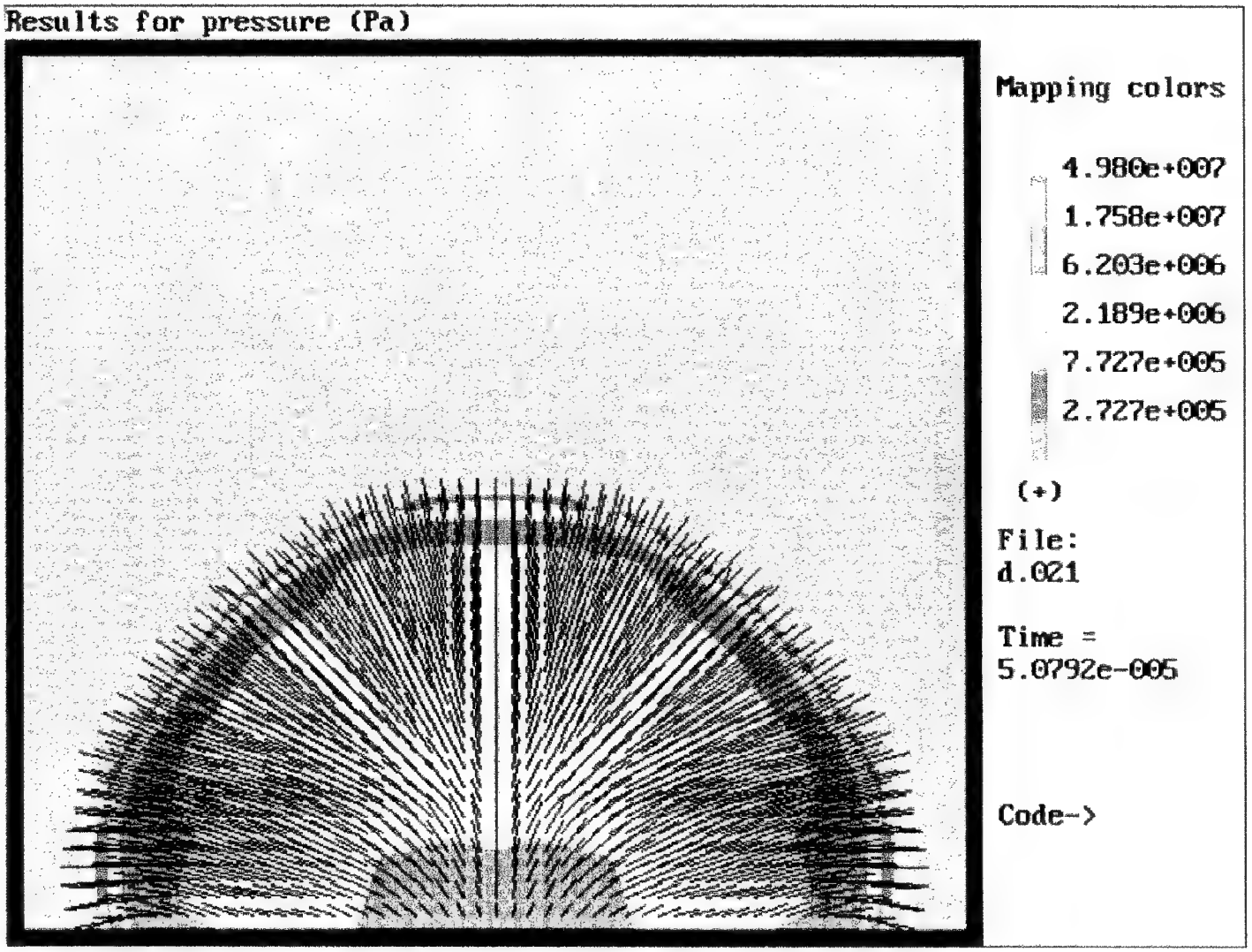
Results for pressure (Pa)
Mapping colors
4.980e+007
1.758e+007
6.203e+006
2.189e+006
7.727e+005
2.727e+005
(+)
File:
d.021
Time =
5.0792e-005
Code->

Fig. 3.d.

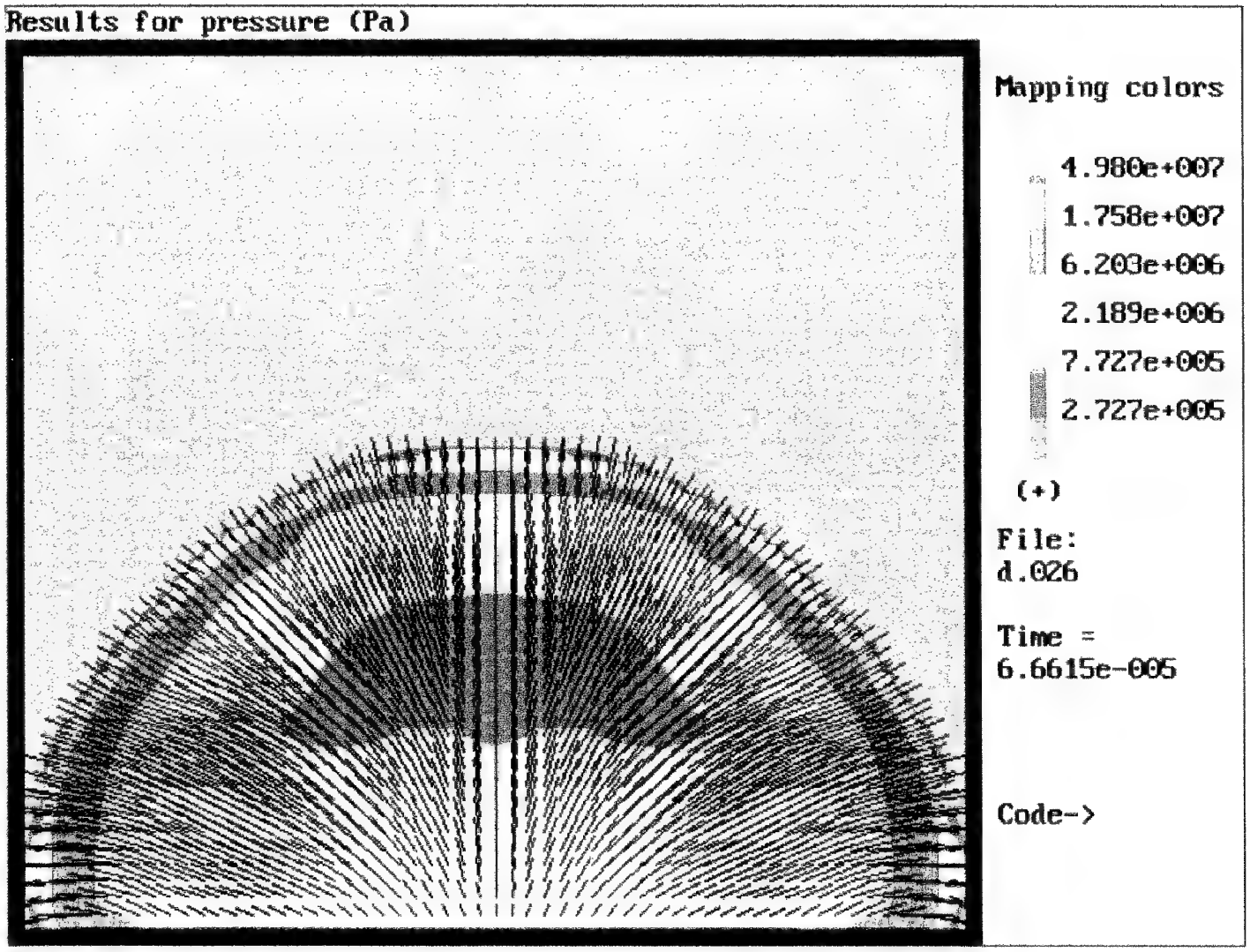
Results for pressure (Pa)
Mapping colors
4.980e+007
1.758e+007
6.203e+006
2.189e+006
7.727e+005
2.727e+005
(+)
File:
d.026
Time =
6.6615e-005
Code->

Fig. 3.e.

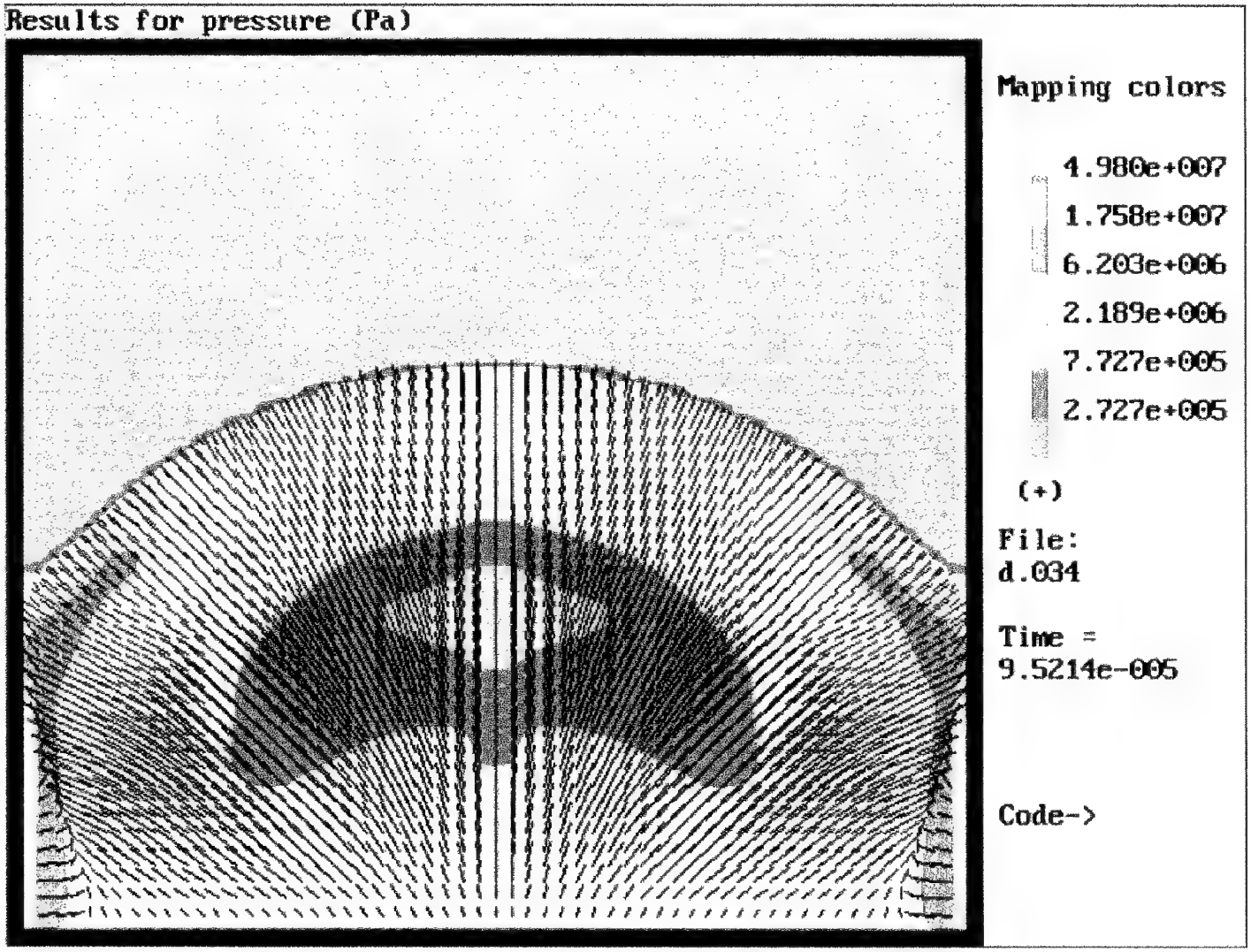
Results for pressure (Pa)
Mapping colors
4.980e+007
1.758e+007
6.203e+006
2.189e+006
7.727e+005
2.727e+005
(+)
File:
d.034
Time =
9.5214e-005
Code->

Fig. 3.f.

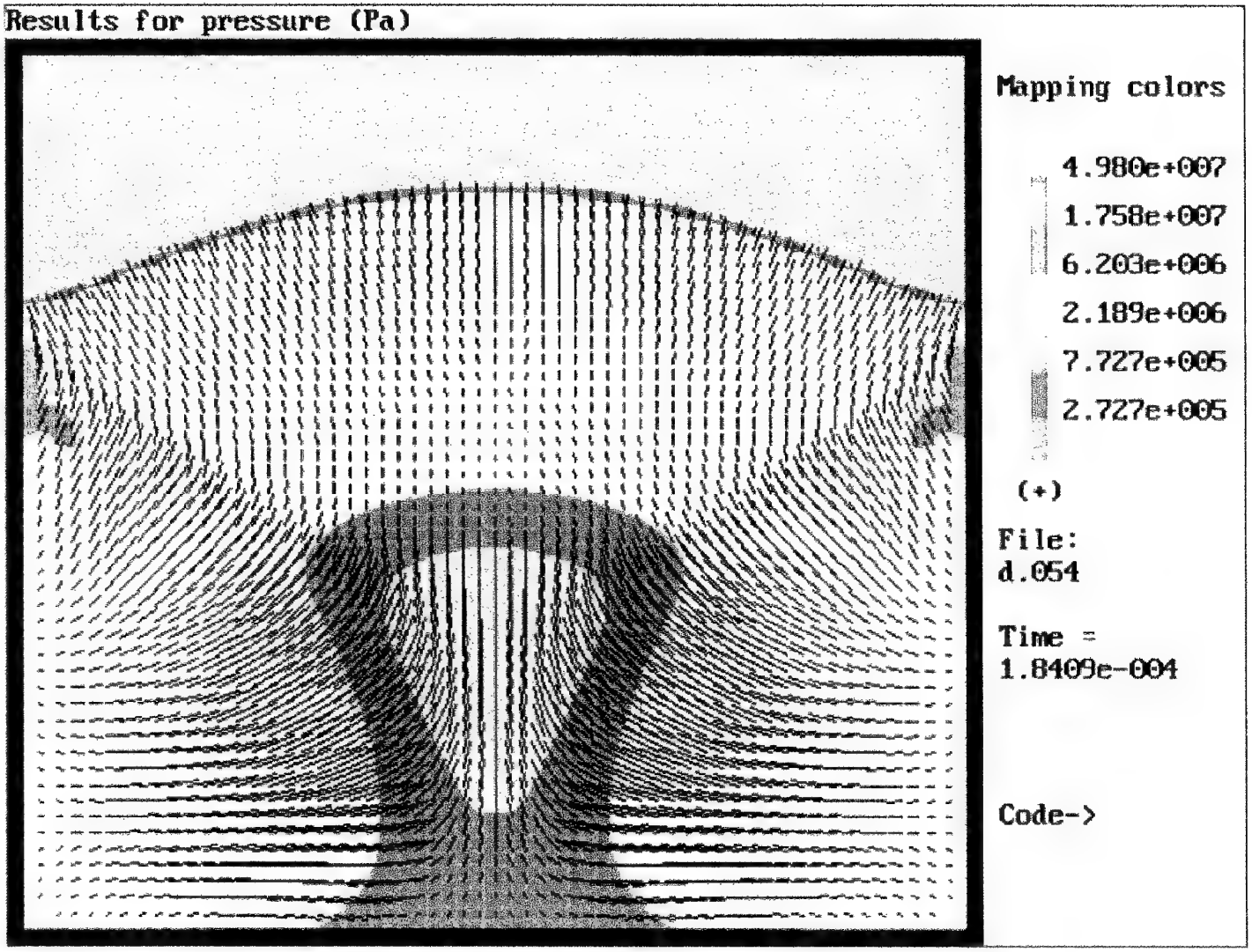
Results for pressure (Pa)
Mapping colors
4.980e+007
1.758e+007
6.203e+006
2.189e+006
7.727e+005
2.727e+005
(+)
File:
d.054
Time =
1.8409e-004
Code->

Fig. 3.9.

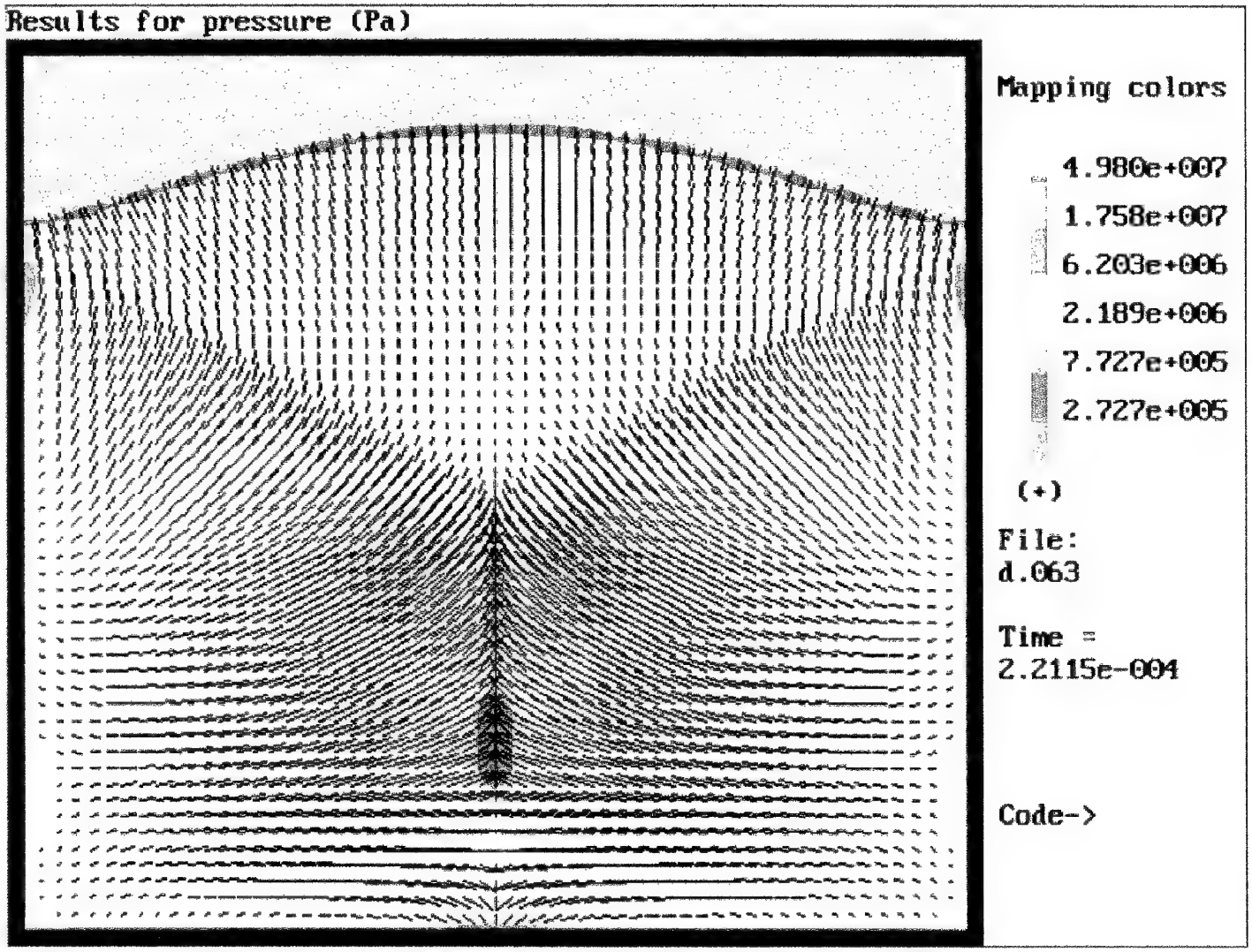
Results for pressure (Pa)
Mapping colors
4.980e+007
1.758e+007
6.203e+006
2.189e+006
7.727e+005
2.727e+005
(+)
File:
d.063
Time =
2.2115e-004
Code->

Fig. 3.h.

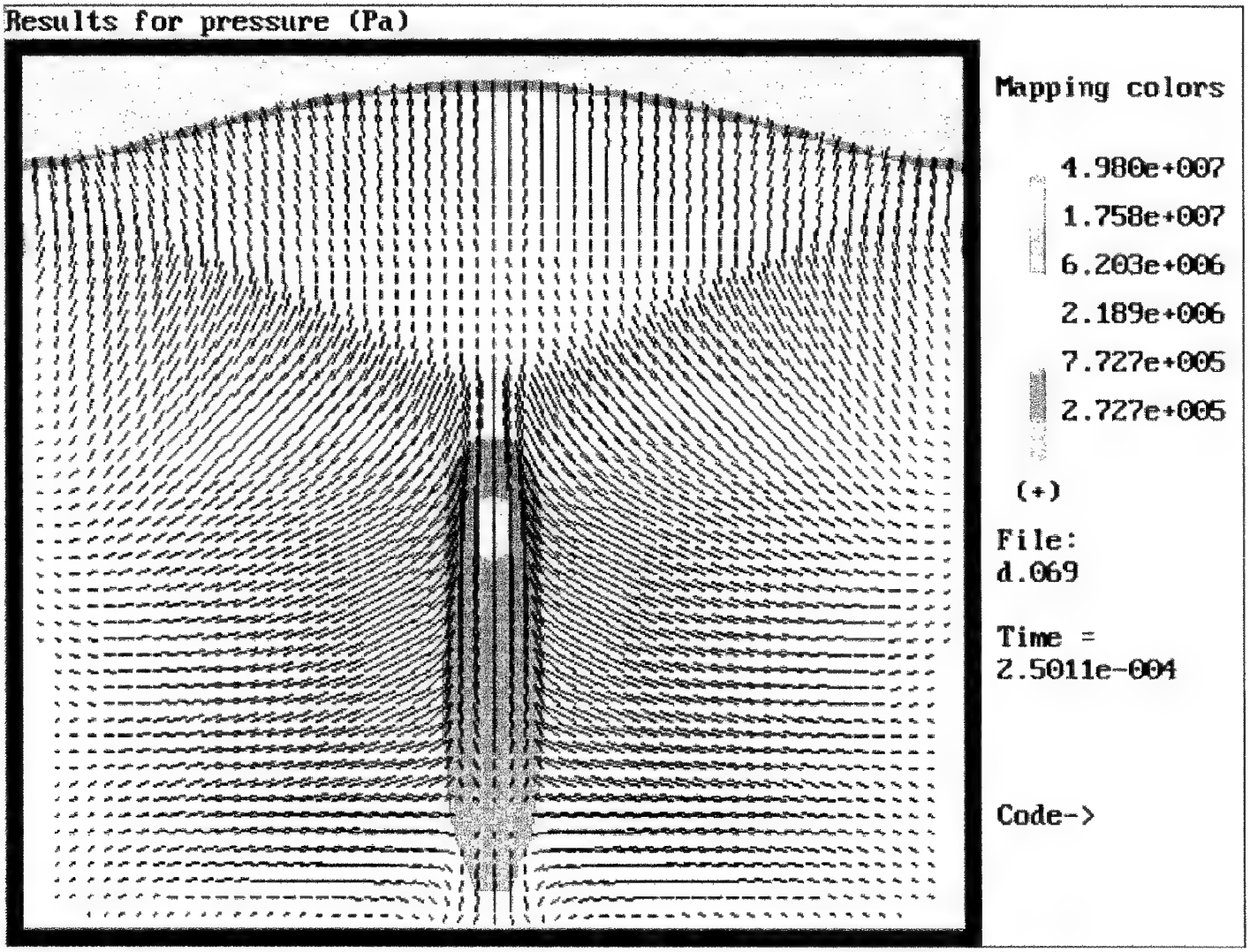
Results for pressure (Pa)
Mapping colors
4.980e+007
1.758e+007
6.203e+006
2.189e+006
7.727e+005
2.727e+005
(+)
File:
d.069
Time =
2.5011e-004
Code->

Fig. 3.c.

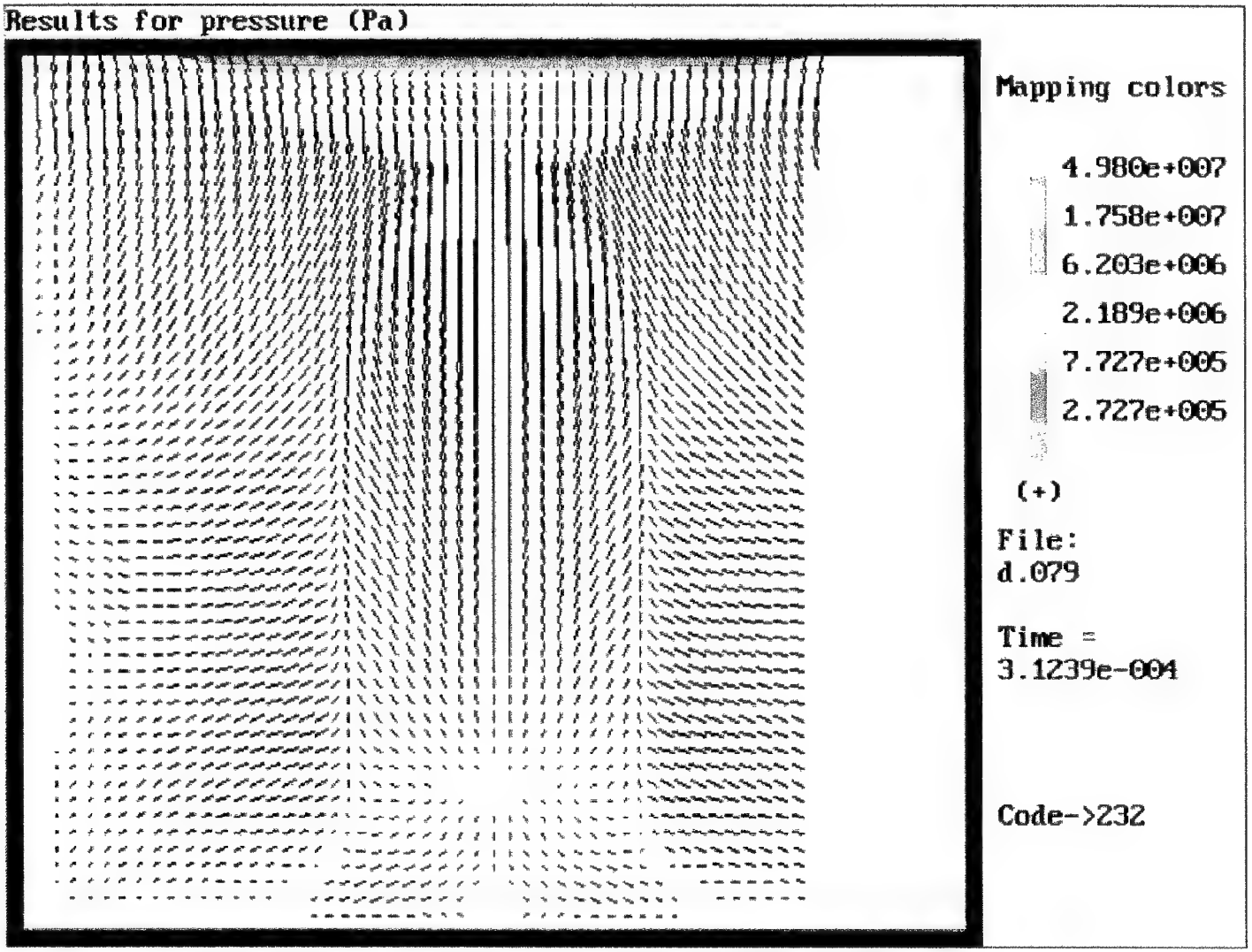
Results for pressure (Pa)
Mapping colors
4.980e+007
1.758e+007
6.203e+006
2.189e+006
7.727e+005
2.727e+005
(+)
File:
d.079
Time =
3.1239e-004
Code->232

Fig. 3.k.

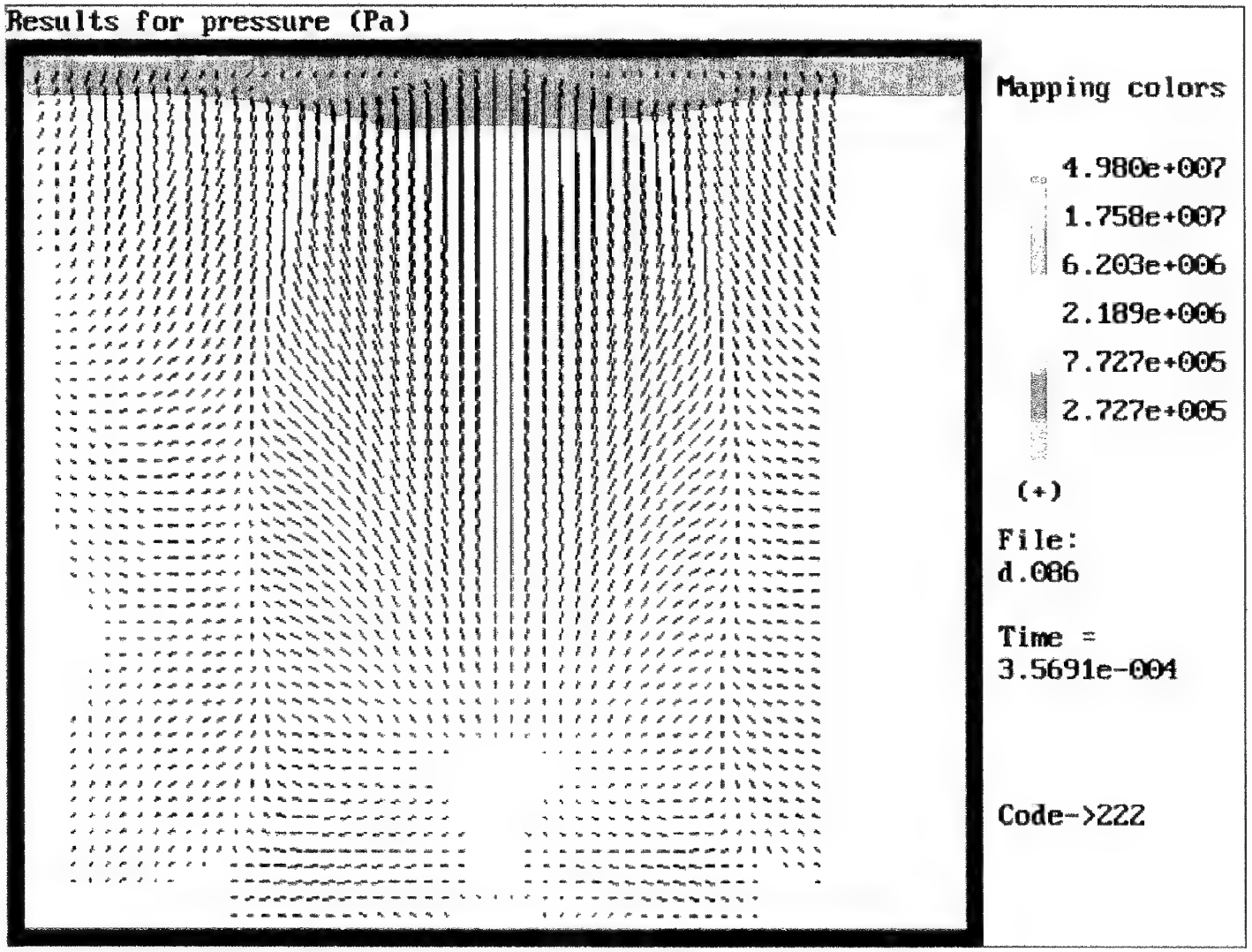
Results for pressure (Pa)
Mapping colors
4.980e+007
1.758e+007
6.203e+006
2.189e+006
7.727e+005
2.727e+005
(+)
File:
d.086
Time =
3.5691e-004
Code->222

Fig. 3.2.

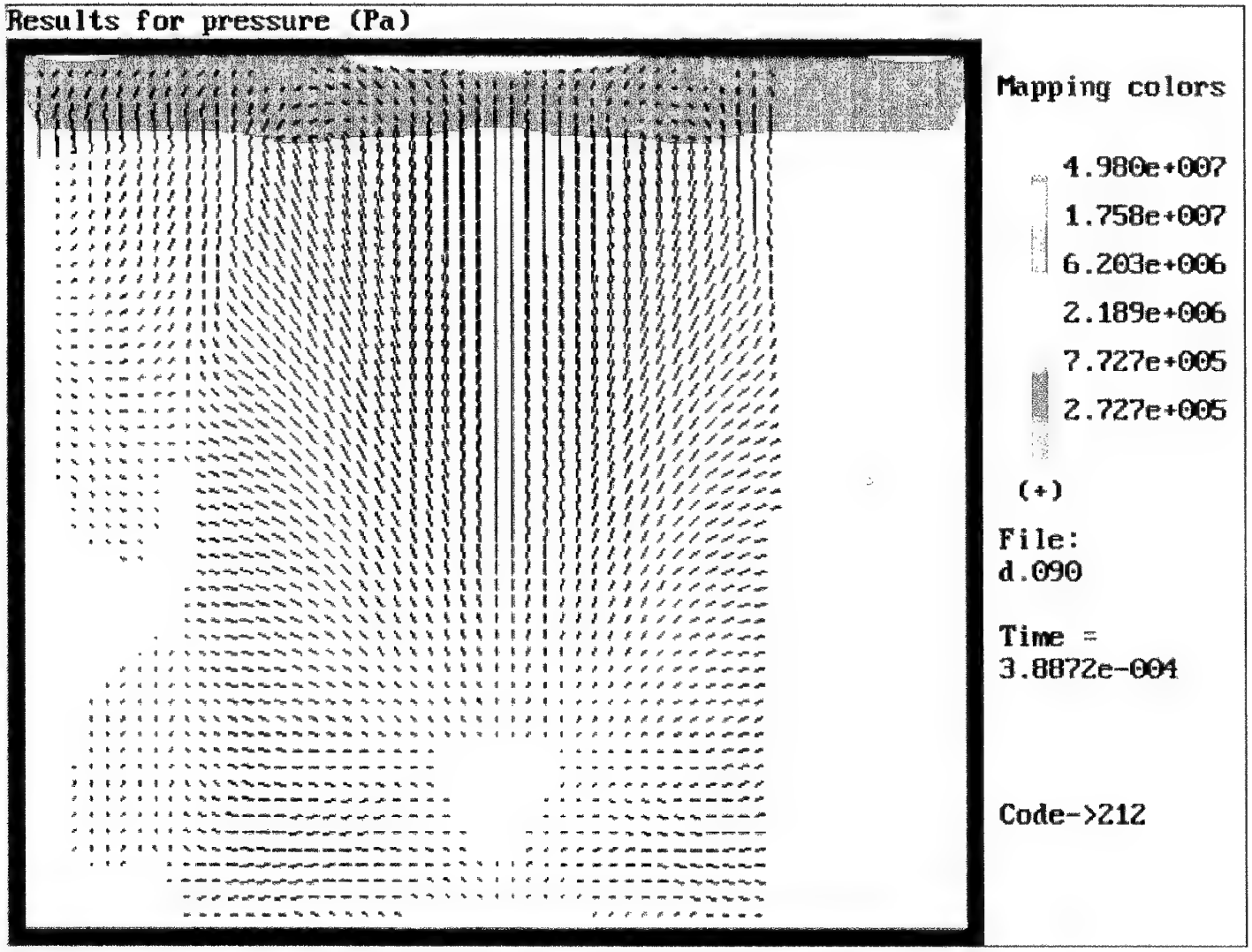
Results for pressure (Pa)
Mapping colors
4.980e+007
1.758e+007
6.203e+006
2.189e+006
7.727e+005
2.727e+005
(+)
File:
d.090
Time =
3.8872e-004
Code->212

Fig. 3.m.

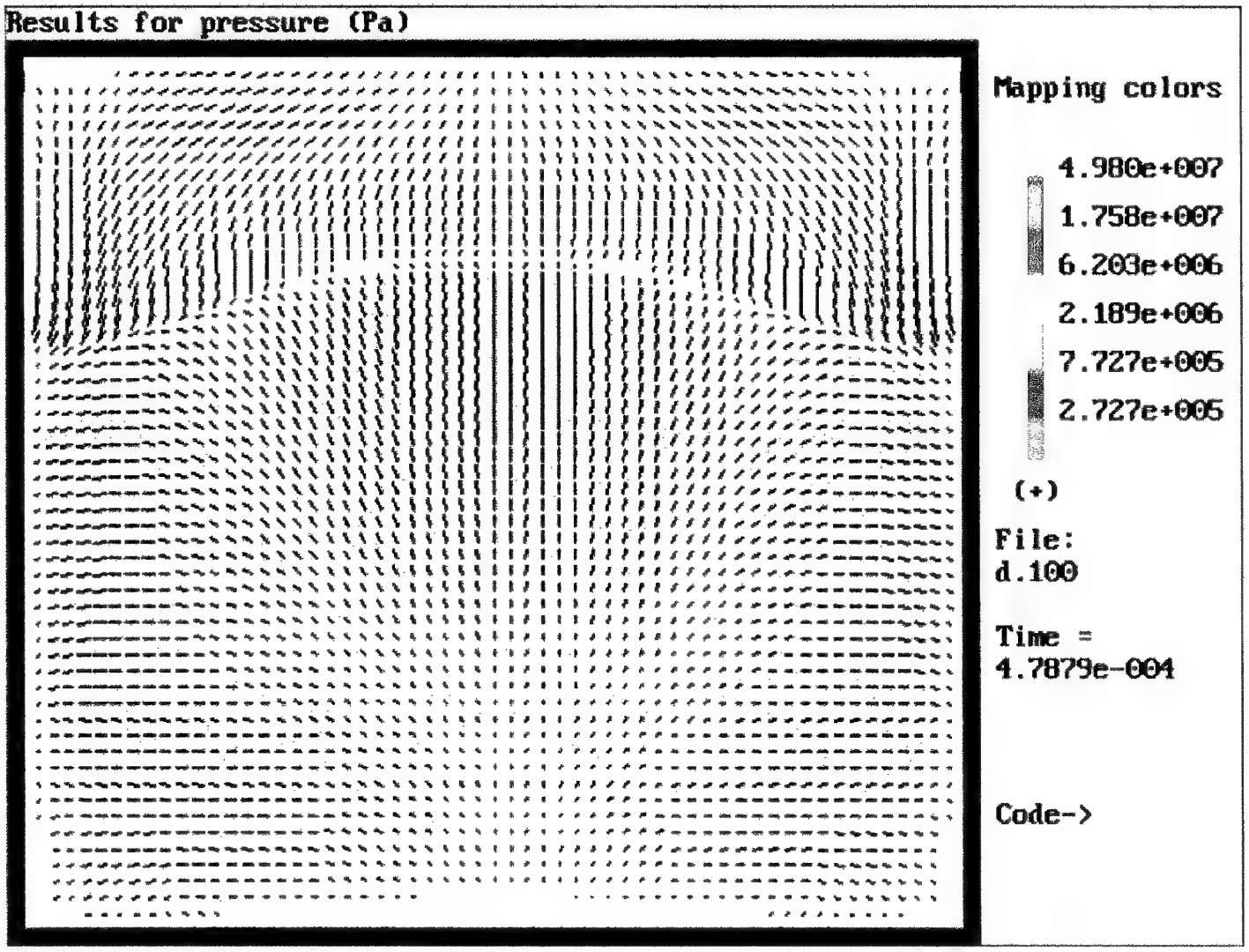
Results for pressure (Pa)
Mapping colors
4.980e+007
1.758e+007
6.203e+006
2.189e+006
7.727e+005
2.727e+005
(+)
File:
d.100
Time =
4.7879e-004
Code->

Fig. 3.n.

2.3 Dynamical deforming of walls and accumulation of damages.

Here we describe the results of model calculations of shell parameters under the influence of internal loading. The characteristic values of material parameters are given in the Table 1. The two cases of loading – uniform and nonuniform – are regarded. The characteristic value of the critical dissipation was taken arbitrary. The model incorporates as well three additional material constants characterizing the resistance of the laminate to accumulating the damages in shear, tension and delamination. The values of those parameters were also chosen arbitrary due to the lack of kinetic data on accumulation of damages in the laminates.

2.3.1 Evolution of the shell parameters in uniform dynamical loading.

The simplified case of uniform internal loading was regarded to investigate the expansion of the shell and accumulation of damages wherein nonuniformity was introduced only by the initial difference of curvatures in different zones of the shell. The internal loading was organized due to uniform pressure increase inside the containment up to $p_{max} = 10^7 Pa$ with the characteristic time $10^{-3}s$. The initial thickness of shell was $h = 10^{-2}m$, initial radius - $1m$, initial length - $2m$.

Fig.4 shows the initial shape of the containment in Euler coordinate system and Fig.5 – in a Lagrangian one. The characteristic internal loading profile for the present case is shown in Fig.6. The shape of the deformed containment for the characteristic time $5.95 \cdot 10^{-3}s$ is shown in Fig.7. It can be seen from the Fig.7 that the shell expanded and changed the curvatures.

Figs.8 $a-b$ show the curvature of the generating line of the cylinder for two successive times. Figs.9 a-b show the curvature of the orthogonal geodesical line for the same times. It can be seen from the figures that both curvatures have the tendency to change (increase or decrease) towards the mean value.

Figs.10 $a-b$ show the displacements of the shells elements in the directions orthogonal to the surface (along the lagrangian axis z). The vertical lines in the Figs.10 and successive figures indicate the places of initial discontinuities of curvatures. The local maxima of displacements w are found in the zones of the minimal initial curvature that corresponds

with the tendency of the containment to come to a spherical shape under the influence of a uniform loading.

Figs.11 $a - b$ show the displacements of the shell's elements u along the generating line in lagrangian coordinates s. The displacements along the s-axis have different signs for different elements. The positive or negative displacements are determined by the initial positions of the elements in respect to the boundaries and the middle point. The displacements of the elements located on the axis of symmetry (boundaries) and in the middle zone are equal to zero. The inverse symmetry in respect to the middle point is also evident. These results qualitatively testify the accuracy of the worked out model.

Figs.12 $a-i$ illustrate the velocity profiles for the orthogonal displacements for different times. It is seen that at the initial stage of the process velocities of displacements change their values and signs very rapidly. The behaviour of the velocities shows the oscillating character of the expansion of the shell in rapid dynamical loading. Later the attenuation of the oscillations takes place due to viscous dissipation and the expansion velocity is stabilized.

Figs.13 $a - m$ illustrate the velocity profiles for tangential displacements along the generating line for different times. The results of numerical modelling evidently illustrate the tangential oscillations of the elements and nonuniformities in velocity profiles caused by the initial difference of curvatures in different zones of the shell. Thus even in a uniform internal dynamical loading of shells with variable curvatures there appear nonuniformities in the parameters for different elements of the shell.

Figs.14-16 show the profiles of tangential strains in both orthogonal geodesical directions of the shell $\epsilon_1^0, \epsilon_2^0$ and the strain ϵ_{1z}^0 for one and the same time. It is seen from Fig.14 that ϵ_1^0 reaches its maximal value in the zones of largest curvature of the generating line. The Fig.15 shows that the maximal values of ϵ_2^0 can be found in the middle zone wherein the radial displacements are also maximal. And local extrema of the ϵ_{1z}^0 (Fig.16) are in the zones of initial discontinuity of the curvature of the generating line of the shell. The above results correspond well with the physical nature of the phenomenon.

Figs.17-19 show the profiles of the corresponding elastic strains e_1^0, e_2^0, e_{1z}^0 for the same times. It can be seen that by that time the difference between the elastic and total deformations has already become significant.

Figs.20-21 show the profiles of parameters Δ_+ and Δ_- characterising the difference of composite components' strains in the layers plane [2].

Figs.22-24 show the profiles of damage parameters $\omega, \alpha, \omega_\Delta$ reflecting accumulation of damages in tension, shear and delamination. The zones of maxima of damages in tension coinside with that for delamination while the zones of maxima of damages in shear are

located near the places of initial discontinuity of curvature of the generating line of the shell.

Figs.25 $a - b$ illustrate the N_1 force in the shell along the generating line for the two successive times. Figs.26 $a - b$ illustrate the tangential to the shell N_2 force in the orthogonal direction for the same times. Figs.27 $a - c$ show the profiles of the force Q orthogonal to the tangent plane.

Fig.28 illustrates the temperature increase in the shell due to irreversible processes. At the initial instant it has the zero level. It is seen that the maximal increase of temperature can be found in the zones of maximal gradients of curvature of the generating line.

Figs.29 $a - d$ show the accumulation of the specific dissipation D in the shell for successive times. The growth of specific dissipation is maximal in the zones of maximal gradients of curvature of the generating line and in the zones of maximal deformations as well (the midle point).

The results show that for axisymmetrical shells under the influence of a uniform internal loading the damaged zones are likely to appear in the zones of maximal curvature gradients and in the zones of maximal expansion. Thus the presence of angles essentially increases the probability of a breakup contrary to the spherical shape of the containment that is proved to be optimal for the cases of uniform internal loading. This coinsidence of the numerical results with the conclusions derived from the existing theoretical solutions makes us sure that the worked out model of the damageable thermoviscoelastic laminated composite material adequately describes the physical processes in internal loading.

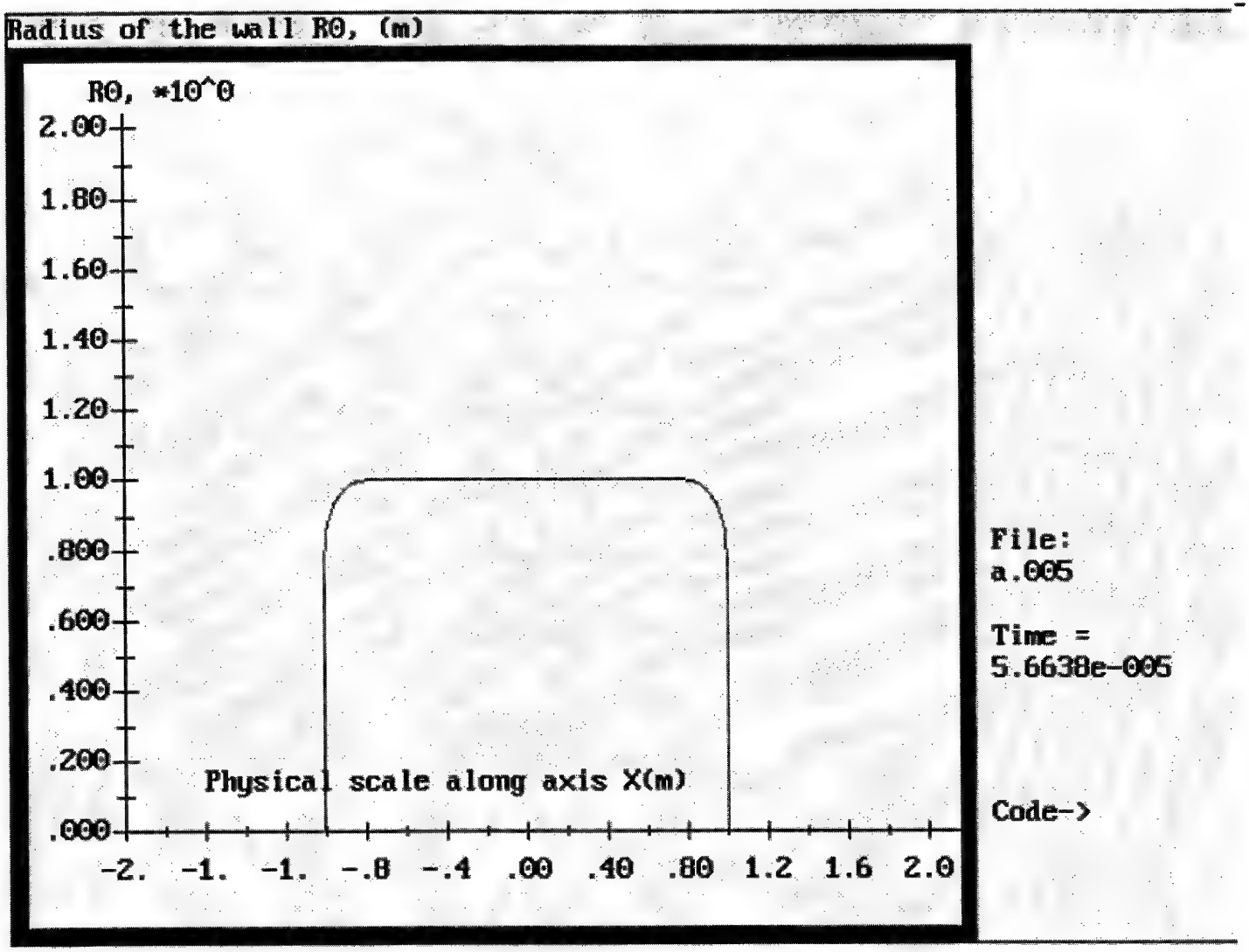
Radius of the wall R0, (m)
R0, *10^0
2.00
1.80
1.60
1.40
1.20
1.00
.800
.600
.400
.200
.000
Physical scale along axis X(m)
-2. -1. -1. -.8 -.4 .00 .40 .80 1.2 1.6 2.0
File:
a.005
Time =
5.6638e-005
Code->

Fig. 4.

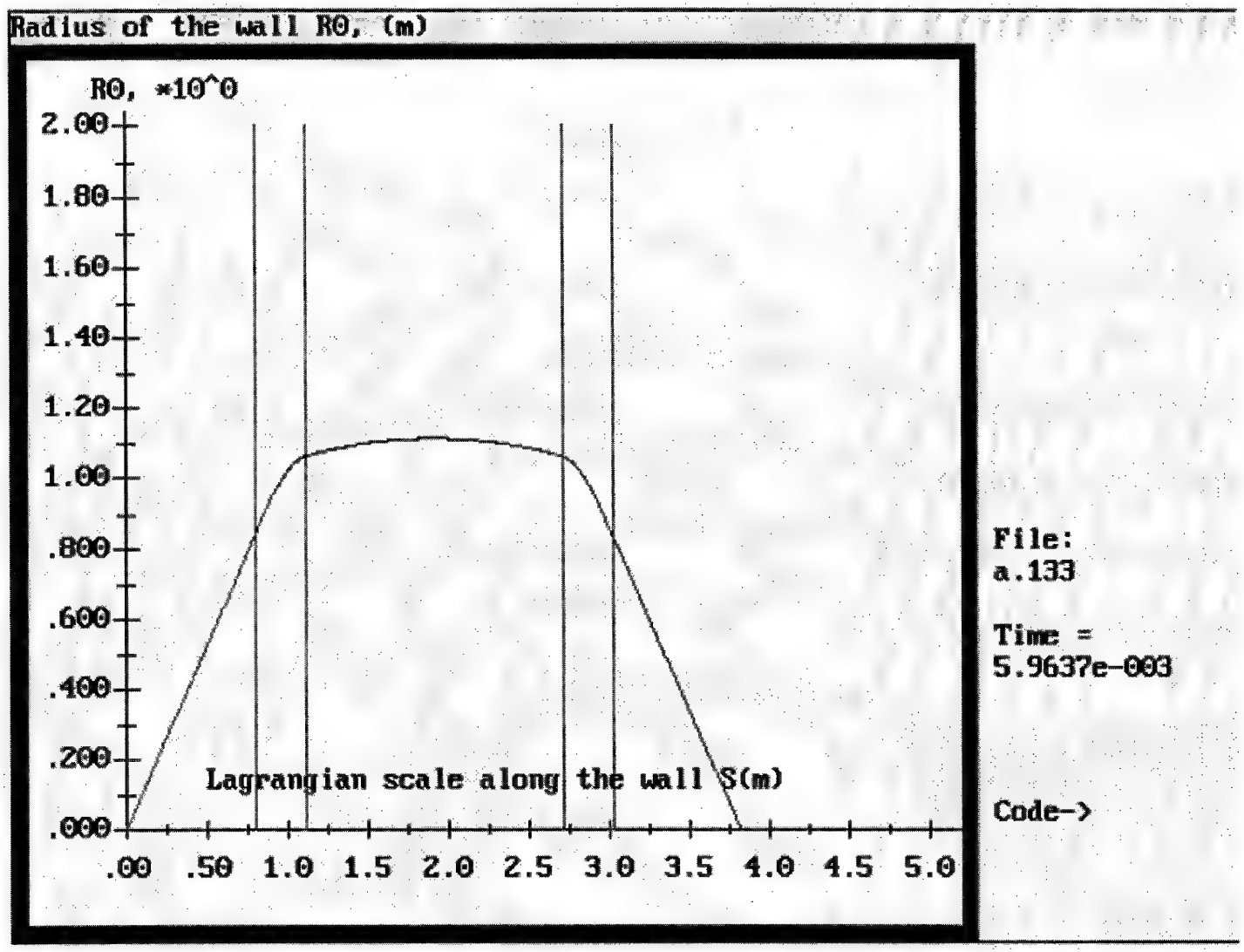
Radius of the wall R0, (m)
R0, *10^0
2.00
1.80
1.60
1.40
1.20
1.00
.800
.600
.400
.200
.000
.00 .50 1.0 1.5 2.0 2.5 3.0 3.5 4.0 4.5 5.0
Lagrangian scale along the wall S(m)
File:
a.133
Time =
5.9637e-003
Code->

Fig. 5.

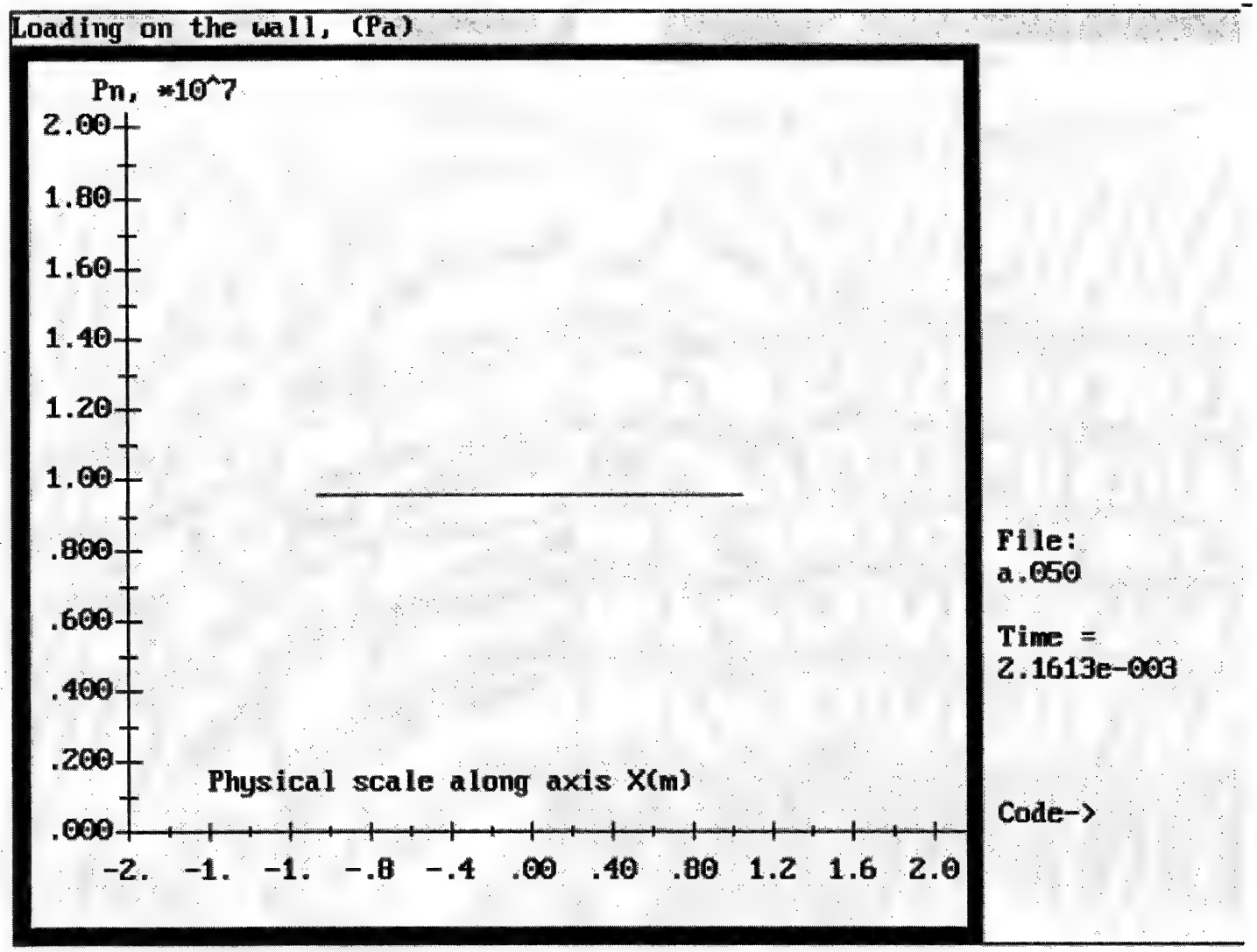
Loading on the wall, (Pa)
Pn, *10^7
2.00
1.80
1.60
1.40
1.20
1.00
.800
.600
.400
.200
.000
Physical scale along axis X(m)
-2. -1. -1. -.8 -.4 .00 .40 .80 1.2 1.6 2.0
File:
a.050
Time =
2.1613e-003
Code->

Fig. 6.

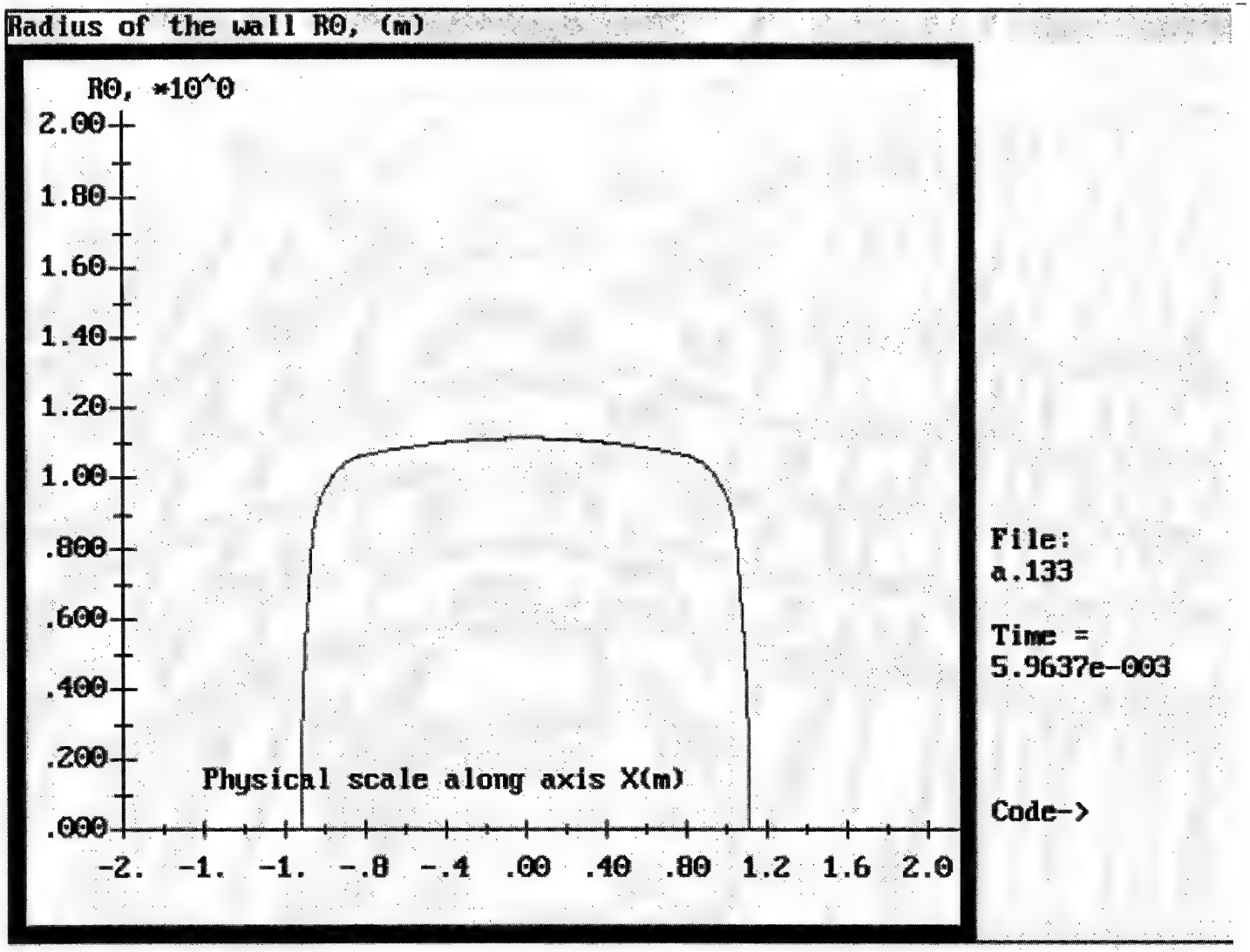
Radius of the wall R0, (m)
R0, *10^0
2.00
1.80
1.60
1.40
1.20
1.00
.800
.600
.400
.200
.000
-2. -1. -1. -.8 -.4 .00 .40 .80 1.2 1.6 2.0
Physical scale along axis X(m)
File:
a.133
Time =
5.9637e-003
Code->

Fig. 7,

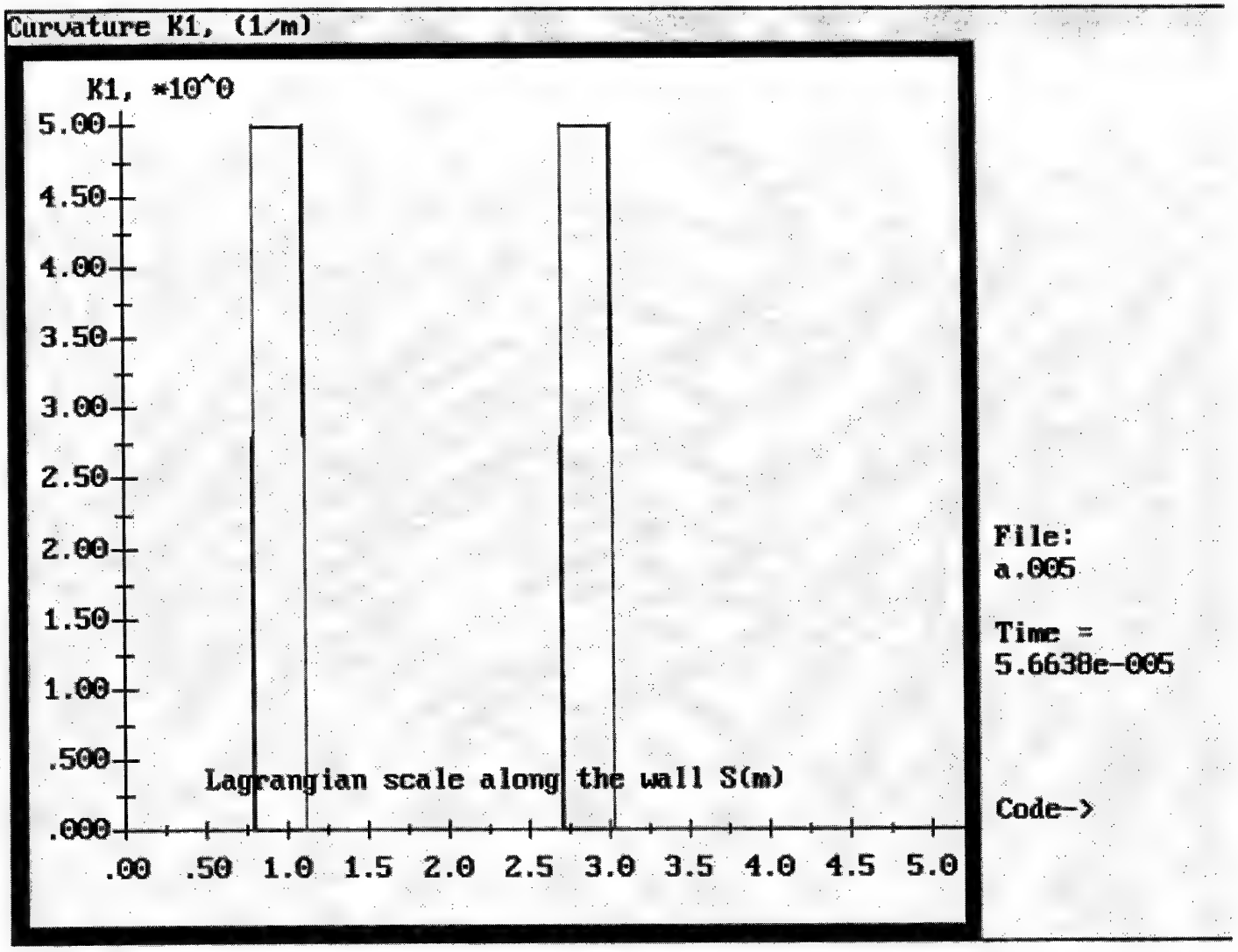
Curvature K1, (1/m)
K1, *10^0
5.00
4.50
4.00
3.50
3.00
2.50
2.00
1.50
1.00
.500
.000
Lagrangian scale along the wall S(m)
.00 .50 1.0 1.5 2.0 2.5 3.0 3.5 4.0 4.5 5.0
File:
a.005
Time =
5.6638e-005
Code->

Fig. 8.a.

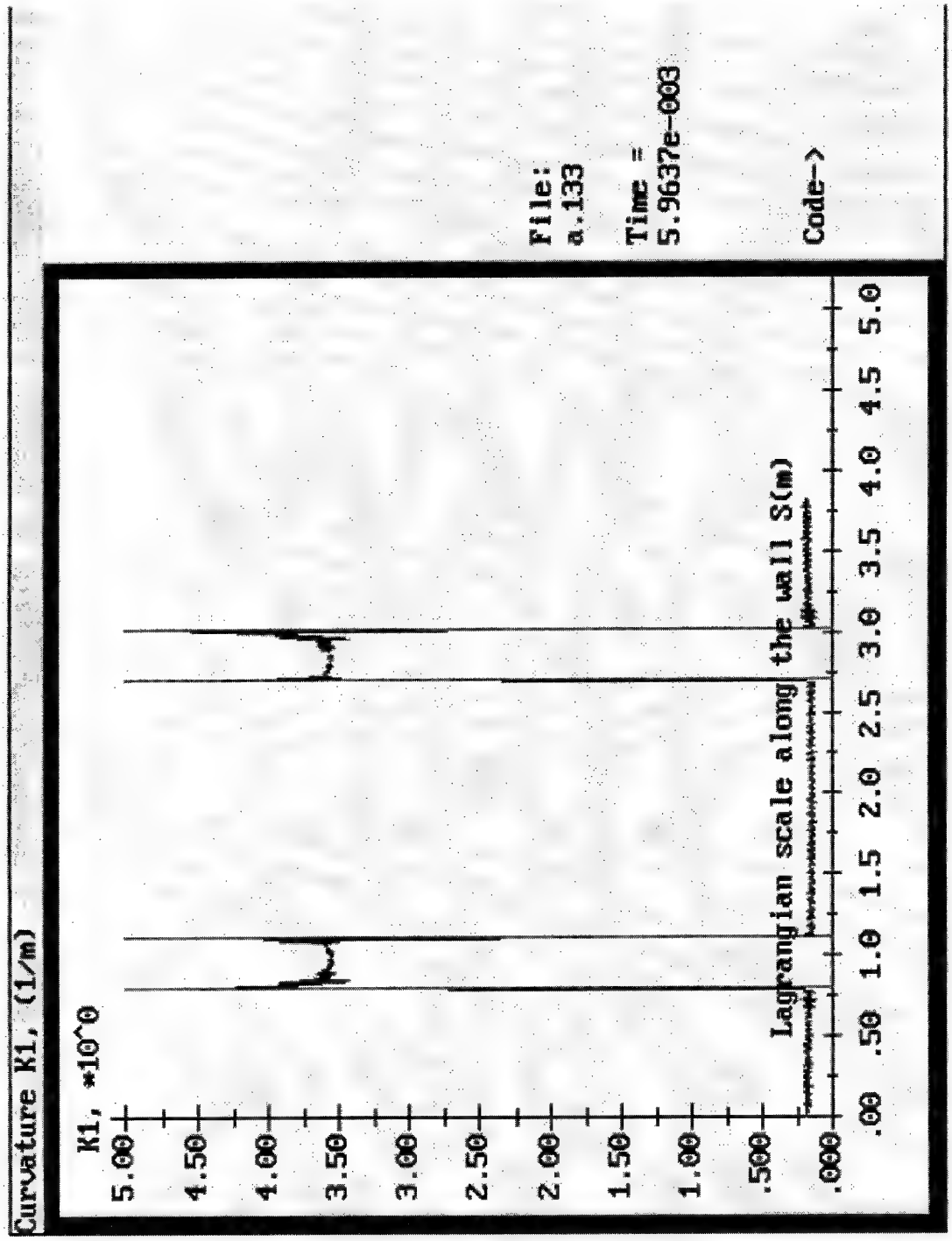
Curvature K1, (1/m)
K1, *10^0
5.00
4.50
4.00
3.50
3.00
2.50
2.00
1.50
1.00
.500
.000
.00
.50
1.0
1.5
2.0
2.5
3.0
3.5
4.0
4.5
5.0
Lagrangian scale along the wall S(m)
File:
a.133
Time =
5.9637e-003
Code->

Fig. 8. b.

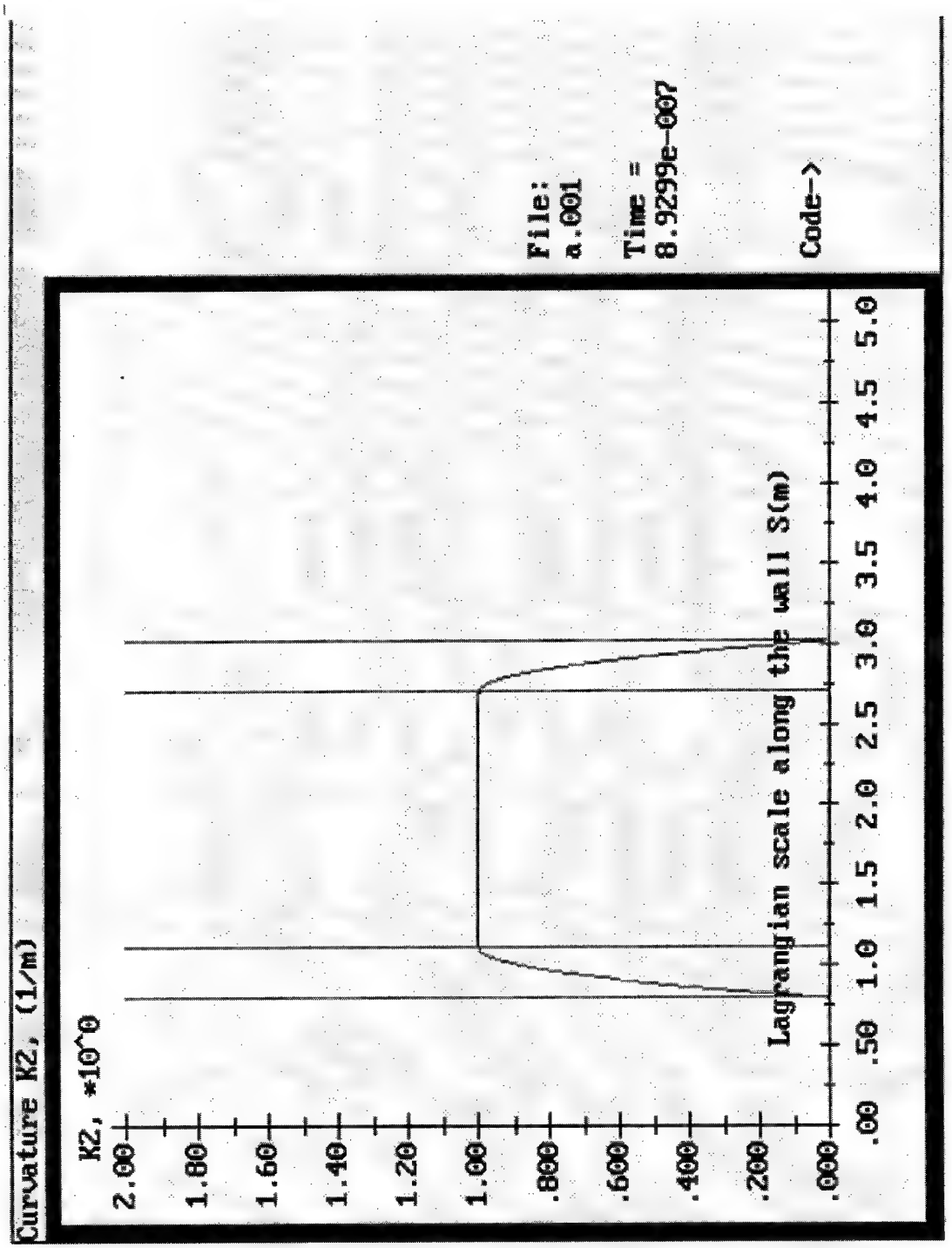
Curvature KZ, (1/m)
KZ, *10^0
2.00
1.80
1.60
1.40
1.20
1.00
.800
.600
.400
.200
.000
.00
.50
1.0
1.5
2.0
2.5
3.0
3.5
4.0
4.5
5.0
Lagrangian scale along the wall S(m)
File:
a.001
Time =
8.9299e-007
Code->

Fig. 9.a

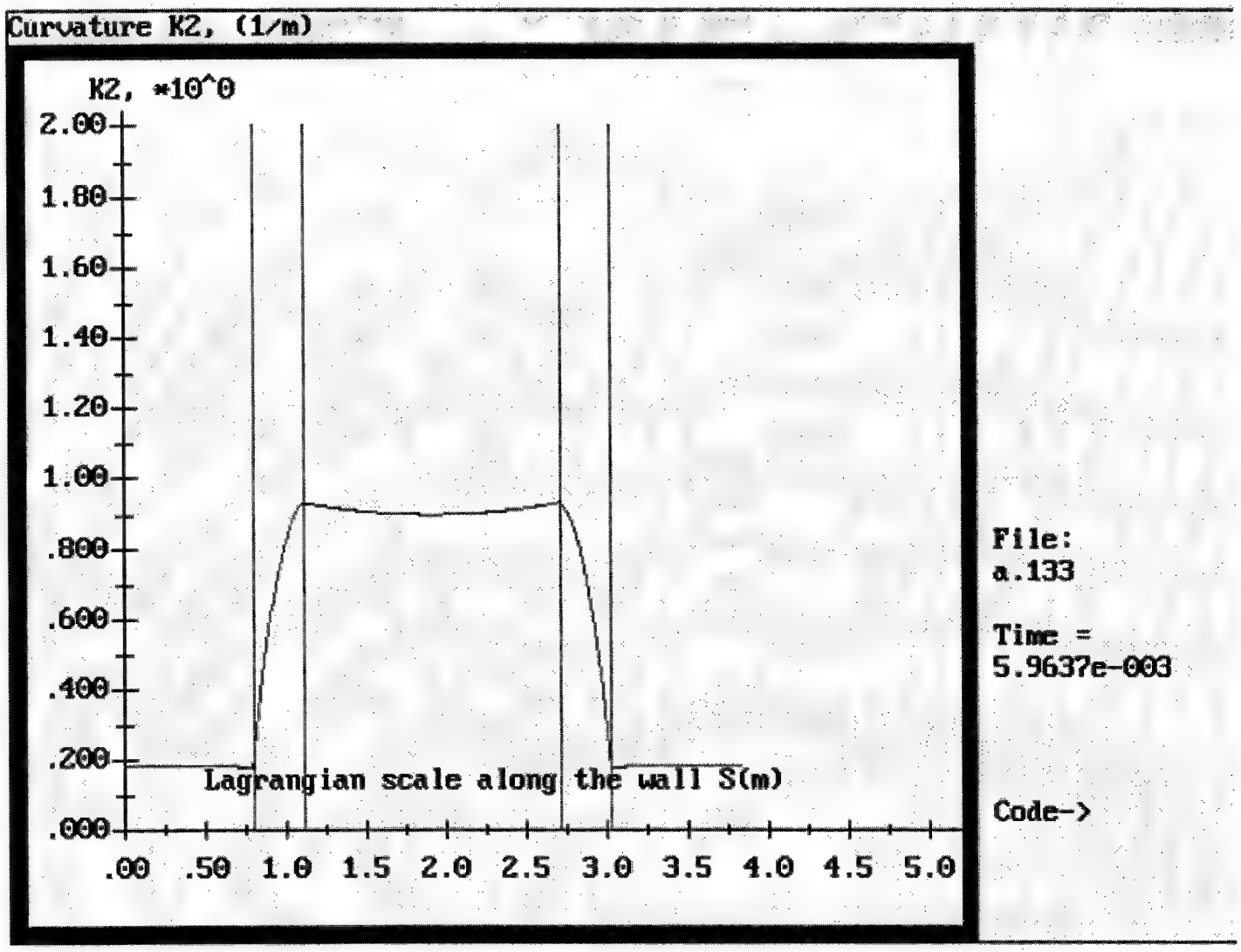
Curvature K2, (1/m)
K2, *10^0
2.00
1.80
1.60
1.40
1.20
1.00
.800
.600
.400
.200
.000
.00 .50 1.0 1.5 2.0 2.5 3.0 3.5 4.0 4.5 5.0
Lagrangian scale along the wall S(m)
File:
a.133
Time =
5.9637e-003
Code->

Fig. 9.8

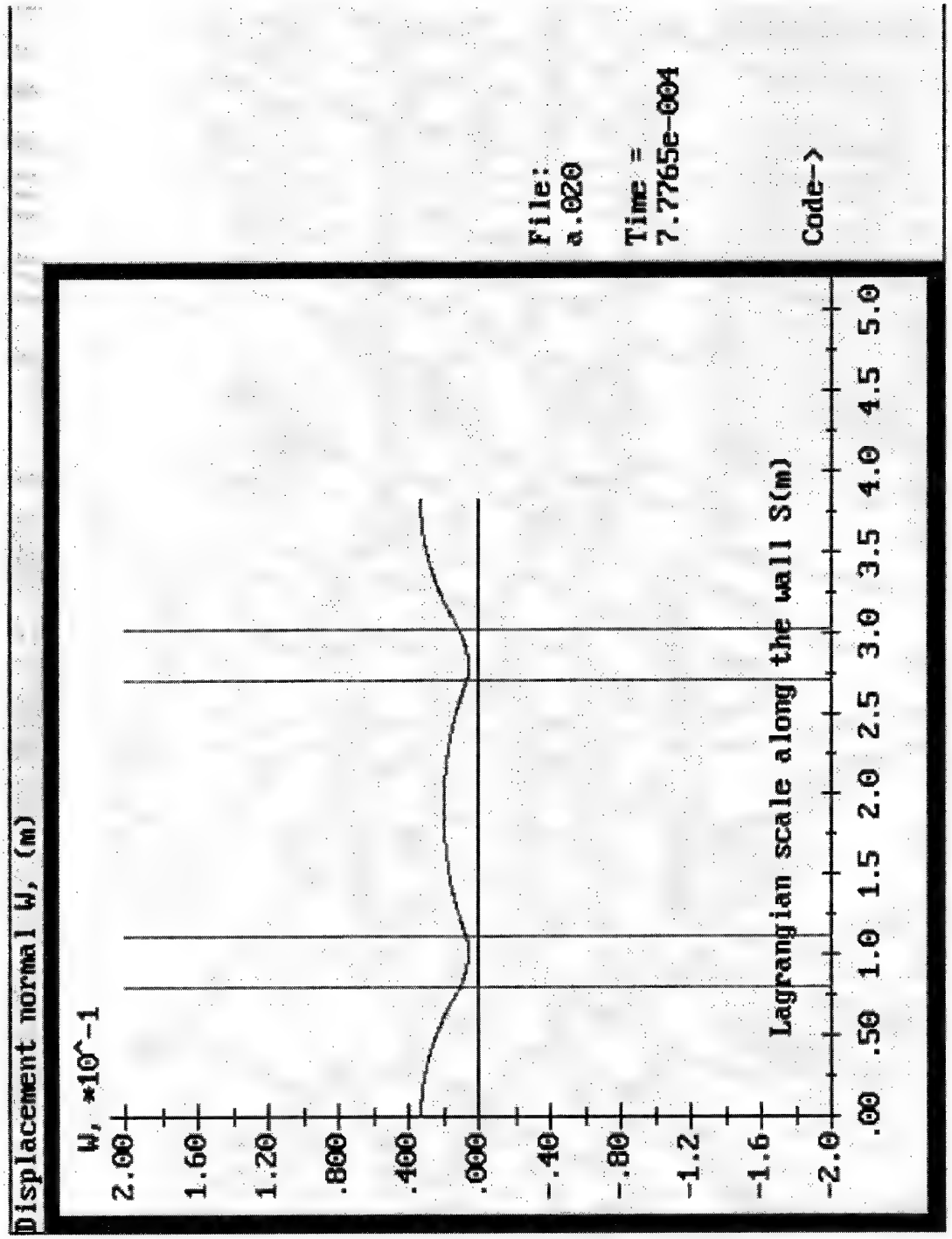
Displacement normal W, (m)
W, *10^-1
2.00
1.60
1.20
.800
.400
.000
-.40
-.80
-1.2
-1.6
-2.0
.00
.50
1.0
1.5
2.0
2.5
3.0
3.5
4.0
4.5
5.0
Lagrangian scale along the wall S(m)
File:
a.020
Time =
7.7765e-004
Code->

Fig. 10.a.

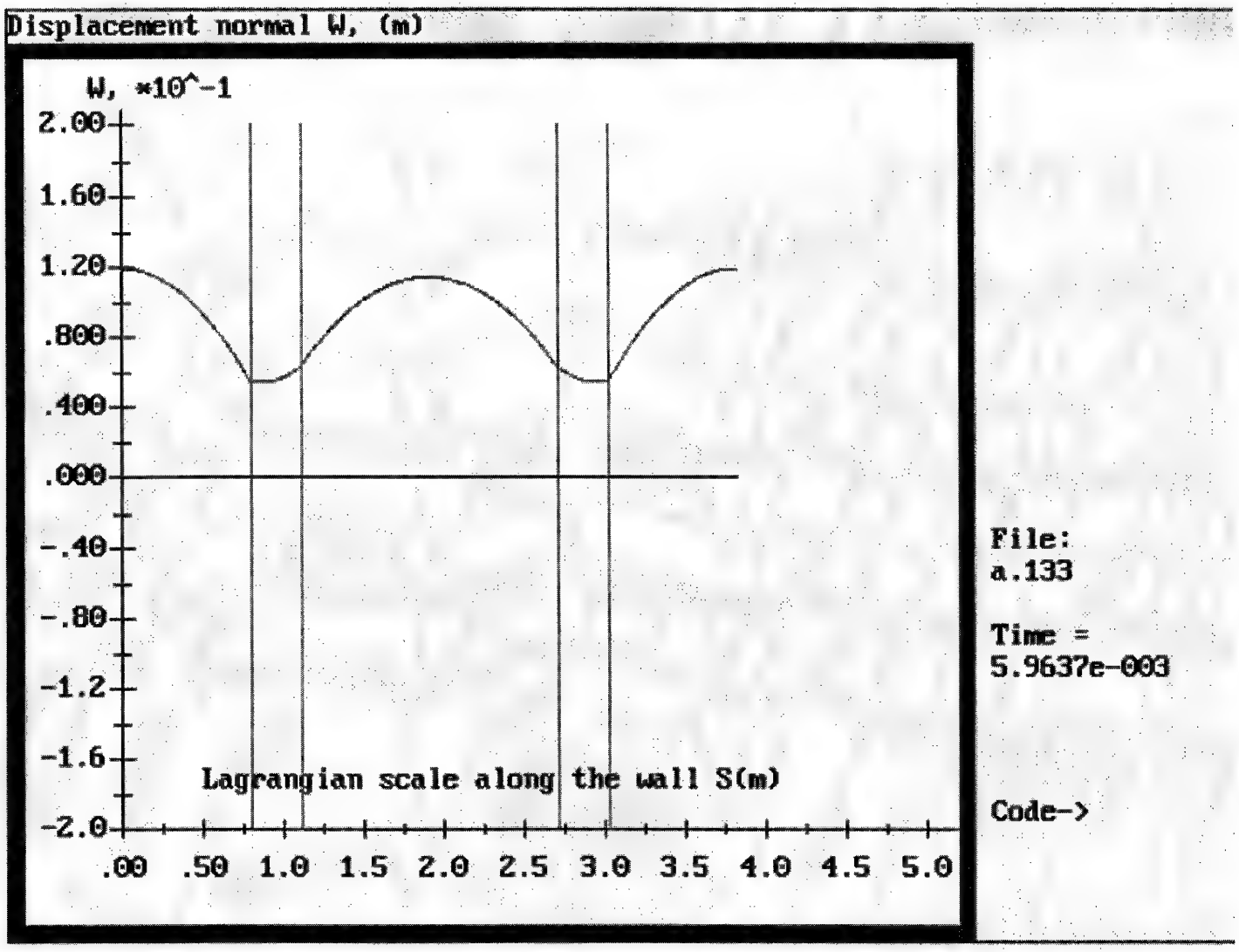
Displacement normal W, (m)
W, *10^-1
2.00
1.60
1.20
.800
.400
.000
-.40
-.80
-1.2
-1.6
-2.0
Lagrangian scale along the wall S(m)
.00 .50 1.0 1.5 2.0 2.5 3.0 3.5 4.0 4.5 5.0
File:
a.133
Time =
5.9637e-003
Code->

Fig. 10.6.

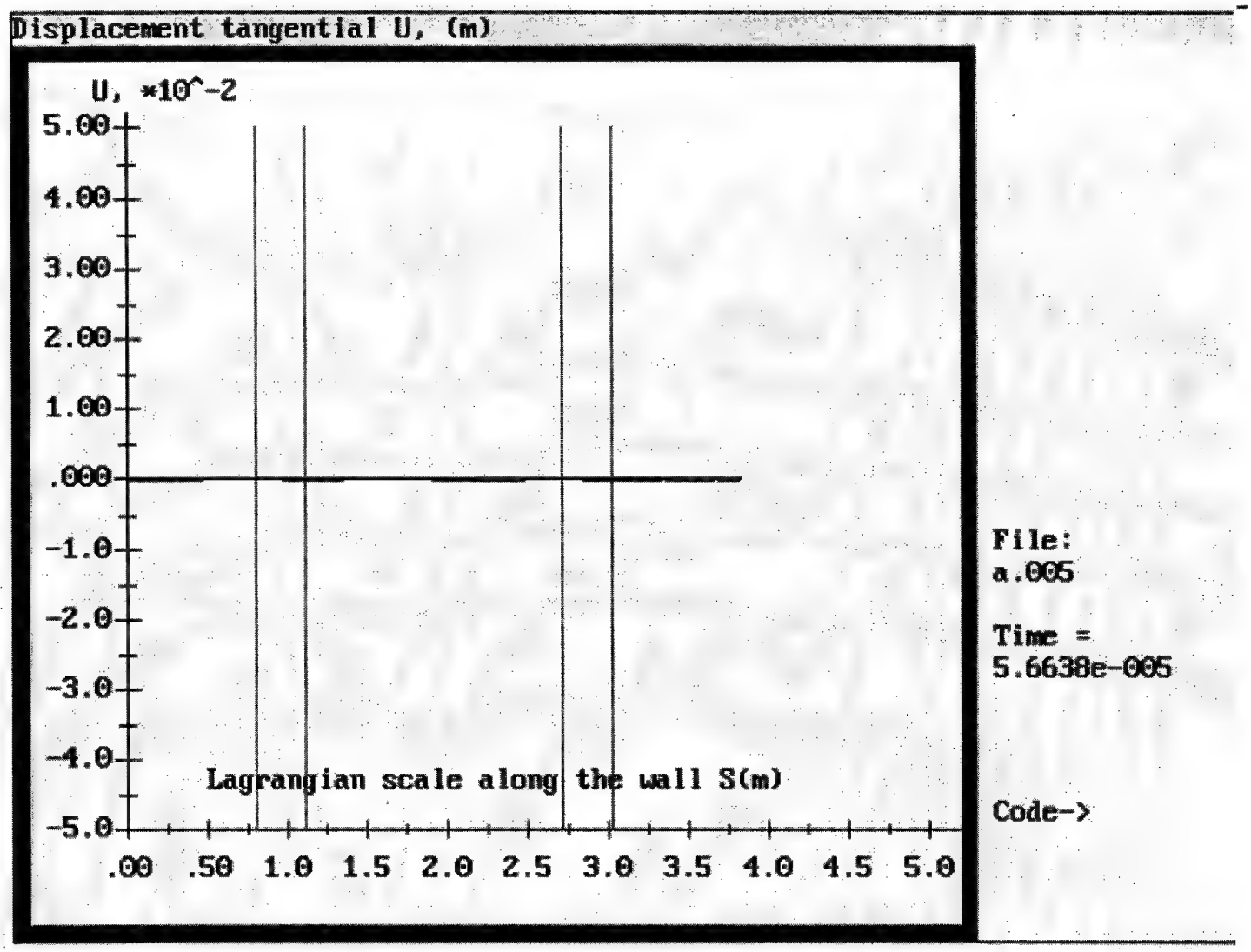
Displacement tangential U, (m)
U, *10^-2
5.00
4.00
3.00
2.00
1.00
.000
-1.0
-2.0
-3.0
-4.0
-5.0
Lagrangian scale along the wall S(m)
.00 .50 1.0 1.5 2.0 2.5 3.0 3.5 4.0 4.5 5.0
File:
a.005
Time =
5.6638e-005
Code->

Fig. 11.a.

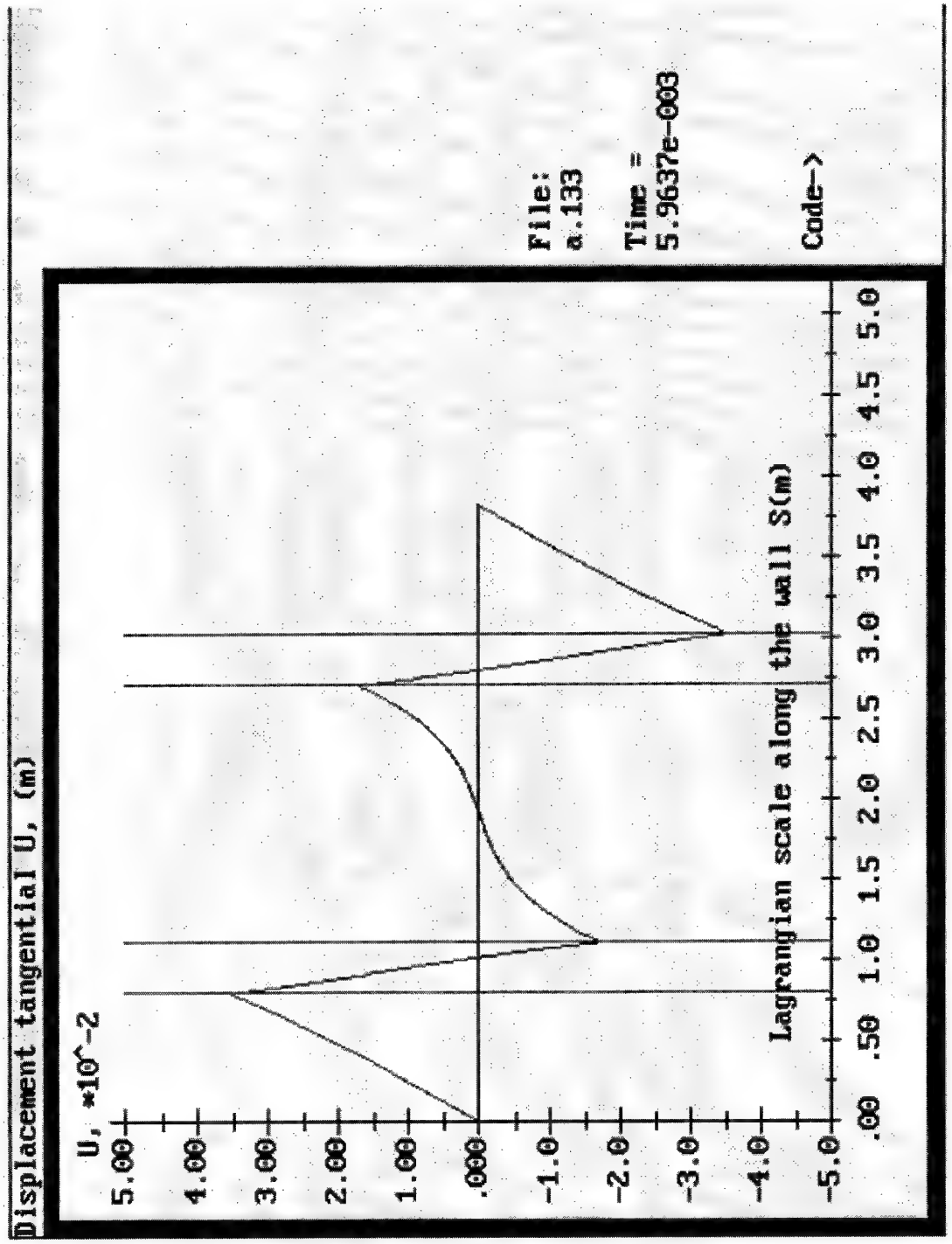
Displacement tangential U, (m)
U, *10^-2
5.00
4.00
3.00
2.00
1.00
.000
-1.0
-2.0
-3.0
-4.0
-5.0
.00
.50
1.0
1.5
2.0
2.5
3.0
3.5
4.0
4.5
5.0
Lagrangian scale along the wall S(m)
File:
a.133
Time =
5.9637e-003
Code->

Fig. 11. b.

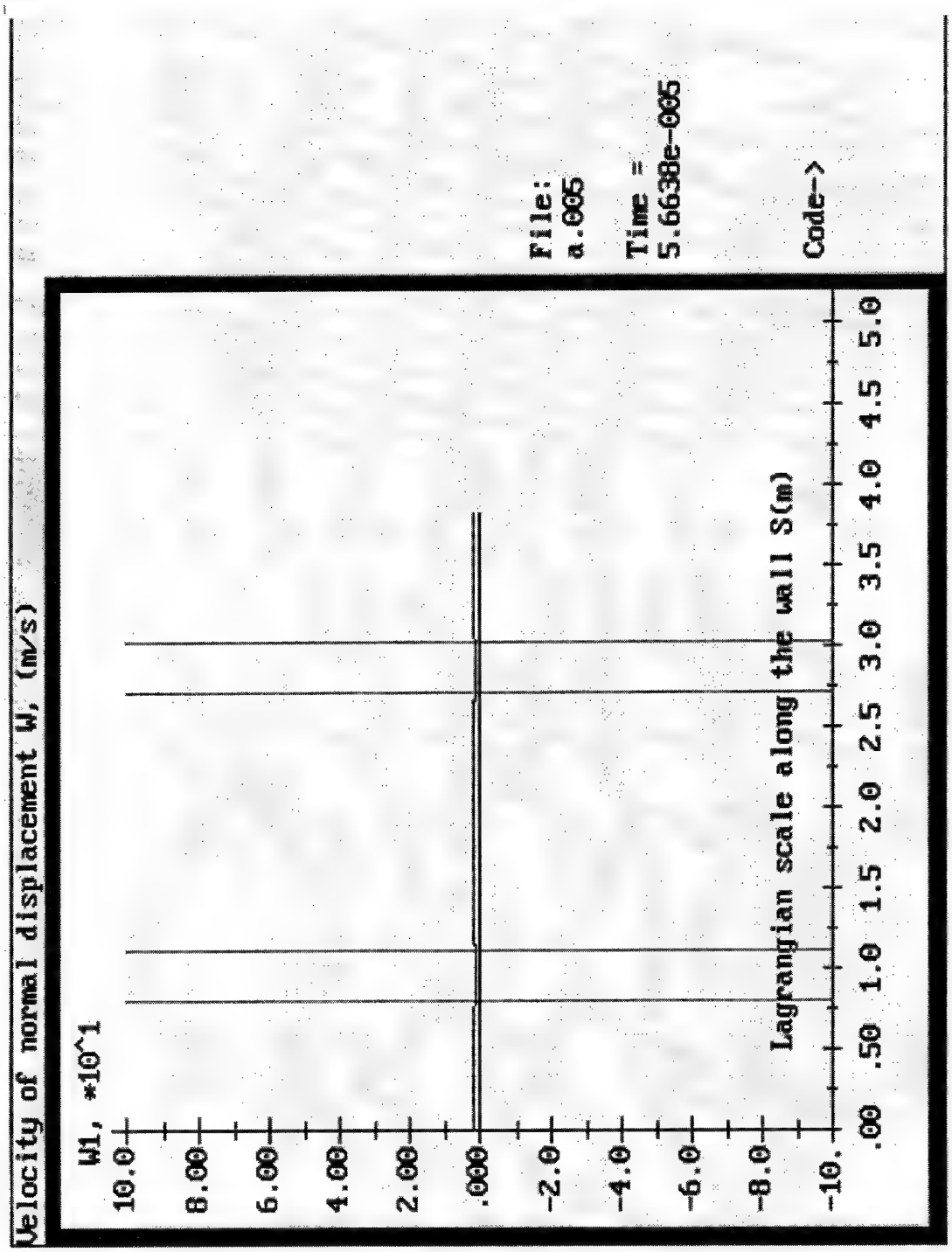
Velocity of normal displacement W, (m/s)
W1, *10^1
10.0
8.00
6.00
4.00
2.00
.000
-2.0
-4.0
-6.0
-8.0
-10.
.00
.50
1.0
1.5
2.0
2.5
3.0
3.5
4.0
4.5
5.0
Lagrangian scale along the wall S(m)
File:
a.005
Time =
5.6638e-005
Code->

Fig. 12.a.

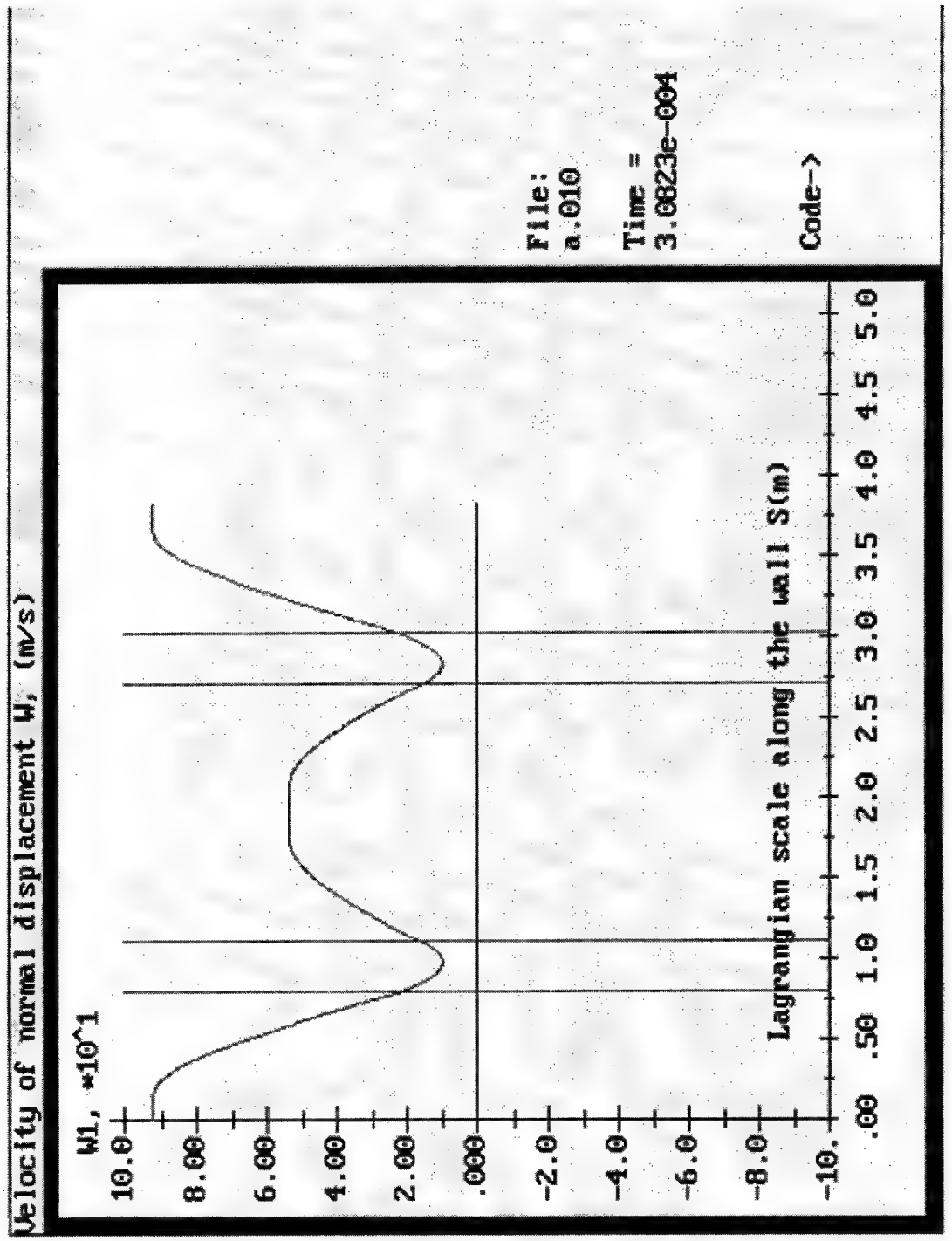
Velocity of normal displacement W, (m/s)
W1, *10^1
10.0
8.00
6.00
4.00
2.00
.000
-2.0
-4.0
-6.0
-8.0
-10.
.00
.50
1.0
1.5
2.0
2.5
3.0
3.5
4.0
4.5
5.0
Lagrangian scale along the wall S(m)
File:
a.010
Time =
3.0823e-004
Code->

Fig. 12. b.

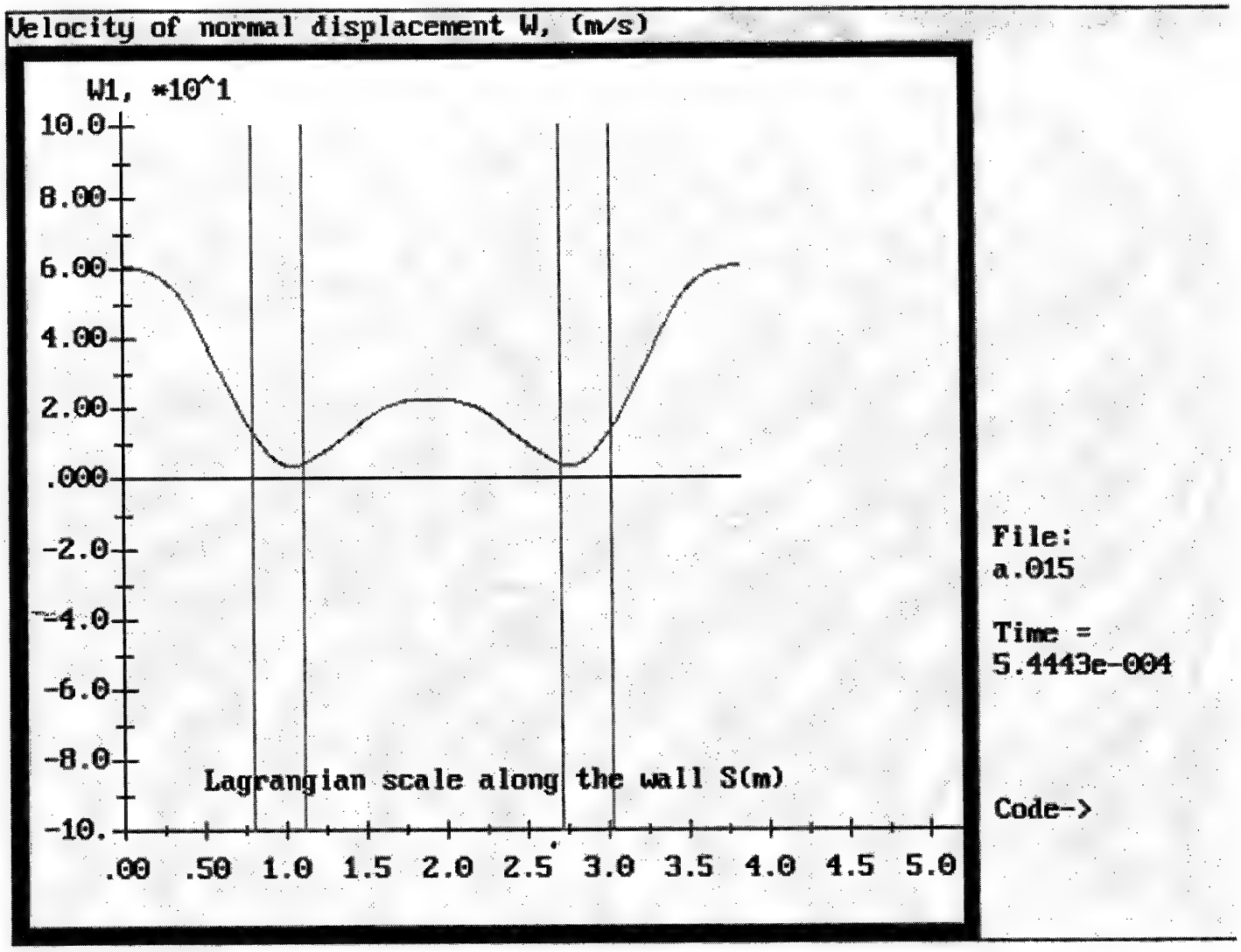
Velocity of normal displacement W, (m/s)
W1, *10^1
10.0
8.00
6.00
4.00
2.00
.000
-2.0
-4.0
-6.0
-8.0
-10.
.00
.50
1.0
1.5
2.0
2.5
3.0
3.5
4.0
4.5
5.0
Lagrangian scale along the wall S(m)
File:
a.015
Time =
5.4443e-004
Code->

Fig. 12.c.

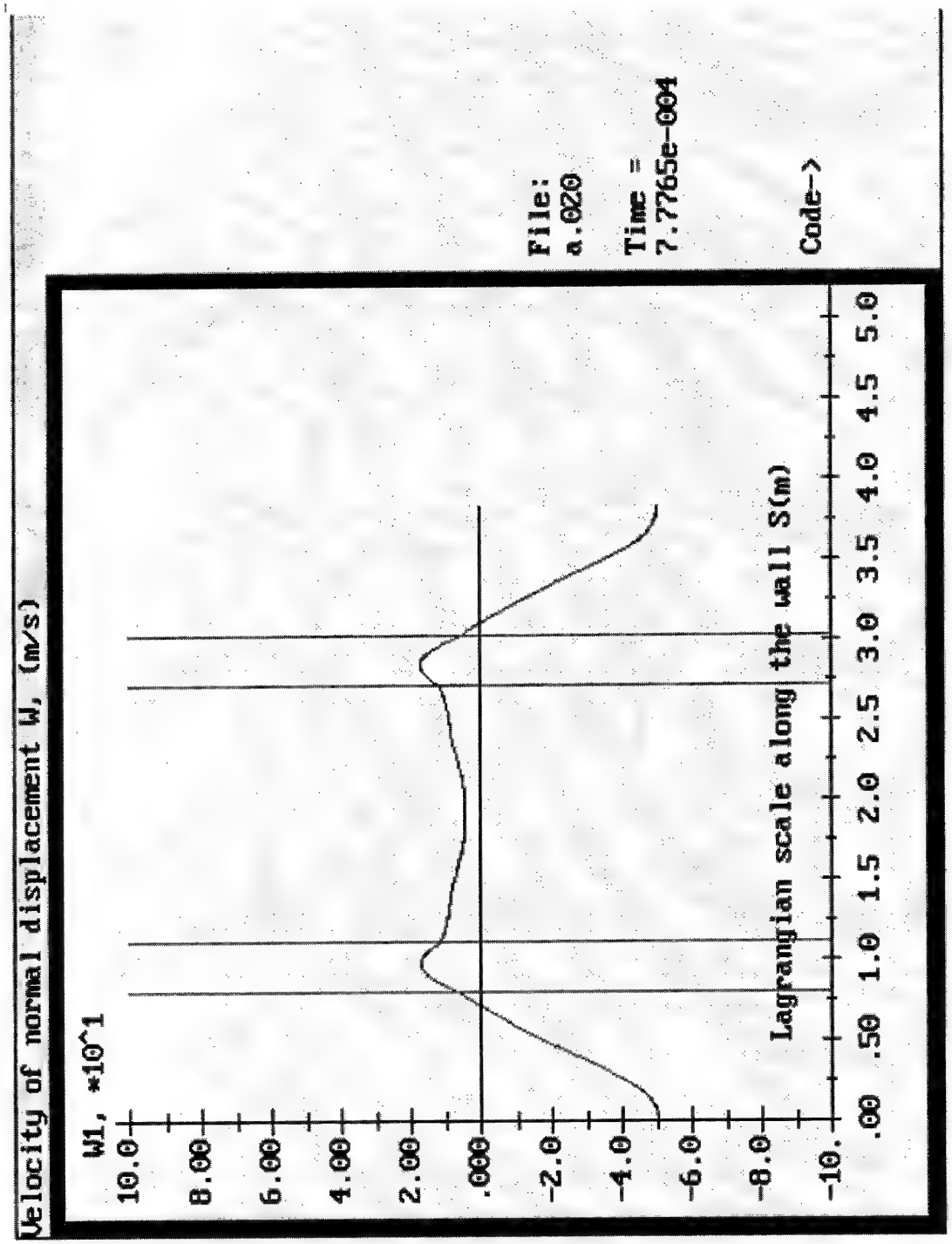
Velocity of normal displacement W, (m/s)
W1, *10^1
10.0
8.00
6.00
4.00
2.00
.000
-2.0
-4.0
-6.0
-8.0
-10.
.00
.50
1.0
1.5
2.0
2.5
3.0
3.5
4.0
4.5
5.0
Lagrangian scale along the wall S(m)
File:
a.020
Time =
7.7765e-004
Code->

Fig. 12.d.

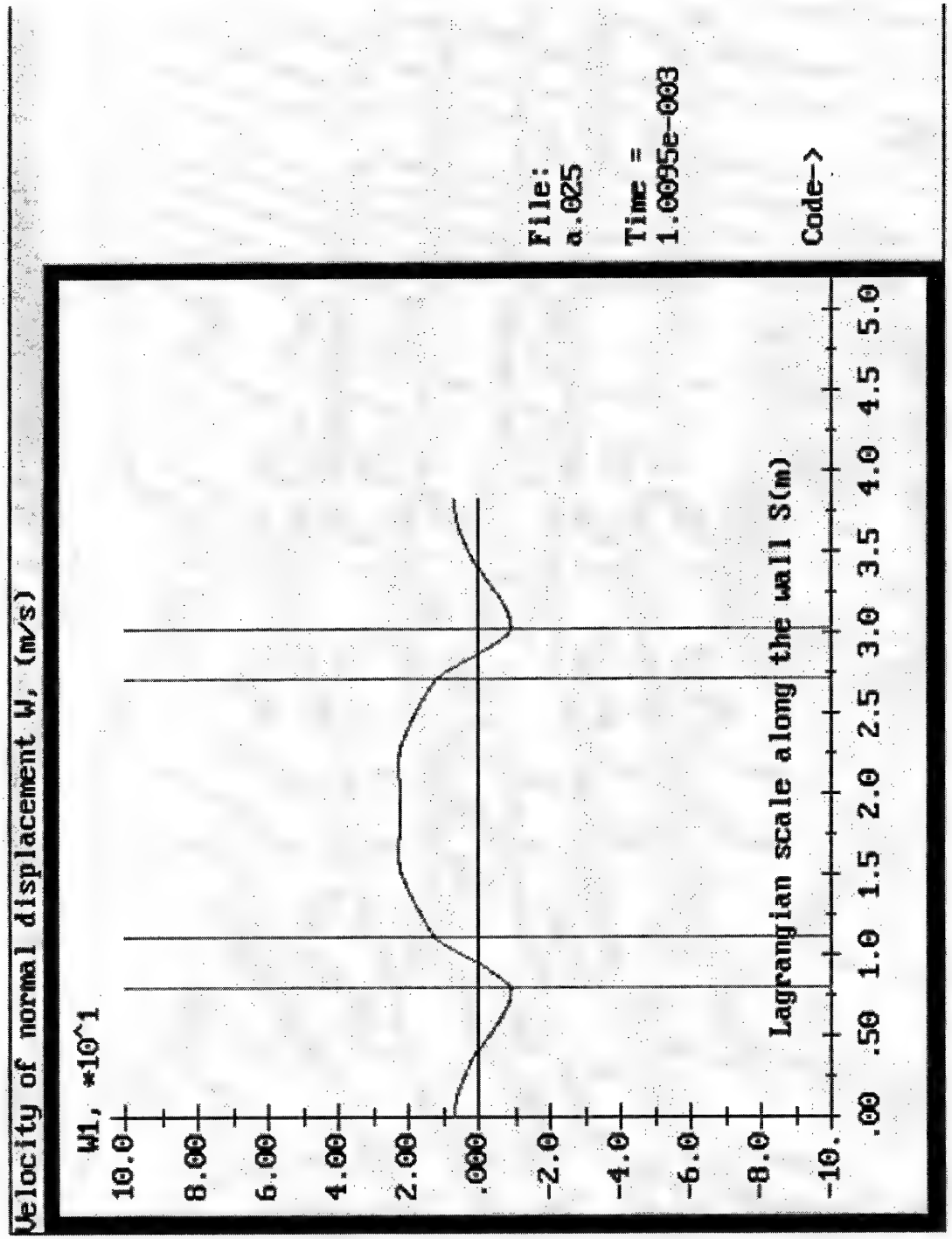
Velocity of normal displacement W, (m/s)
W1, *10^1
10.0
8.00
6.00
4.00
2.00
.000
-2.0
-4.0
-6.0
-8.0
-10.
.00
.50
1.0
1.5
2.0
2.5
3.0
3.5
4.0
4.5
5.0
Lagrangian scale along the wall S(m)
File:
a.025
Time =
1.0095e-003
Code->

Fig. 12. e.

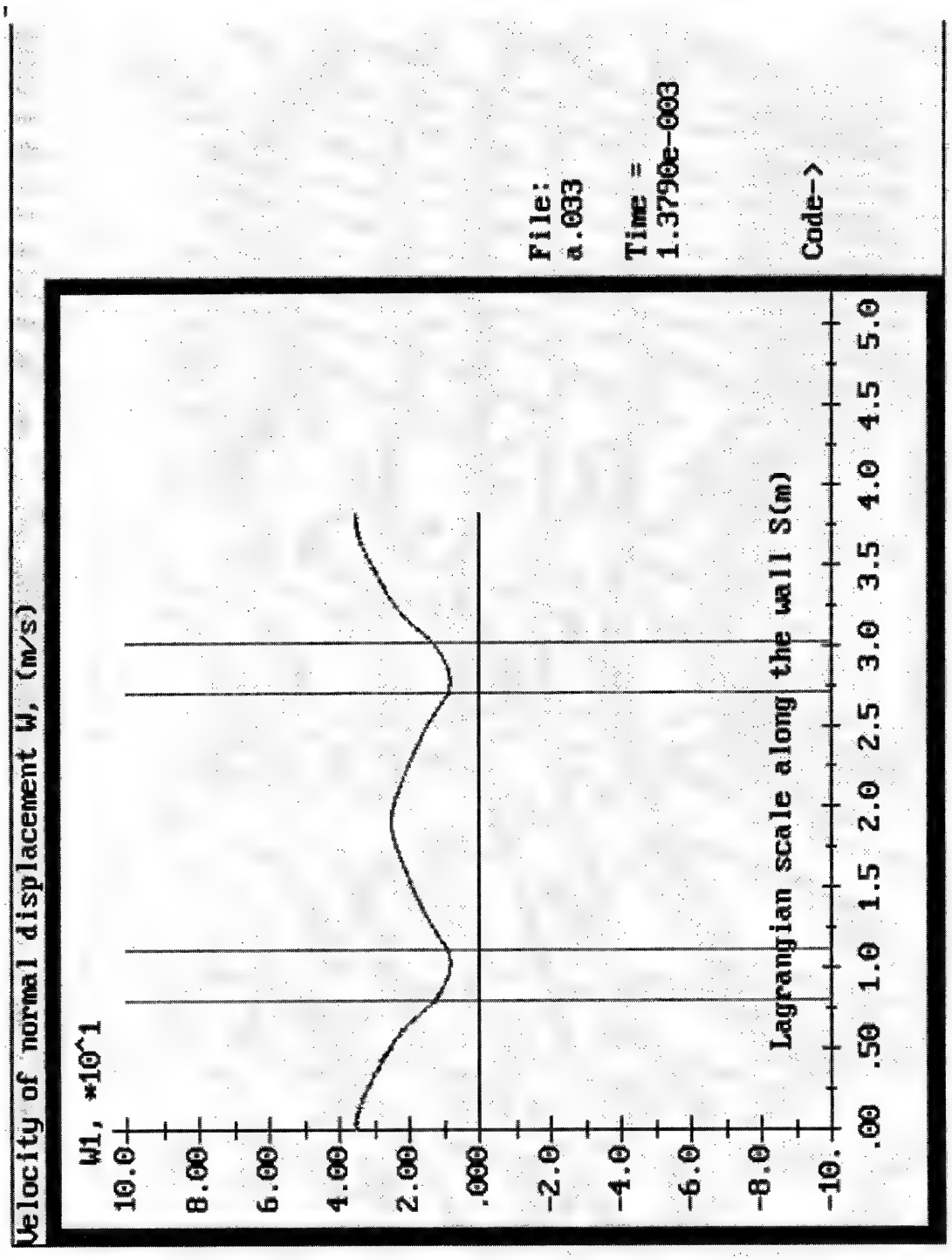
Velocity of normal displacement W, (m/s)
W1, *10^1
10.0
8.00
6.00
4.00
2.00
.000
-2.0
-4.0
-6.0
-8.0
-10.
.00
.50
1.0
1.5
2.0
2.5
3.0
3.5
4.0
4.5
5.0
Lagrangian scale along the wall S(m)
File:
a.033
Time =
1.3790e-003
Code->

Fig. 12. f.

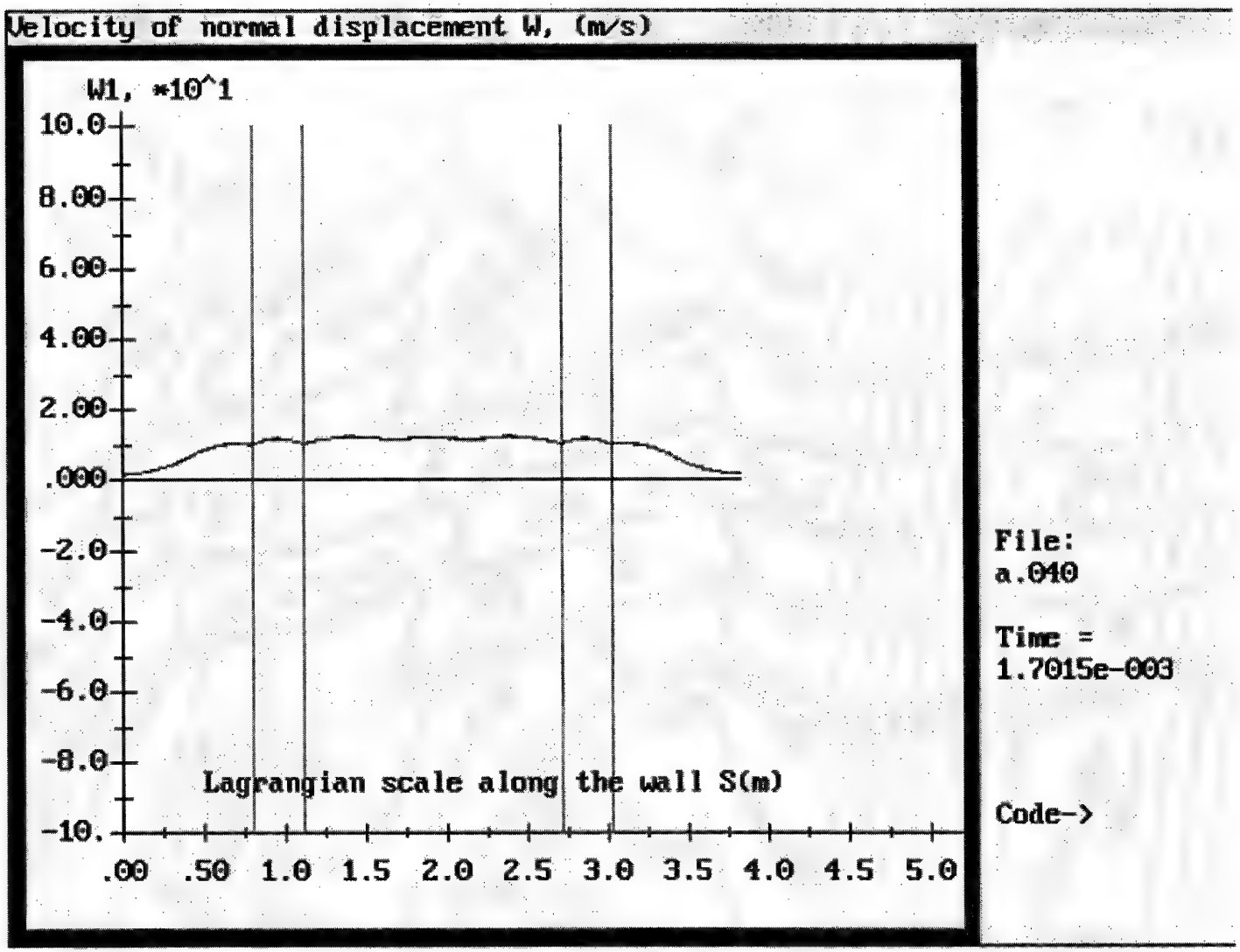
Velocity of normal displacement W, (m/s)
W1, *10^1
10.0
8.00
6.00
4.00
2.00
.000
-2.0
-4.0
-6.0
-8.0
-10.
Lagrangian scale along the wall S(m)
.00 .50 1.0 1.5 2.0 2.5 3.0 3.5 4.0 4.5 5.0
File:
a.040
Time =
1.7015e-003
Code->

Fig. 12.9.

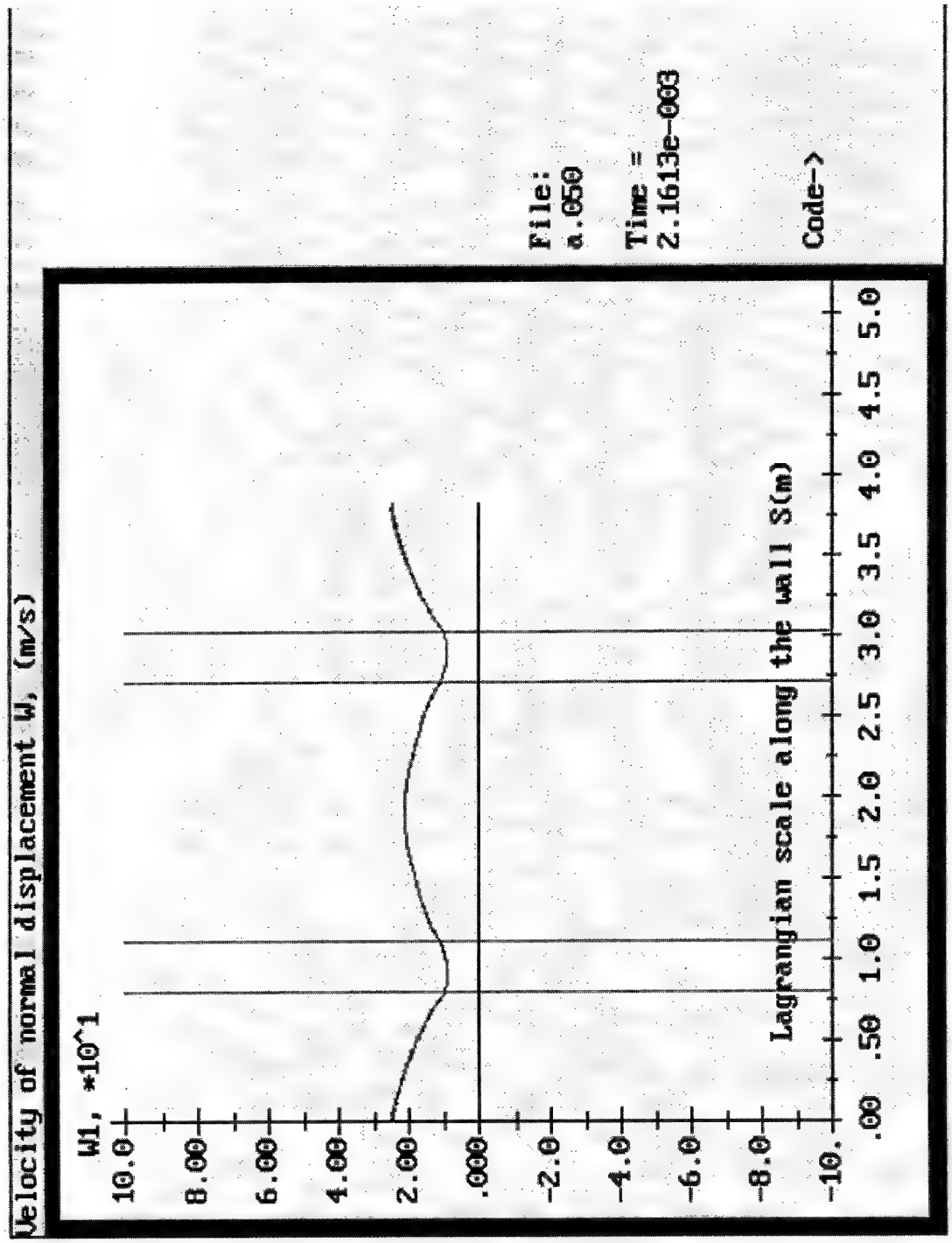
Velocity of normal displacement W, (m/s)
W1, *10^1
10.0
8.00
6.00
4.00
2.00
.000
-2.0
-4.0
-6.0
-8.0
-10.
.00
.50
1.0
1.5
2.0
2.5
3.0
3.5
4.0
4.5
5.0
Lagrangian scale along the wall S(m)
File:
a.050
Time =
2.1613e-003
Code->

Fig. 12. h.

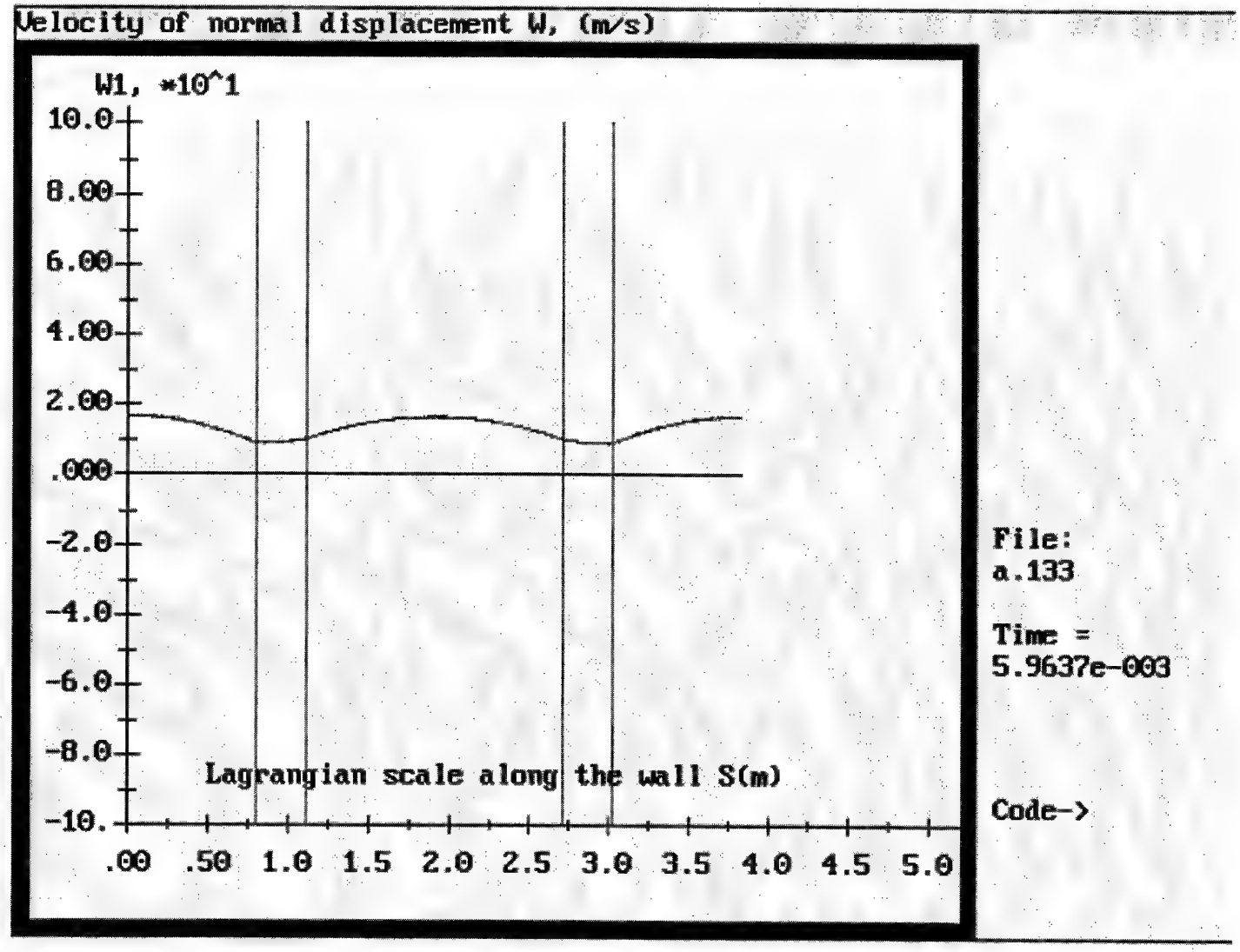
Velocity of normal displacement W, (m/s)
W1, *10^1
10.0
8.00
6.00
4.00
2.00
.000
-2.0
-4.0
-6.0
-8.0
-10.
Lagrangian scale along the wall S(m)
.00 .50 1.0 1.5 2.0 2.5 3.0 3.5 4.0 4.5 5.0
File:
a.133
Time =
5.9637e-003
Code->

Fig. 12.i.

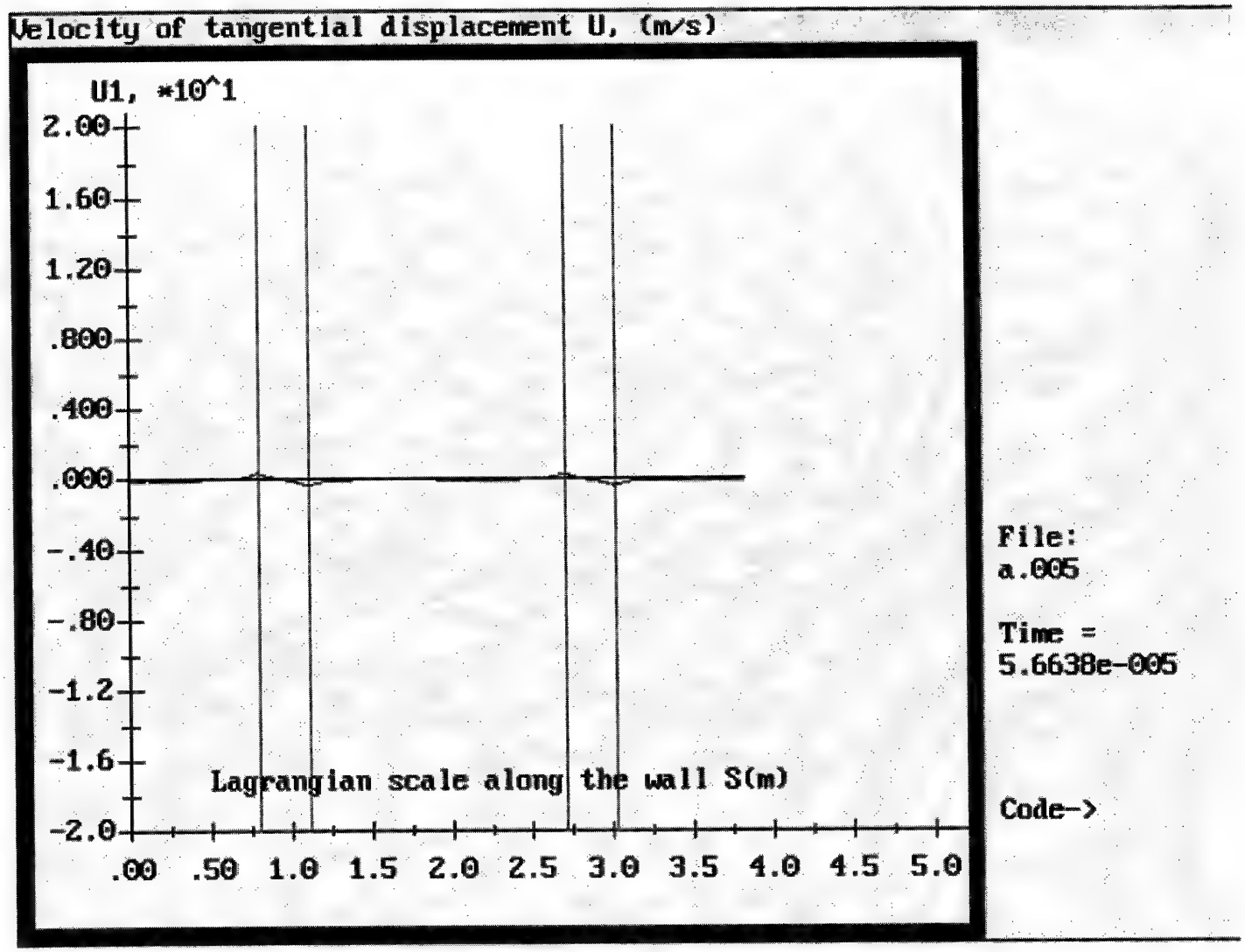
Velocity of tangential displacement U, (m/s)
U1, *10^1
2.00
1.60
1.20
.800
.400
.000
-.40
-.80
-1.2
-1.6
-2.0
Lagrangian scale along the wall S(m)
.00 .50 1.0 1.5 2.0 2.5 3.0 3.5 4.0 4.5 5.0
File:
a.005
Time =
5.6638e-005
Code->

Fig. 13.a

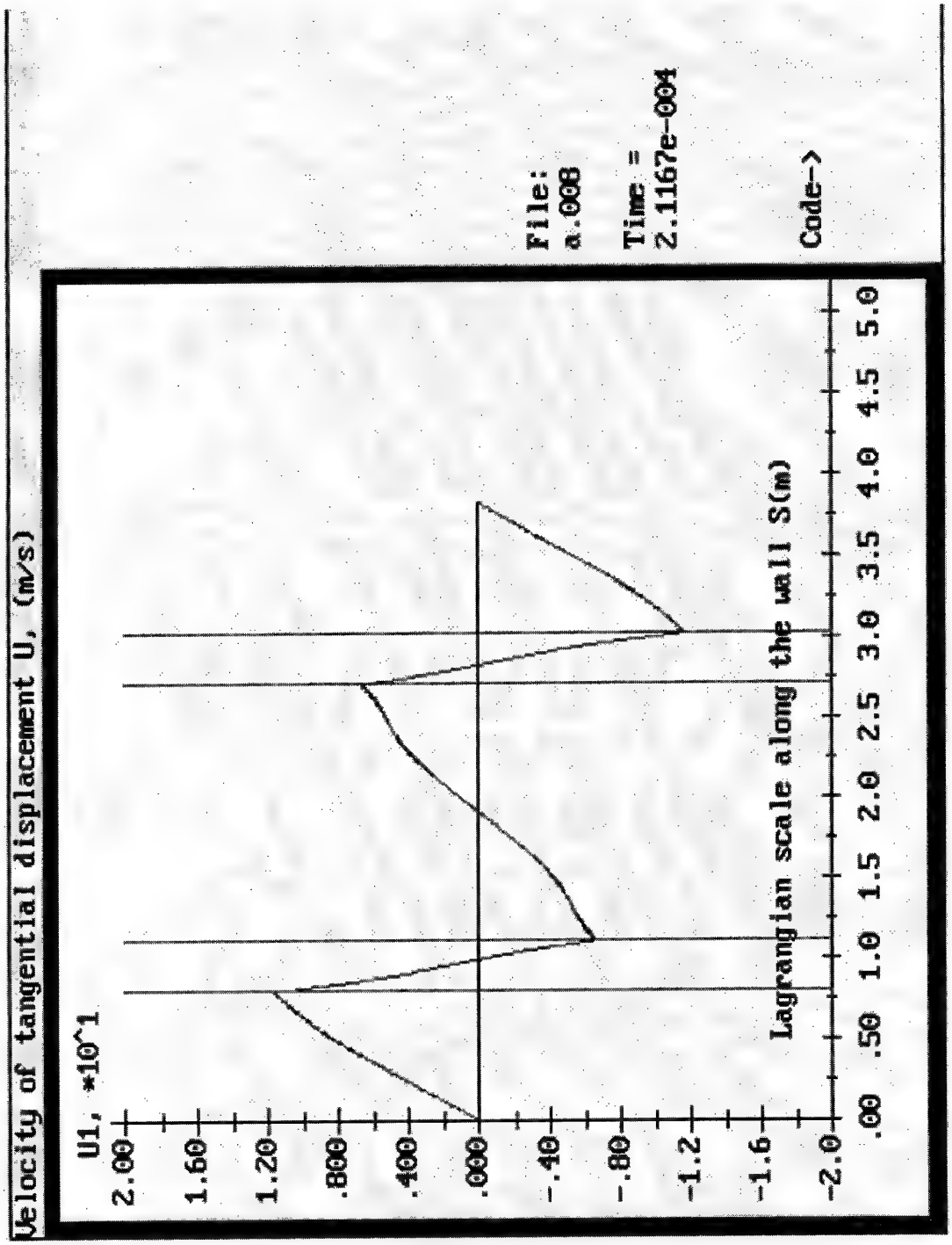
Velocity of tangential displacement U, (m/s)
U1, *10^1
2.00
1.60
1.20
.800
.400
.000
-.40
-.80
-1.2
-1.6
-2.0
.00
.50
1.0
1.5
2.0
2.5
3.0
3.5
4.0
4.5
5.0
Lagrangian scale along the wall S(m)
File:
a.008
Time =
2.1167e-004
Code->

Fig. 13. b.

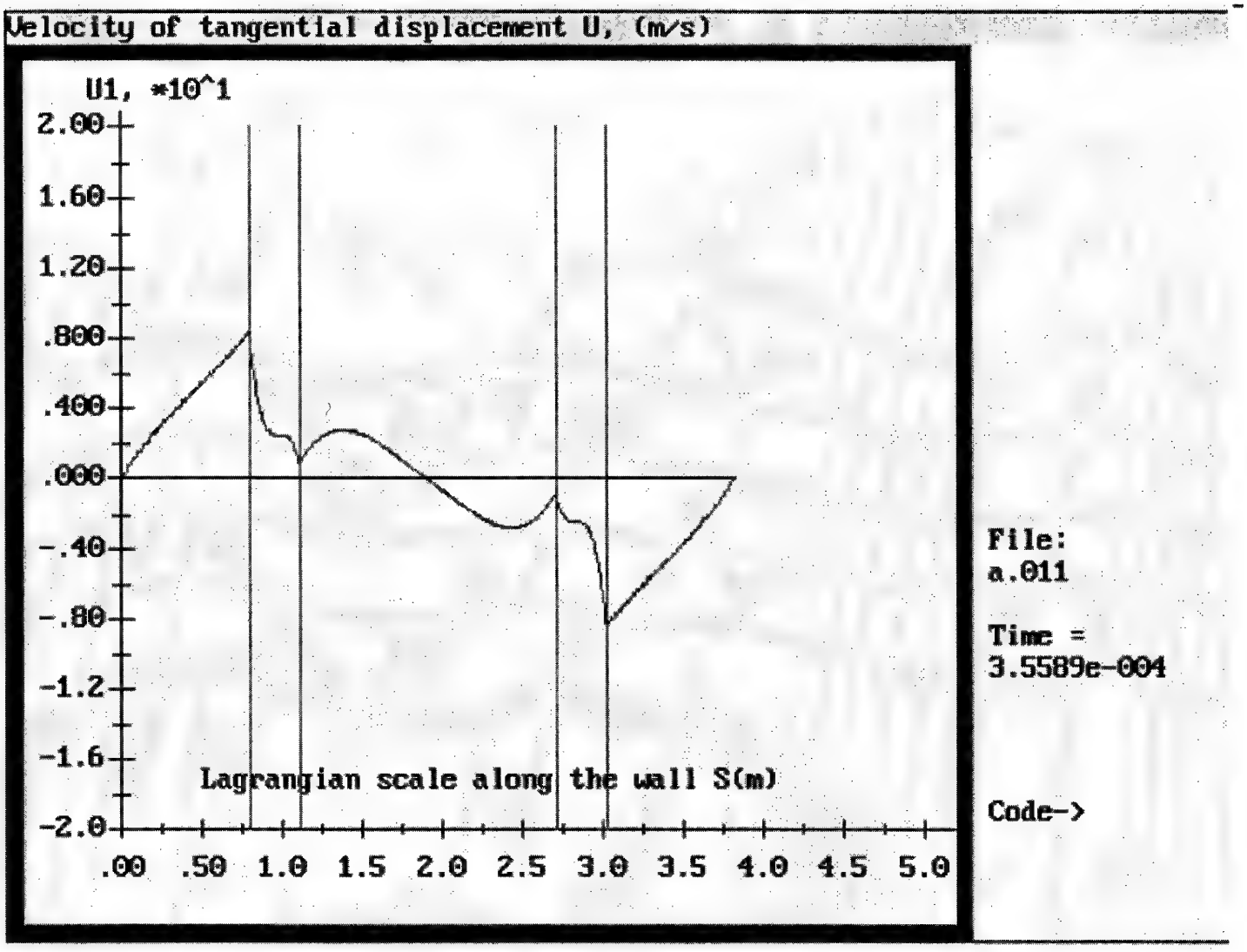
Velocity of tangential displacement U, (m/s)
U1, *10^1
2.00
1.60
1.20
.800
.400
.000
-.40
-.80
-1.2
-1.6
-2.0
Lagrangian scale along the wall S(m)
.00 .50 1.0 1.5 2.0 2.5 3.0 3.5 4.0 4.5 5.0
File:
a.011
Time =
3.5589e-004
Code->

Fig. 13.c.

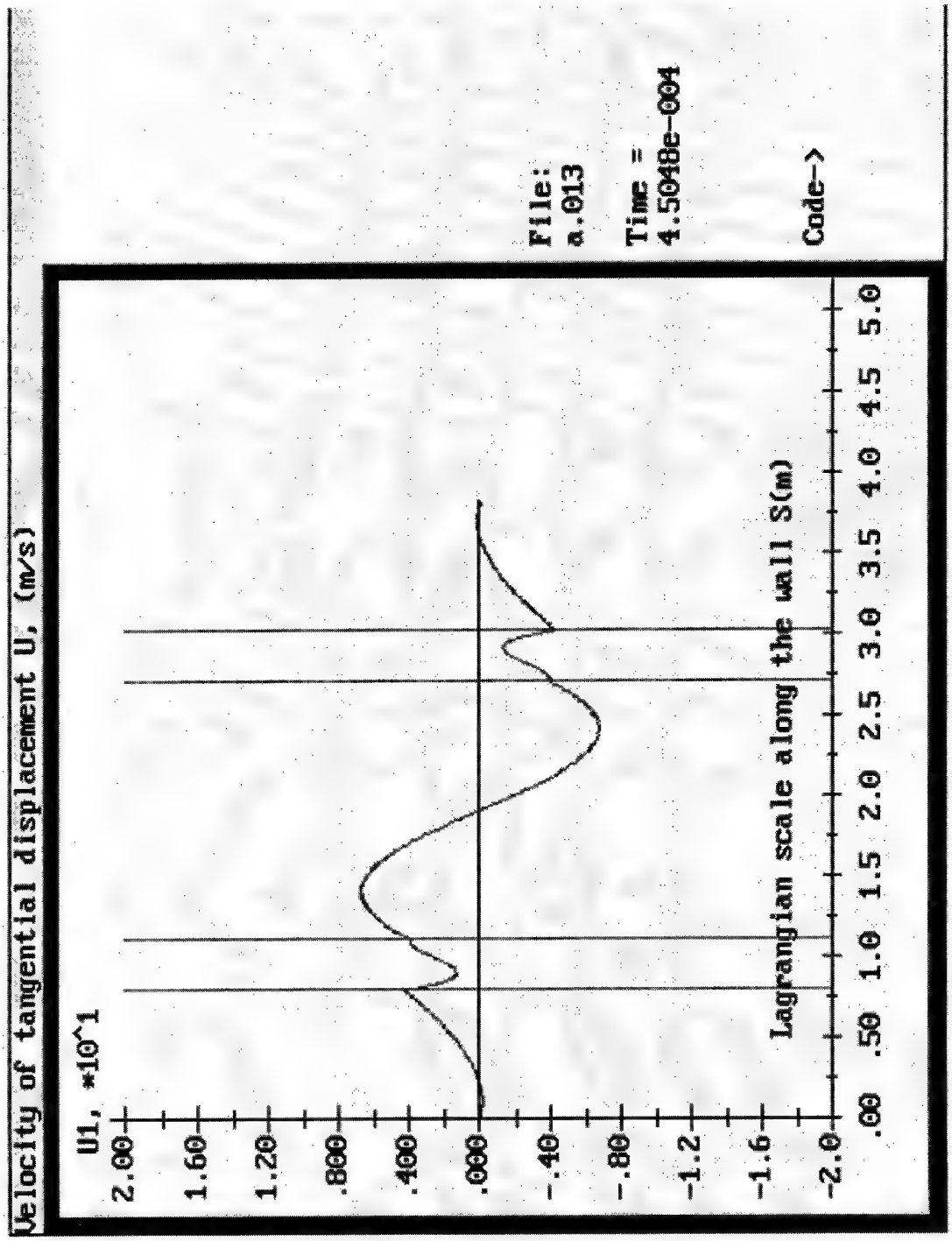
Velocity of tangential displacement U, (m/s)
U1, *10^1
2.00
1.60
1.20
.800
.400
.000
-.40
-.80
-1.2
-1.6
-2.0
.00
.50
1.0
1.5
2.0
2.5
3.0
3.5
4.0
4.5
5.0
Lagrangian scale along the wall S(m)
File:
a.013
Time =
4.5048e-004
Code->

Fig. 13.d.

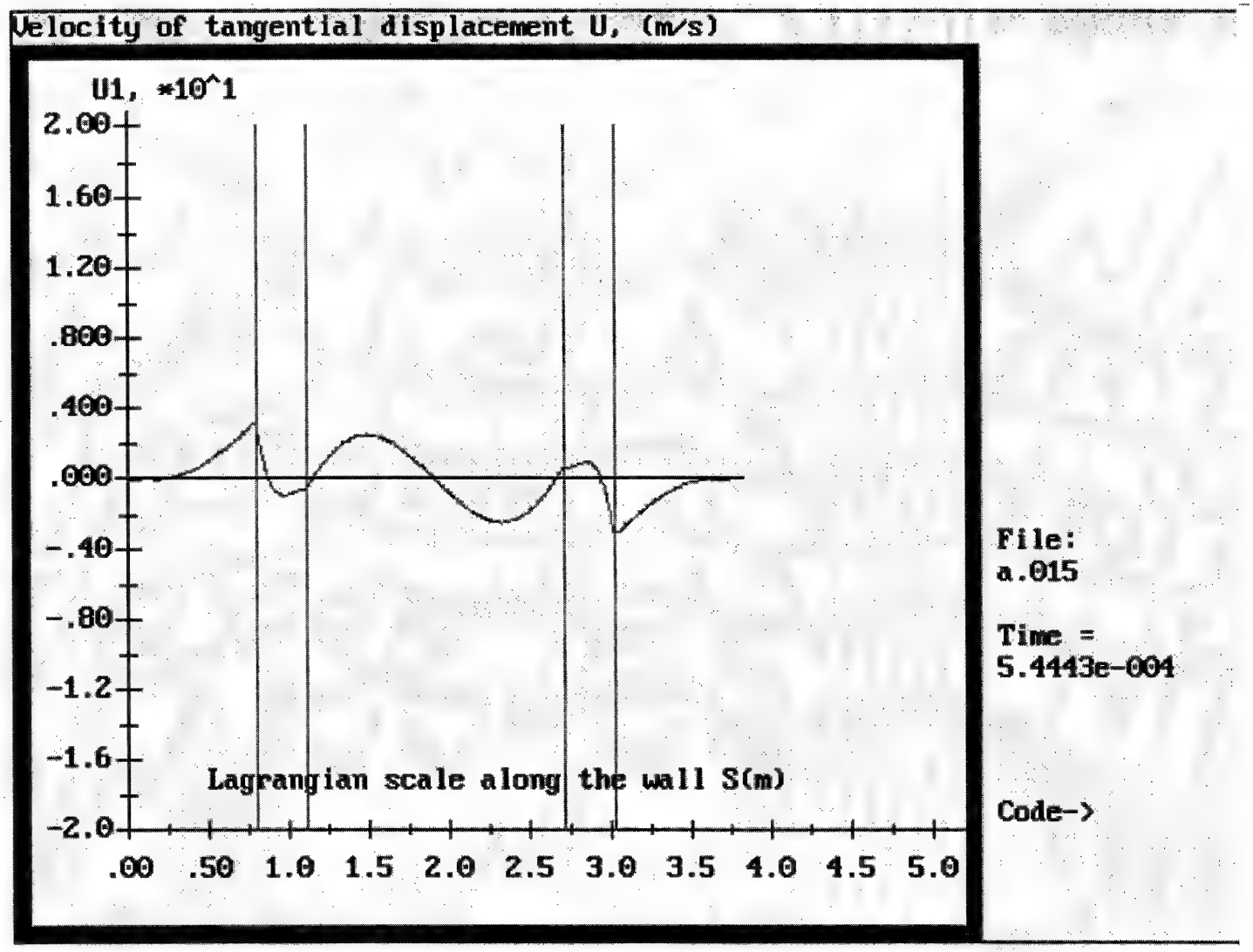
Velocity of tangential displacement U, (m/s)
U1, *10^1
2.00
1.60
1.20
.800
.400
.000
-.40
-.80
-1.2
-1.6
-2.0
Lagrangian scale along the wall S(m)
.00 .50 1.0 1.5 2.0 2.5 3.0 3.5 4.0 4.5 5.0
File:
a.015
Time =
5.4443e-004
Code->

Fig. 13.e.

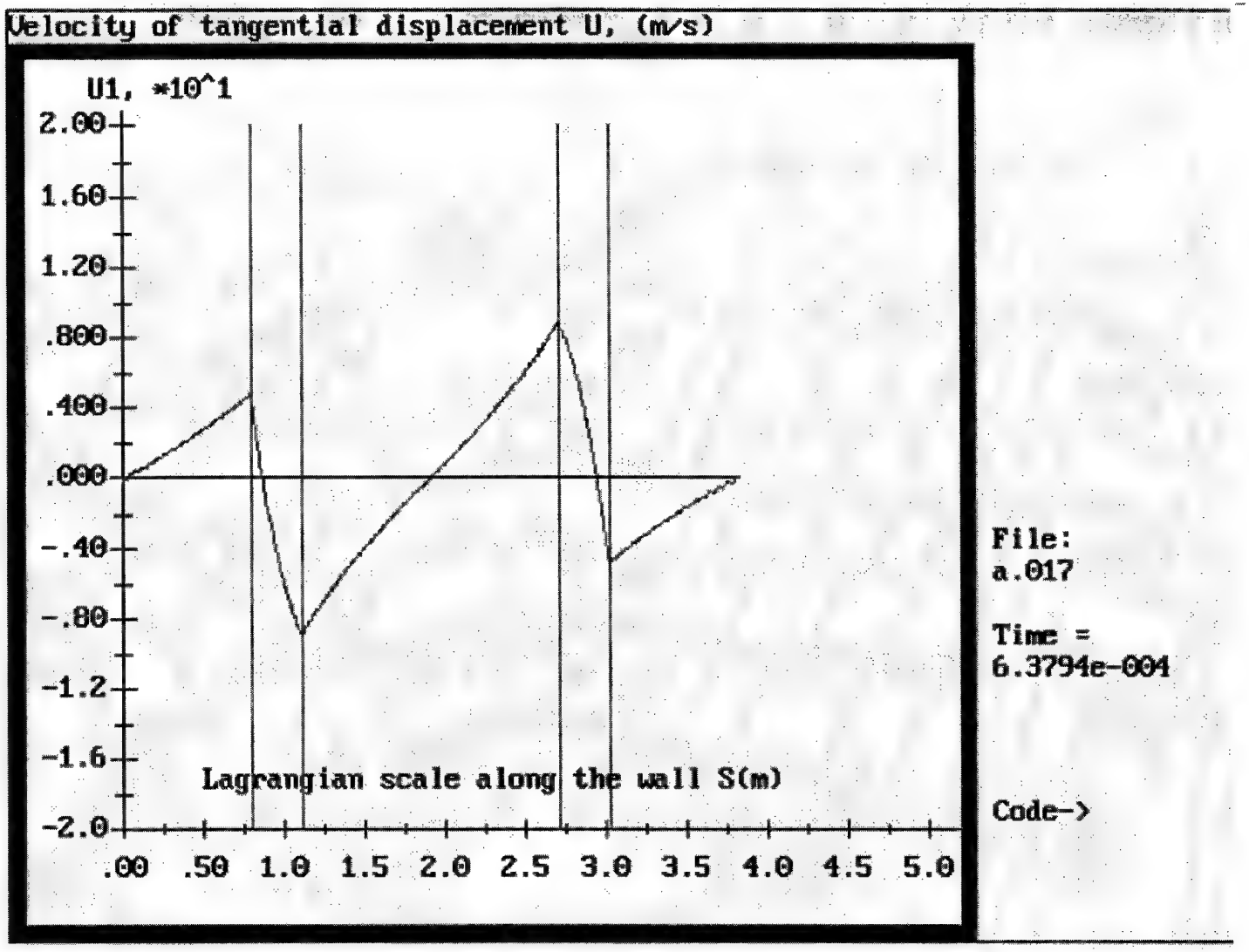
Velocity of tangential displacement U, (m/s)
U1, *10^1
2.00
1.60
1.20
.800
.400
.000
-.40
-.80
-1.2
-1.6
-2.0
.00
.50
1.0
1.5
2.0
2.5
3.0
3.5
4.0
4.5
5.0
Lagrangian scale along the wall S(m)
File:
a.017
Time =
6.3794e-004
Code->

Fig. 13. f.

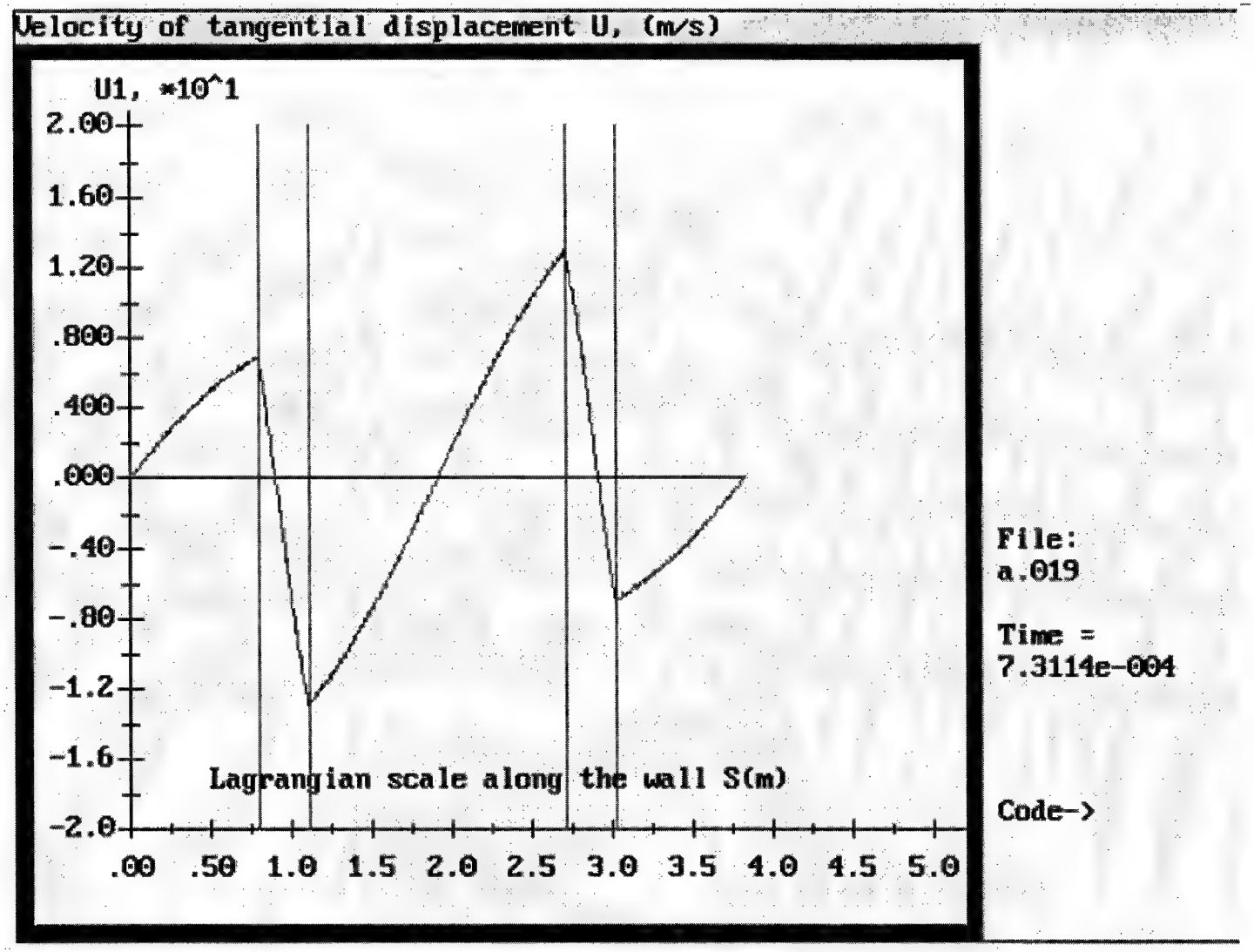
Velocity of tangential displacement U, (m/s)
U1, *10^1
2.00
1.60
1.20
.800
.400
.000
-.40
-.80
-1.2
-1.6
-2.0
.00
.50
1.0
1.5
2.0
2.5
3.0
3.5
4.0
4.5
5.0
Lagrangian scale along the wall S(m)
File:
a.019
Time =
7.3114e-004
Code->

Fig. 13.g.

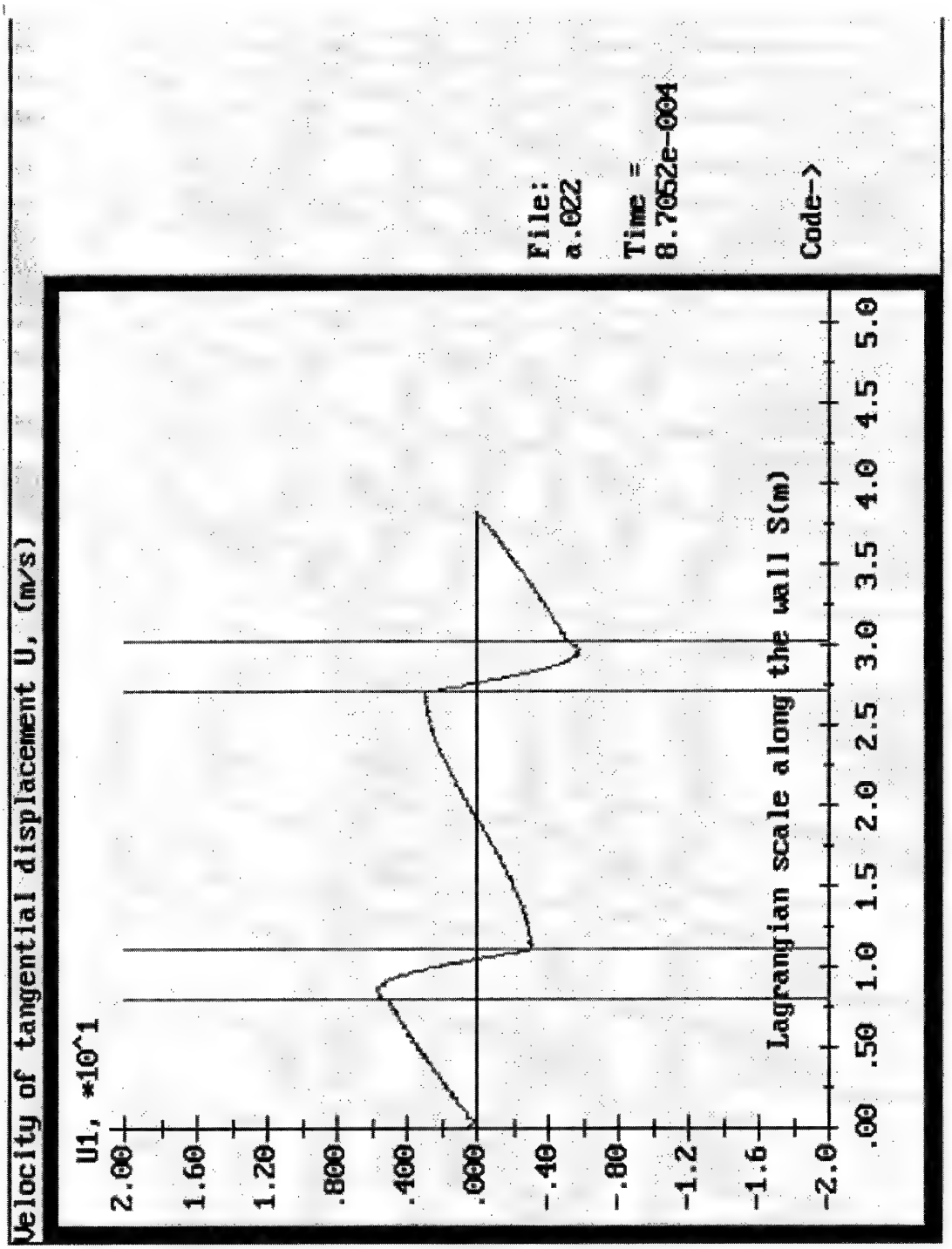
Velocity of tangential displacement U, (m/s)
U1, *10^1
2.00
1.60
1.20
.800
.400
.000
-.40
-.80
-1.2
-1.6
-2.0
.00
.50
1.0
1.5
2.0
2.5
3.0
3.5
4.0
4.5
5.0
Lagrangian scale along the wall S(m)
File:
a.022
Time =
8.7052e-004
Code->

Fig. 13. h.

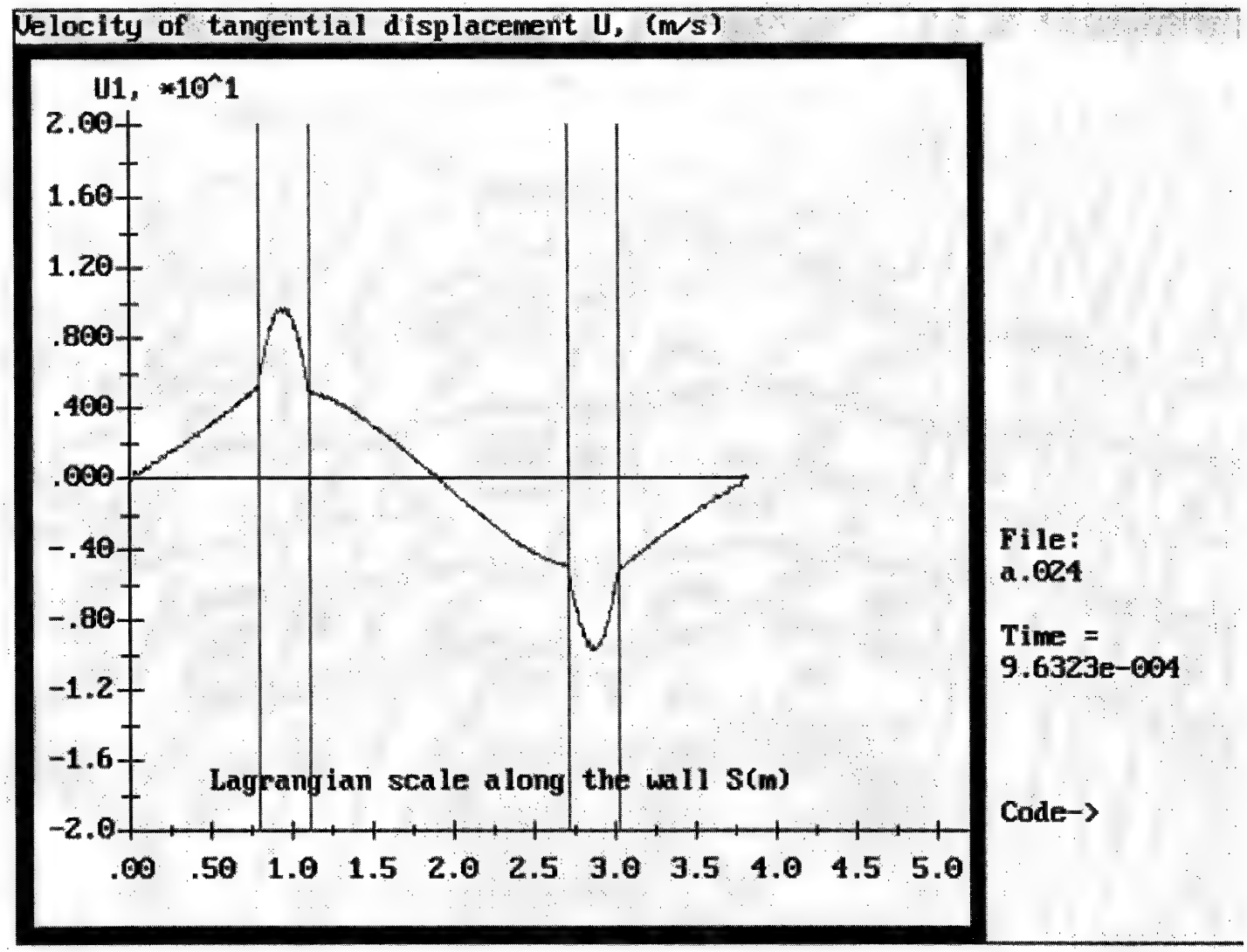
Velocity of tangential displacement U, (m/s)
U1, *10^1
2.00
1.60
1.20
.800
.400
.000
-.40
-.80
-1.2
-1.6
-2.0
Lagrangian scale along the wall S(m)
.00 .50 1.0 1.5 2.0 2.5 3.0 3.5 4.0 4.5 5.0
File:
a.024
Time =
9.6323e-004
Code->

Fig. 13.1.

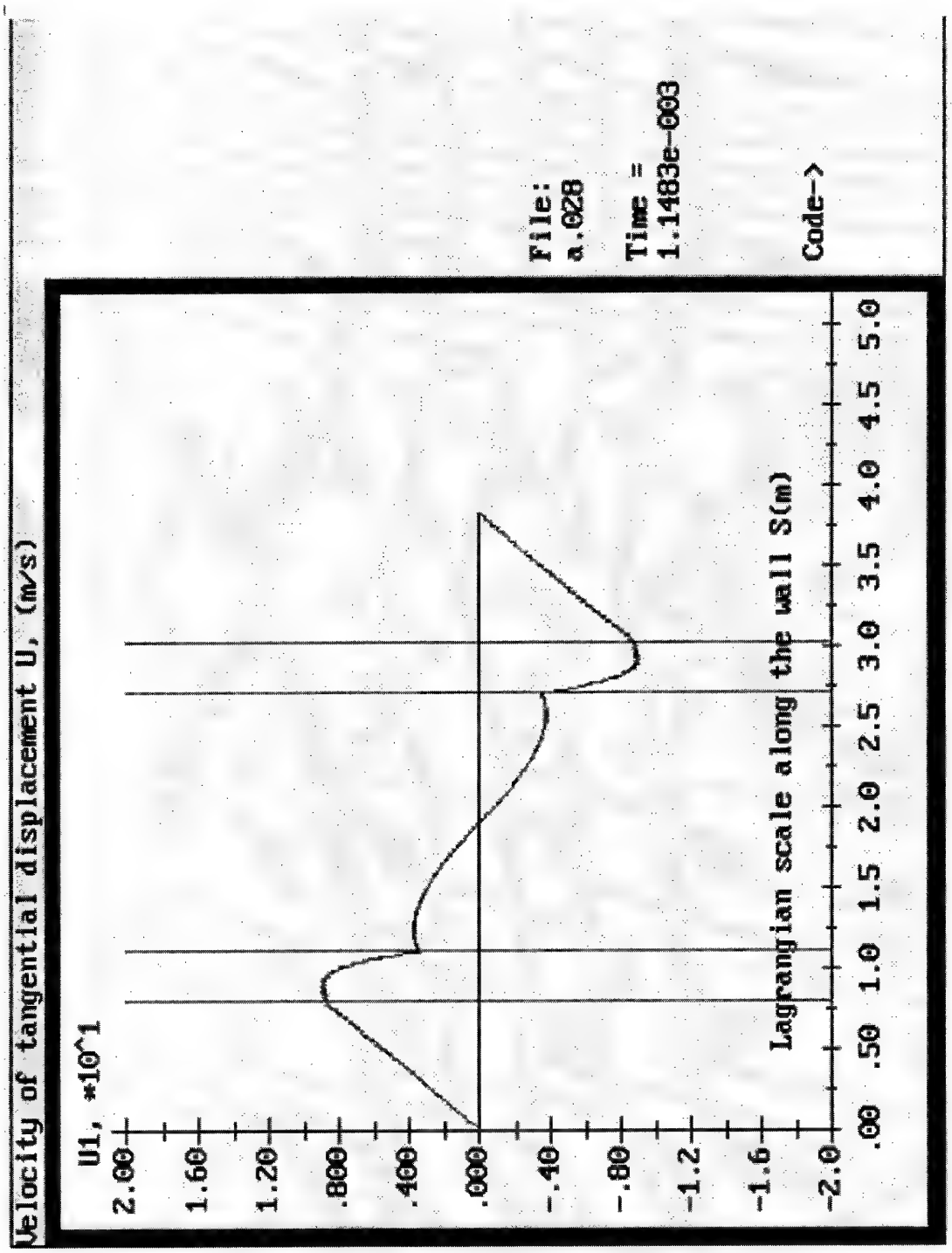
Velocity of tangential displacement U, (m/s)
U1, *10^1
2.00
1.60
1.20
.800
.400
.000
-.40
-.80
-1.2
-1.6
-2.0
.00
.50
1.0
1.5
2.0
2.5
3.0
3.5
4.0
4.5
5.0
Lagrangian scale along the wall S(m)
File:
a.028
Time =
1.1483e-003
Code->

Fig. 13. k.

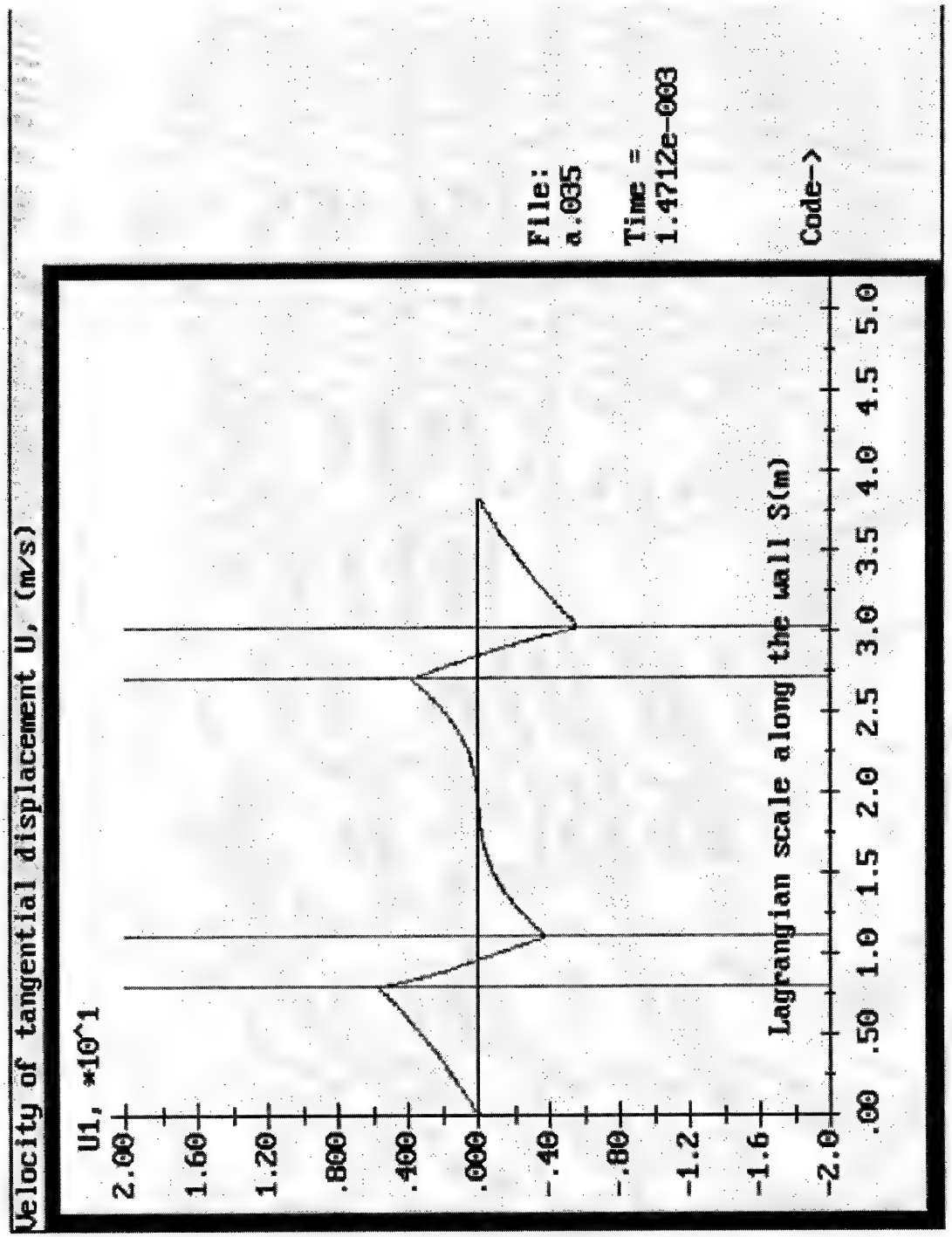
Velocity of tangential displacement U, (m/s)
U1, *10^1
2.00
1.60
1.20
.800
.400
.000
-.40
-.80
-1.2
-1.6
-2.0
.00
.50
1.0
1.5
2.0
2.5
3.0
3.5
4.0
4.5
5.0
Lagrangian scale along the wall S(m)
File:
a.035
Time =
1.4712e-003
Code->

Fig. 13. l.

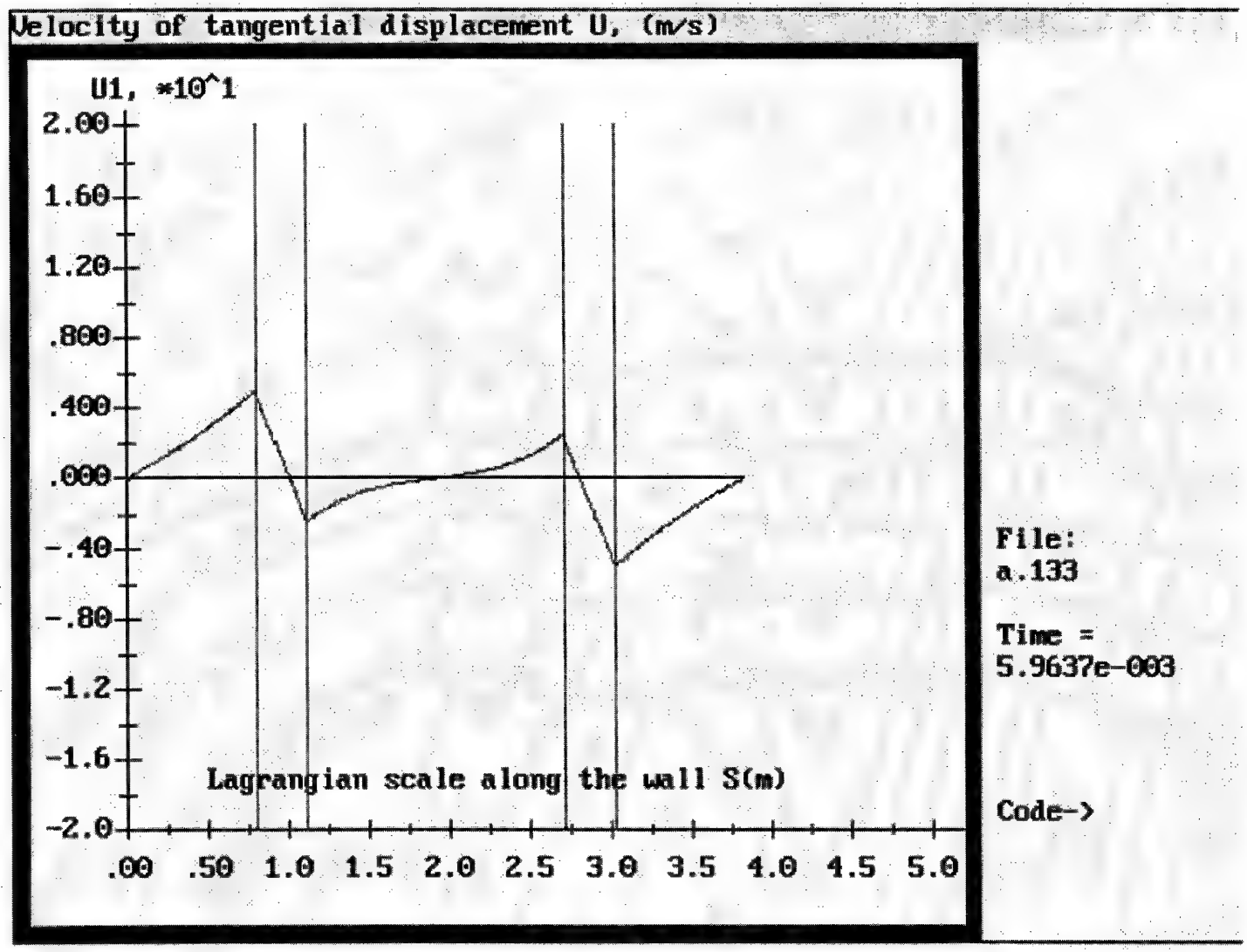
Velocity of tangential displacement U, (m/s)
U1, *10^1
2.00
1.60
1.20
.800
.400
.000
-.40
-.80
-1.2
-1.6
-2.0
.00
.50
1.0
1.5
2.0
2.5
3.0
3.5
4.0
4.5
5.0
Lagrangian scale along the wall S(m)
File:
a.133
Time =
5.9637e-003
Code->

Fig. 13.m.

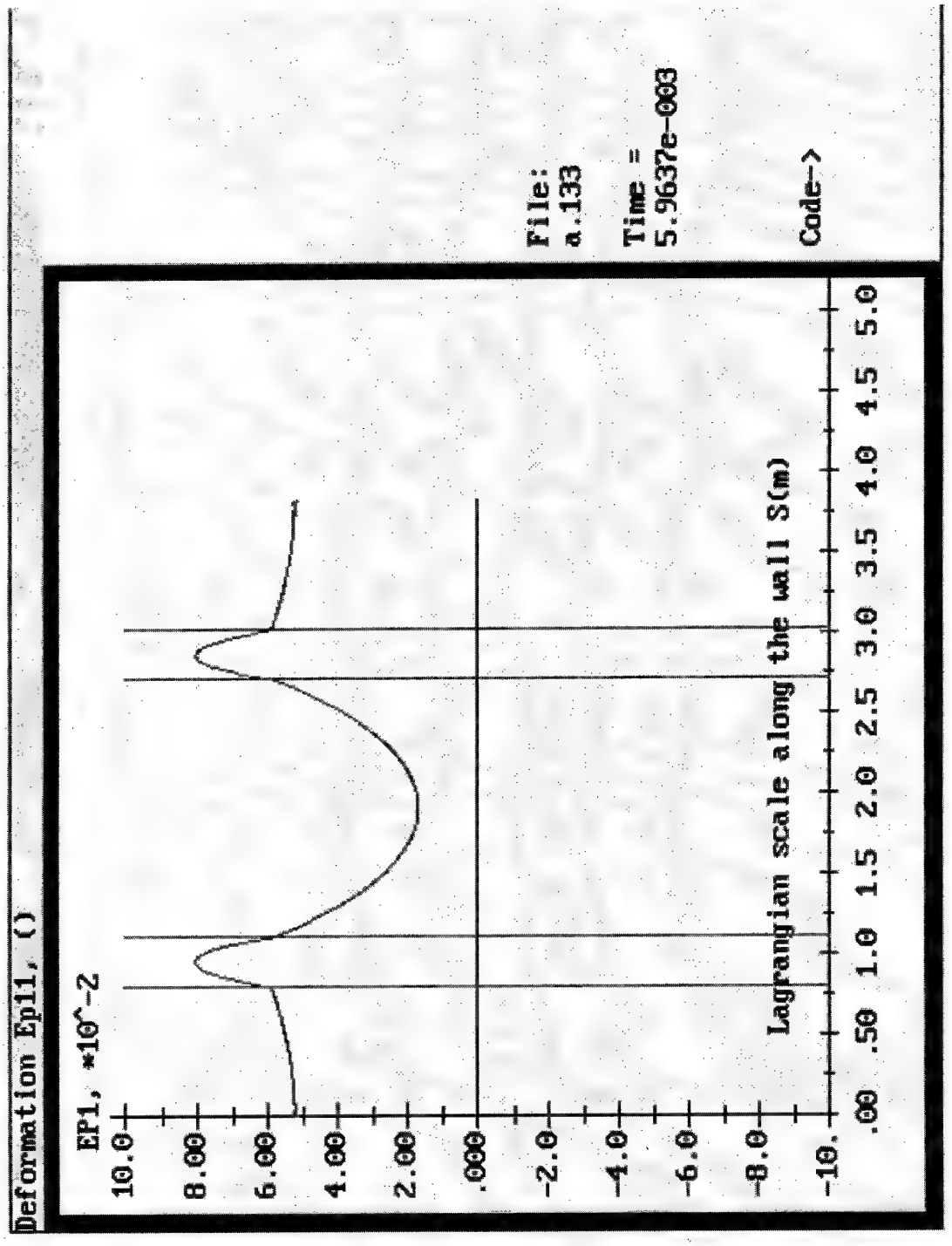
Deformation Ep11, ()
EP1, *10^-2
10.0
8.00
6.00
4.00
2.00
.0000
-2.0
-4.0
-6.0
-8.0
-10.
.00
.50
1.0
1.5
2.0
2.5
3.0
3.5
4.0
4.5
5.0
Lagrangian scale along the wall S(m)
File:
a.133
Time =
5.9637e-003
Code->

Fig. 14.

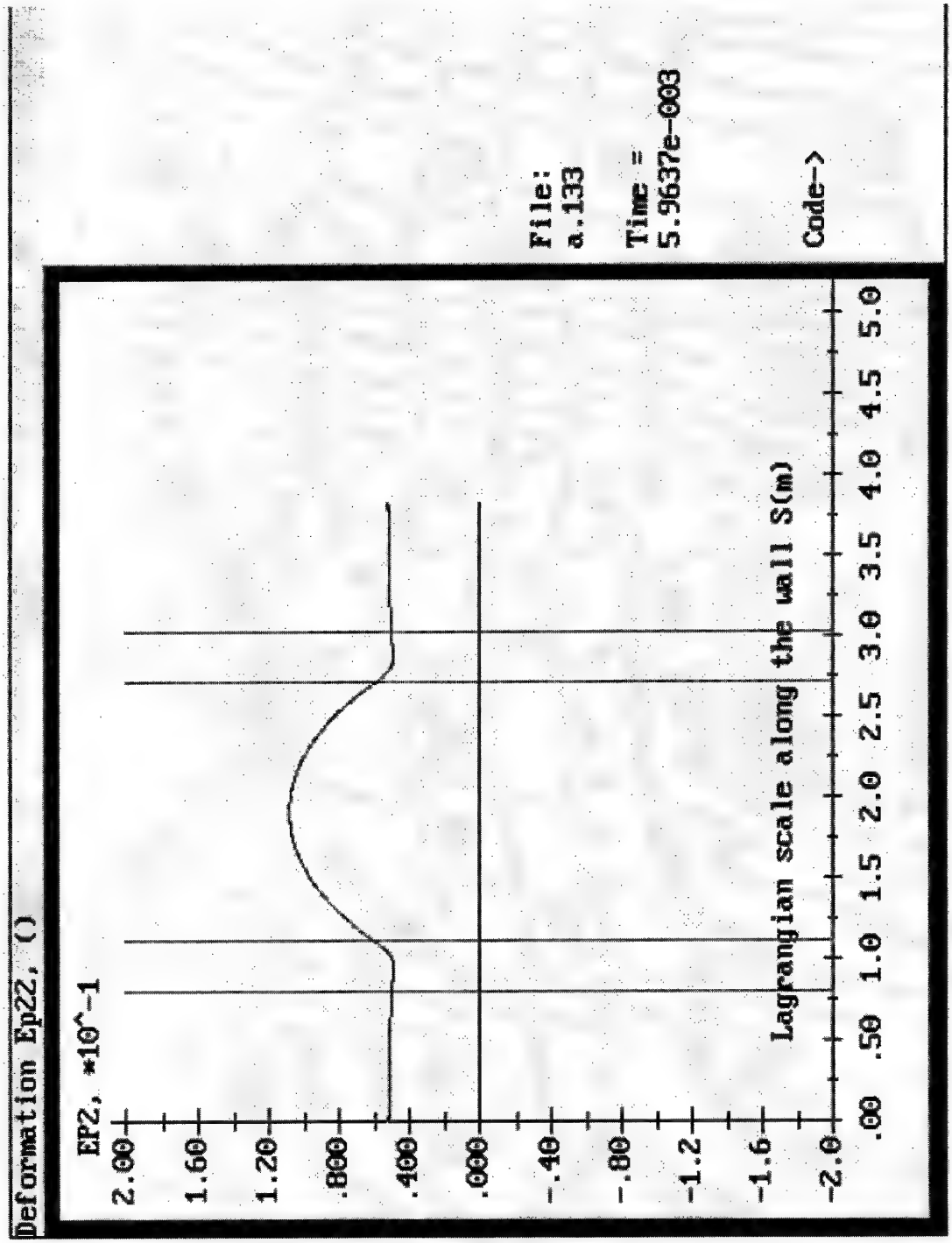
Deformation Ep22, ()
EP2, *10^-1
2.00
1.60
1.20
.800
.400
.000
-.40
-.80
-1.2
-1.6
-2.0
.00
.50
1.0
1.5
2.0
2.5
3.0
3.5
4.0
4.5
5.0
Lagrangian scale along the wall S(m)
File:
a.133
Time =
5.9637e-003
Code->

Fig. 15.

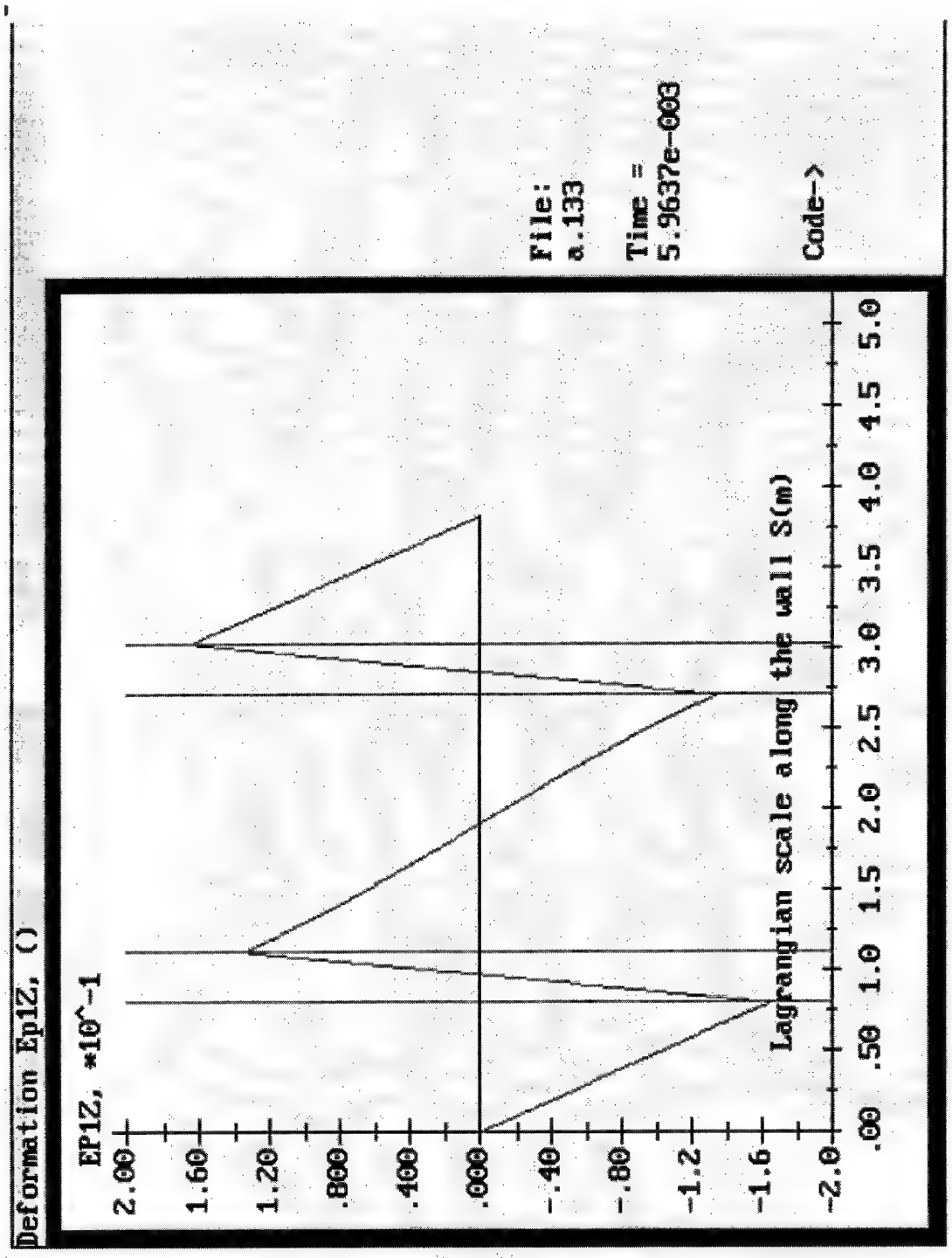
Deformation Ep1Z, ()
EP1Z, *10^-1
2.00
1.60
1.20
.800
.400
.000
-.40
-.80
-1.2
-1.6
-2.0
.00
.50
1.0
1.5
2.0
2.5
3.0
3.5
4.0
4.5
5.0
Lagrangian scale along the wall S(m)
File:
a.133
Time =
5.9637e-003
Code->

Fig. 16.

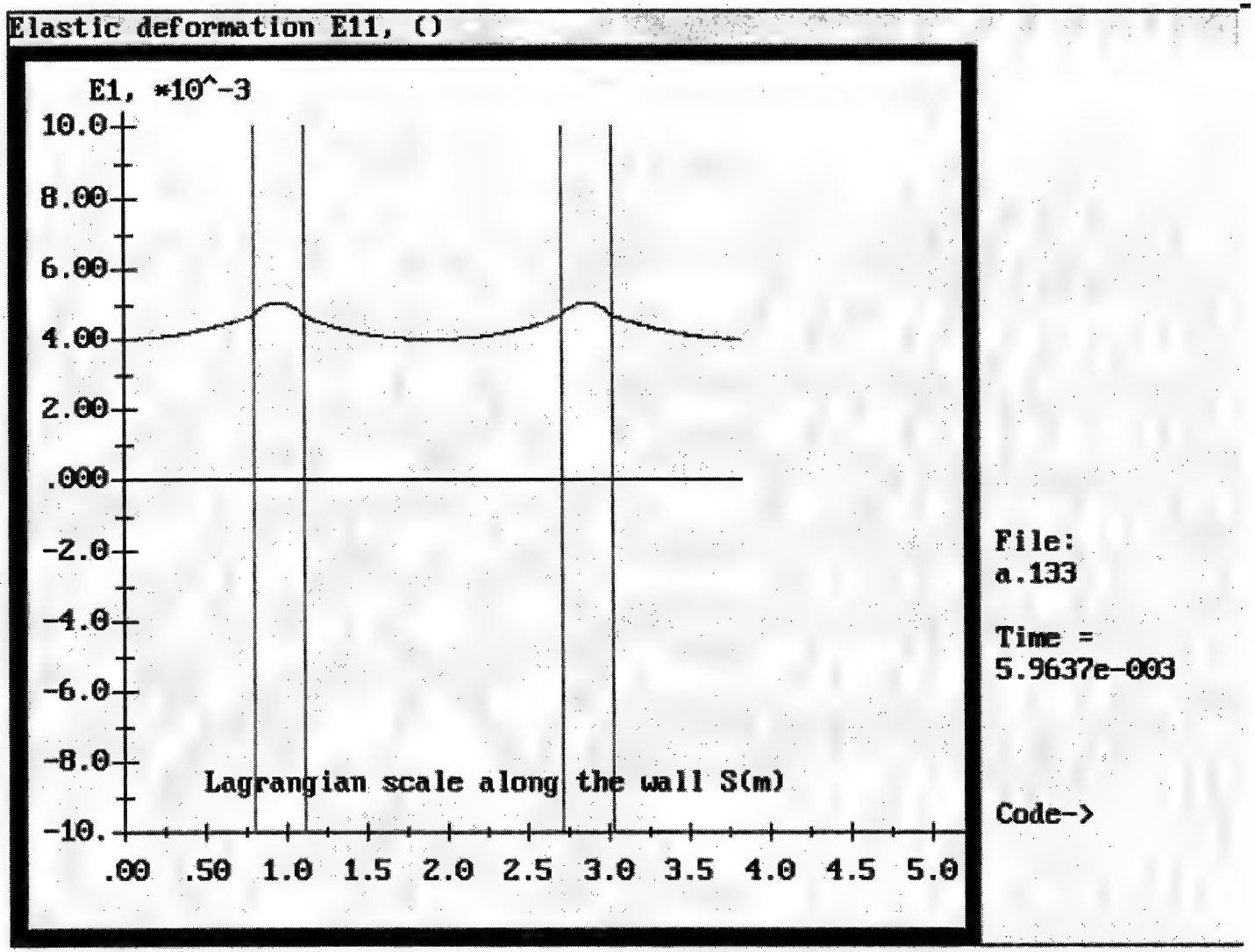
Elastic deformation E11, ()
E1, *10^-3
10.0
8.00
6.00
4.00
2.00
.000
-2.0
-4.0
-6.0
-8.0
-10.
.00 .50 1.0 1.5 2.0 2.5 3.0 3.5 4.0 4.5 5.0
Lagrangian scale along the wall S(m)
File:
a.133
Time =
5.9637e-003
Code->

Fig. 17.

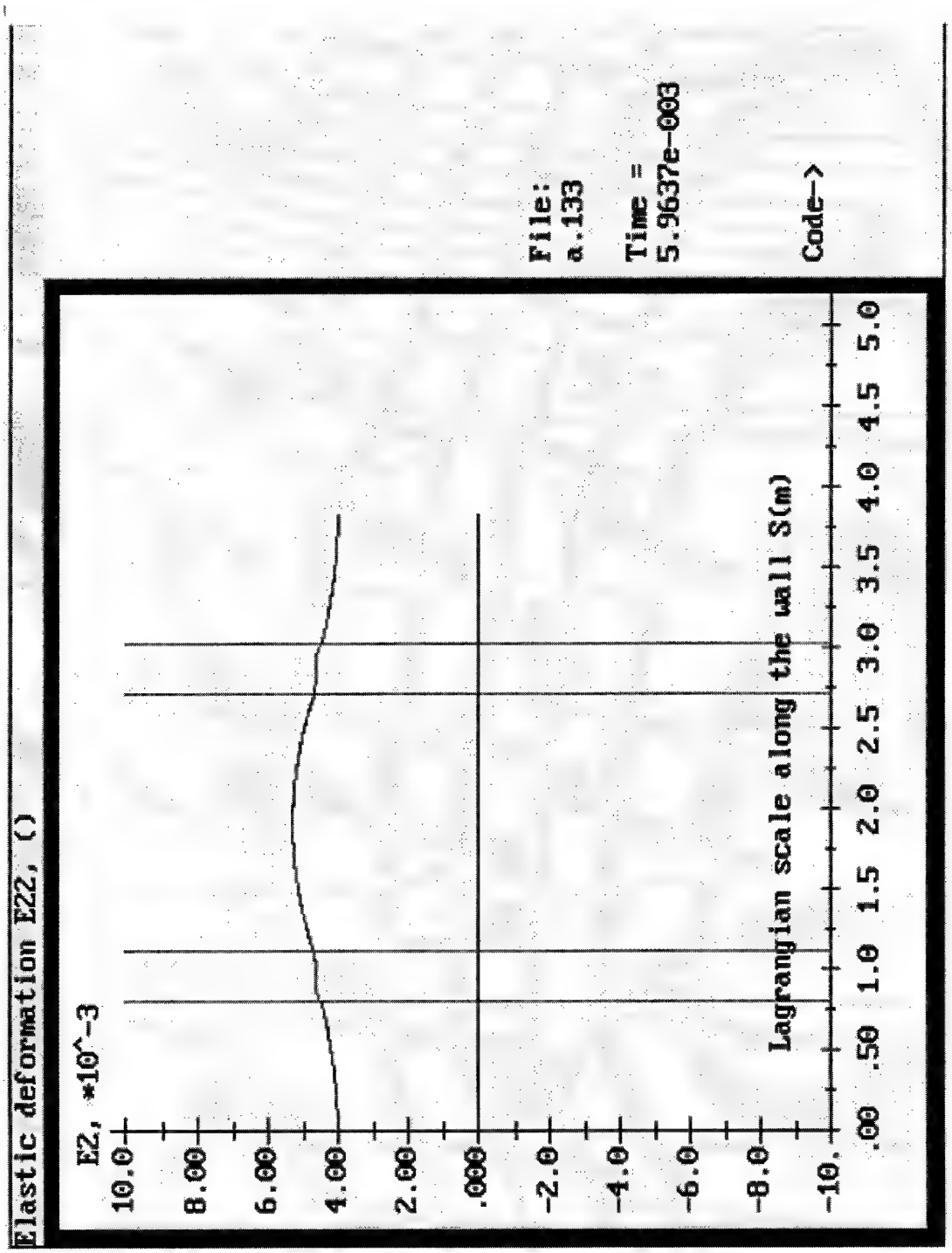
Elastic deformation E22, ()
E2, *10^-3
10.0
8.00
6.00
4.00
2.00
.000
-2.0
-4.0
-6.0
-8.0
-10.
.00
.50
1.0
1.5
2.0
2.5
3.0
3.5
4.0
4.5
5.0
Lagrangian scale along the wall S(m)
File:
a.133
Time =
5.9637e-003
Code->

Fig. 18.

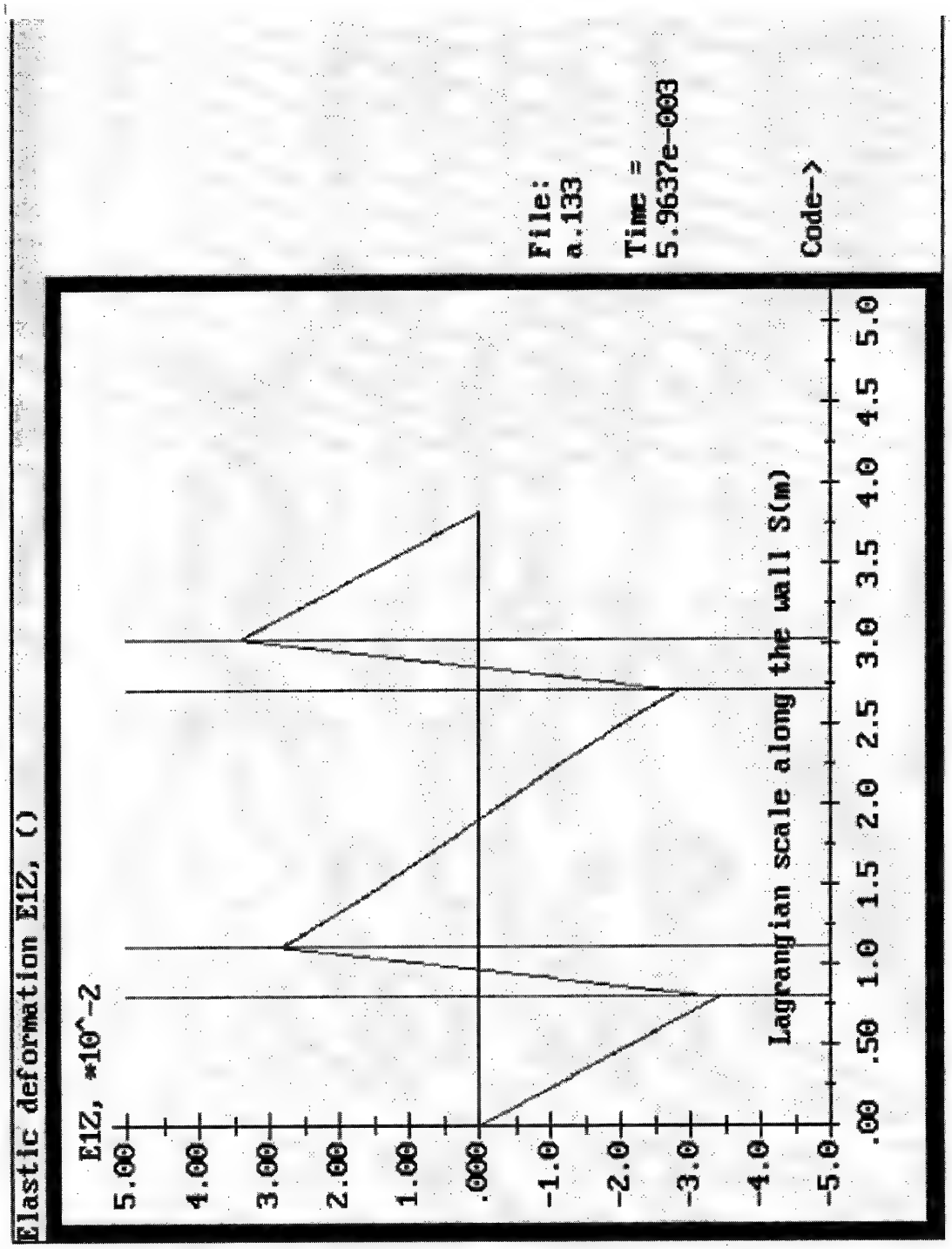
Elastic deformation E1Z, ()
E1Z, *10^-2
5.00
4.00
3.00
2.00
1.00
.000
-1.0
-2.0
-3.0
-4.0
-5.0
.00
.50
1.0
1.5
2.0
2.5
3.0
3.5
4.0
4.5
5.0
Lagrangian scale along the wall S(m)
File:
a.133
Time =
5.9637e-003
Code->

Fig. 19.

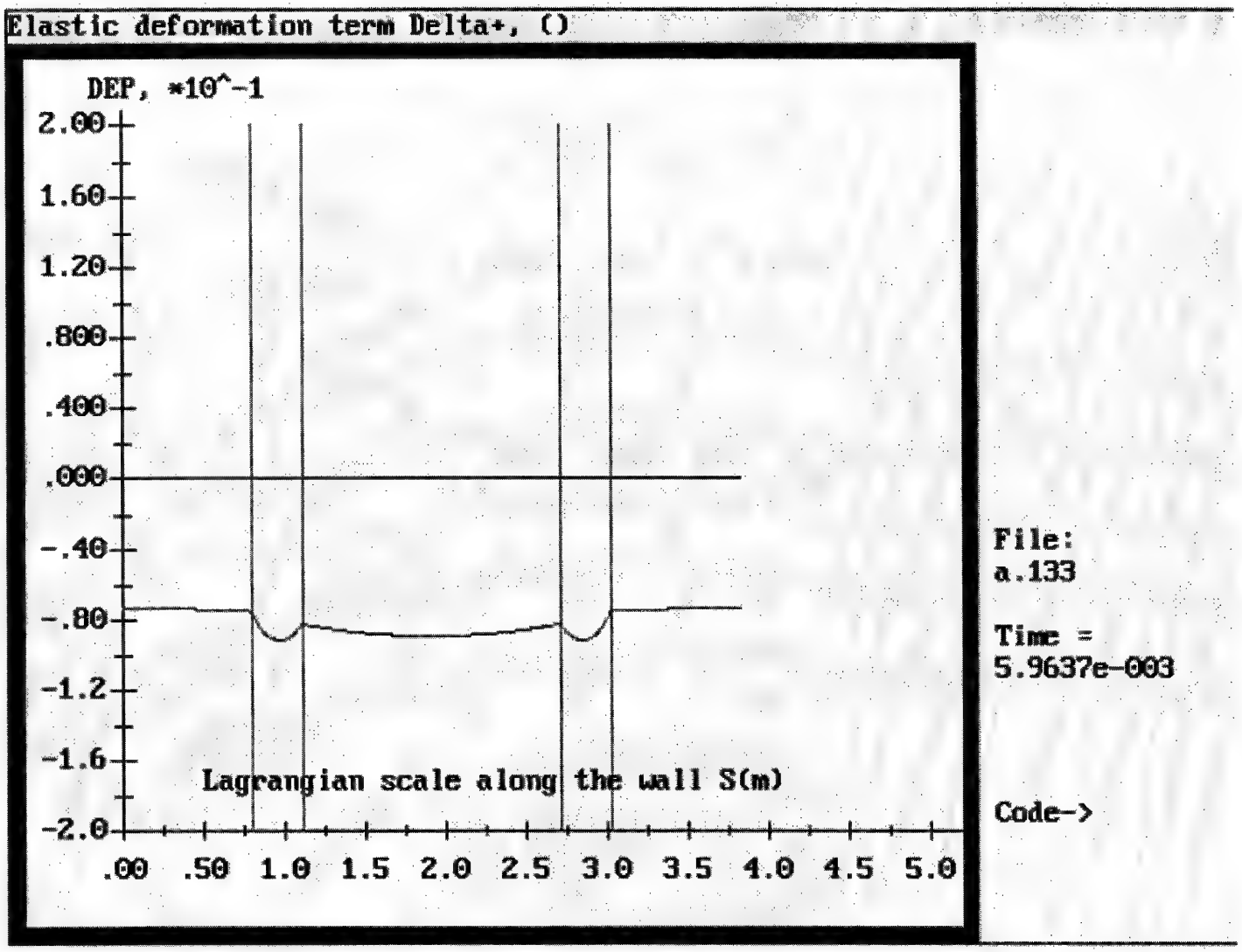
Elastic deformation term Delta+, ()
DEP, *10^-1
2.00
1.60
1.20
.800
.400
.000
-.40
-.80
-1.2
-1.6
-2.0
Lagrangian scale along the wall S(m)
.00 .50 1.0 1.5 2.0 2.5 3.0 3.5 4.0 4.5 5.0
File:
a.133
Time =
5.9637e-003
Code->

Fig. 20.

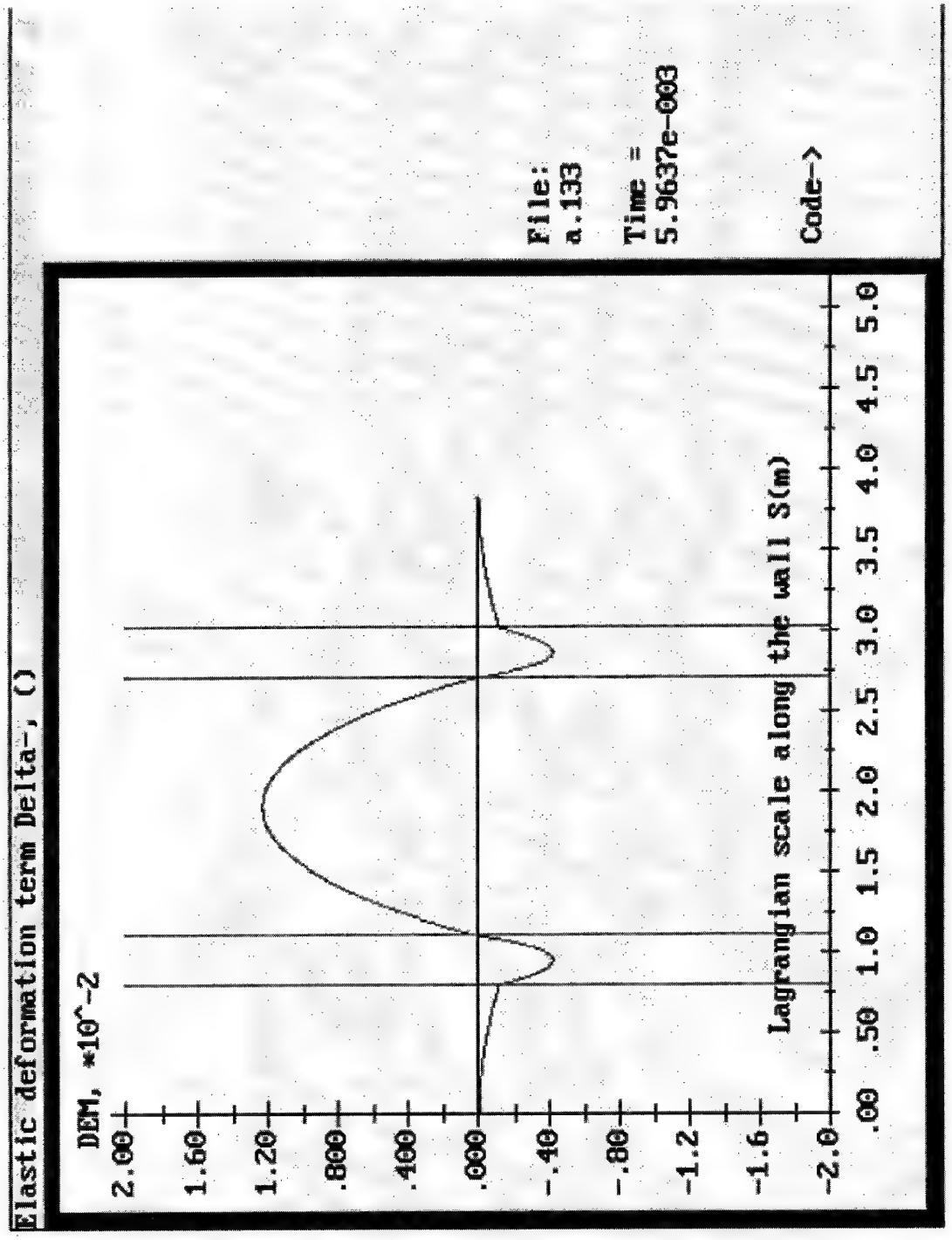
Elastic deformation term Delta-, ()
DEM, *10^-2
2.00
1.60
1.20
.800
.400
.000
-.40
-.80
-1.2
-1.6
-2.0
.00
.50
1.0
1.5
2.0
2.5
3.0
3.5
4.0
4.5
5.0
Lagrangian scale along the wall S(m)
File:
a.133
Time =
5.9637e-003
Code->

Fig. 21.

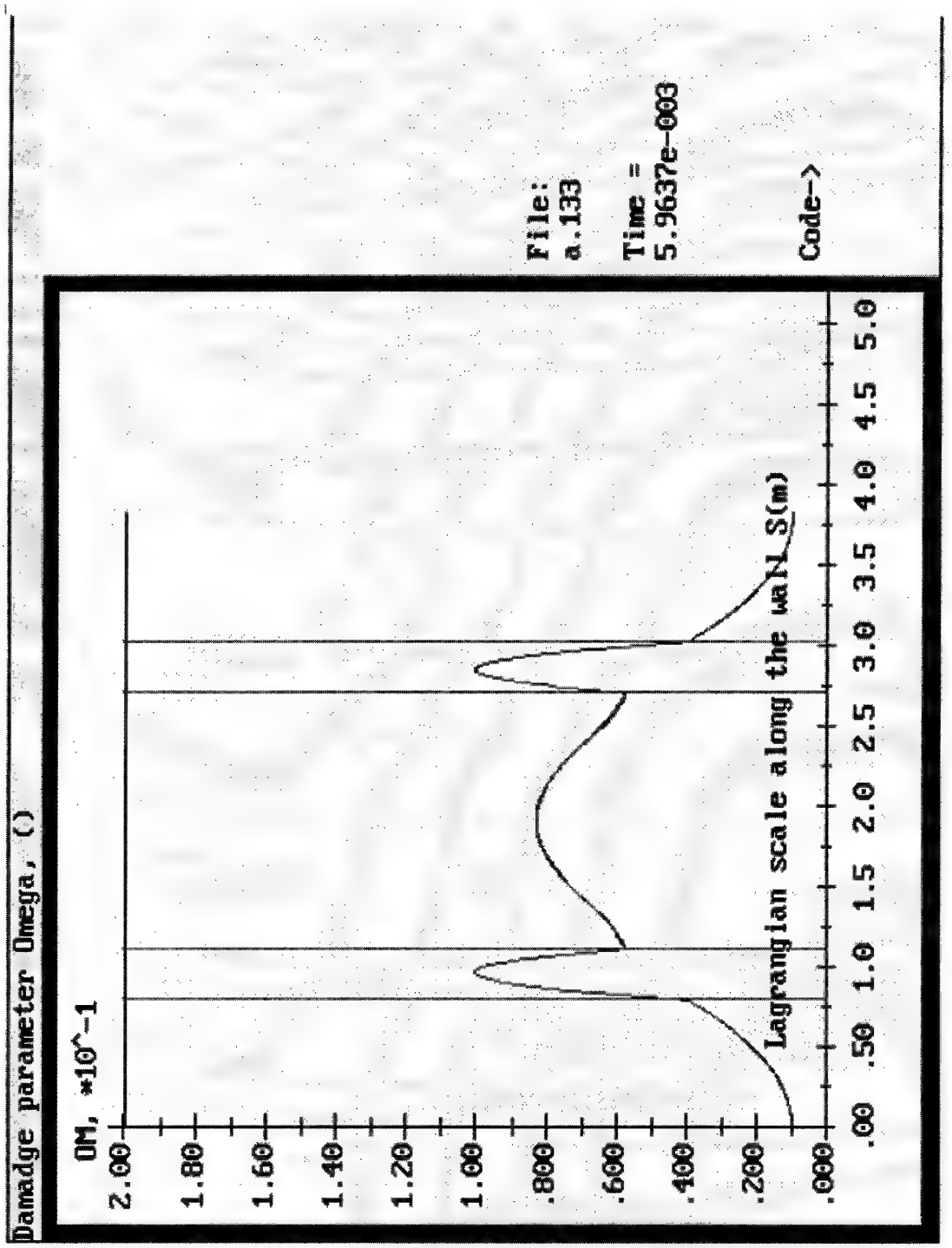
Damadge parameter Omega, ()
OM, *10^-1
2.00
1.80
1.60
1.40
1.20
1.00
.800
.600
.400
.200
.000
.00
.50
1.0
1.5
2.0
2.5
3.0
3.5
4.0
4.5
5.0
Lagrangian scale along the wall S(m)
File:
a.133
Time =
5.9637e-003
Code->

Fig. 22.

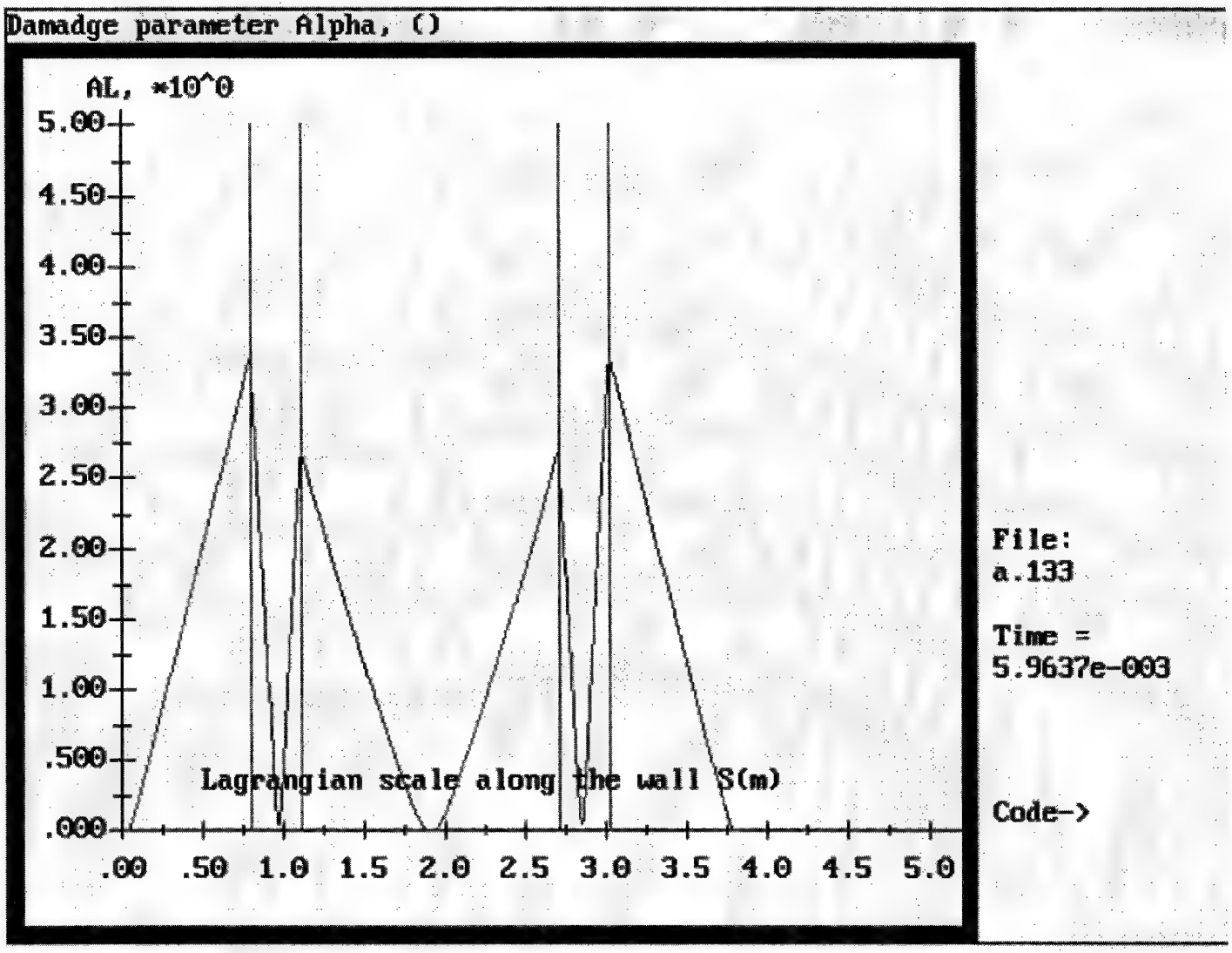
Damadge parameter Alpha, ()
AL, *10^0
5.00
4.50
4.00
3.50
3.00
2.50
2.00
1.50
1.00
.500
.000
.00
.50
1.0
1.5
2.0
2.5
3.0
3.5
4.0
4.5
5.0
Lagrangian scale along the wall S(m)
File:
a.133
Time =
5.9637e-003
Code->

Fig. 23.

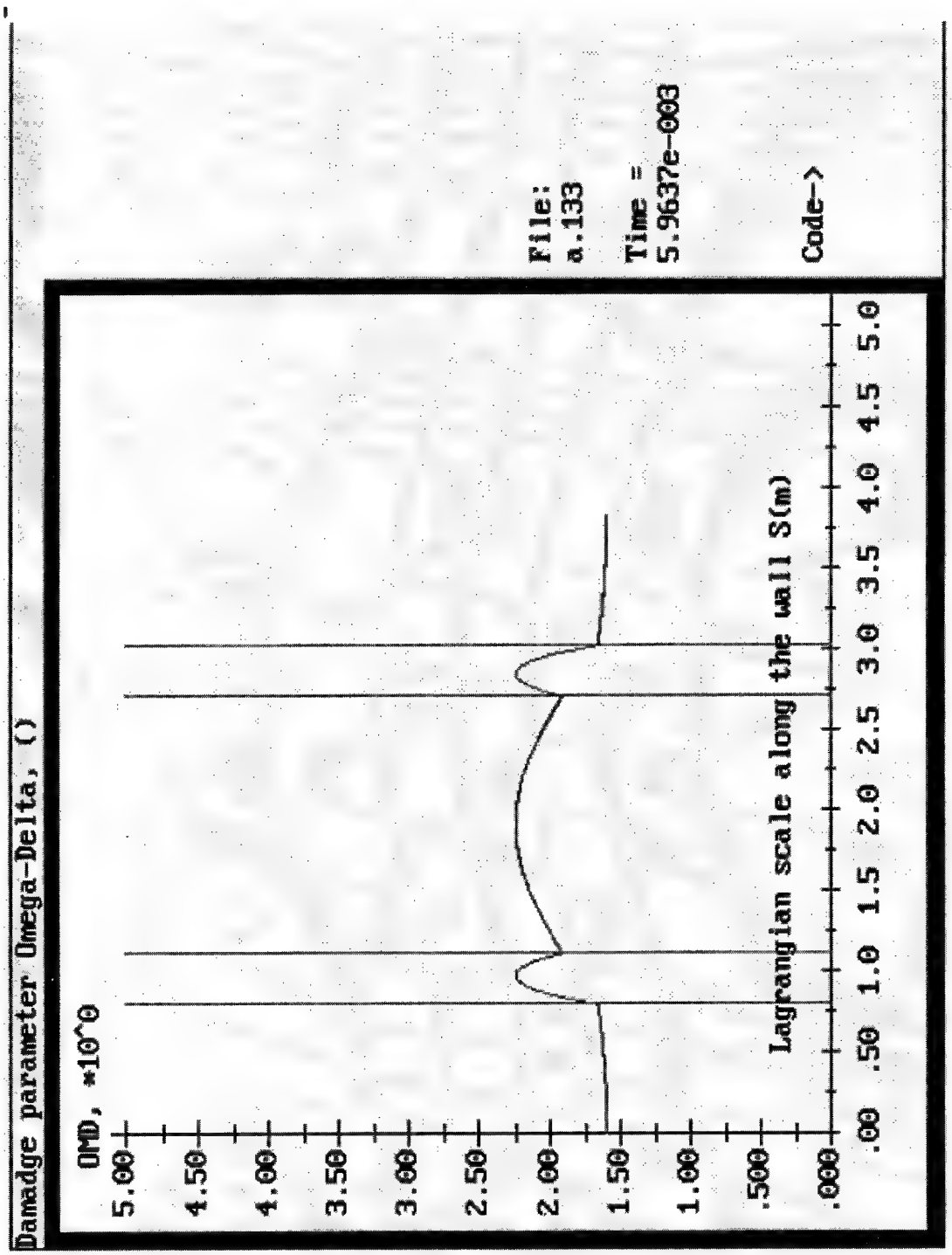
Damadge parameter Omega-Delta, ()
DMD, *10^0
5.00
4.50
4.00
3.50
3.00
2.50
2.00
1.50
1.00
.500
.000
.00
.50
1.0
1.5
2.0
2.5
3.0
3.5
4.0
4.5
5.0
Lagrangian scale along the wall S(m)
File:
a.133
Time =
5.9637e-003
Code->

Fig. 24.

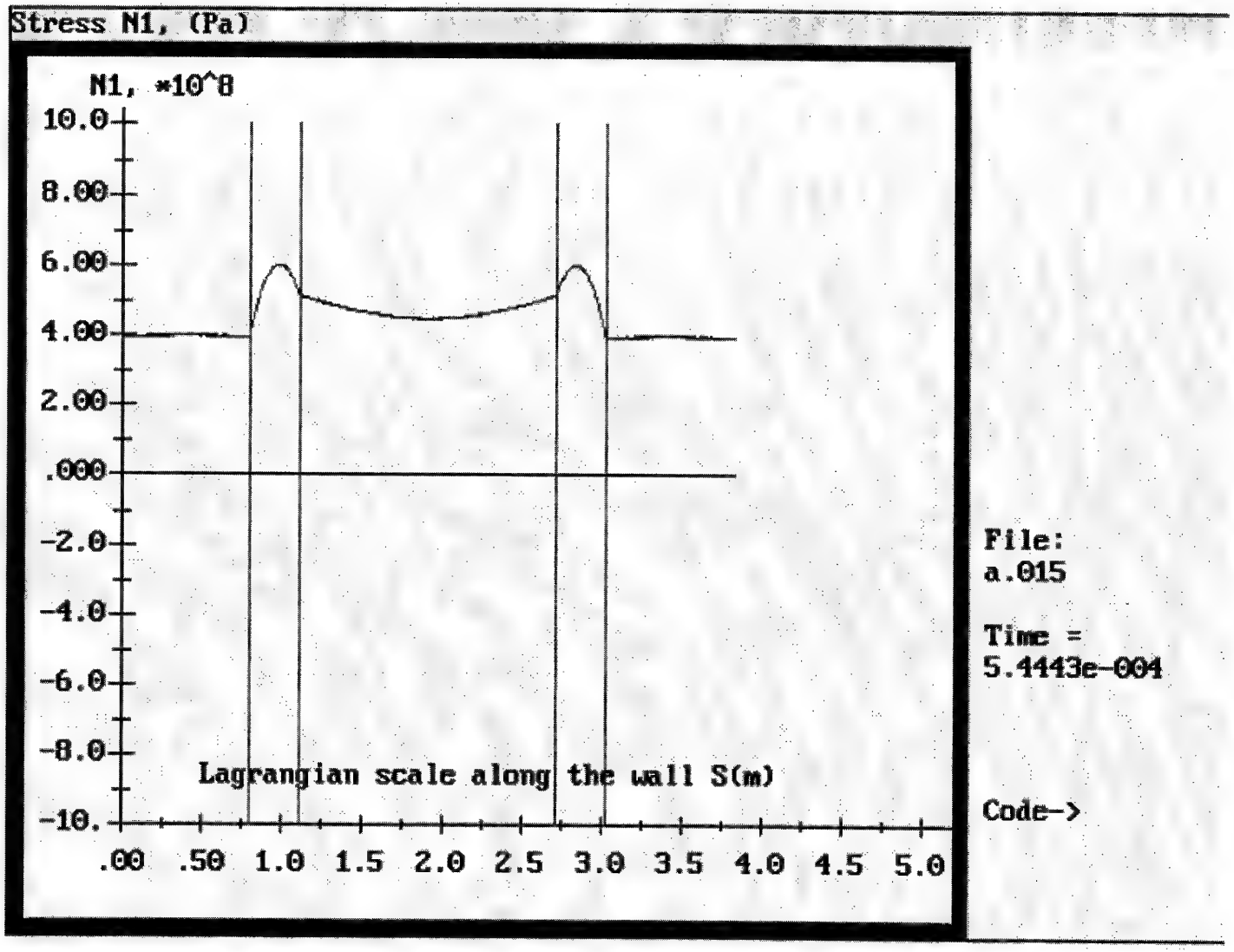
Stress N1, (Pa)
N1, *10^8
10.0
8.00
6.00
4.00
2.00
.000
-2.0
-4.0
-6.0
-8.0
-10.
.00 .50 1.0 1.5 2.0 2.5 3.0 3.5 4.0 4.5 5.0
Lagrangian scale along the wall S(m)
File:
a.015
Time =
5.4443e-004
Code->

Fig. 25.a

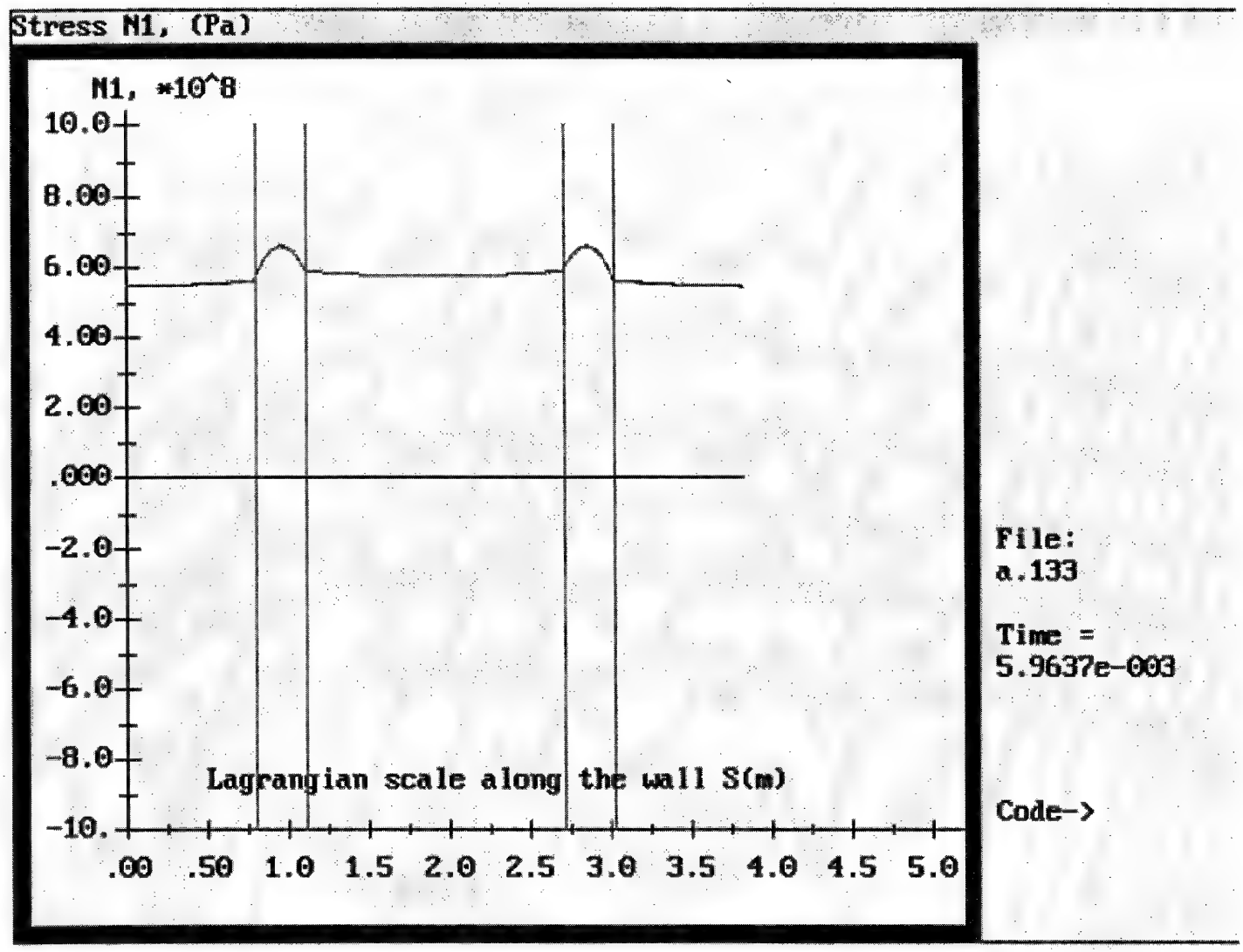
Stress N1, (Pa)
N1, *10^8
10.0
8.00
6.00
4.00
2.00
.000
-2.0
-4.0
-6.0
-8.0
-10.
Lagrangian scale along the wall S(m)
.00 .50 1.0 1.5 2.0 2.5 3.0 3.5 4.0 4.5 5.0
File:
a.133
Time =
5.9637e-003
Code->

Fig. 25, b

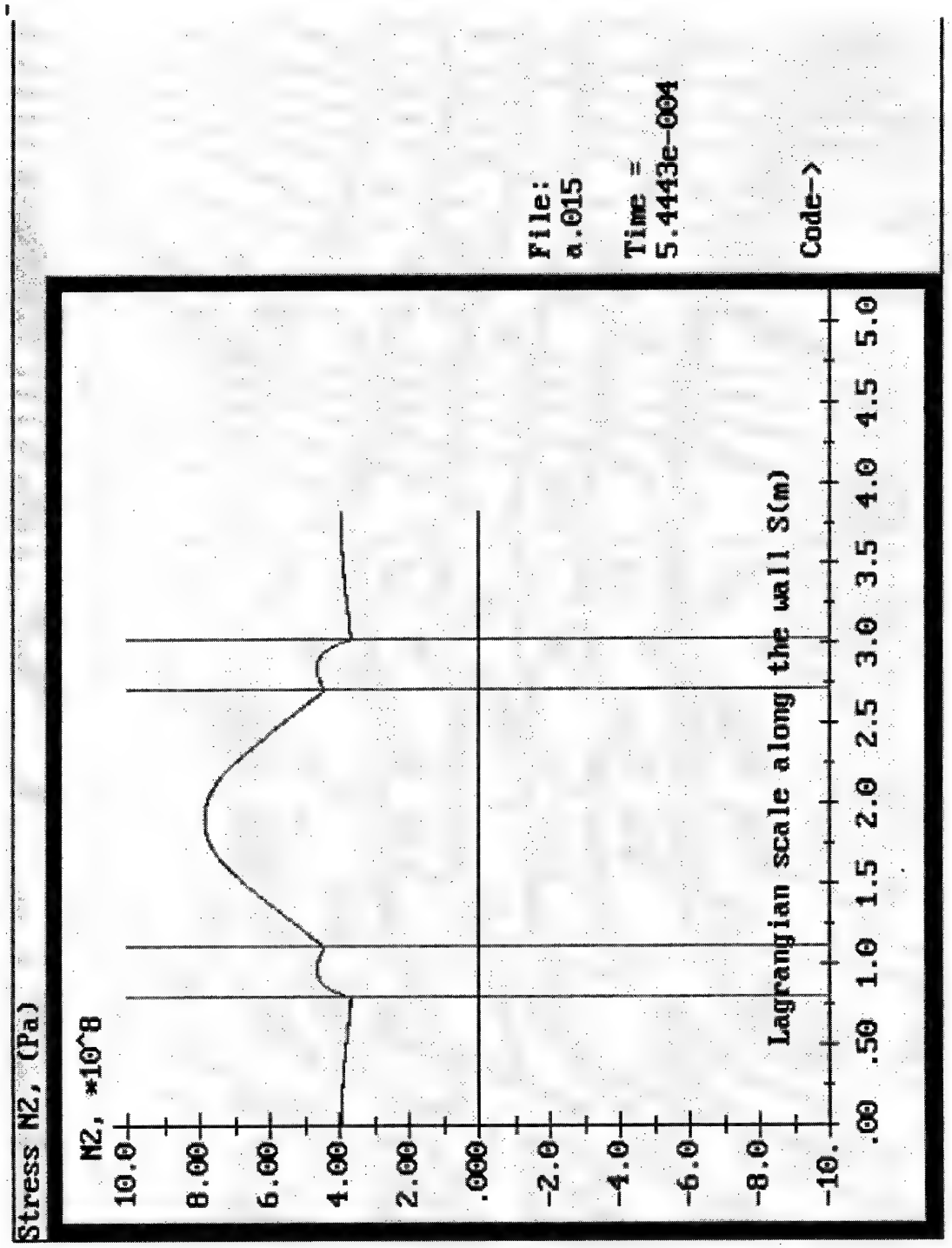
Stress N2, (Pa)
N2, *10^8
10.0
8.00
6.00
4.00
2.00
.000
-2.0
-4.0
-6.0
-8.0
-10.
.00
.50
1.0
1.5
2.0
2.5
3.0
3.5
4.0
4.5
5.0
Lagrangian scale along the wall S(m)
File:
a.015
Time =
5.4443e-004
Code->

Fig. 26.a.

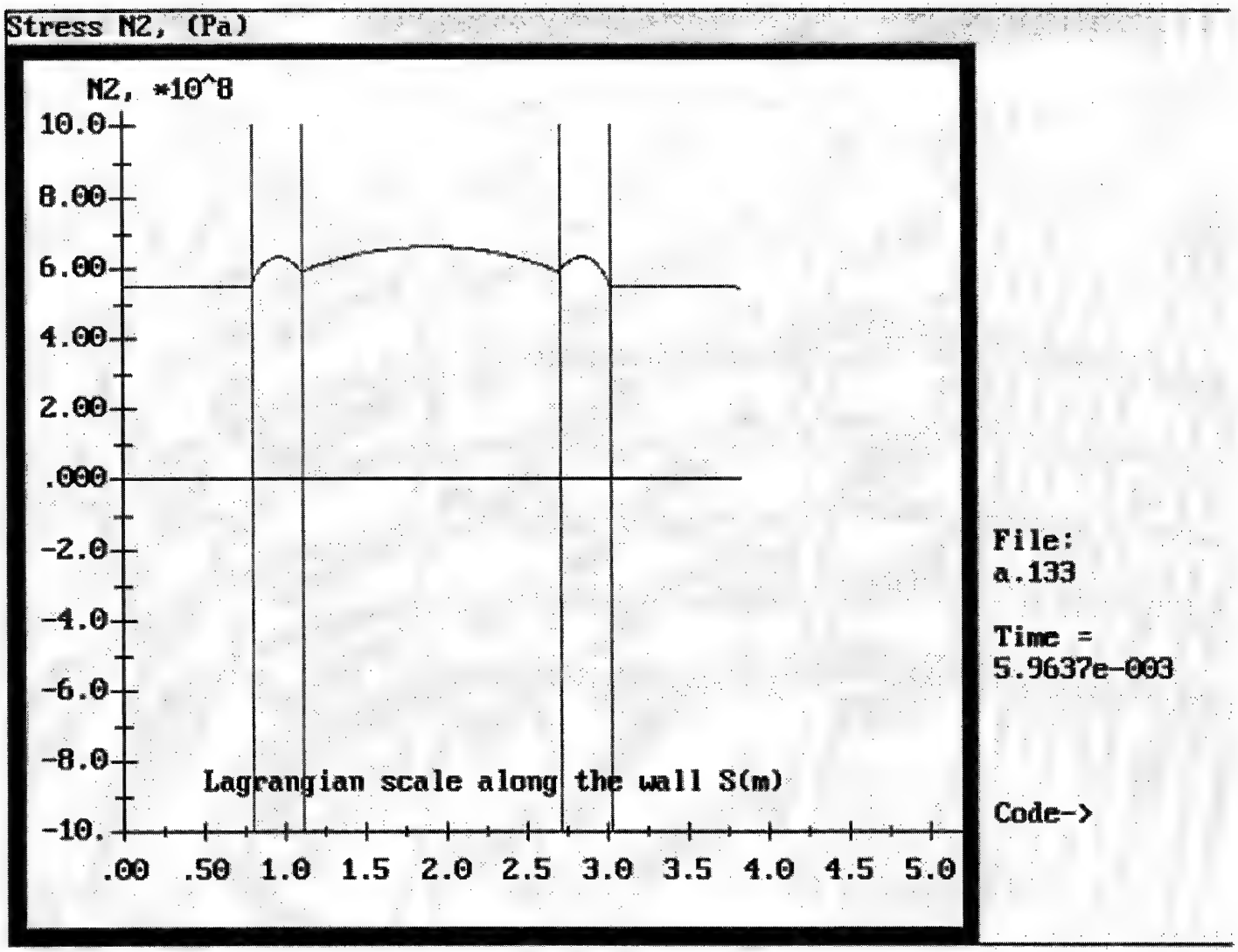
Stress N2, (Pa)
N2, *10^8
10.0
8.00
6.00
4.00
2.00
.000
-2.0
-4.0
-6.0
-8.0
-10.
Lagrangian scale along the wall S(m)
.00 .50 1.0 1.5 2.0 2.5 3.0 3.5 4.0 4.5 5.0
File:
a.133
Time =
5.9637e-003
Code->

Fig. 26. b.

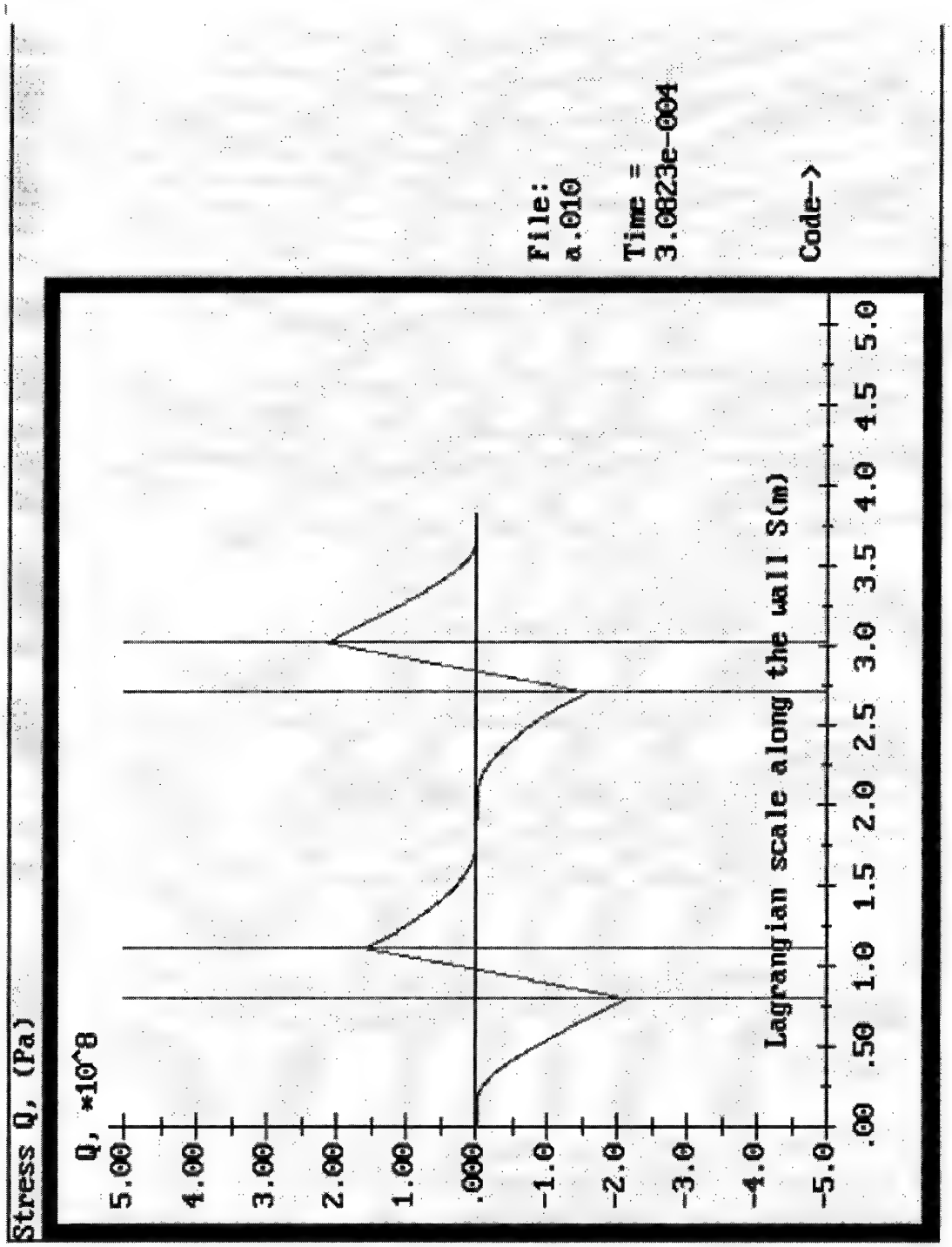
Stress Q, (Pa)
Q, *10^8
5.00
4.00
3.00
2.00
1.00
.000
-1.0
-2.0
-3.0
-4.0
-5.0
.00
.50
1.0
1.5
2.0
2.5
3.0
3.5
4.0
4.5
5.0
Lagrangian scale along the wall S(m)
File:
a.010
Time =
3.0823e-004
Code->

Fig. 27.a.

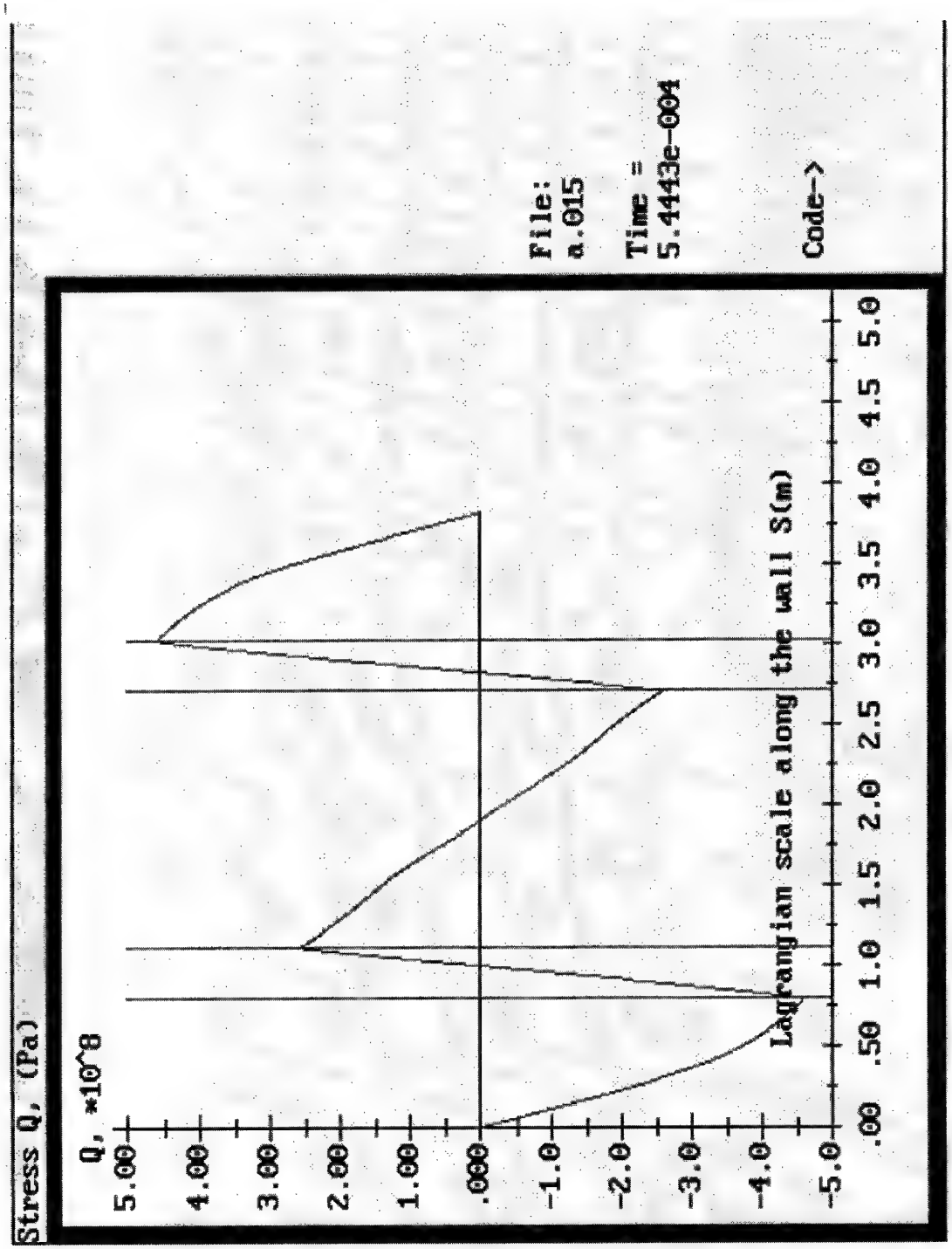
Stress Q, (Pa)
Q, *10^8
5.00
4.00
3.00
2.00
1.00
.000
-1.0
-2.0
-3.0
-4.0
-5.0
.00
.50
1.0
1.5
2.0
2.5
3.0
3.5
4.0
4.5
5.0
Lagrangian scale along the wall S(m)
File:
a.015
Time =
5.4443e-004
Code->
Code->
Code->

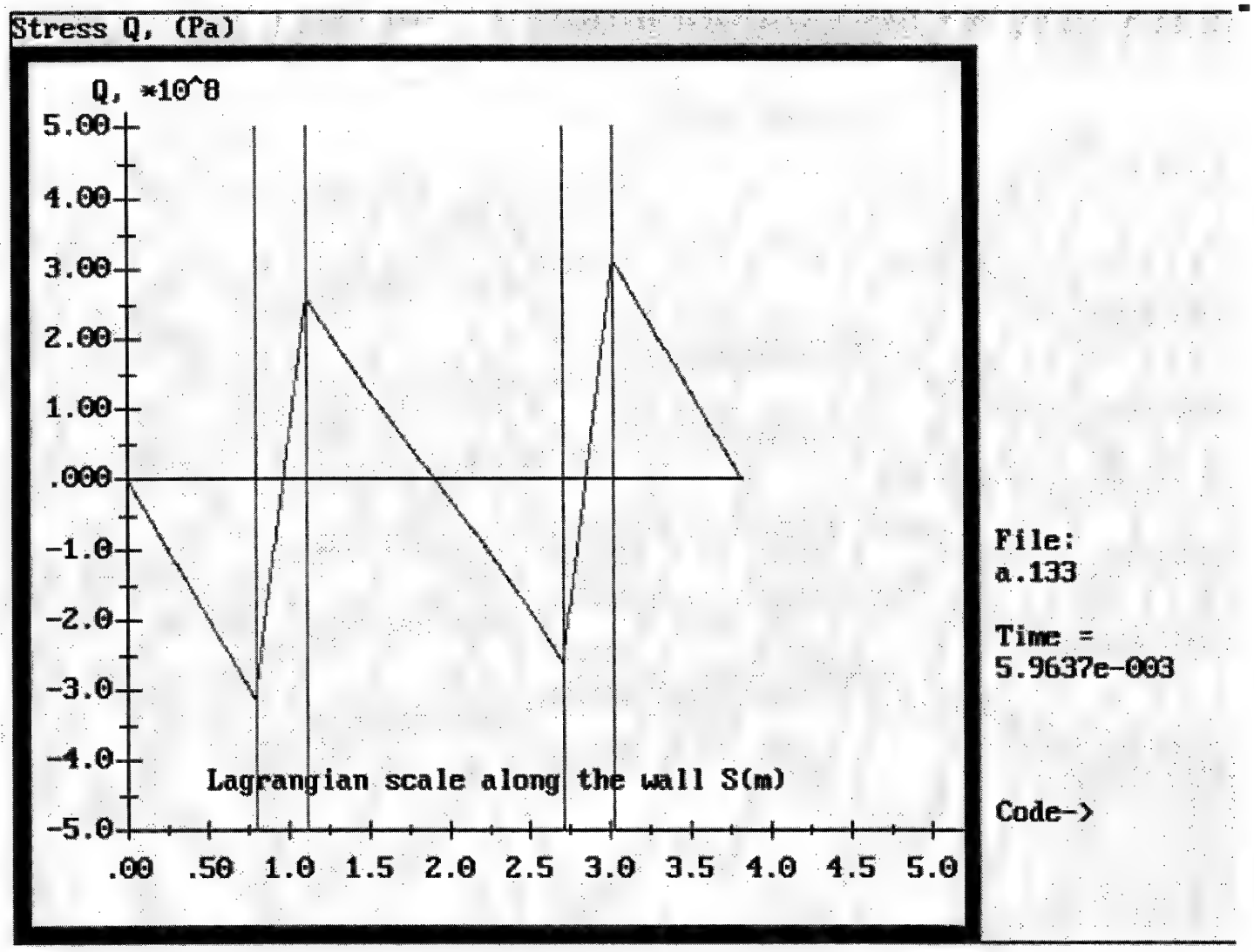
Stress Q, (Pa)
Q, *10^8
5.00
4.00
3.00
2.00
1.00
.000
-1.0
-2.0
-3.0
-4.0
-5.0
Lagrangian scale along the wall S(m)
.00
.50
1.0
1.5
2.0
2.5
3.0
3.5
4.0
4.5
5.0
File:
a.133
Time =
5.9637e-003
Code->

Fig. 27.c.

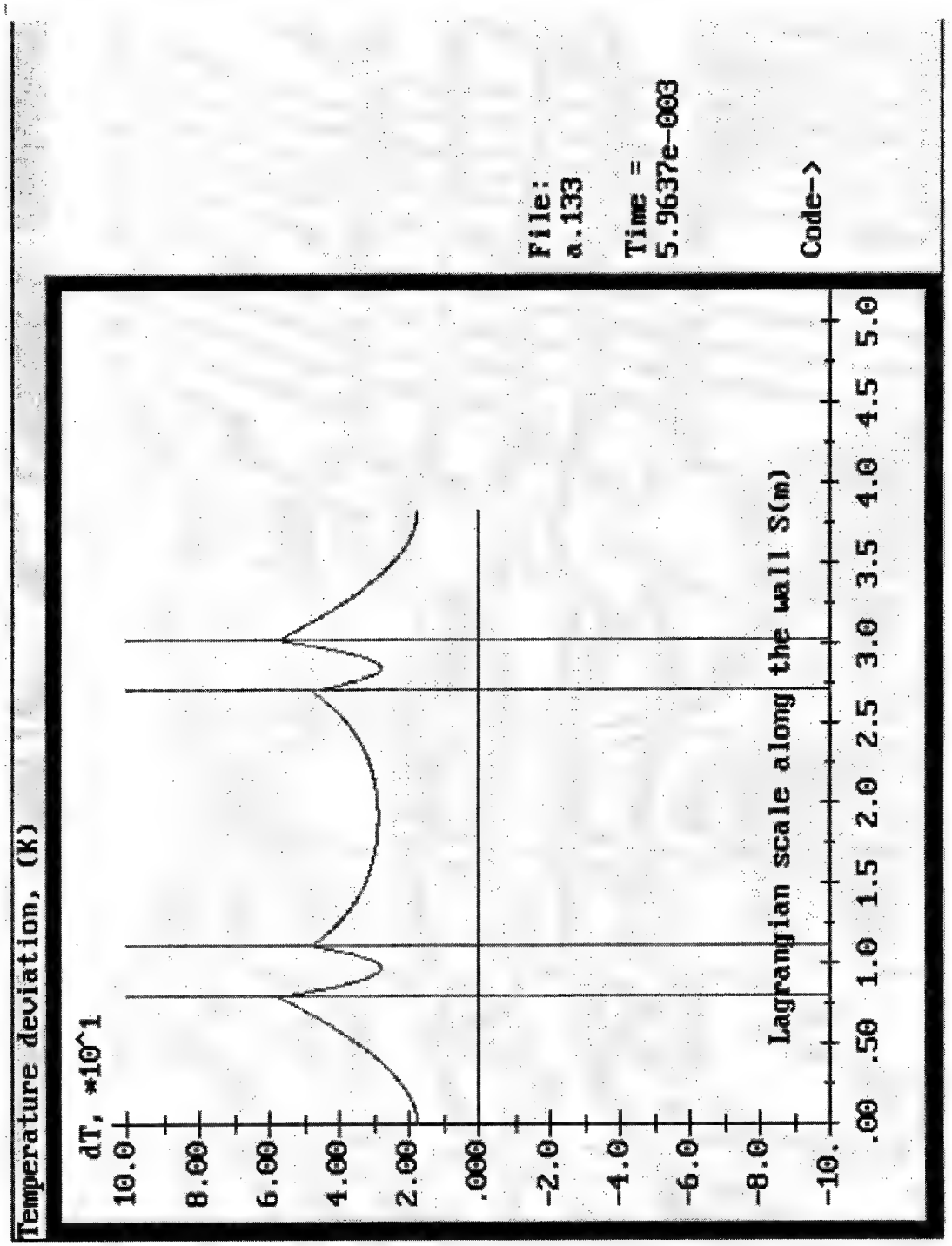
Temperature deviation, (K)
dT, *10^1
10.0
8.00
6.00
4.00
2.00
.000
-2.0
-4.0
-6.0
-8.0
-10.
.00
.50
1.0
1.5
2.0
2.5
3.0
3.5
4.0
4.5
5.0
Lagrangian scale along the wall S(m)
File:
a.133
Time =
5.9637e-003
Code->

Fig. 28.

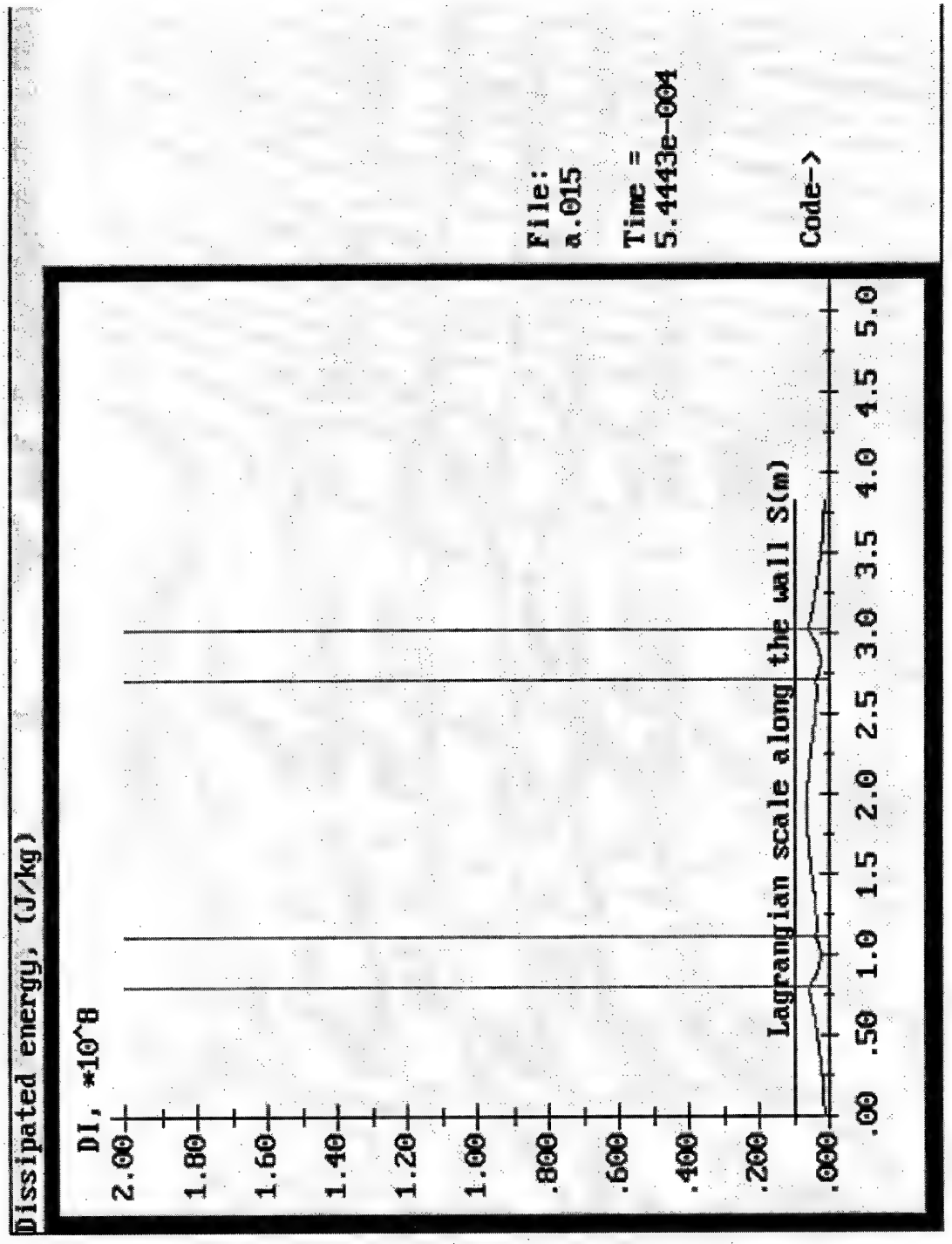
Dissipated energy, (J/kg)
DI, *10^8
2.00
1.80
1.60
1.40
1.20
1.00
.800
.600
.400
.200
.000
.00
.50
1.0
1.5
2.0
2.5
3.0
3.5
4.0
4.5
5.0
Lagrangian scale along the wall S(m)
File:
a.015
Time =
5.4443e-004
Code->

Fig. 29. a.

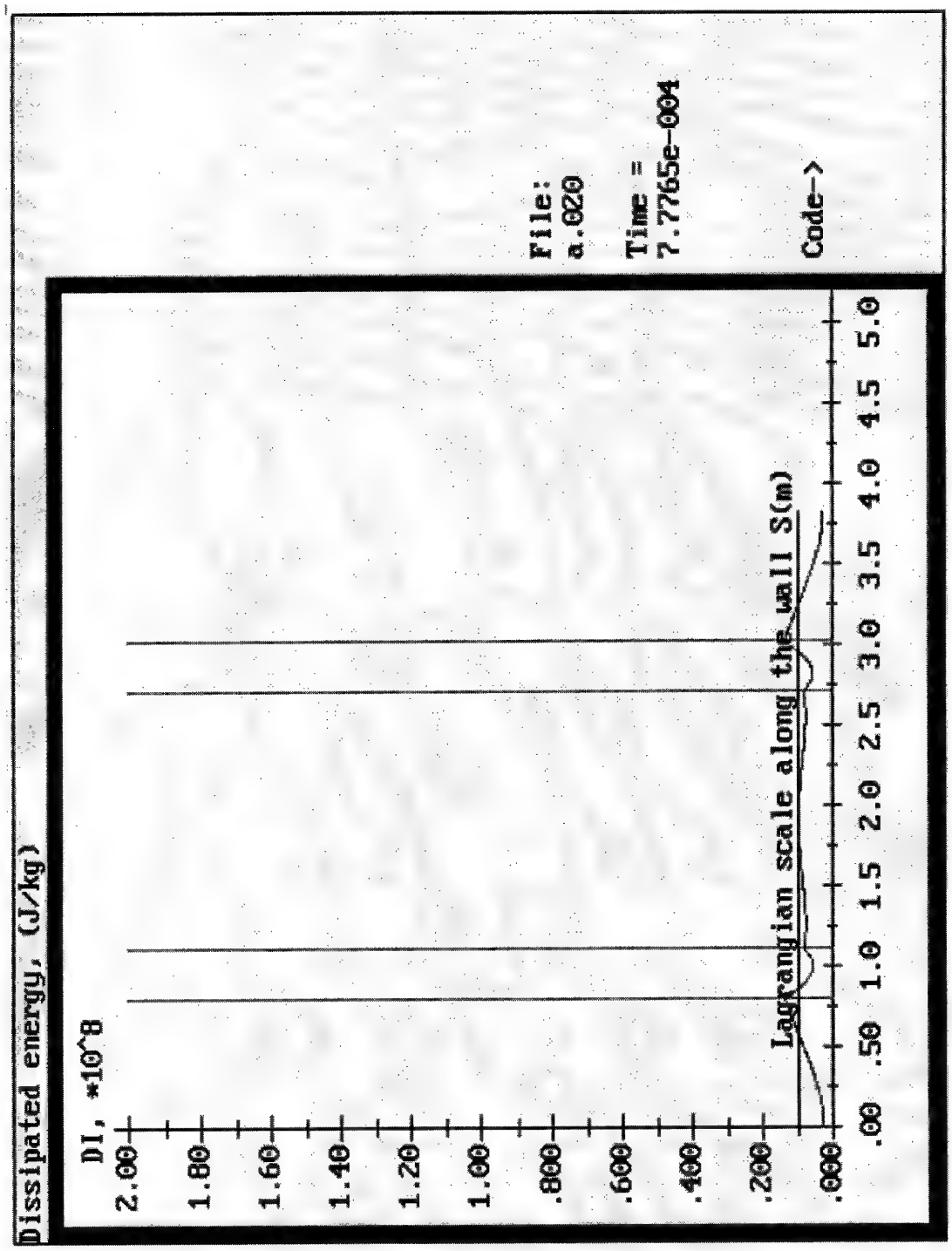
Dissipated energy, (J/kg)
DI, *10^8
2.00
1.80
1.60
1.40
1.20
1.00
.800
.600
.400
.200
.000
.00
.50
1.0
1.5
2.0
2.5
3.0
3.5
4.0
4.5
5.0
Lagrangian scale along the wall S(m)
File:
a.020
Time =
7.7765e-004
Code->

Fig. 29. b.

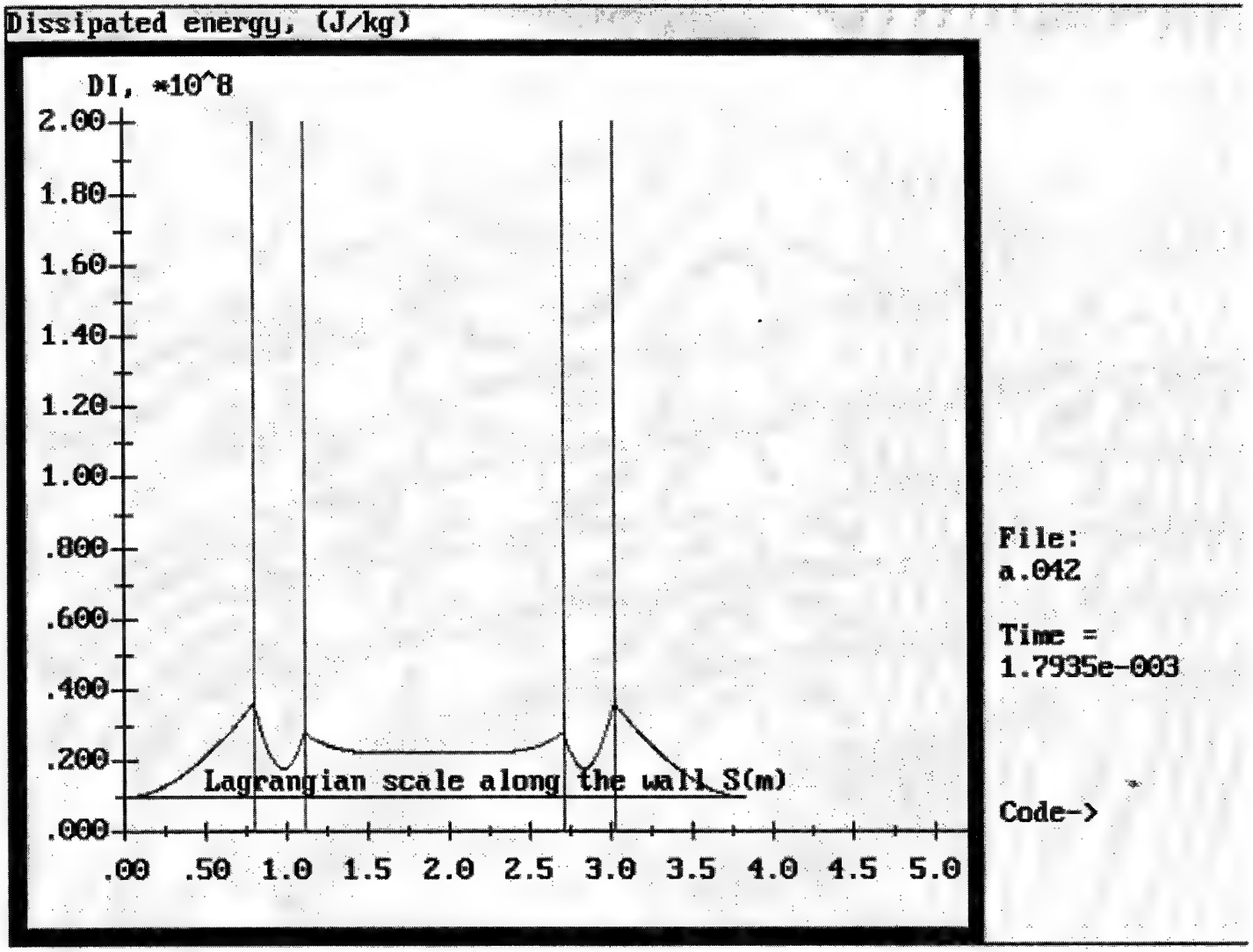
Dissipated energy, (J/kg)
DI, *10^8
2.00
1.80
1.60
1.40
1.20
1.00
.800
.600
.400
.200
.000
.00 .50 1.0 1.5 2.0 2.5 3.0 3.5 4.0 4.5 5.0
Lagrangian scale along the wall S(m)
File:
a.042
Time =
1.7935e-003
Code->

Fig. 29.c.

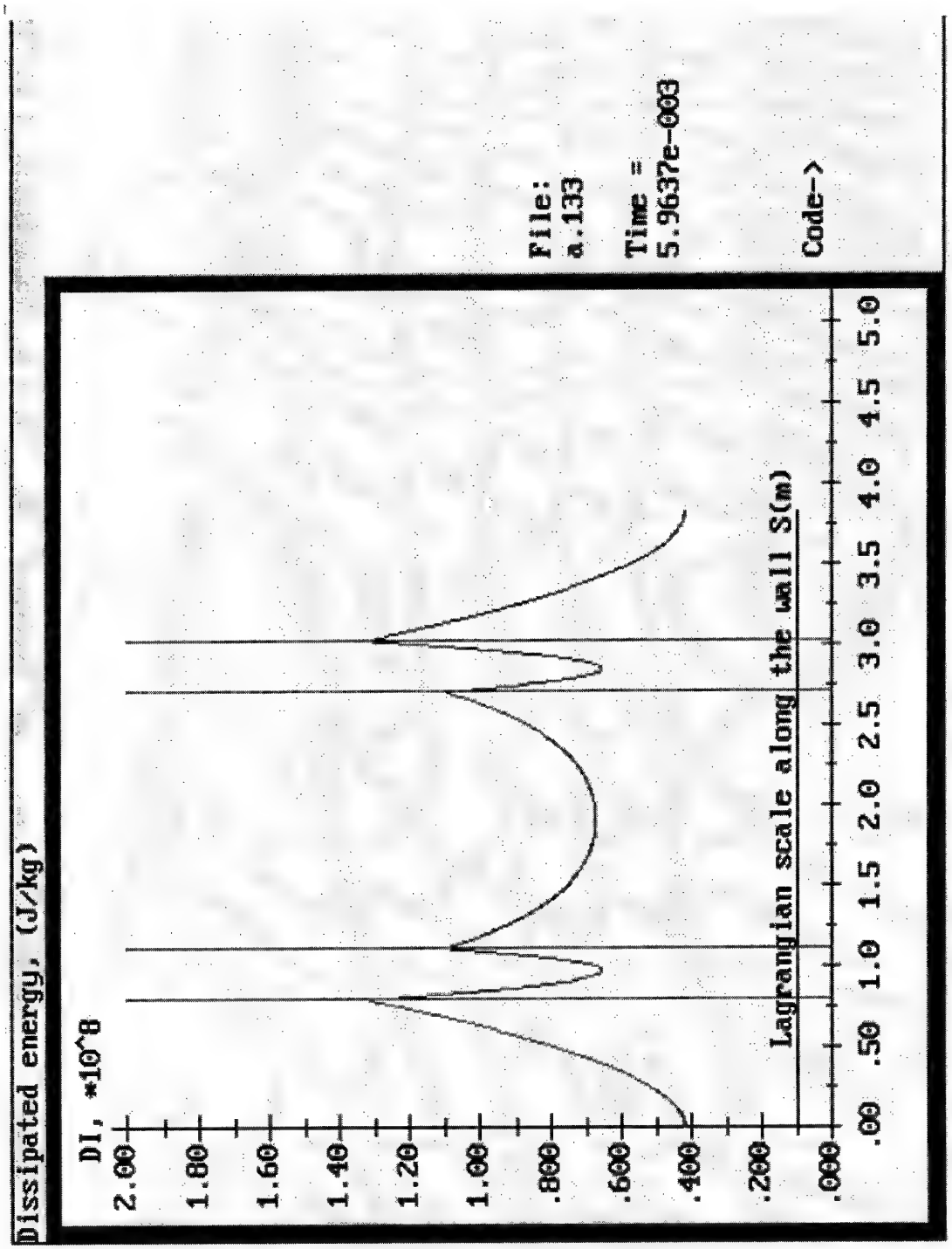
Dissipated energy, (J/kg)
DI, *10^8
2.00
1.80
1.60
1.40
1.20
1.00
.800
.600
.400
.200
.000
.00
.50
1.0
1.5
2.0
2.5
3.0
3.5
4.0
4.5
5.0
Lagrangian scale along the wall S(m)
File:
a.133
Time =
5.9637e-003
Code->

Fig. 29. d.

2.3.2 Shell parameters in nonuniform dynamical loading.

To investigate the behaviour of a shell in nonuniform loading the dynamics of wall loading was assumed to be that determined in the section 2.1. The characteristic size of the shell was assumed the following: length - $1m$, radius - $0.5m$, initial wall thickness - $0.5 \cdot 10^{-2}m$. The size of the shell corresponds with that of the containment described in 2.1. Thus the present shell is twice smaller than the one investigated in the previous section in a uniform loading. To keep the similarity the thickness was also reduced twice in comparisson with the previous case. That agrees with the static similarity criterion but of course can introduce differences for a dinamical case.

The Figs.30$a - m$ show the internal wall pressure distribution along the generating line of the containment (the lagrangian coordinate s) for different times for the case of nonuniform loading described in the section 2.1. It is seen that in the very beginning of the process there is a sharp pressure increase near the bottom (Figs.30.$a - b$.) that is accompanied by the increase of pressure near the side walls in reflected waves (Figs.30.$c - d$). But the high loadings are not durable and pressure decays very quichly due to the influence of the rarefaction waves. After the multiple reflection from the upper wall (the right hand side of the figure) and the pressure increase(Fig.30.$f - h$) the loading stabilizes and small axial oscillations of pressure can be observed (Figs.30.$k - m$). The mean pressure in the containment finally is much less than that in the previous case for the uniform loading.

Figs.31.$a - e$ illustrate the behaviour of tangential displacement u in nonuniform loading for the successive times. The displacements are oscillating nonsymmetrically in the initial stage of the process but finally they form a steady profile similar to that for the case of uniform loading. Comparisson of the Fig.31.e with the Fig.11.b testifies the fact.

Fig.32.$a - e$ illustrates the changes in normal displacements w of the shell. It is seen that the sell's elements start mooving in the left hand side (the bottom wall of the shell) and gradually all the shell is being involved into motion. By the time internal pressure comes to a practically steady uniform distribution the normal displacements form a profile (Fig.32.e.) similar to that for the case of uniform loading described above (Fig.10.b).

The Figs.33.$a - h$ and Figs.34.$a - f$ illustrate the velocities of shell's elements in tangential to the generating line and normal directions respectively for successive times. It is seen that relatively large elastic oscillations present in the beginning are being moderated in the longrun by the increasing dissipation.

The dynamics of the dissipation function for the shell is shown in Figs.35.$a - c$. It is seen that the dissipation function has not reached its critical value by the time of the pressure stabilization inside the containment. That happened due to the fact that even high but short term loadings do not bring much damages to the material due to the relaxations induction. Thus the model is able to take into account the relaxation time for accumulation of damages.

The successive stages of the accumulation of damages in shear α are shown in Figs.36$a-f$.

The last time moment reflected in the figures actually is not the last one for the continuous destruction of the material though the mean internal pressure is rather low already. The presence of large differences in the total and elastic deformations (Figs.37 and 38) shows that the relaxation process is not finished yet and the dissipation will be still increasing for some time. But it is not likely to surpass the criterion.

Fig.39 shows the distribution of temperature deviations in the shell from the initial state. The temperature increase in the right hand side is due to the growth of dissipation. The decrease of temperature in the left hand side is due to cooling of the material in elastic expansion that surpasses the influence of the dissipation growth. The local maxima of temperature in the zones of discontinuity of curvature are due to the influence of the growth of dissipation that is maximal within these zones.

The present example illustrates the fact that nonunifomities of loading being stabilized during a relatively short period of time bring to the deformed picture similar to the case of uniform loading. The intense short term loads bring less accumulated damages than durable loads of smaller values.

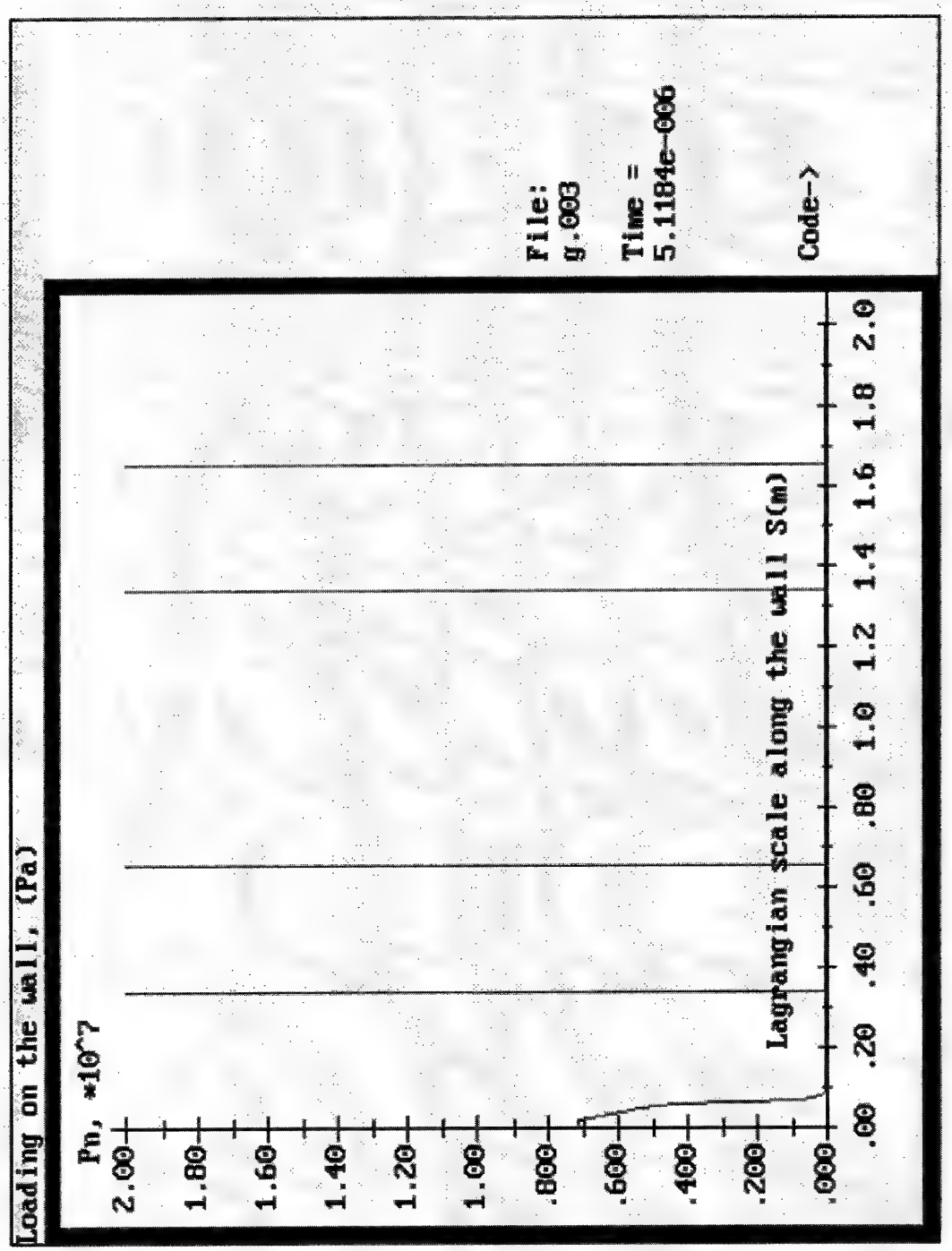
Loading on the wall, (Pa)
Pn, *10^7
2.00
1.80
1.60
1.40
1.20
1.00
.800
.600
.400
.200
.000
.00
.20
.40
.60
.80
1.0
1.2
1.4
1.6
1.8
2.0
Lagrangian scale along the wall S(m)
File:
g.003
Time =
5.1184e-006
Code->

Fig. 30. a

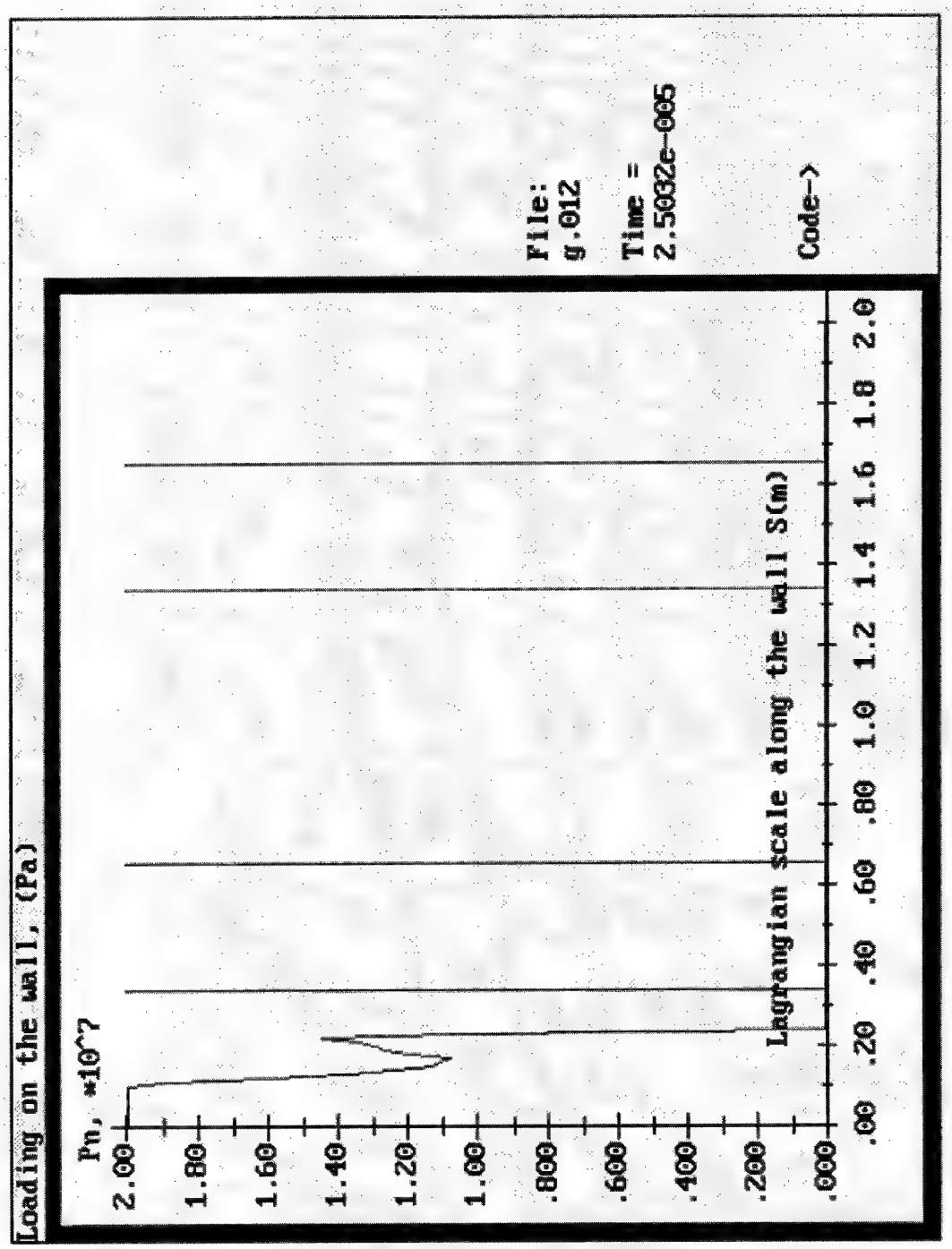
Loading on the wall, (Pa)
Pn, *10^7
2.00
1.80
1.60
1.40
1.20
1.00
.800
.600
.400
.200
.000
.00
.20
.40
.60
.80
1.0
1.2
1.4
1.6
1.8
2.0
Lagrangian scale along the wall S(m)
File:
g.012
Time =
2.5032e-005
Code->

Fig. 30. b.

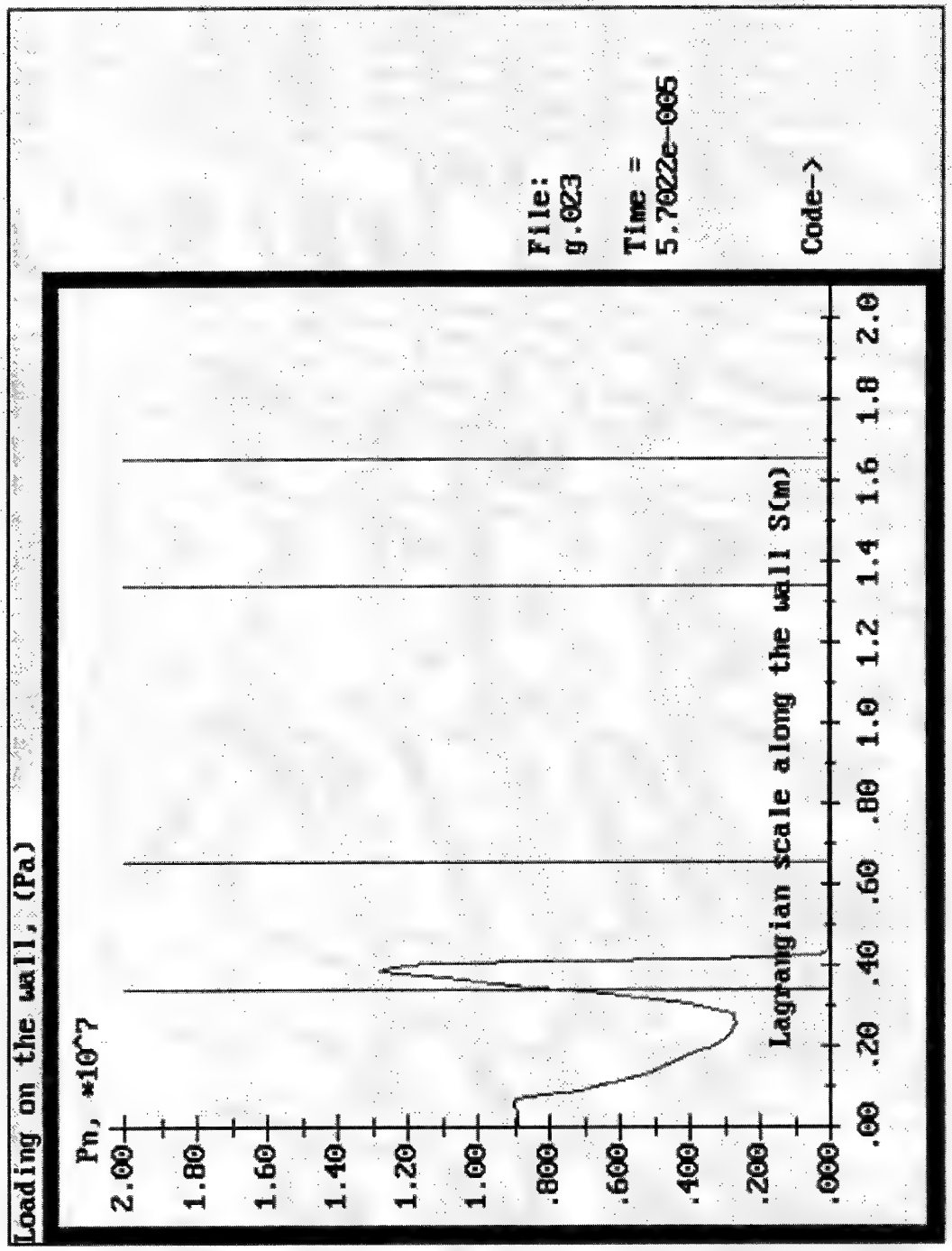
Loading on the wall, (Pa)
Pn, *10^7
2.00
1.80
1.60
1.40
1.20
1.00
.800
.600
.400
.200
.000
.00
.20
.40
.60
.80
1.0
1.2
1.4
1.6
1.8
2.0
Lagrangian scale along the wall S(m)
File:
g.023
Time =
5.7022e-005
Code->

Fig. 30.c.

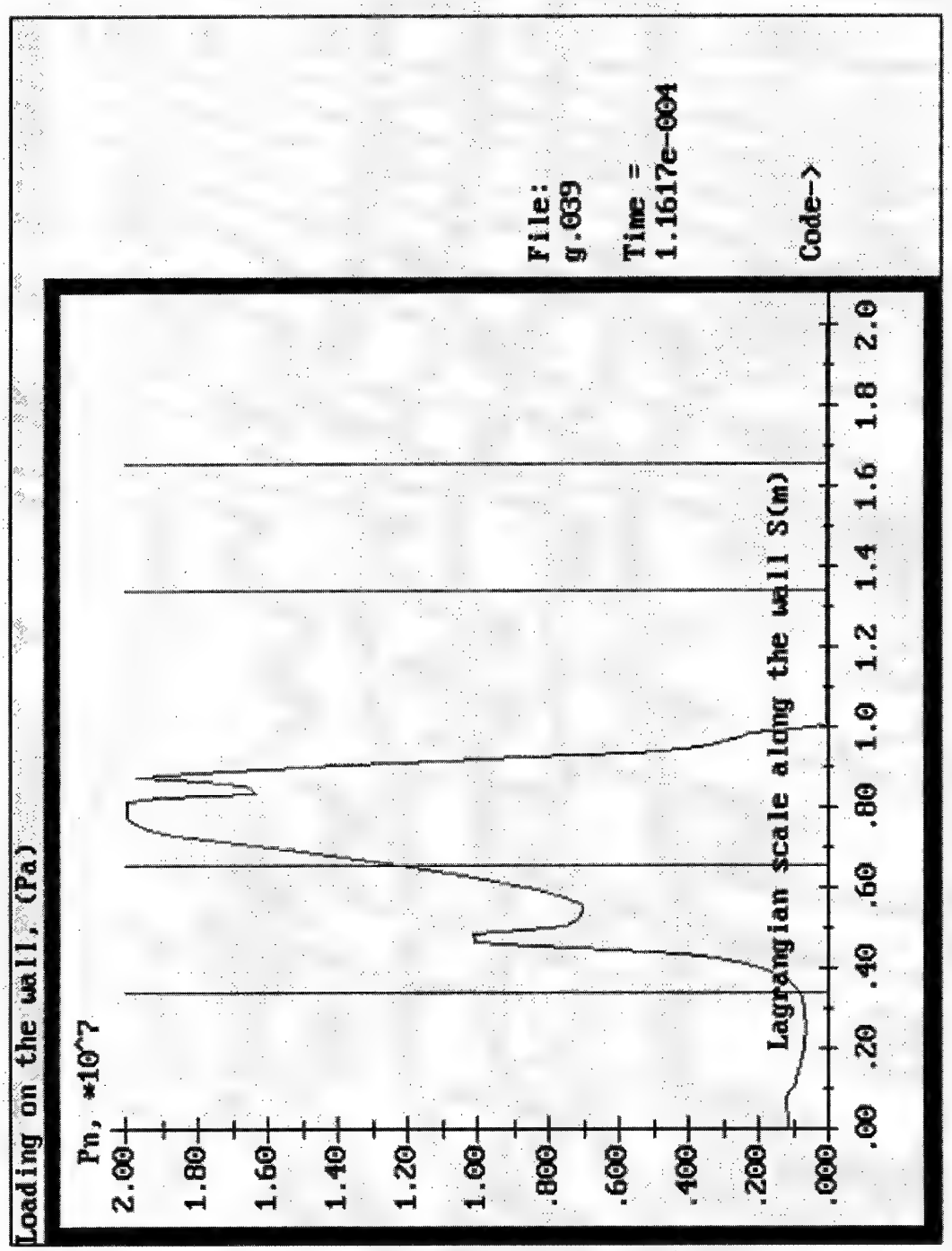
Loading on the wall, (Pa)
Pn, *10^7
2.00
1.80
1.60
1.40
1.20
1.00
.800
.600
.400
.200
.000
.00
.20
.40
.60
.80
1.0
1.2
1.4
1.6
1.8
2.0
Lagrangian scale along the wall S(m)
File:
g.039
Time =
1.1617e-004
Code->

Fig. 30. d.

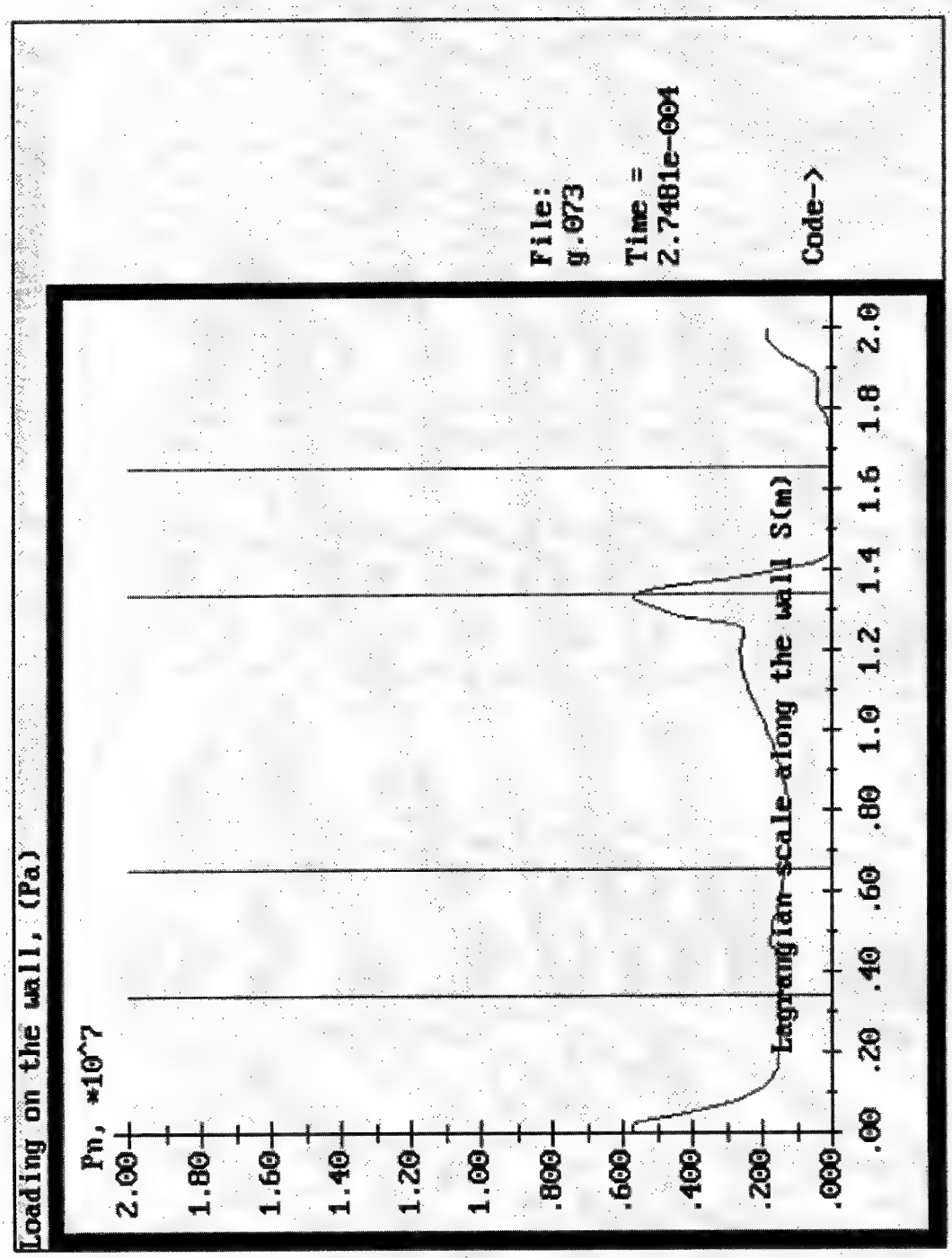
Loading on the wall, (Pa)
Pn, *10^7
2.00
1.80
1.60
1.40
1.20
1.00
.800
.600
.400
.200
.000
.00
.20
.40
.60
.80
1.0
1.2
1.4
1.6
1.8
2.0
Lagrangian scale along the wall S(m)
File:
g.073
Time =
2.7481e-004
Code->

Fig. 30.e.

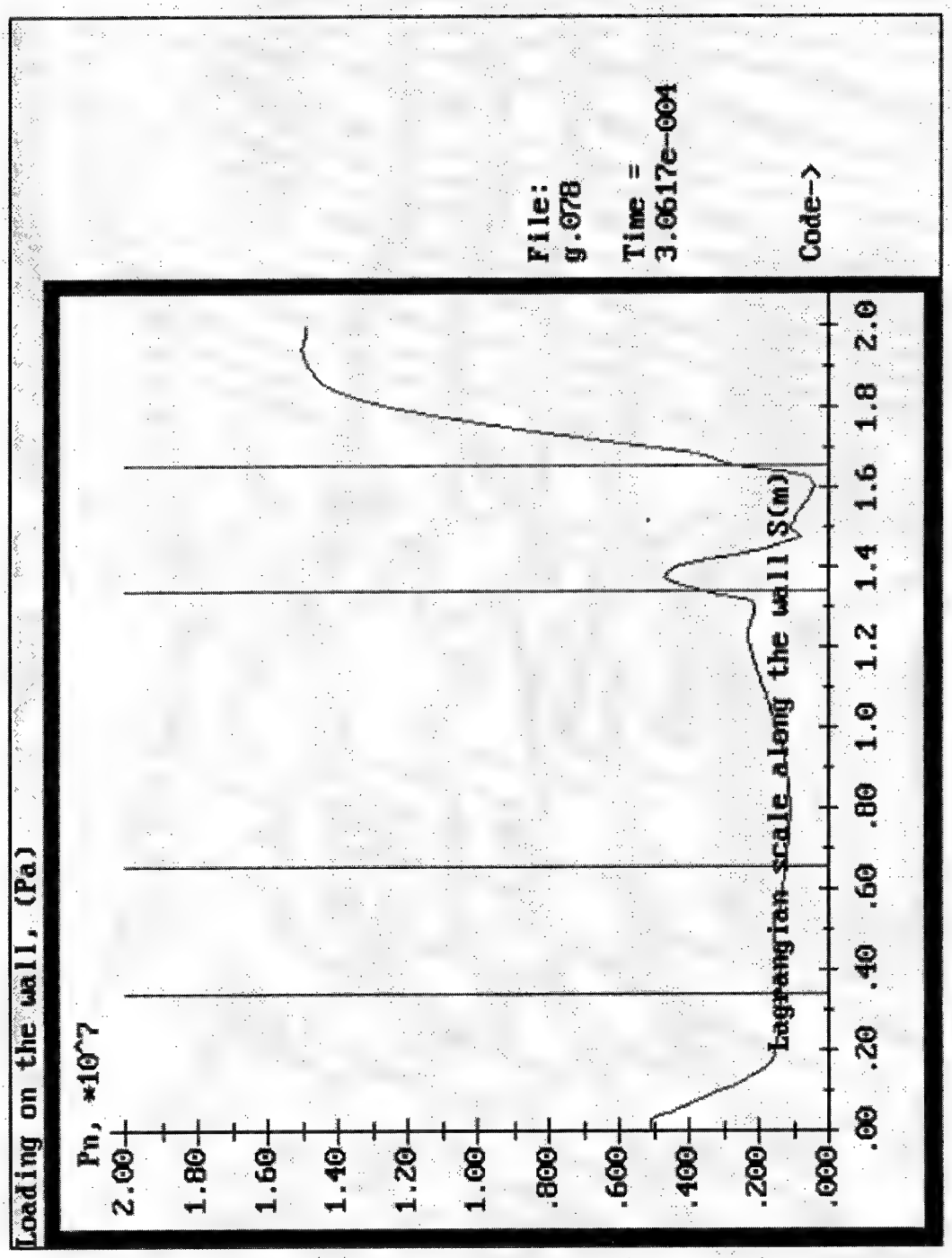
Loading on the wall, (Pa)
Pn, *10^7
2.00
1.80
1.60
1.40
1.20
1.00
.800
.600
.400
.200
.000
.00
.20
.40
.60
.80
1.0
1.2
1.4
1.6
1.8
2.0
Lagrangian scale along the wall S(m)
File:
g.078
Time =
3.0617e-004
Code->

Fig. 30. f.

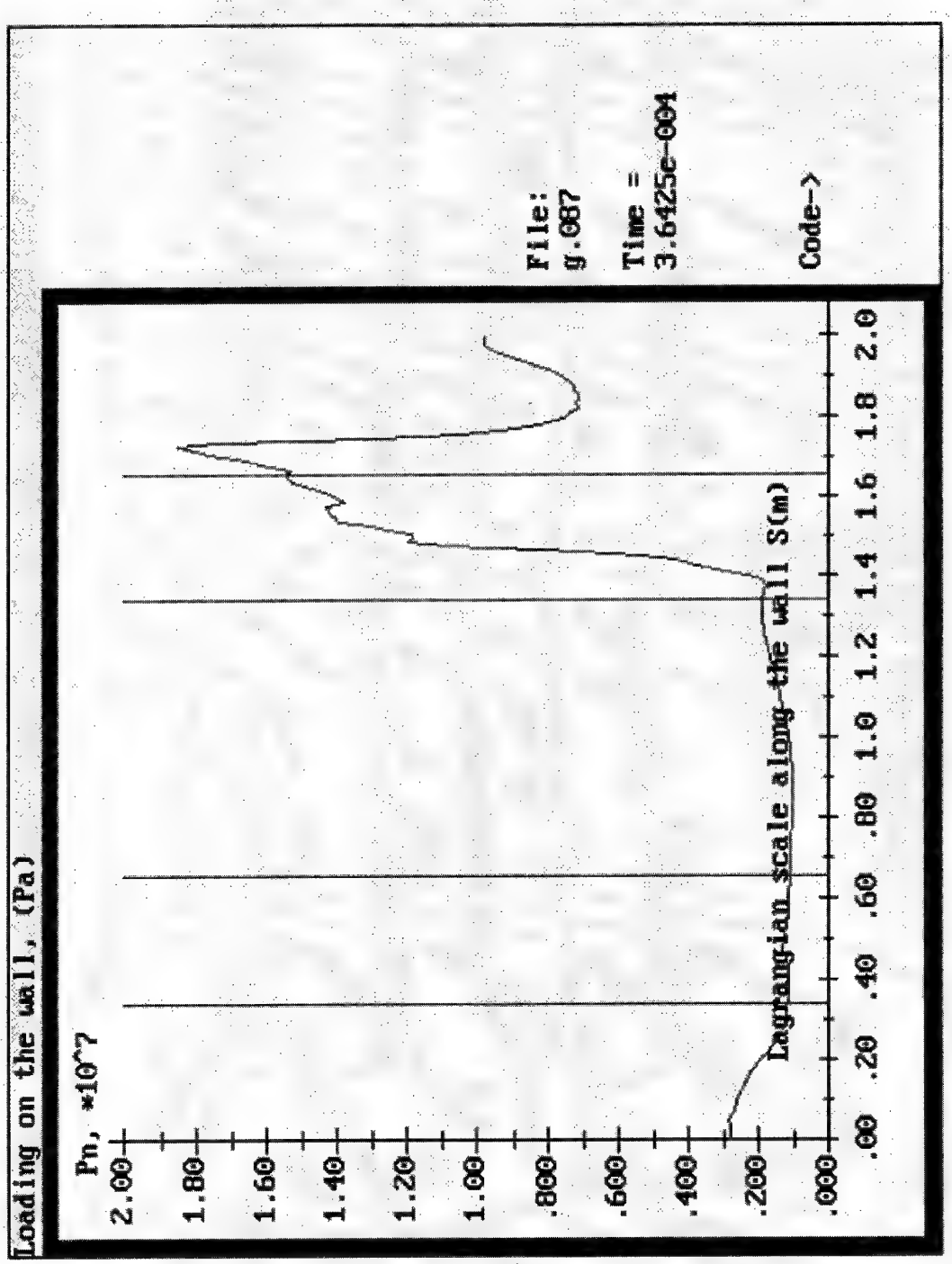
Loading on the wall, (Pa)
Pn, *10^7
2.00
1.80
1.60
1.40
1.20
1.00
.800
.600
.400
.200
.000
.00
.20
.40
.60
.80
1.0
1.2
1.4
1.6
1.8
2.0
Lagrangian scale along the wall S(m)
File:
g.087
Time =
3.6425e-004
Code->

Fig. 30.g.

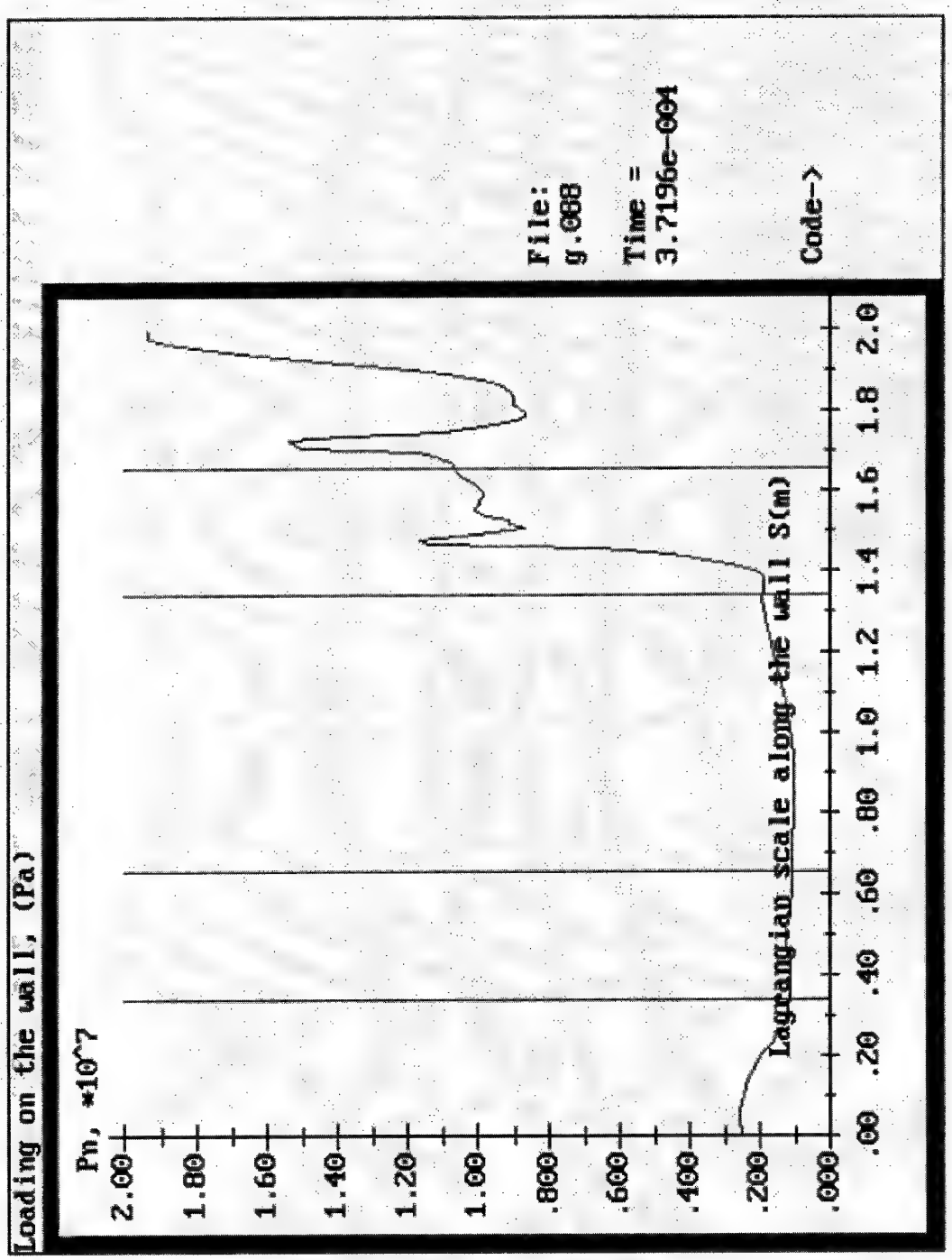
Loading on the wall, (Pa)
Pn, *10^7
2.00
1.80
1.60
1.40
1.20
1.00
.800
.600
.400
.200
.000
.00
.20
.40
.60
.80
1.0
1.2
1.4
1.6
1.8
2.0
Lagrangian scale along the wall S(m)
File:
g.088
Time =
3.7196e-004
Code->

Fig. 30. h.

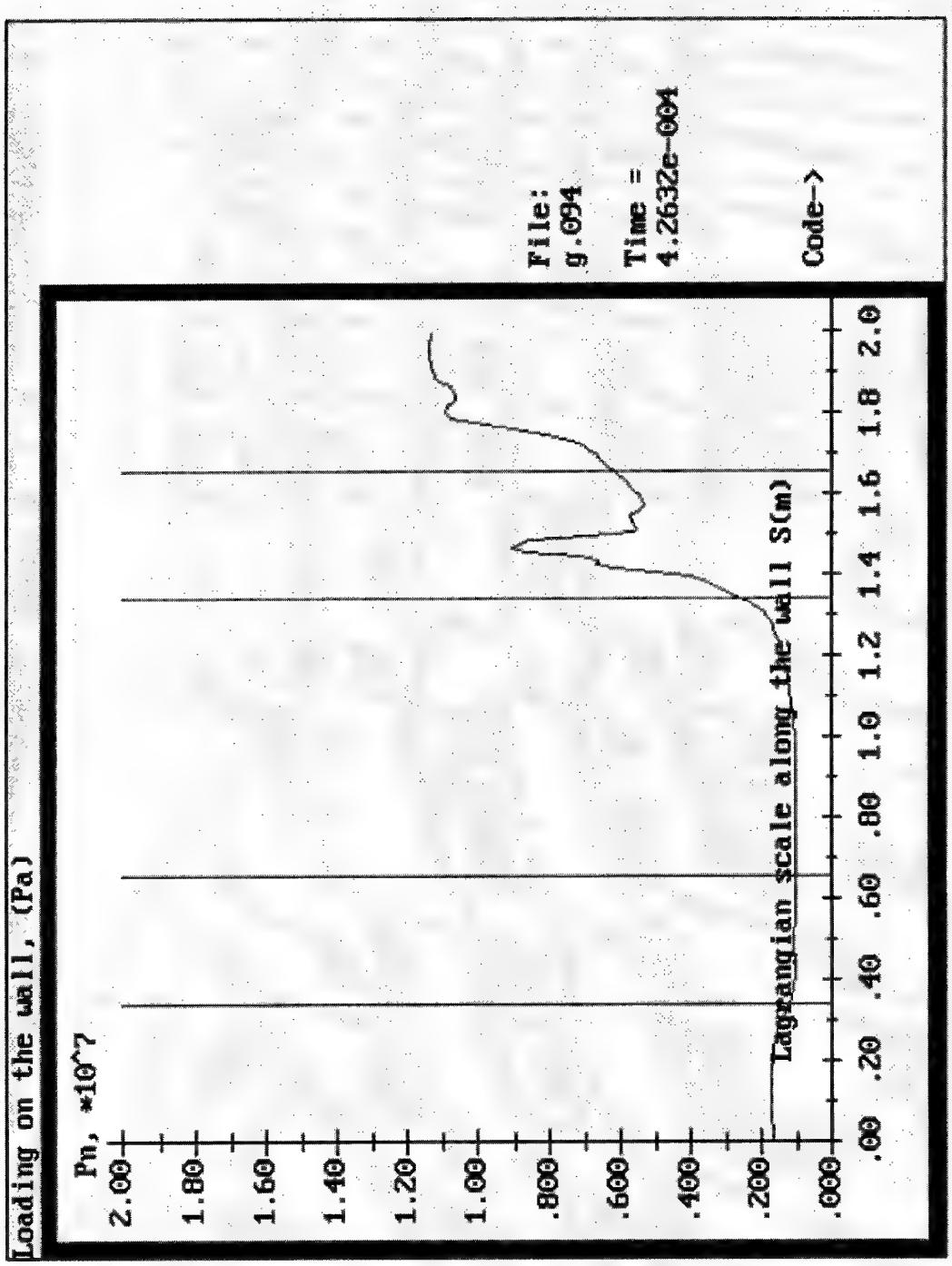
Loading on the wall, (Pa)
Pn, *10^7
2.00
1.80
1.60
1.40
1.20
1.00
.800
.600
.400
.200
.000
.00
.20
.40
.60
.80
1.0
1.2
1.4
1.6
1.8
2.0
Lagrangian scale along the wall S(m)
File:
g.094
Time =
4.2632e-004
Code->

Fig. 30. i.

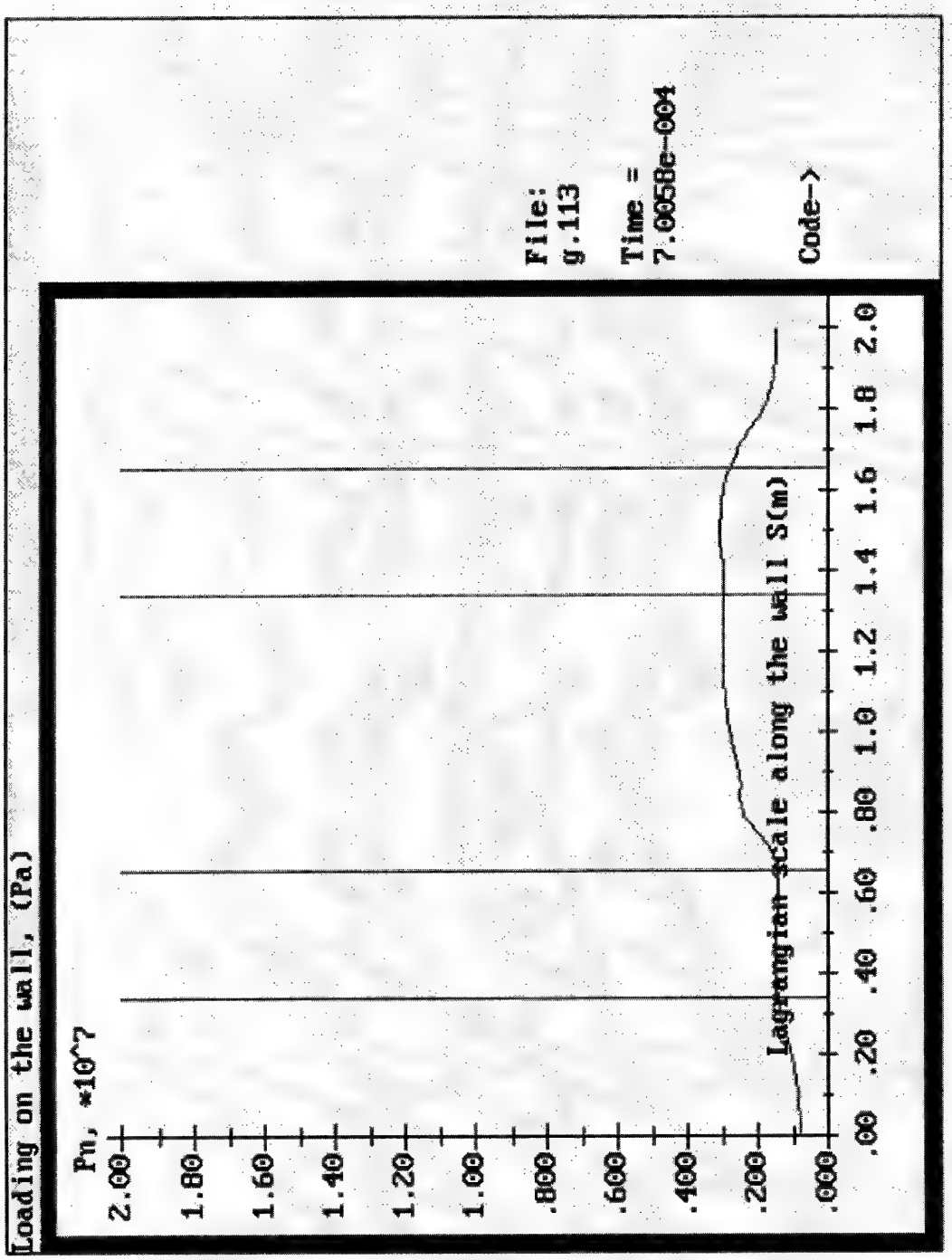
Loading on the wall, (Pa)
Pn, *10^7
2.00
1.80
1.60
1.40
1.20
1.00
.800
.600
.400
.200
.000
.00
.20
.40
.60
.80
1.0
1.2
1.4
1.6
1.8
2.0
Lagrangian scale along the wall S(m)
File:
g.113
Time =
7.0058e-004
Code->

Fig. 30. k.

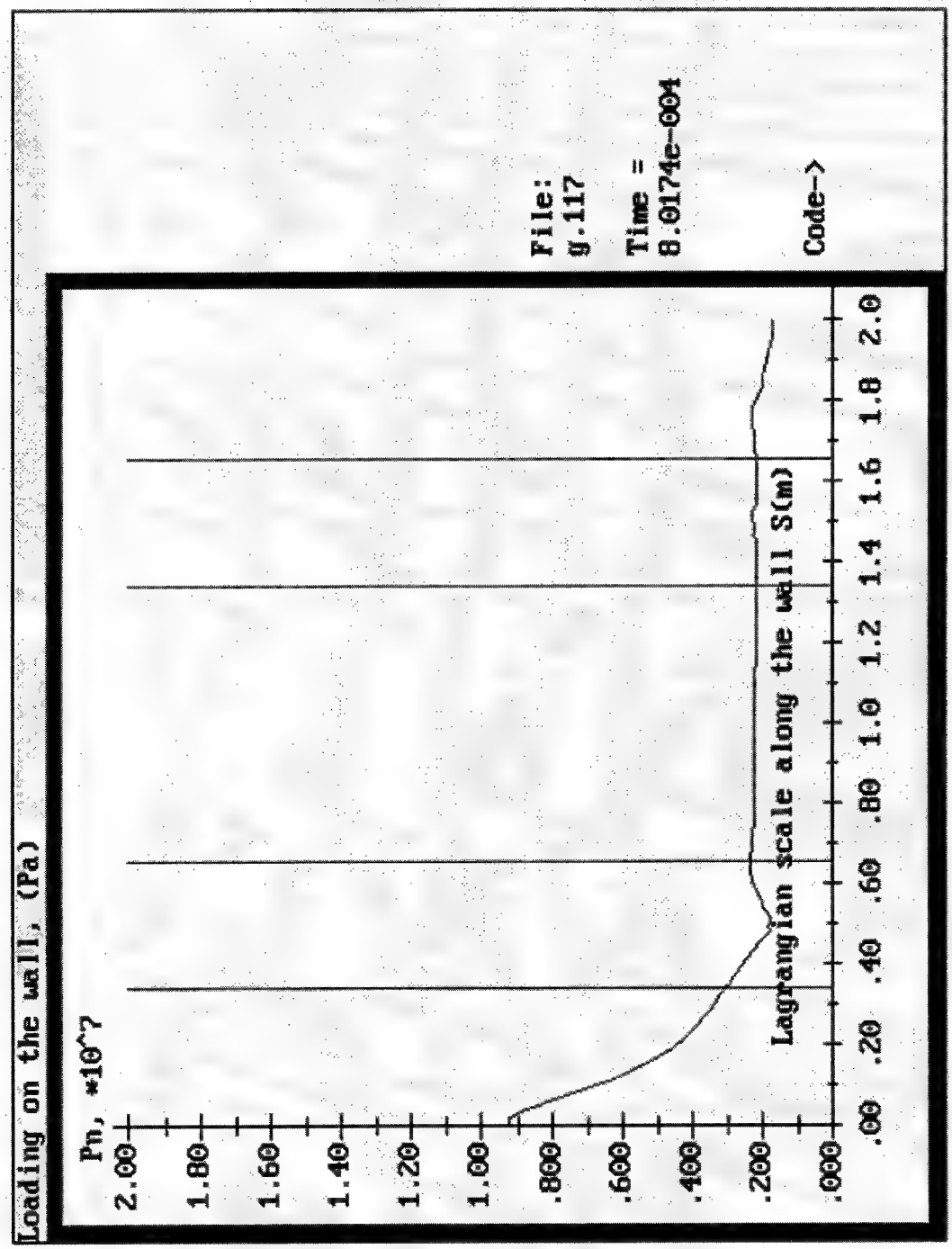
Loading on the wall, (Pa)
Pn, *10^7
2.00
1.80
1.60
1.40
1.20
1.00
.800
.600
.400
.200
.000
.00
.20
.40
.60
.80
1.0
1.2
1.4
1.6
1.8
2.0
Lagrangian scale along the wall S(m)
File:
y.117
Time =
8.0174e-004
Code->

Fig. 30. l.

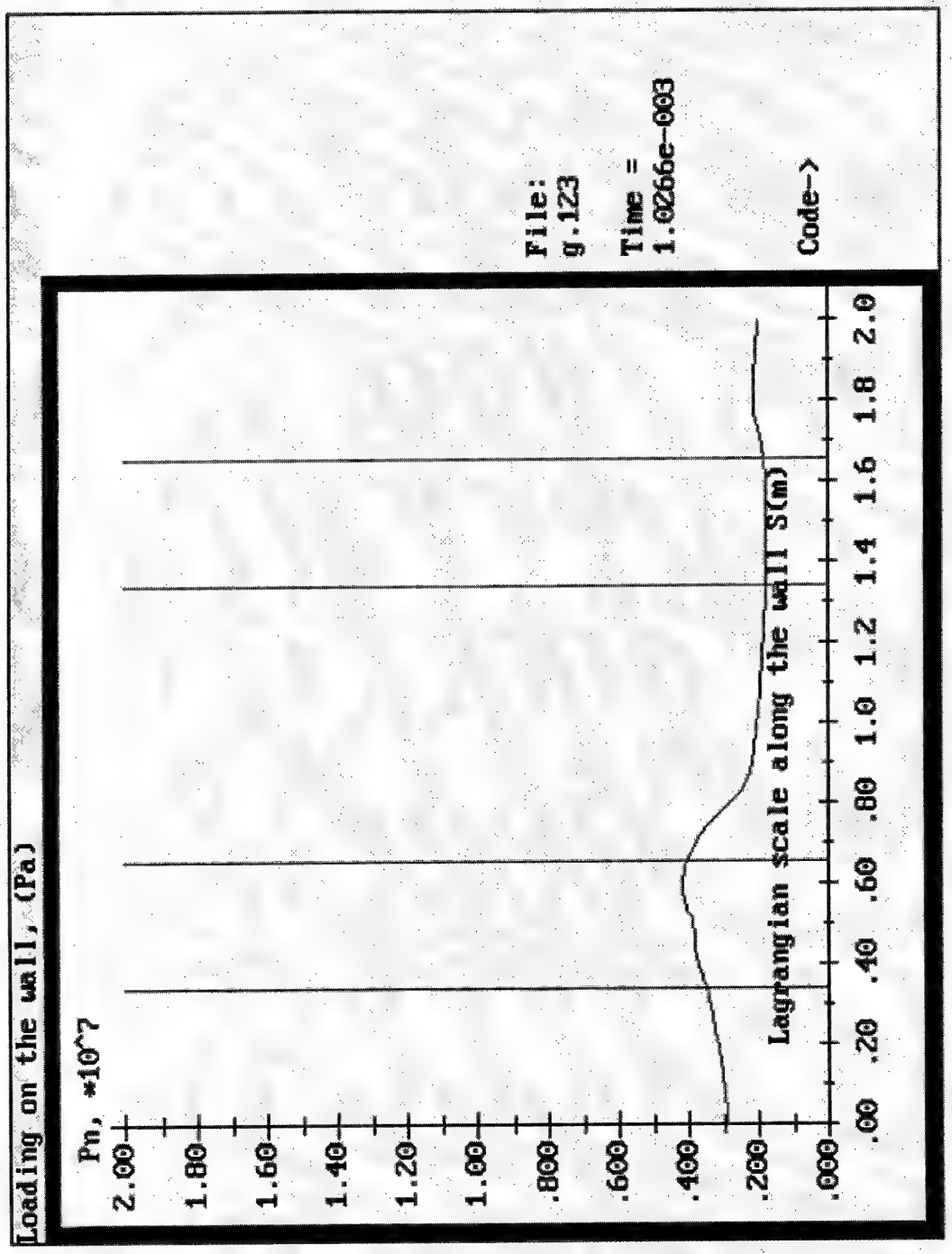
Loading on the wall, (Pa)
Pn, *10^7
2.00
1.80
1.60
1.40
1.20
1.00
.800
.600
.400
.200
.000
.00
.20
.40
.60
.80
1.0
1.2
1.4
1.6
1.8
2.0
Lagrangian scale along the wall S(m)
File:
g.123
Time =
1.0266e-003
Code->

Fig. 30. m.

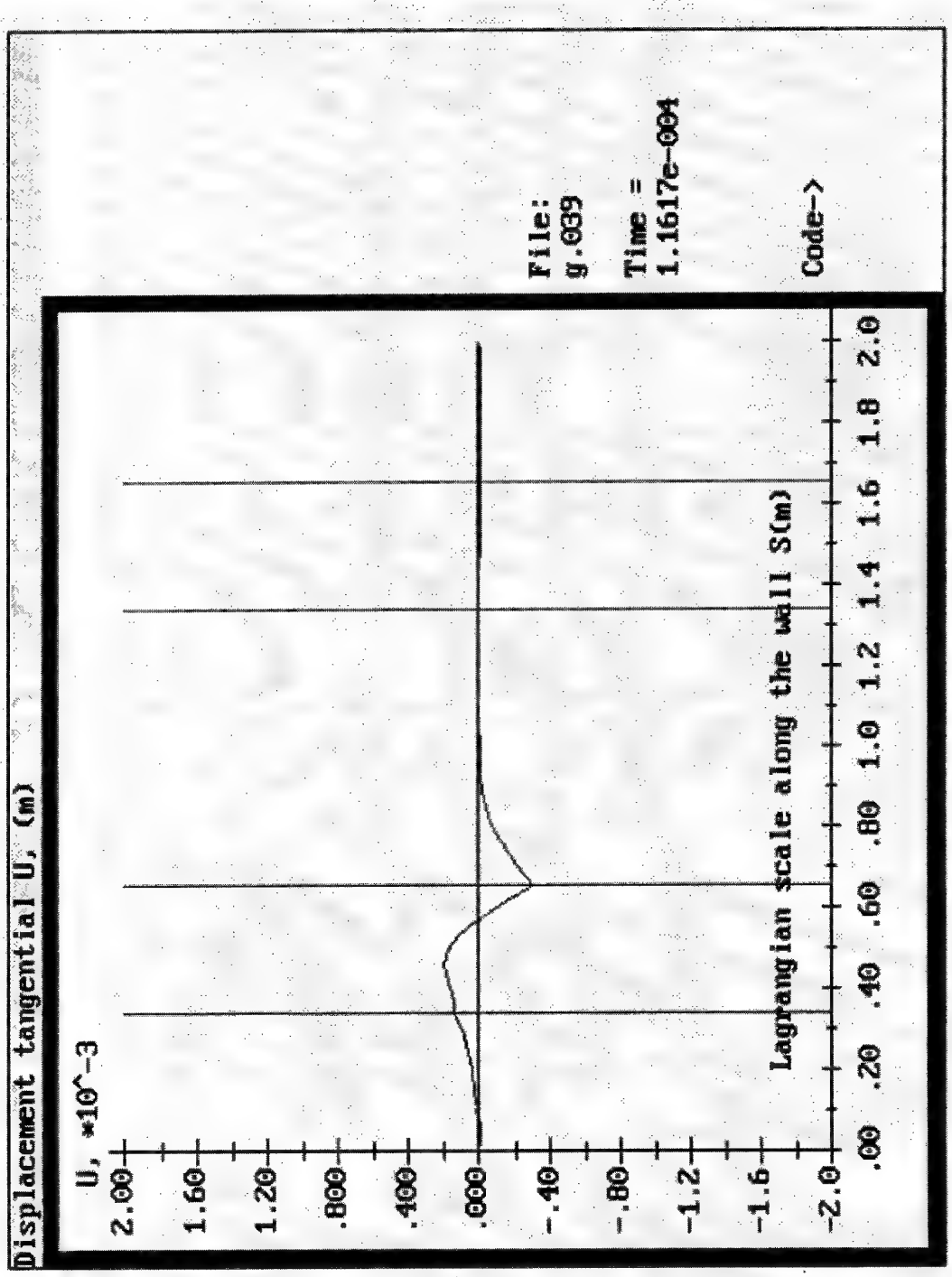
Displacement tangential U, (m)
U, *10^-3
2.00
1.60
1.20
.800
.400
.000
-.40
-.80
-1.2
-1.6
-2.0
.00
.20
.40
.60
.80
1.0
1.2
1.4
1.6
1.8
2.0
Lagrangian scale along the wall S(m)
File:
g.039
Time =
1.1617e-004
Code->

Fig. 31. a.

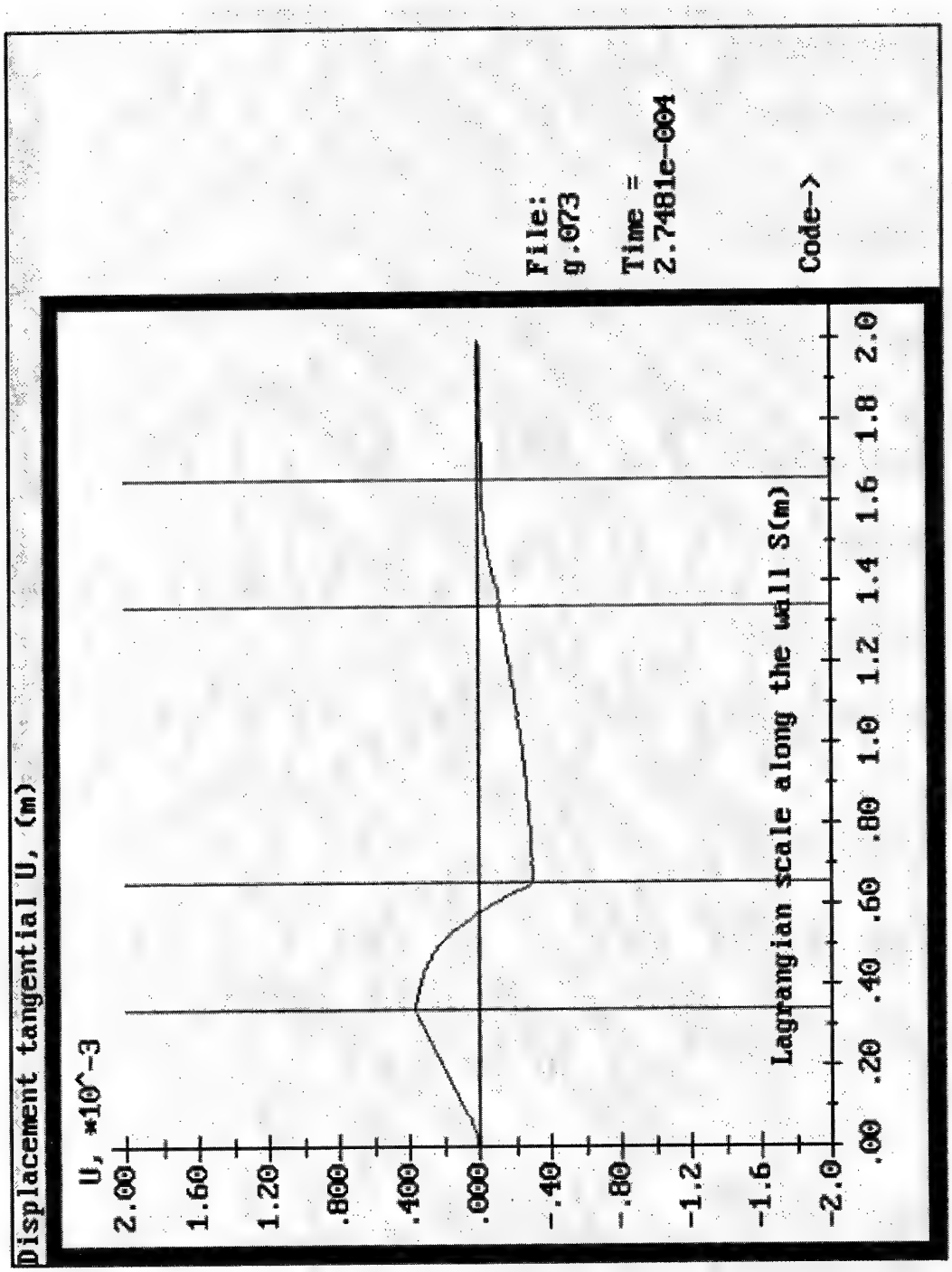
Displacement tangential U, (m)
U, *10^-3
2.00
1.60
1.20
.800
.400
.000
-.40
-.80
-1.2
-1.6
-2.0
.00
.20
.40
.60
.80
1.0
1.2
1.4
1.6
1.8
2.0
Lagrangian scale along the wall S(m)
File:
g.073
Time =
2.7481e-004
Code->

Fig. 31. b.

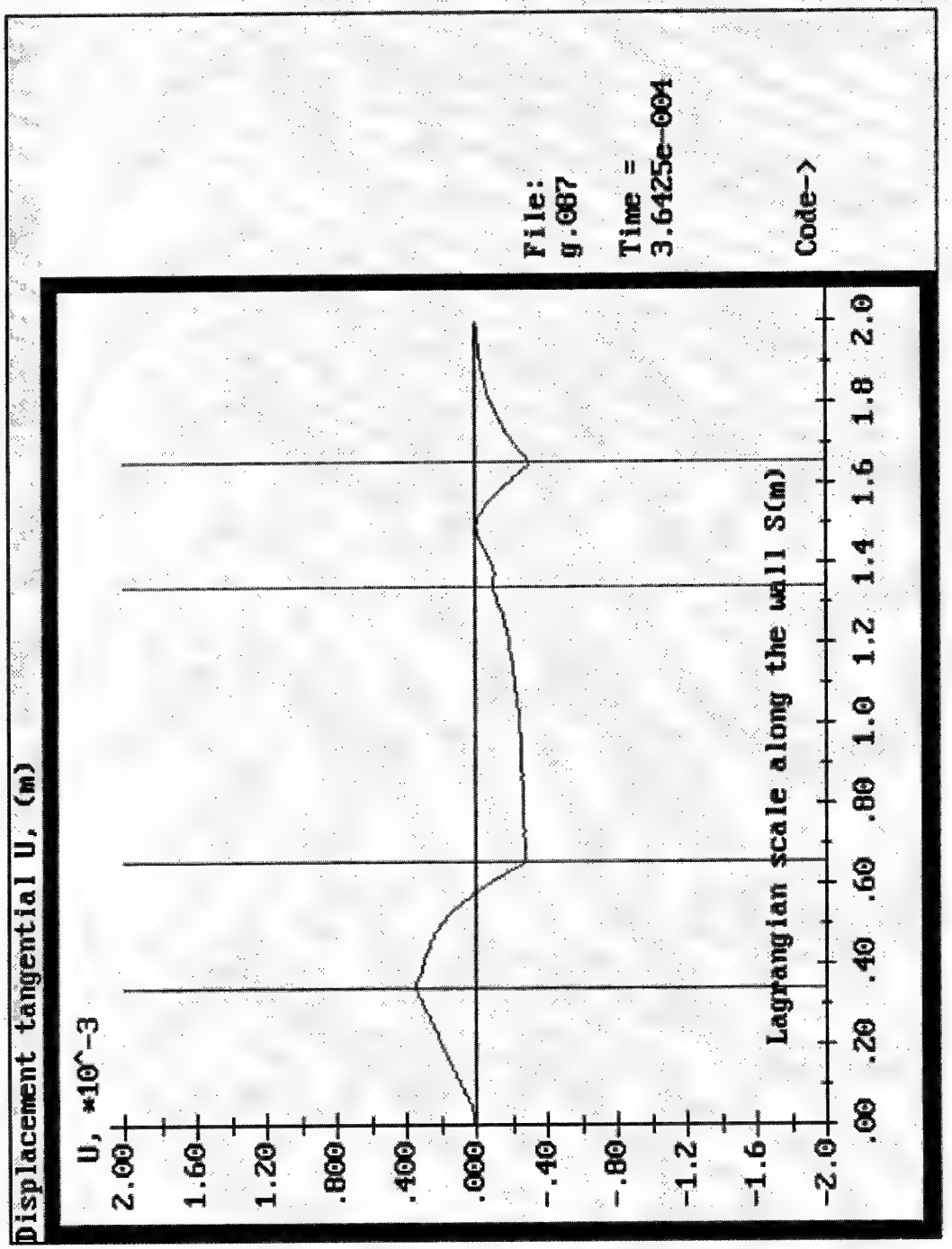
Displacement tangential U, (m)
U, *10^-3
2.00
1.60
1.20
.800
.400
.000
-.40
-.80
-1.2
-1.6
-2.0
.00
.20
.40
.60
.80
1.0
1.2
1.4
1.6
1.8
2.0
Lagrangian scale along the wall S(m)
File:
g.087
Time =
3.6425e-004
Code->

Fig. 31. c.

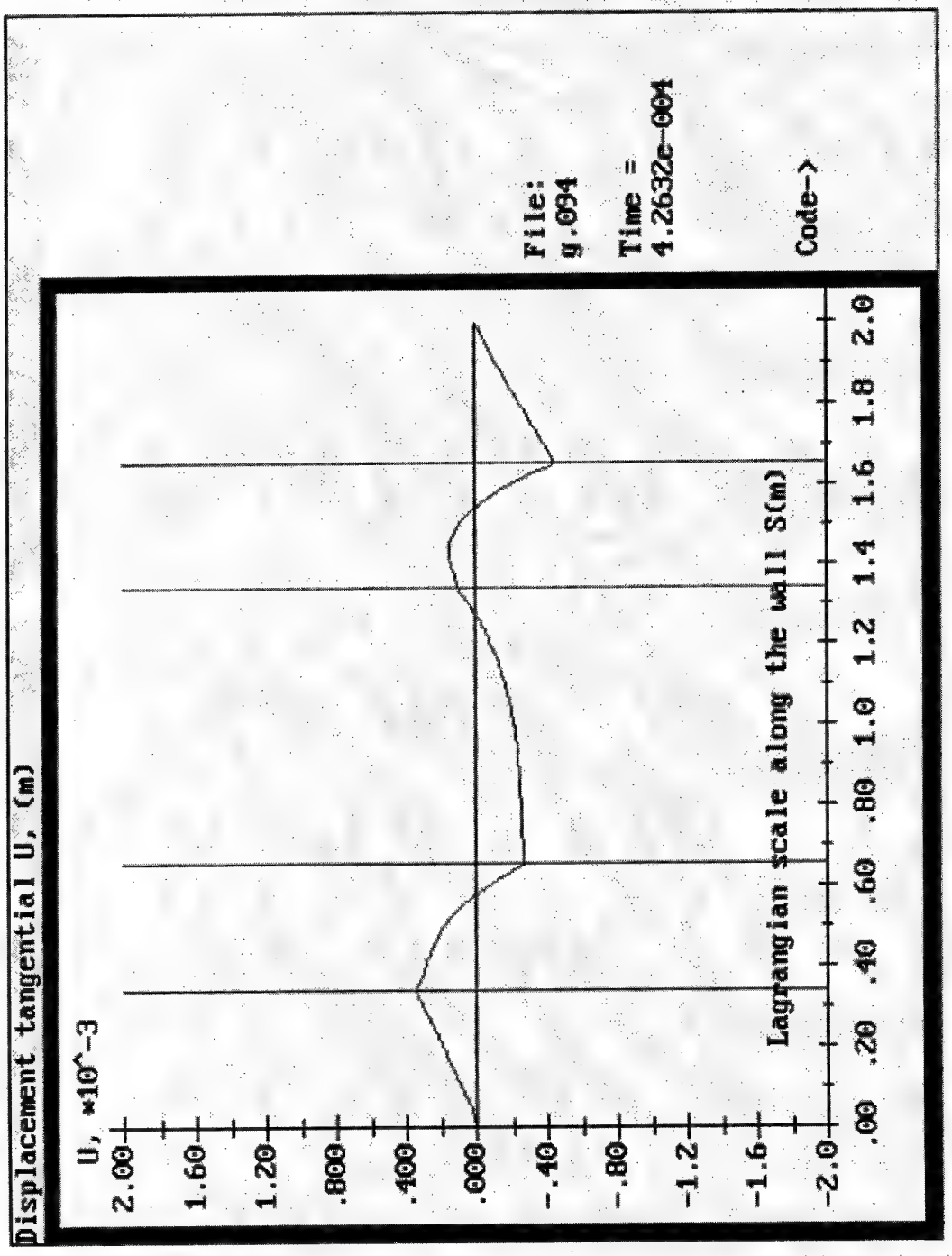
Displacement tangential U, (m)
U, *10^-3
2.00
1.60
1.20
.800
.400
.000
-.40
-.80
-1.2
-1.6
-2.0
.00
.20
.40
.60
.80
1.0
1.2
1.4
1.6
1.8
2.0
Lagrangian scale along the wall S(m)
File:
g.034
Time =
4.2632e-004
Code->

Fig. 31. d.

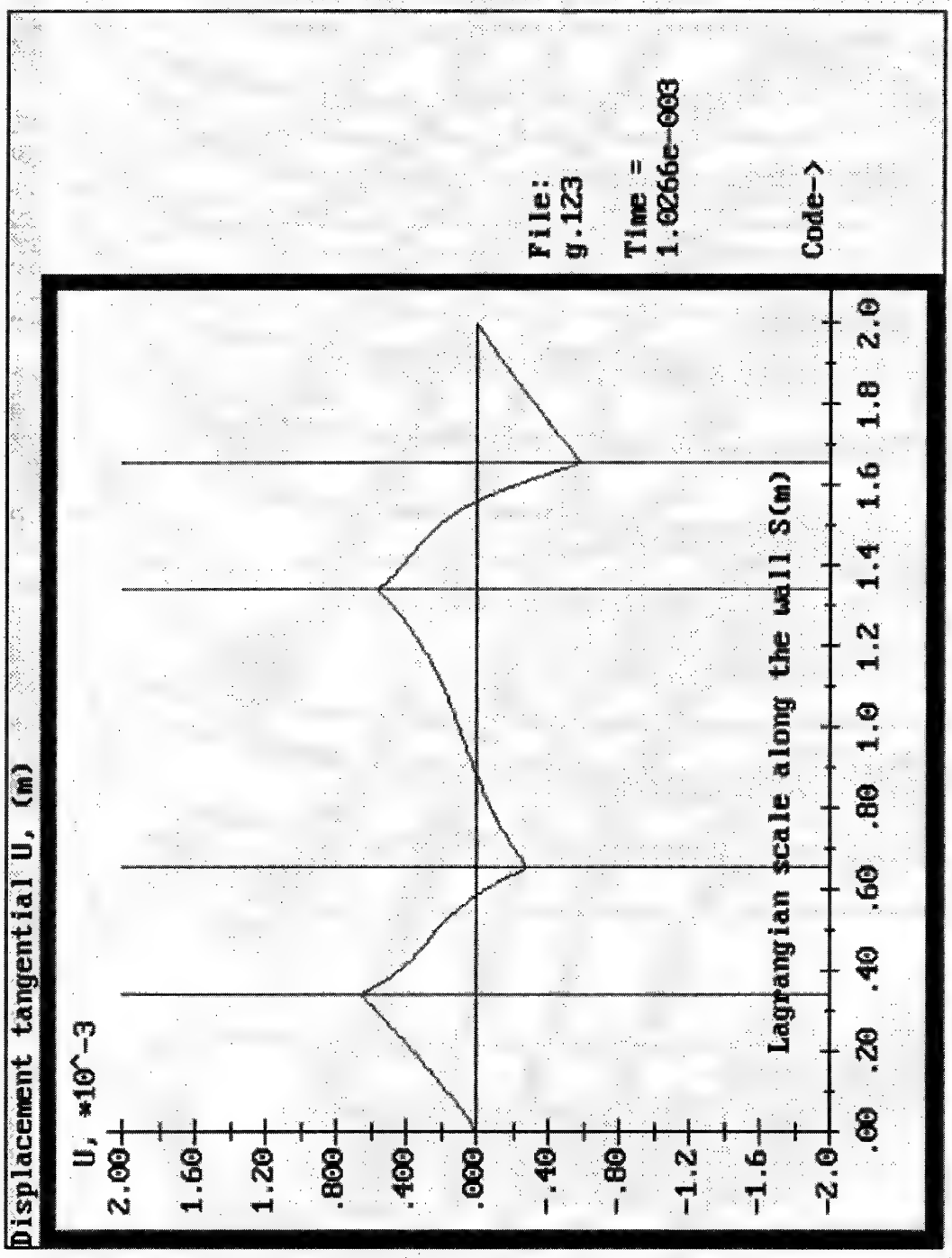
Displacement tangential U, (m)
U, *10^-3
2.00
1.60
1.20
.800
.400
.000
-.40
-.80
-1.2
-1.6
-2.0
.00
.20
.40
.60
.80
1.0
1.2
1.4
1.6
1.8
2.0
Lagrangian scale along the wall S(m)
File:
g.123
Time =
1.0266e-003
Code->

Fig. 31.e.

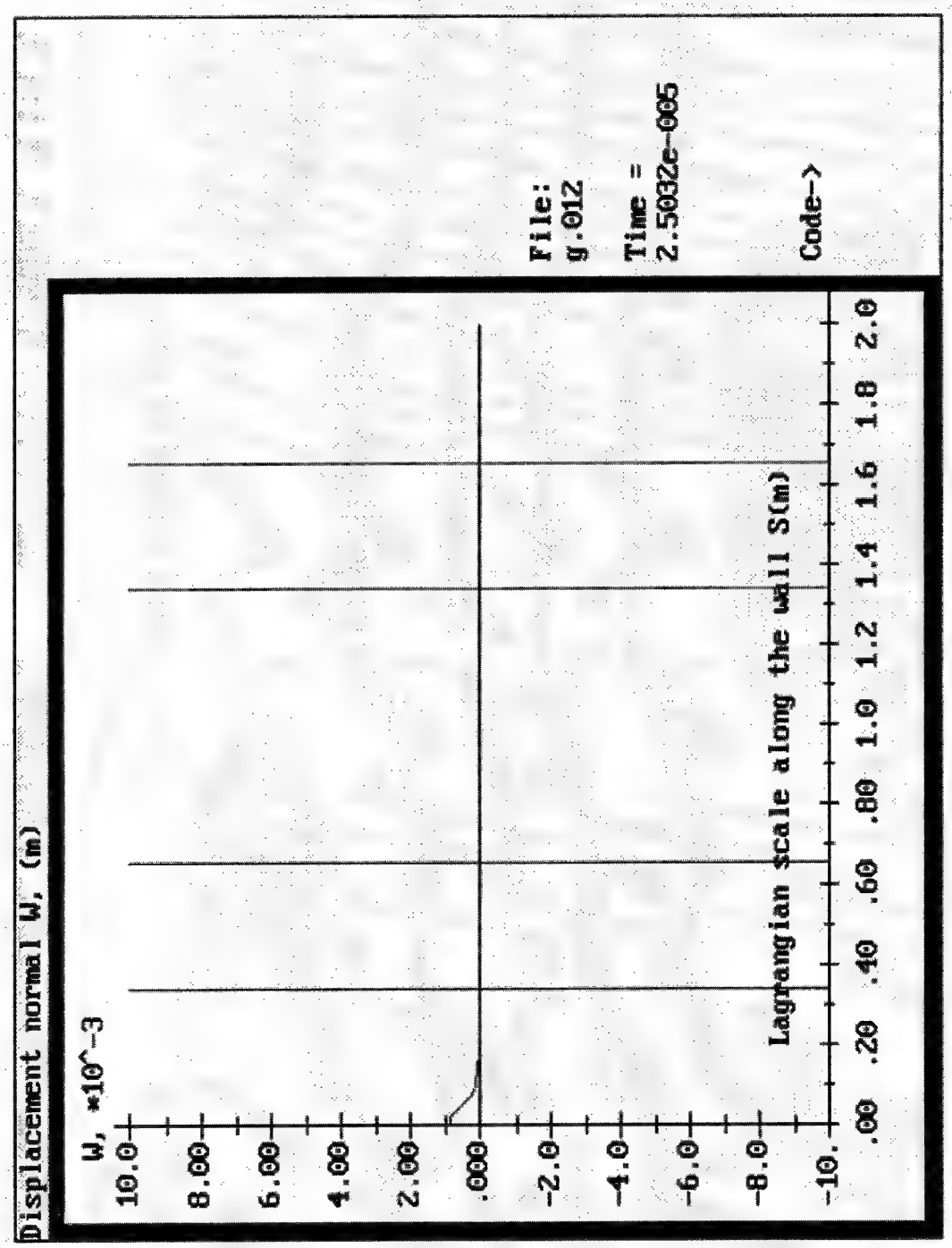
Displacement normal W, (m)
W, *10^-3
10.0
8.00
6.00
4.00
2.00
.000
-2.0
-4.0
-6.0
-8.0
-10.
.00
.20
.40
.60
.80
1.0
1.2
1.4
1.6
1.8
2.0
Lagrangian scale along the wall S(m)
File:
g.012
Time =
2.5032e-005
Code->

Fig. 32.a.

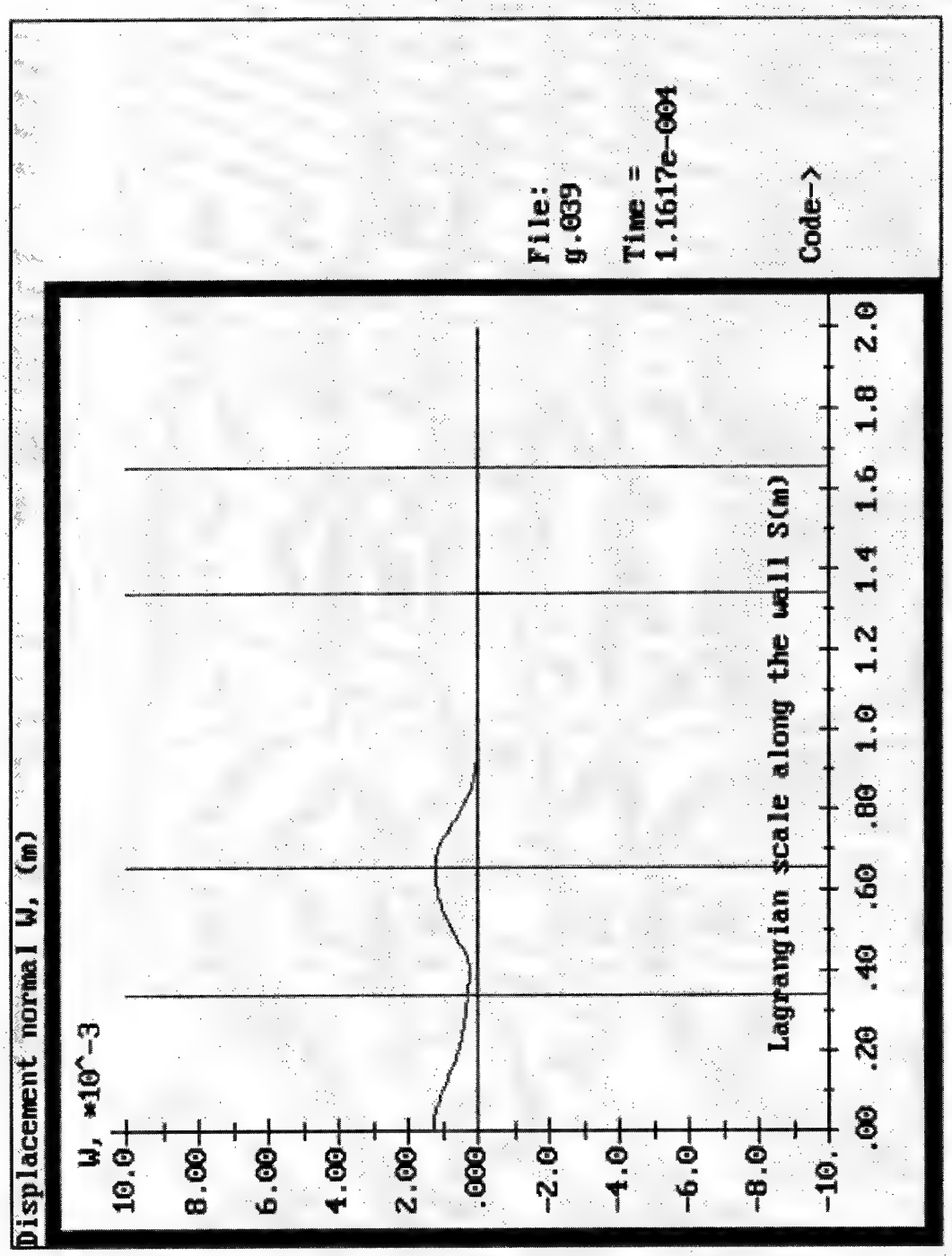
Displacement normal W, (m)
W, *10^-3
10.0
8.00
6.00
4.00
2.00
.000
-2.0
-4.0
-6.0
-8.0
-10.
.00
.20
.40
.60
.80
1.0
1.2
1.4
1.6
1.8
2.0
Lagrangian scale along the wall S(m)
File:
g.039
Time =
1.1617e-004
Code->

Fig. 32. b.

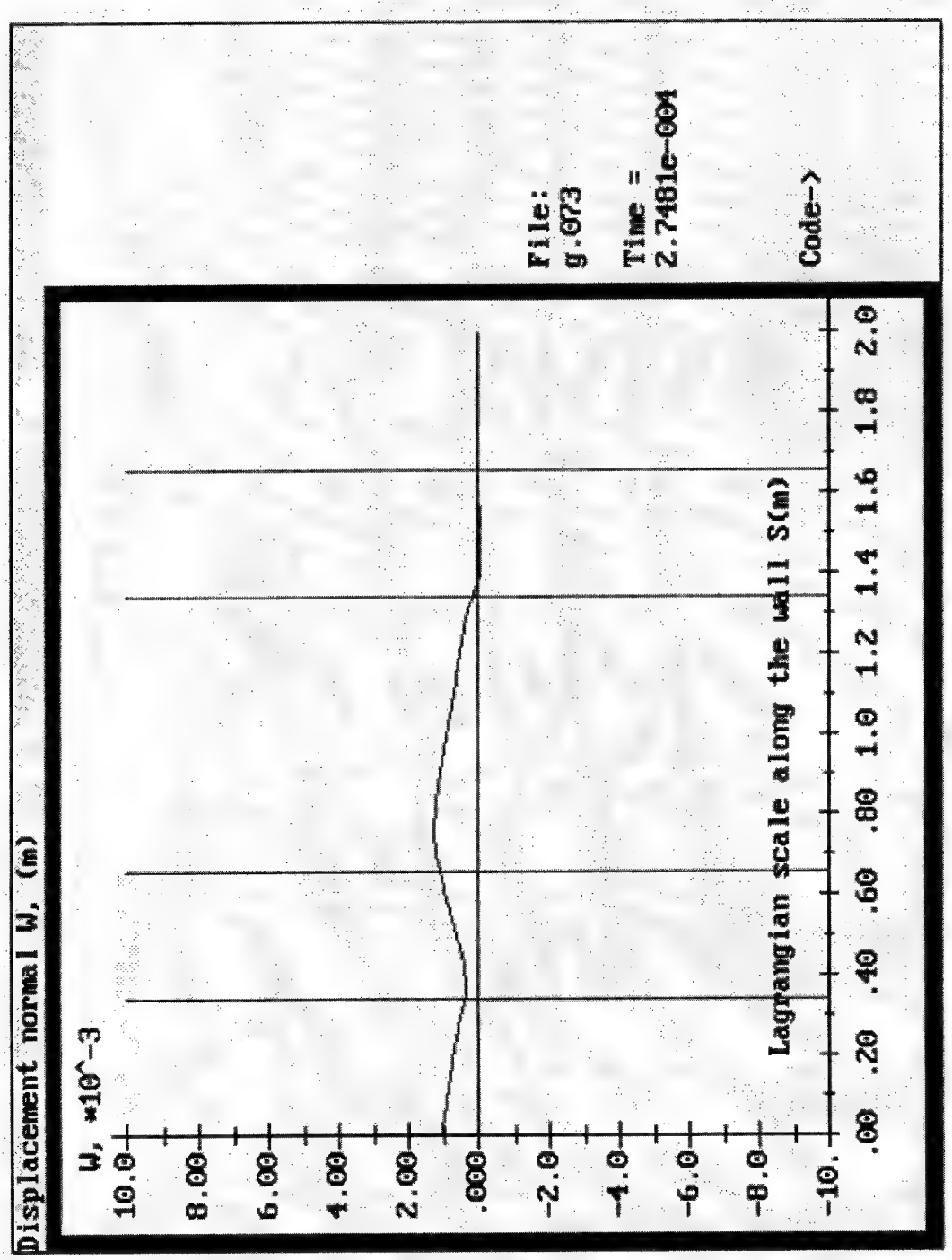
Displacement normal W, (m)
W, *10^-3
10.0
8.00
6.00
4.00
2.00
.000
-2.0
-4.0
-6.0
-8.0
-10.
.00
.20
.40
.60
.80
1.0
1.2
1.4
1.6
1.8
2.0
Lagrangian scale along the wall S(m)
File:
g.073
Time =
2.7481e-004
Code->

Fig. 32. c.

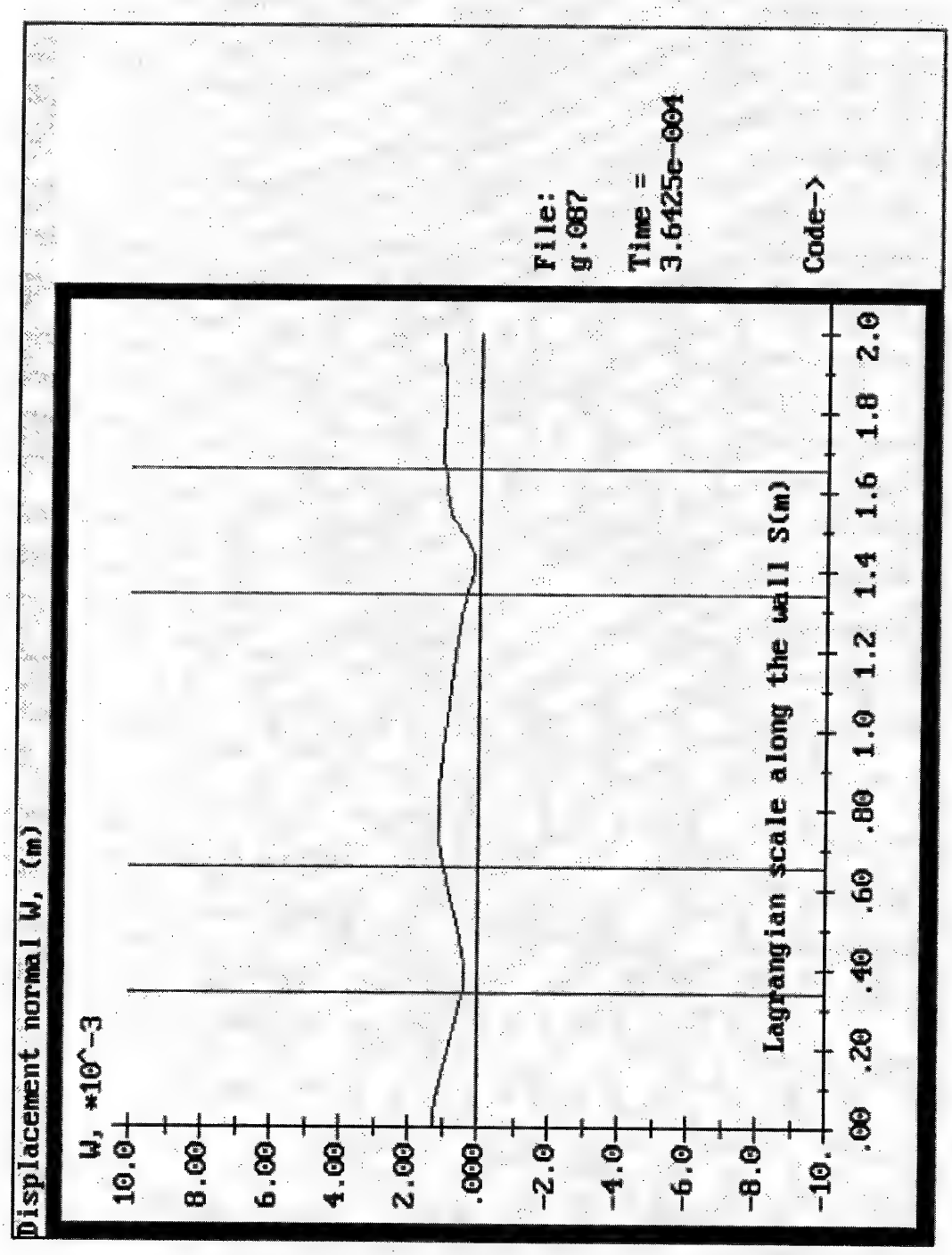
Displacement normal W, (m)
W, *10^-3
10.0
8.00
6.00
4.00
2.00
.000
-2.0
-4.0
-6.0
-8.0
-10.
.00
.20
.40
.60
.80
1.0
1.2
1.4
1.6
1.8
2.0
Lagrangian scale along the wall S(m)
File:
g.087
Time =
3.6425e-004
Code->

Fig. 32. d.

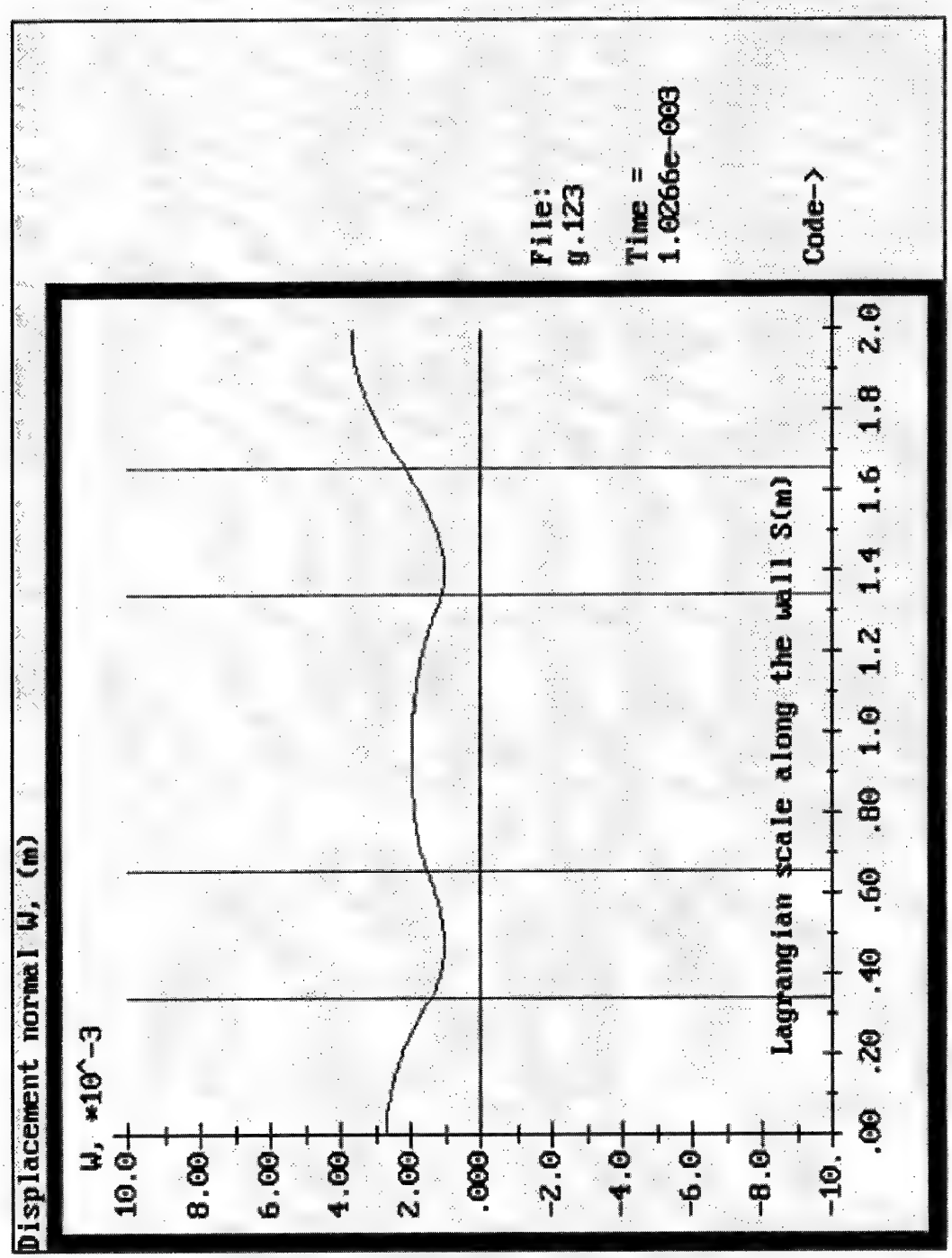
Displacement normal W, (m)
W, *10^-3
10.0
8.00
6.00
4.00
2.00
.000
-2.0
-4.0
-6.0
-8.0
-10.
.00
.20
.40
.60
.80
1.0
1.2
1.4
1.6
1.8
2.0
Lagrangian scale along the wall S(m)
File:
g.123
Time =
1.0266e-003
Code->

Fig. 32. e.

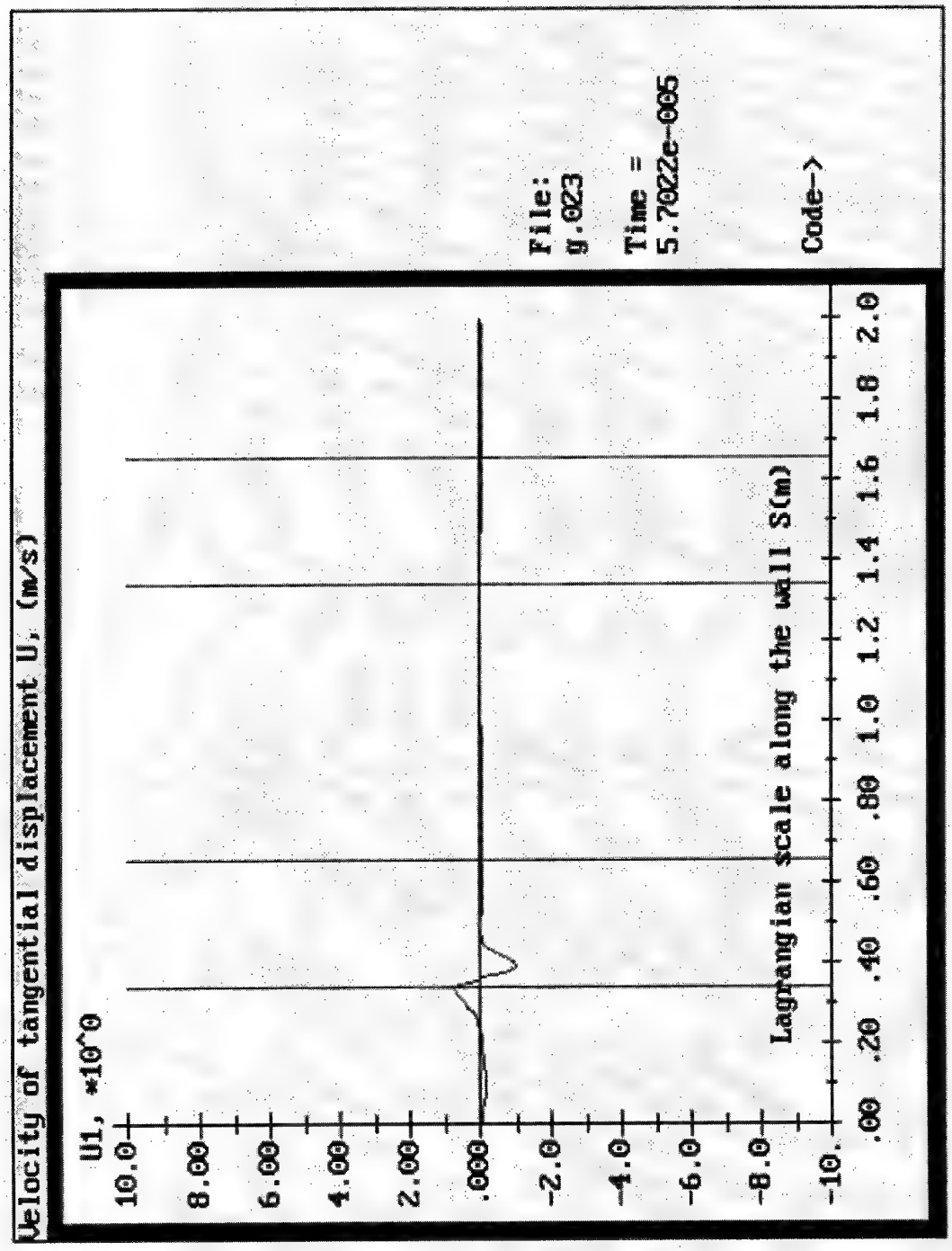
Velocity of tangential displacement U, (m/s)
U1, *10^0
10.0
8.00
6.00
4.00
2.00
.000
-2.0
-4.0
-6.0
-8.0
-10.
.00
.20
.40
.60
.80
1.0
1.2
1.4
1.6
1.8
2.0
Lagrangian scale along the wall S(m)
File:
g.023
Time =
5.7022e-005
Code->

Fig. 33. a.

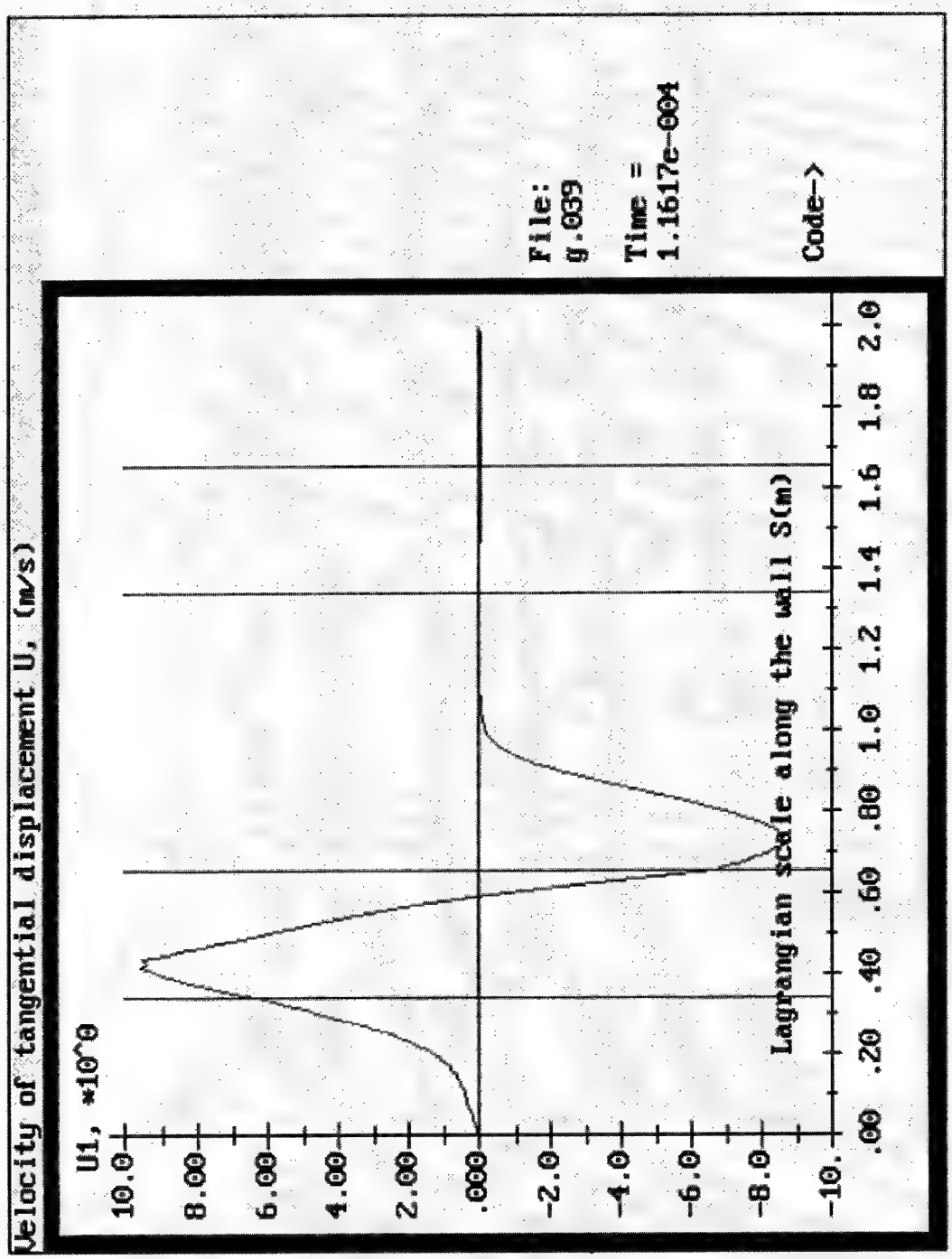
Velocity of tangential displacement U, (m/s)
U1, *10^0
10.0
8.00
6.00
4.00
2.00
.000
-2.0
-4.0
-6.0
-8.0
-10.
.00
.20
.40
.60
.80
1.0
1.2
1.4
1.6
1.8
2.0
Lagrangian scale along the wall S(m)
File:
g.039
Time =
1.1617e-004
Code->

Fig. 33. b.

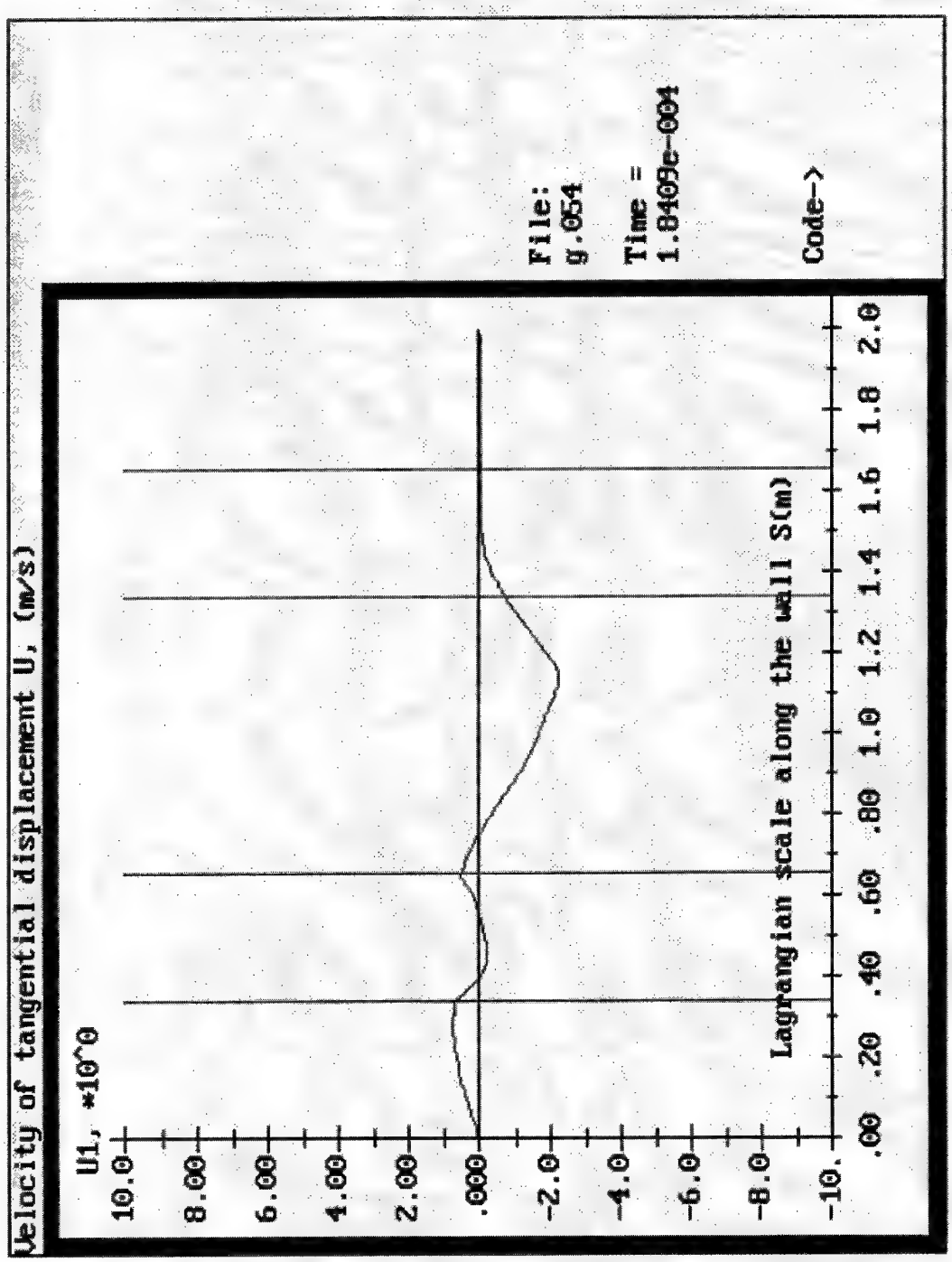
Velocity of tangential displacement U, (m/s)
U1, *10^0
10.0
8.00
6.00
4.00
2.00
.000
-2.0
-4.0
-6.0
-8.0
-10.
.00
.20
.40
.60
.80
1.0
1.2
1.4
1.6
1.8
2.0
Lagrangian scale along the wall S(m)
File:
g.054
Time =
1.8409e-004
Code->

Fig. 33. c.

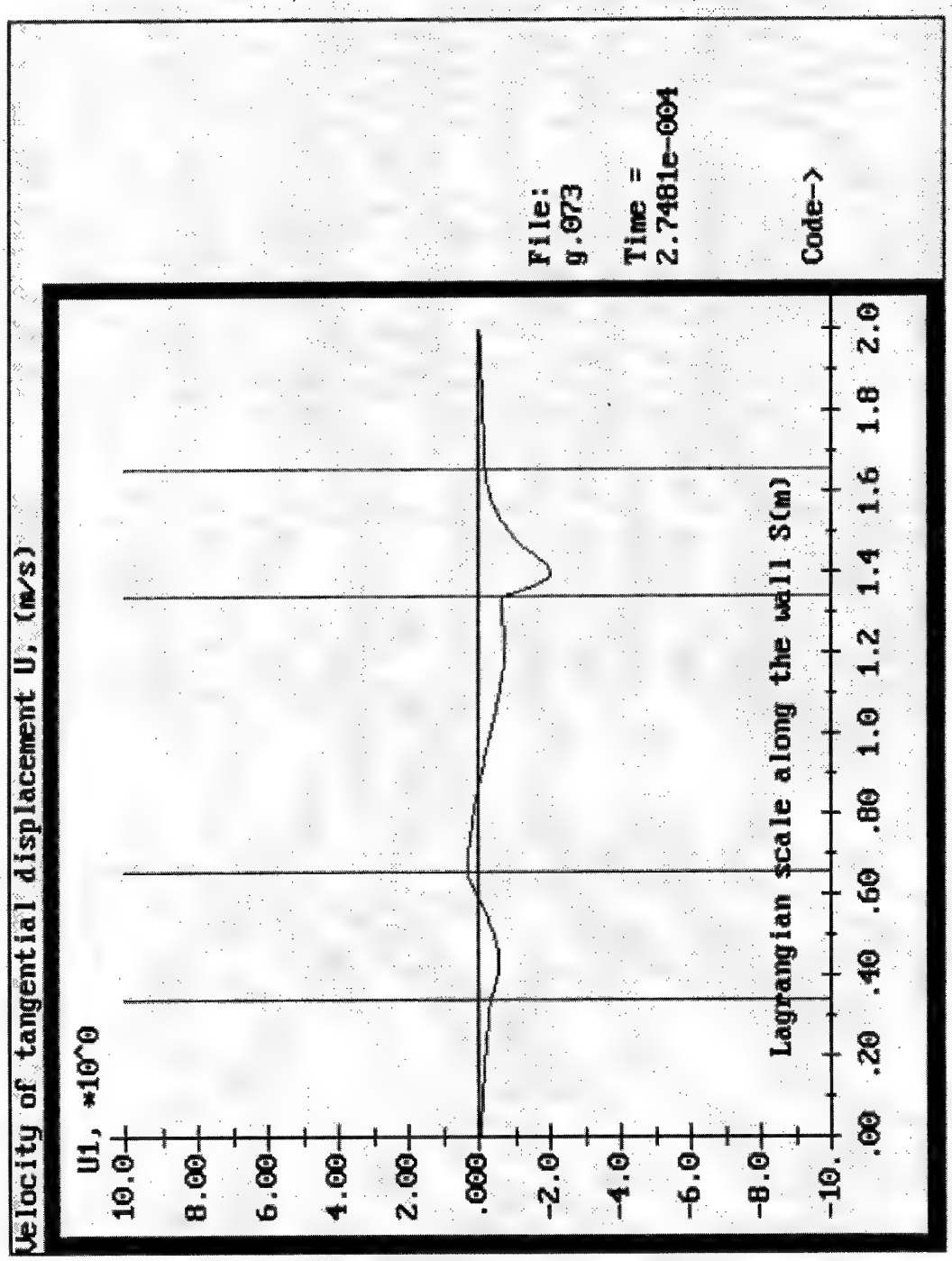
Velocity of tangential displacement U, (m/s)
U1, *10^0
10.0
8.00
6.00
4.00
2.00
.000
-2.0
-4.0
-6.0
-8.0
-10.
.00
.20
.40
.60
.80
1.0
1.2
1.4
1.6
1.8
2.0
Lagrangian scale along the wall S(m)
File:
g.073
Time =
2.7481e-004
Code->

Fig. 33.d.

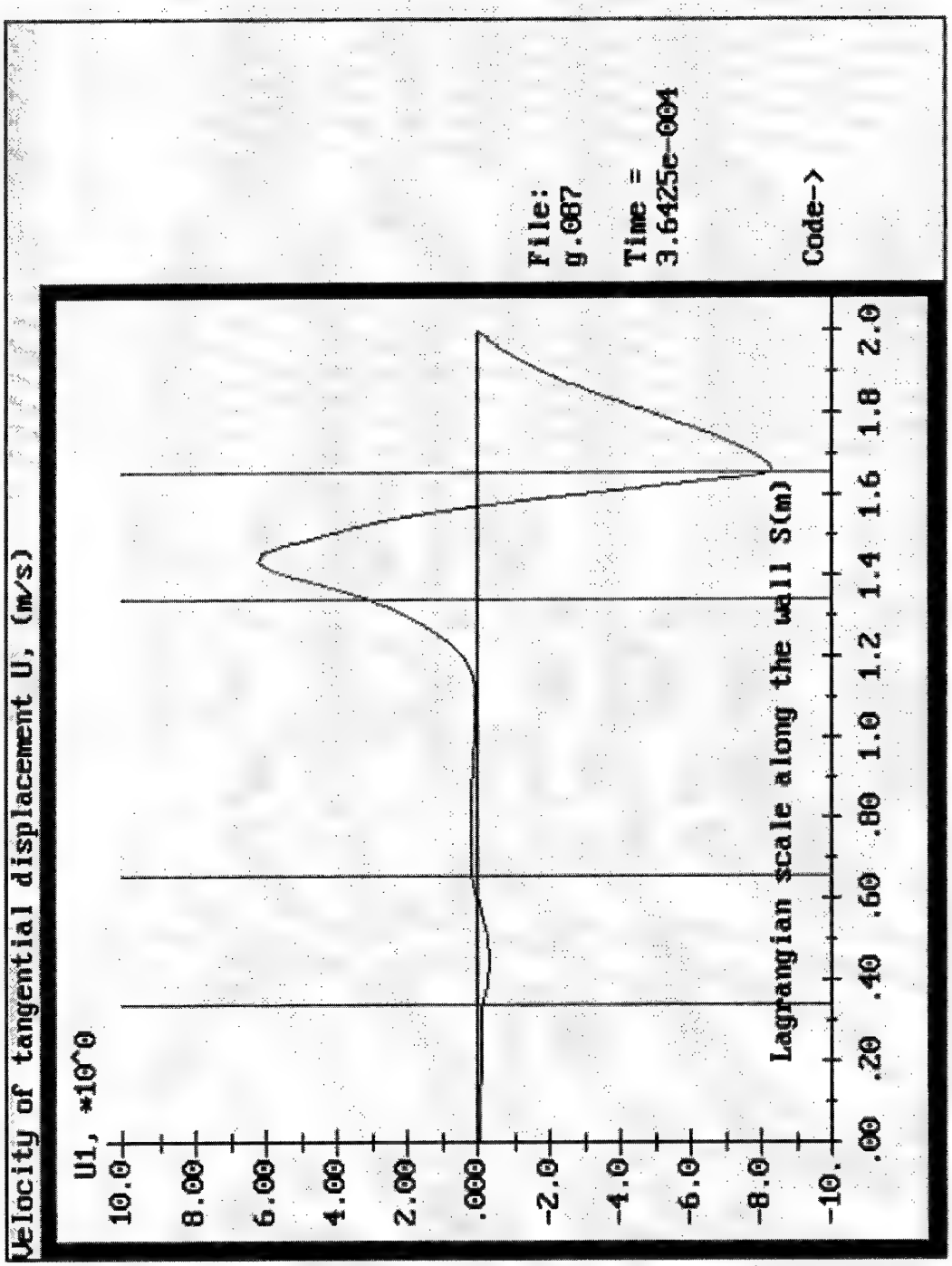
Velocity of tangential displacement U, (m/s)
U1, *10^0
10.0
8.00
6.00
4.00
2.00
.000
-2.0
-4.0
-6.0
-8.0
-10.
.00
.20
.40
.60
.80
1.0
1.2
1.4
1.6
1.8
2.0
Lagrangian scale along the wall S(m)
File:
g.087
Time =
3.6425e-004
Code->

Fig. 33. e.

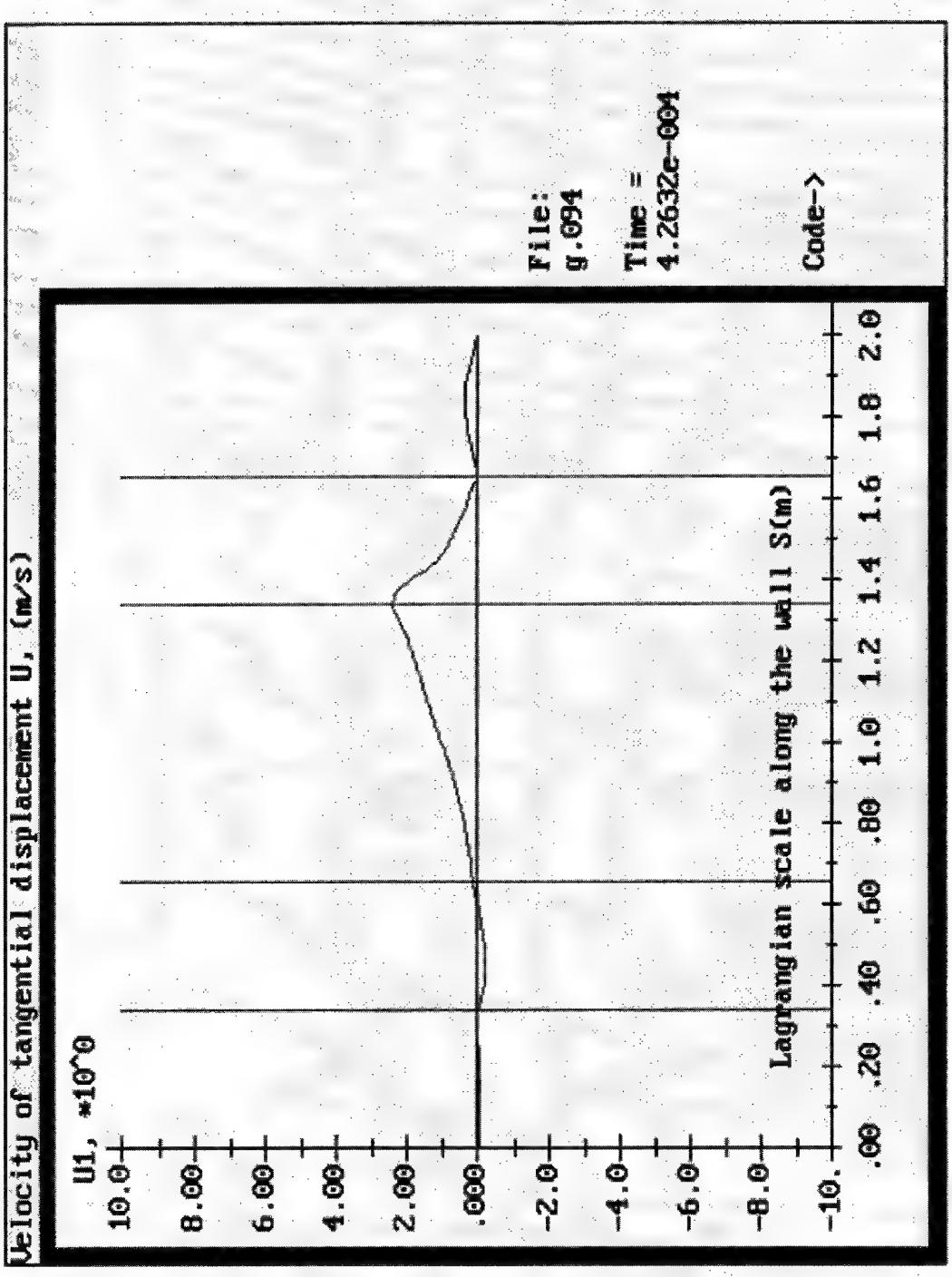
Velocity of tangential displacement U, (m/s)
U1, *10^0
10.0
8.00
6.000
4.00
2.00
.000
-2.0
-4.0
-6.0
-8.0
-10.
.00
.20
.40
.60
.80
1.0
1.2
1.4
1.6
1.8
2.0
Lagrangian scale along the wall S(m)
File:
g.094
Time =
4.2632e-004
Code->

Fig. 33.f.

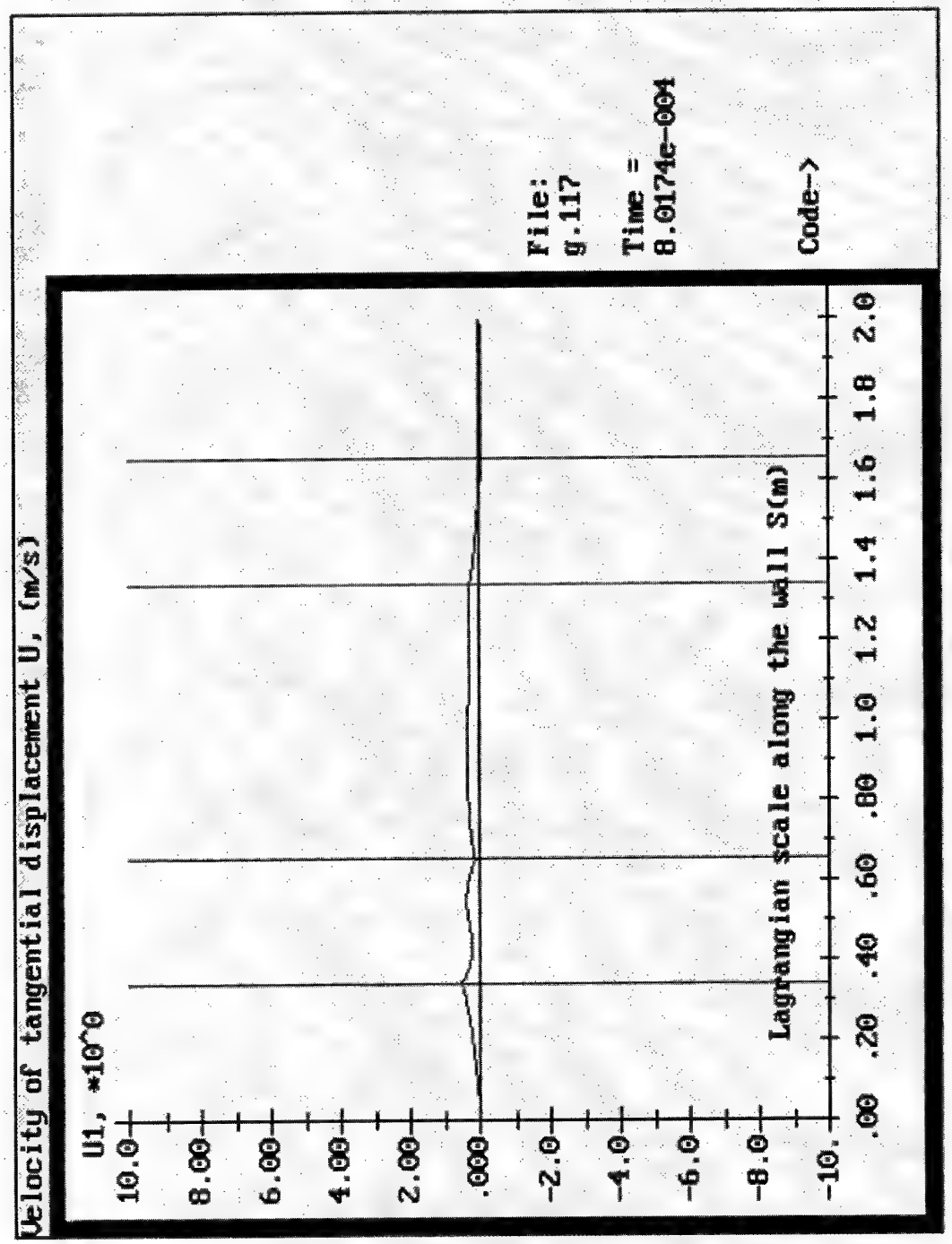
Velocity of tangential displacement U, (m/s)
U1, *10^0
10.0
8.00
6.00
4.00
2.00
.000
-2.0
-4.0
-6.0
-8.0
-10.
.00
.20
.40
.60
.80
1.0
1.2
1.4
1.6
1.8
2.0
Lagrangian scale along the wall S(m)
File:
g.117
Time =
8.0174e-004
Code->

Fig. 33.g.

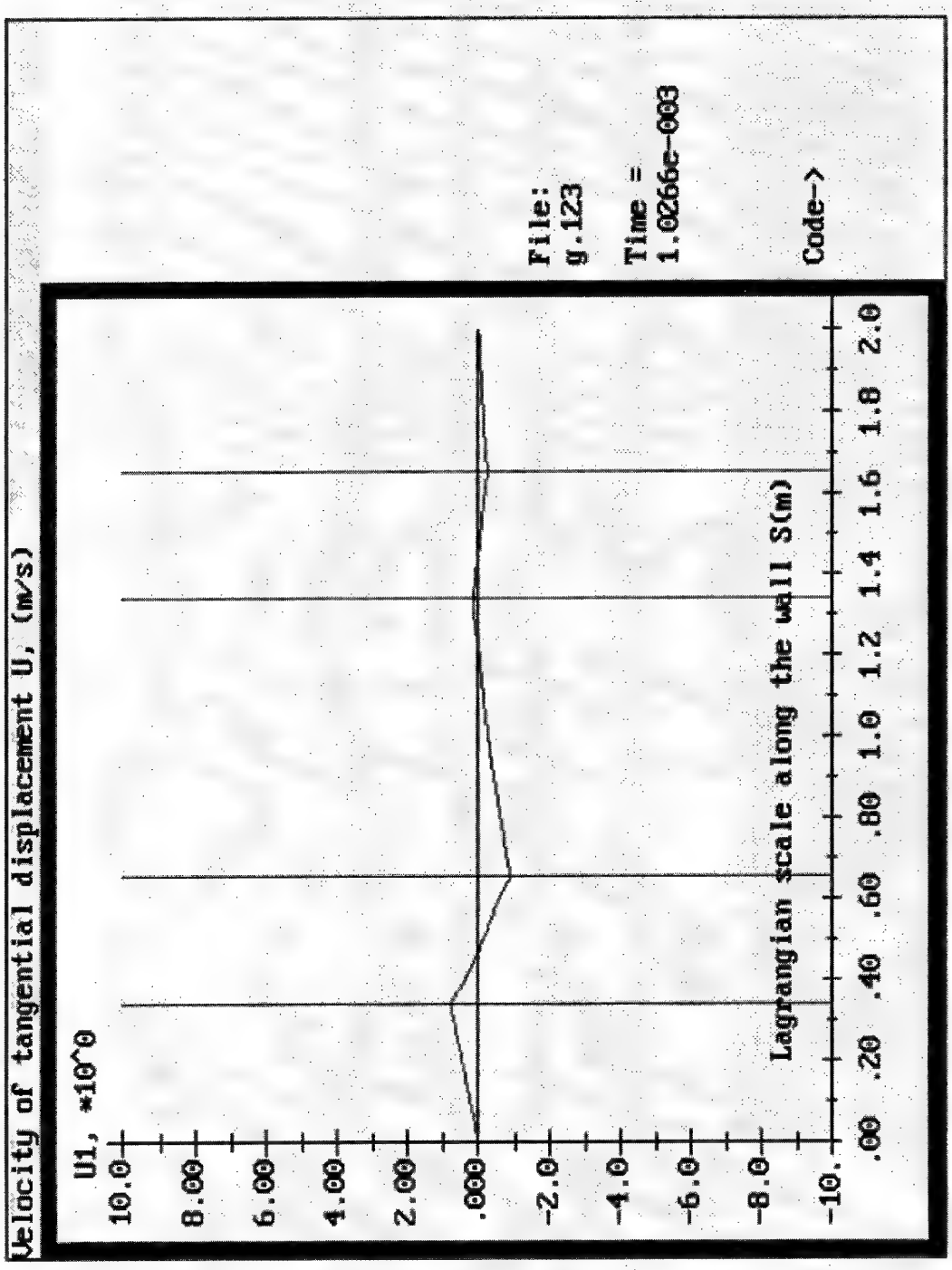
Velocity of tangential displacement U, (m/s)
U1, *10^0
10.0
8.00
6.00
4.00
2.00
.000
-2.0
-4.0
-6.0
-8.0
-10.
.00
.20
.40
.60
.80
1.0
1.2
1.4
1.6
1.8
2.0
Lagrangian scale along the wall S(m)
File:
g.123
Time =
1.0266e-003
Code->

Fig. 33. h.

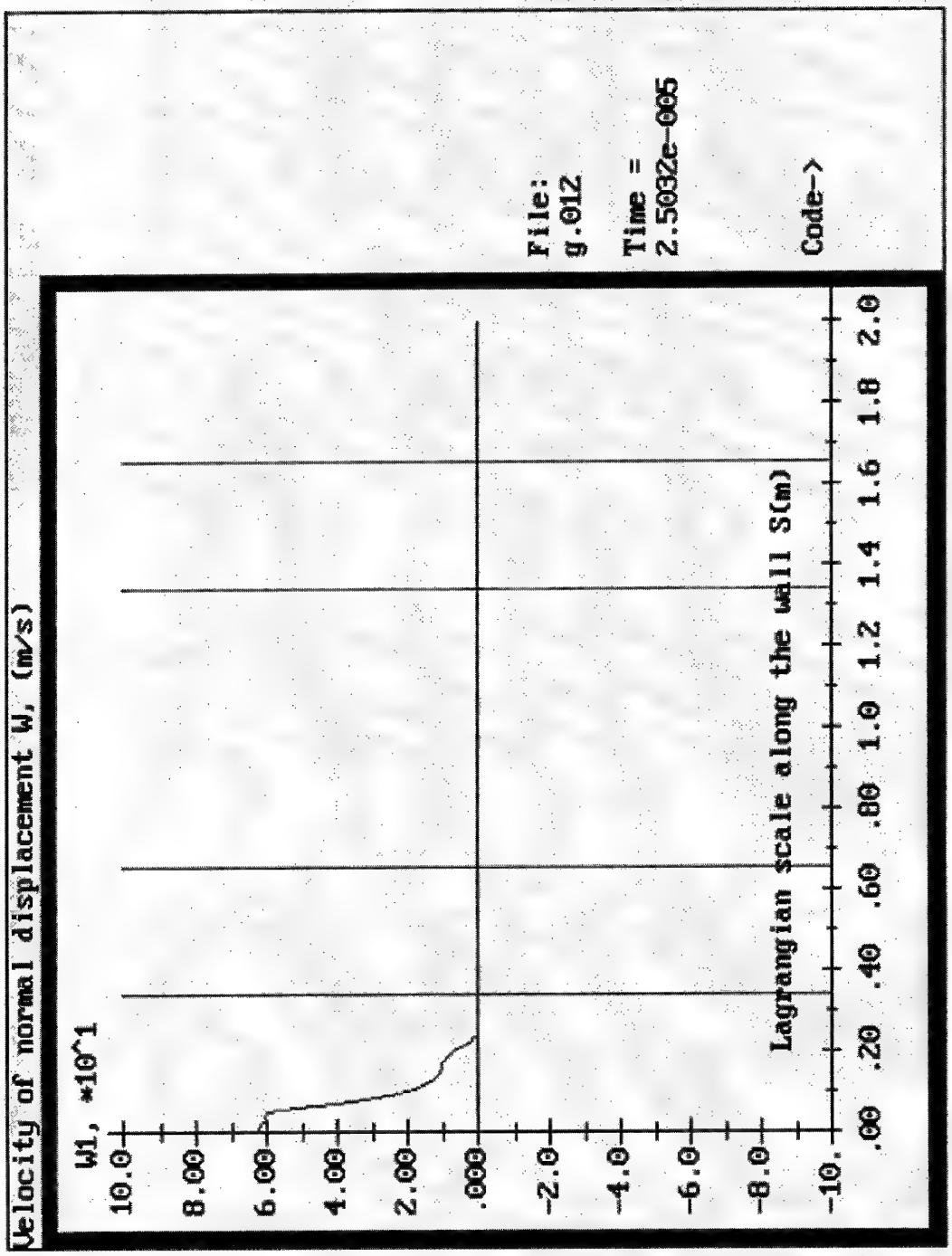
Velocity of normal displacement W, (m/s)
W1, *10^1
10.0
8.00
6.00
4.00
2.00
.000
-2.0
-4.0
-6.0
-8.0
-10.
.00
.20
.40
.60
.80
1.0
1.2
1.4
1.6
1.8
2.0
Lagrangian scale along the wall S(m)
File:
g.012
Time =
2.5032e-005
Code->

Fig. 34.a

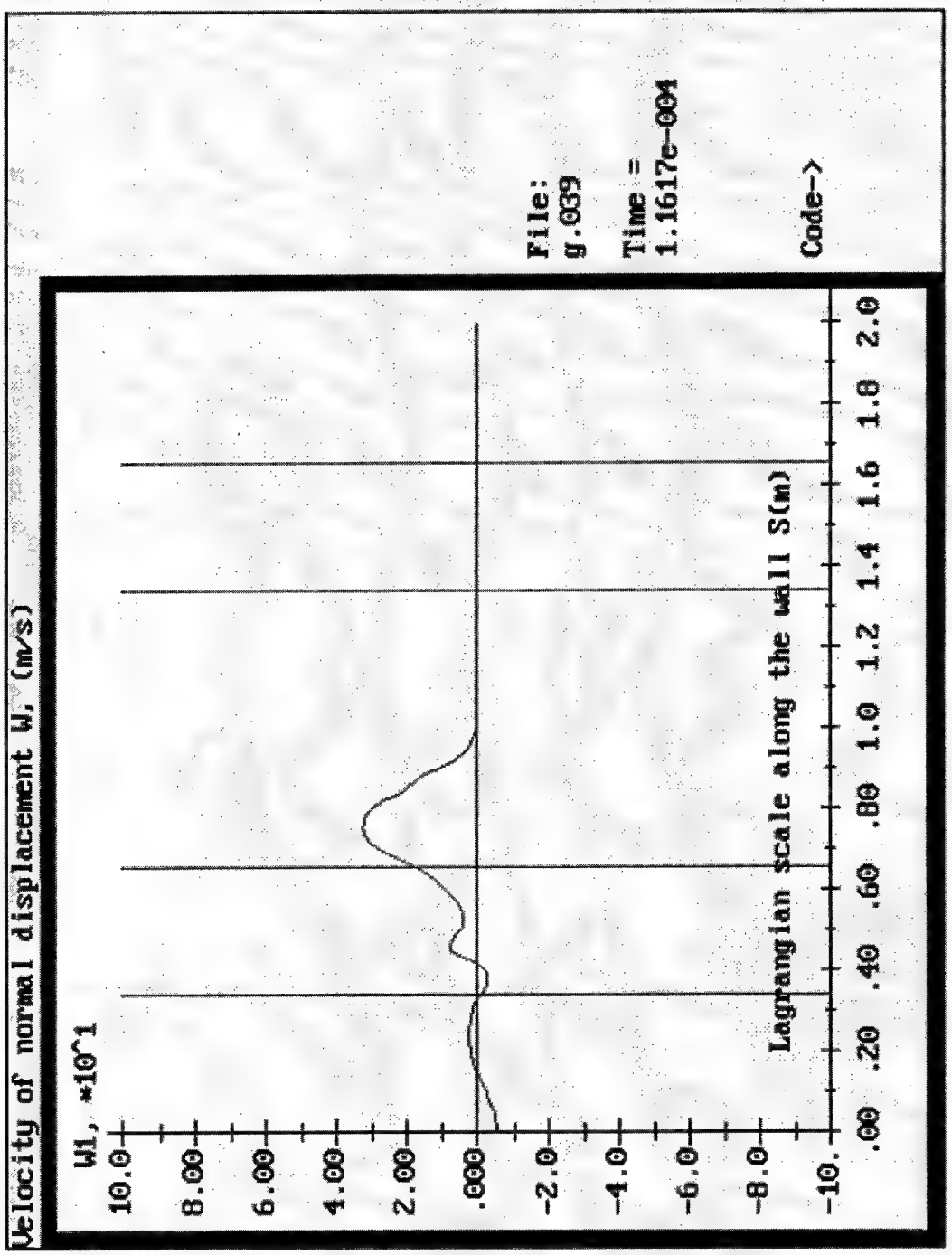
Velocity of normal displacement W, (m/s)
W1, *10^1
10.0
8.00
6.00
4.00
2.00
.000
-2.0
-4.0
-6.0
-8.0
-10.
.00
.20
.40
.60
.80
1.0
1.2
1.4
1.6
1.8
2.0
Lagrangian scale along the wall S(m)
File:
g.039
Time =
1.1617e-004
Code->

Fig. 34.b.

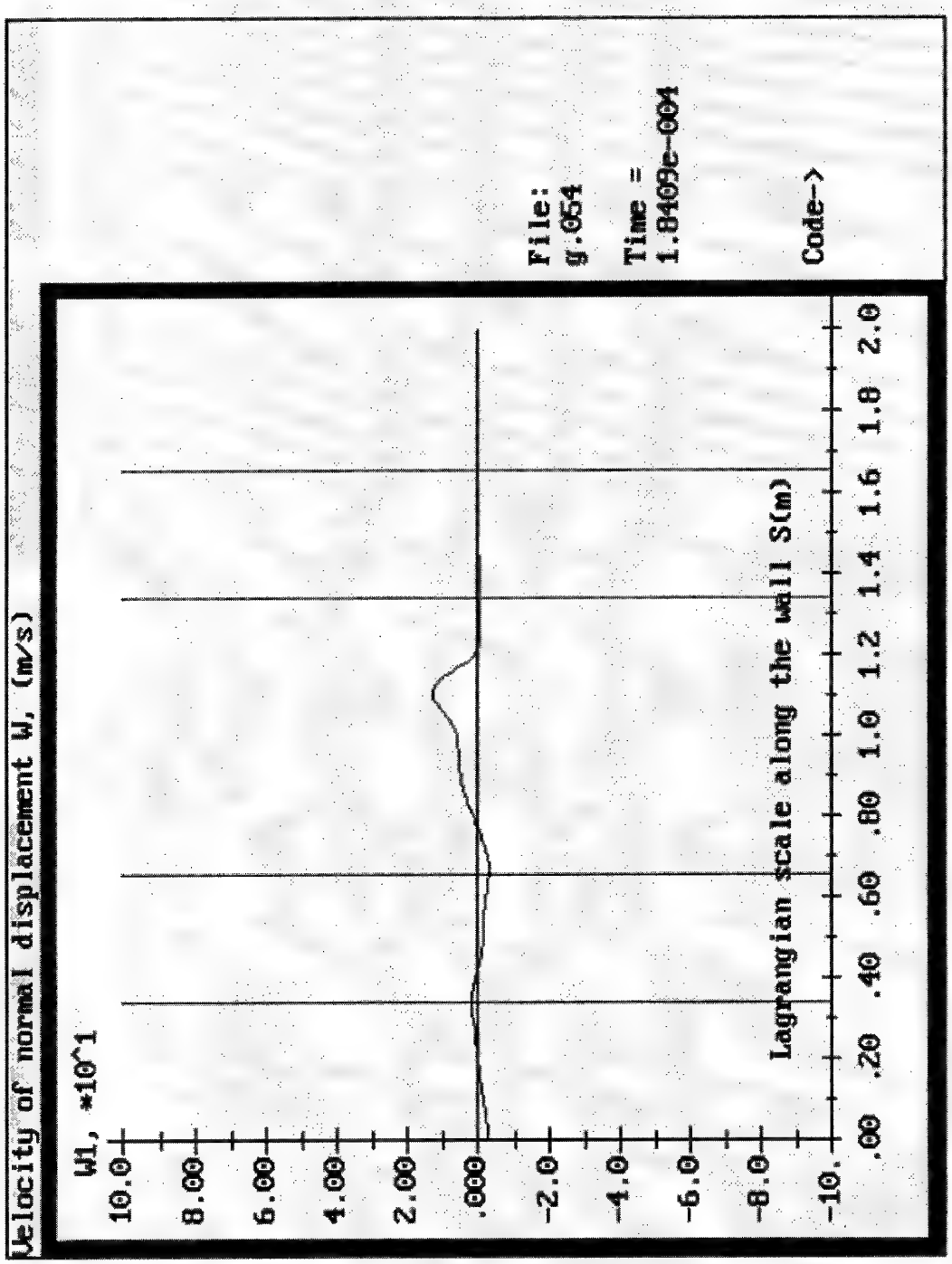
Velocity of normal displacement W, (m/s)
W1, *10^1
10.0
8.00
6.00
4.00
2.00
.000
-2.0
-4.0
-6.0
-8.0
-10.
.00
.20
.40
.60
.80
1.0
1.2
1.4
1.6
1.8
2.0
Lagrangian scale along the wall S(m)
File:
g.054
Time =
1.8409e-004
Code->

Fig. 34.c.

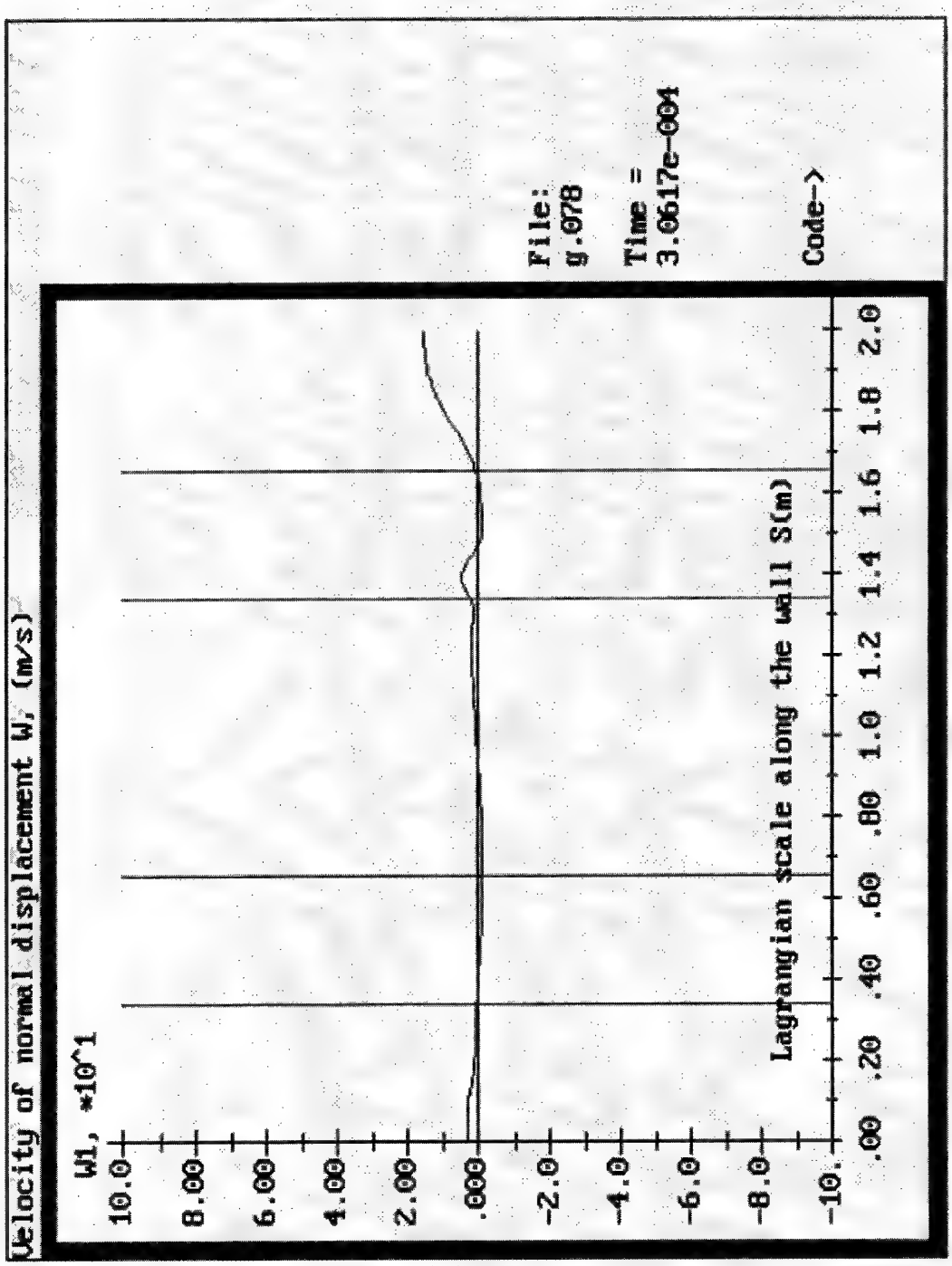
Velocity of normal displacement W, (m/s)
W1, *10^1
10.0
8.00
6.00
4.00
2.00
.000
-2.0
-4.0
-6.0
-8.0
-10.
.00
.20
.40
.60
.80
1.0
1.2
1.4
1.6
1.8
2.0
Lagrangian scale along the wall S(m)
File:
g.078
Time =
3.0617e-004
Code->

Fig. 34. d.

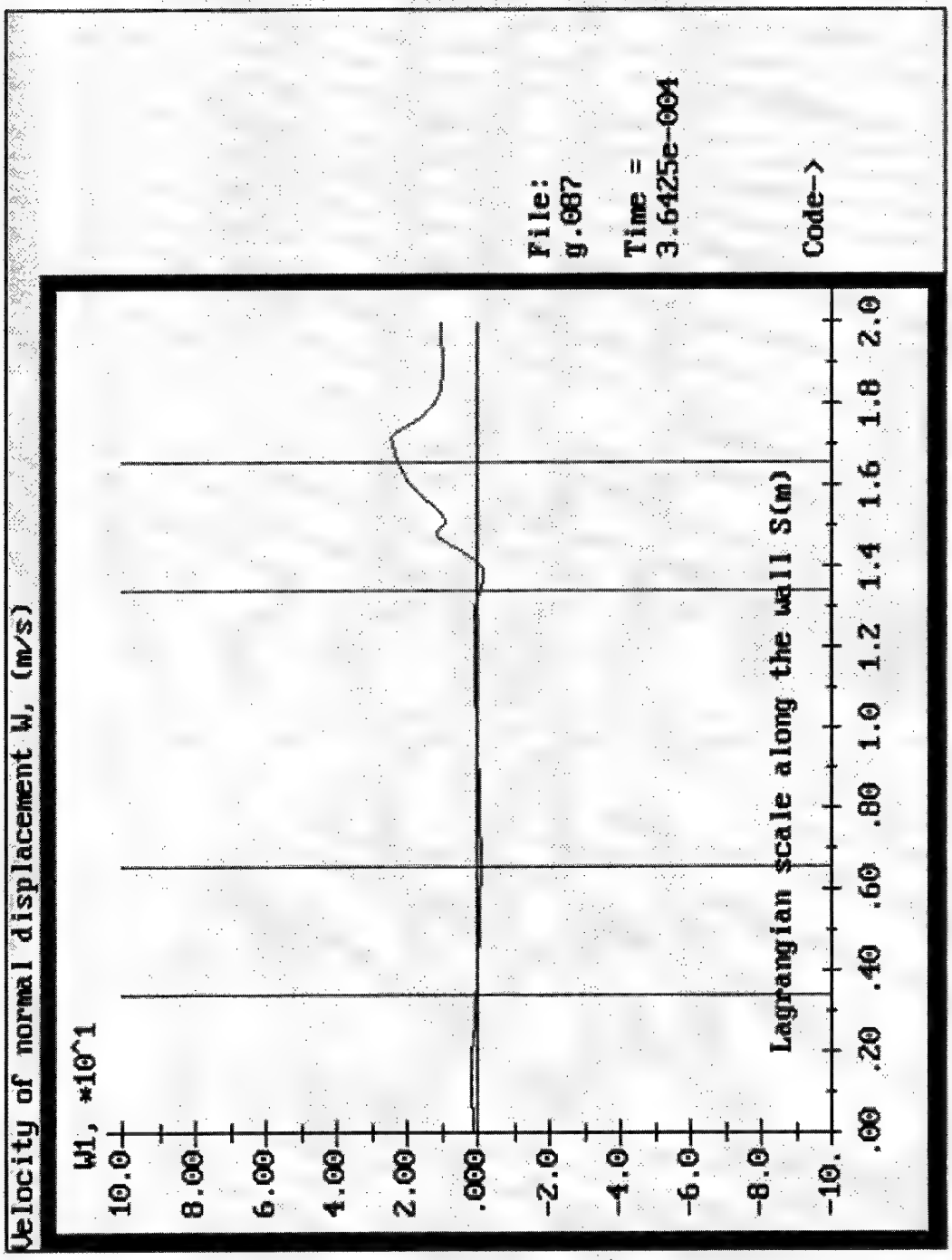
Velocity of normal displacement W, (m/s)
W1, *10^1
10.0
8.00
6.00
4.00
2.00
.000
-2.0
-4.0
-6.0
-8.0
-10.
.00
.20
.40
.60
.80
1.0
1.2
1.4
1.6
1.8
2.0
Lagrangian scale along the wall S(m)
File:
g.087
Time =
3.6425e-004
Code->

Fig. 34. e.

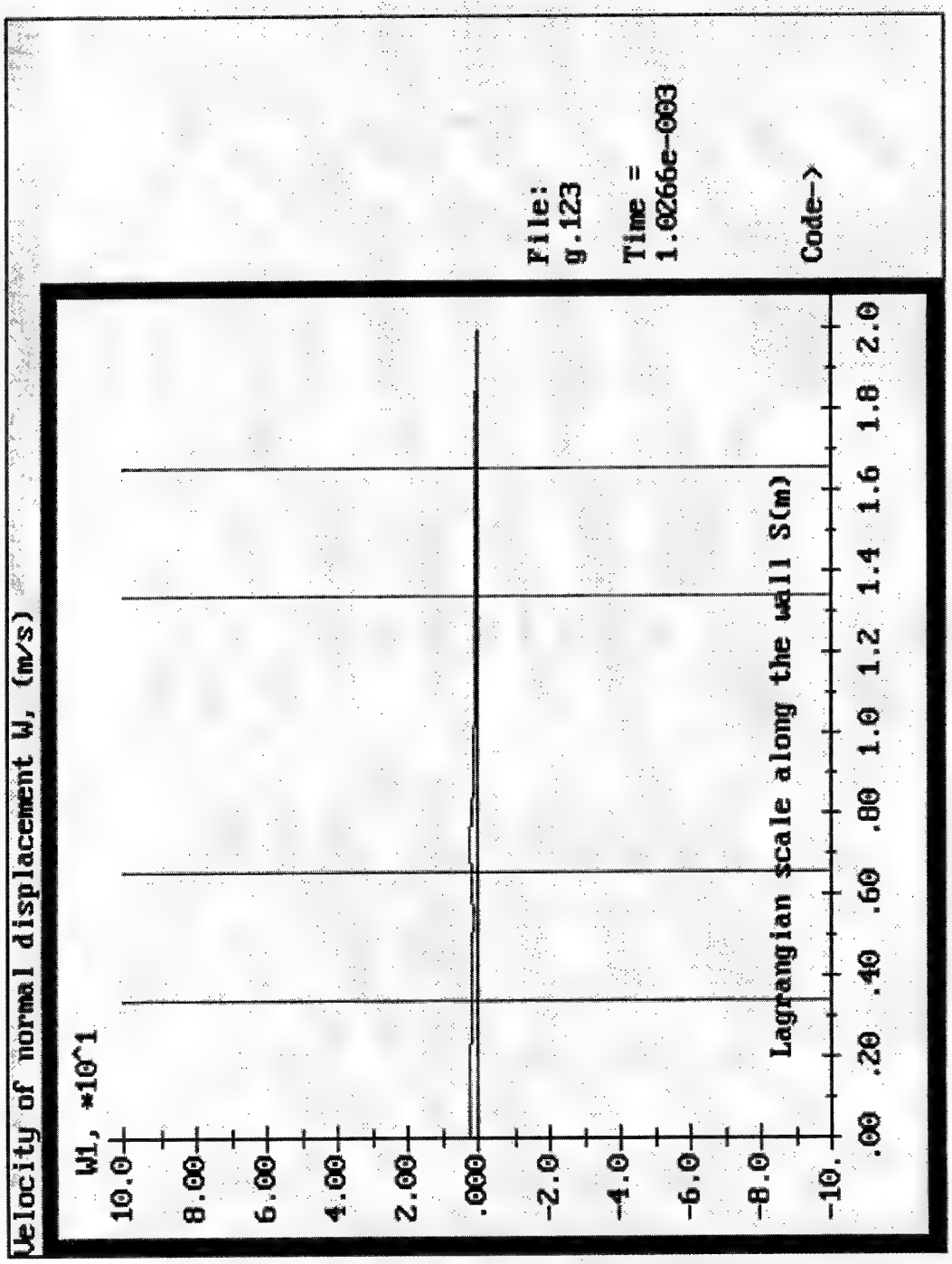
Velocity of normal displacement W, (m/s)
W1, *10^1
10.0
8.00
6.00
4.00
2.00
.000
-2.0
-4.0
-6.0
-8.0
-10.
.00
.20
.40
.60
.80
1.0
1.2
1.4
1.6
1.8
2.0
Lagrangian scale along the wall S(m)
File:
g.123
Time =
1.0266e-003
Code->

Fig. 34. f.

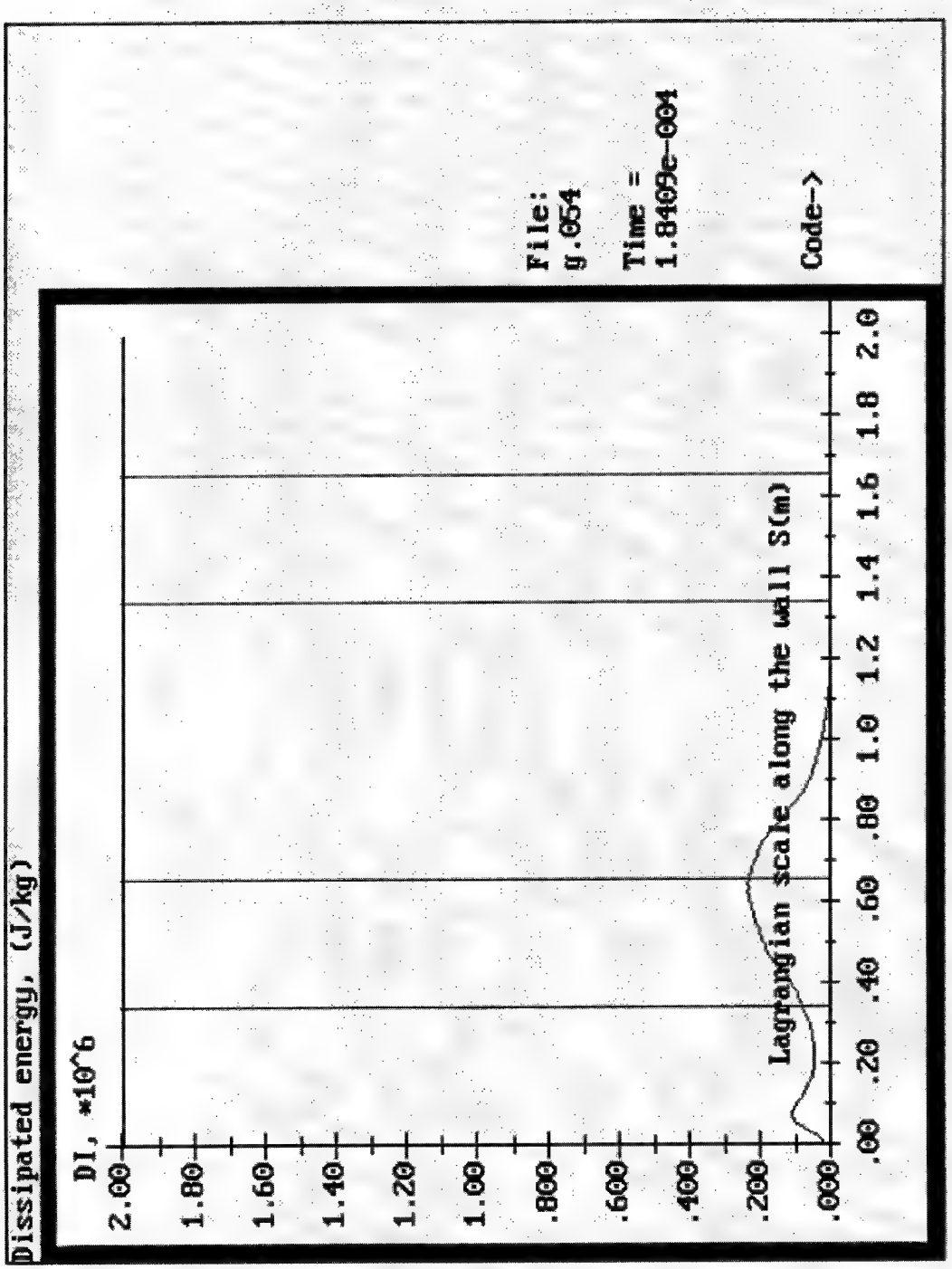
Dissipated energy, (J/kg)
DI, *10^6
2.00
1.80
1.60
1.40
1.20
1.00
.800
.600
.400
.200
.000
.00
.20
.40
.60
.80
1.0
1.2
1.4
1.6
1.8
2.0
Lagrangian scale along the wall S(m)
File:
g.054
Time =
1.8409e-004
Code->

Fig. 35. a.

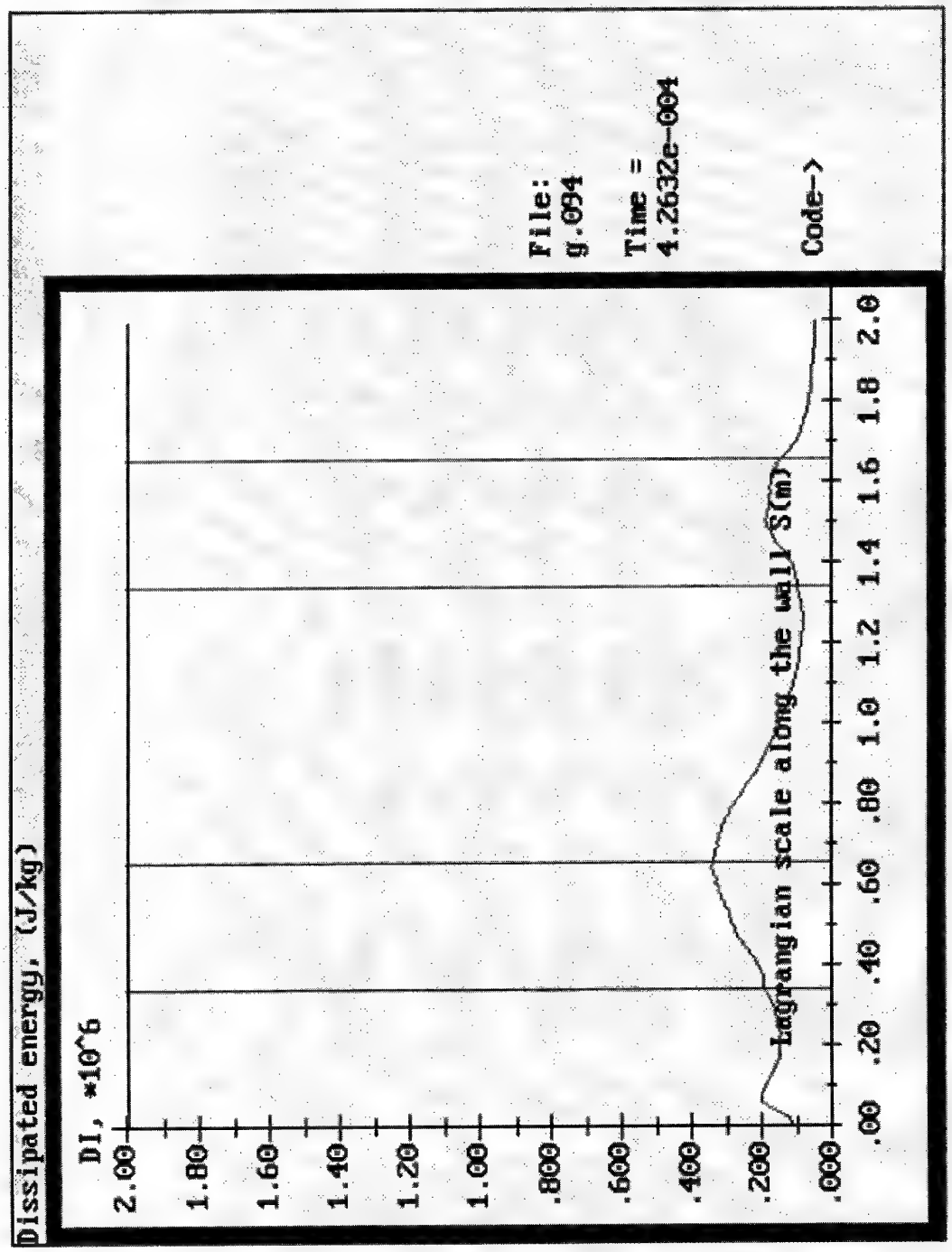
Dissipated energy, (J/kg)
DI, *10^6
2.00
1.80
1.60
1.40
1.20
1.00
.800
.600
.400
.200
.000
.00
.20
.40
.60
.80
1.0
1.2
1.4
1.6
1.8
2.0
Lagrangian scale along the wall S(m)
File:
g.094
Time =
4.2632e-004
Code->

Fig. 35. b.

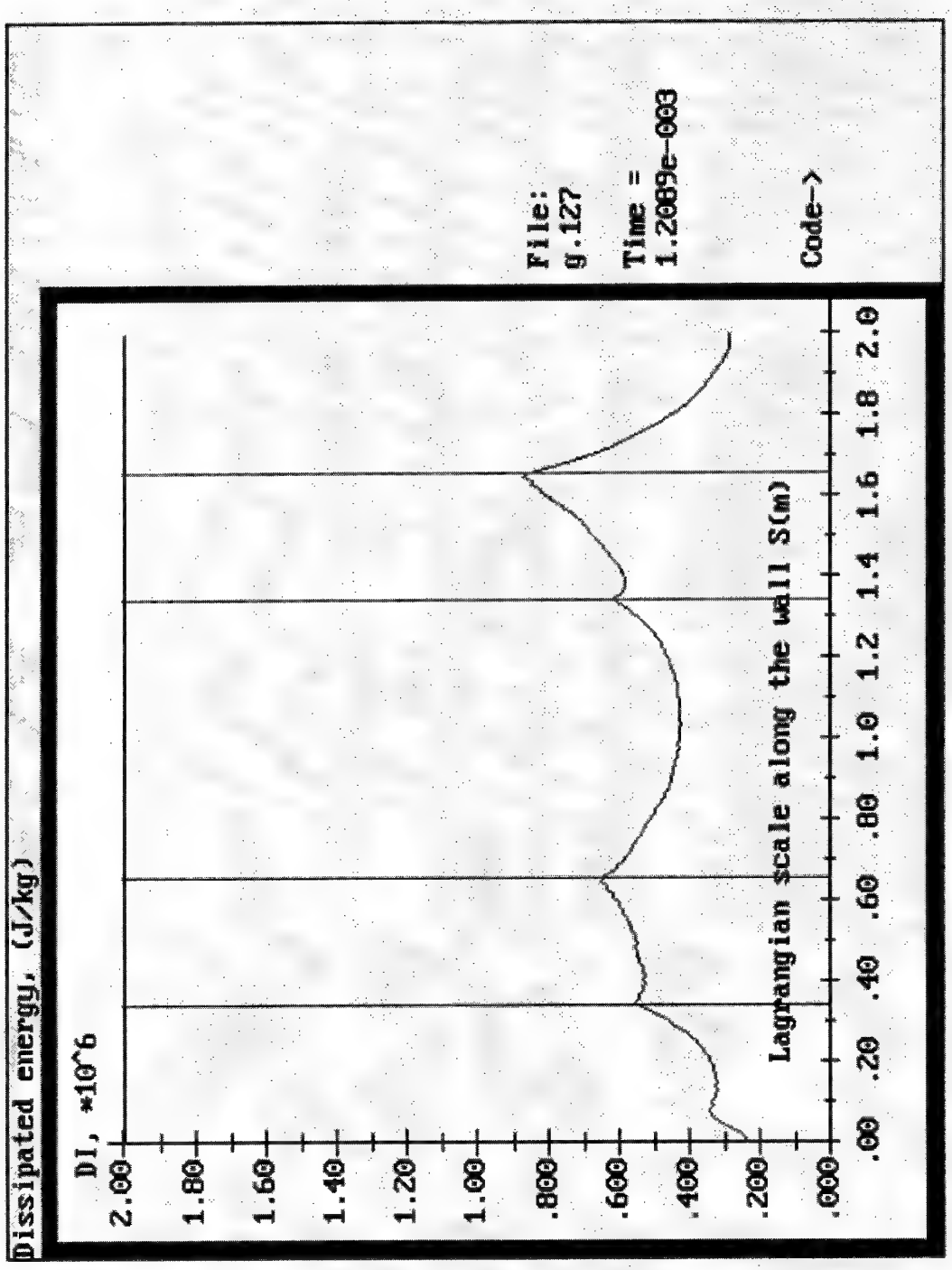
Dissipated energy, (J/kg)
DI, *10^6
2.00
1.80
1.60
1.40
1.20
1.00
.800
.600
.400
.200
.000
.00
.20
.40
.60
.80
1.0
1.2
1.4
1.6
1.8
2.0
Lagrangian scale along the wall S(m)
File:
g.127
Time =
1.2089e-003
Code->

Fig. 35.c.

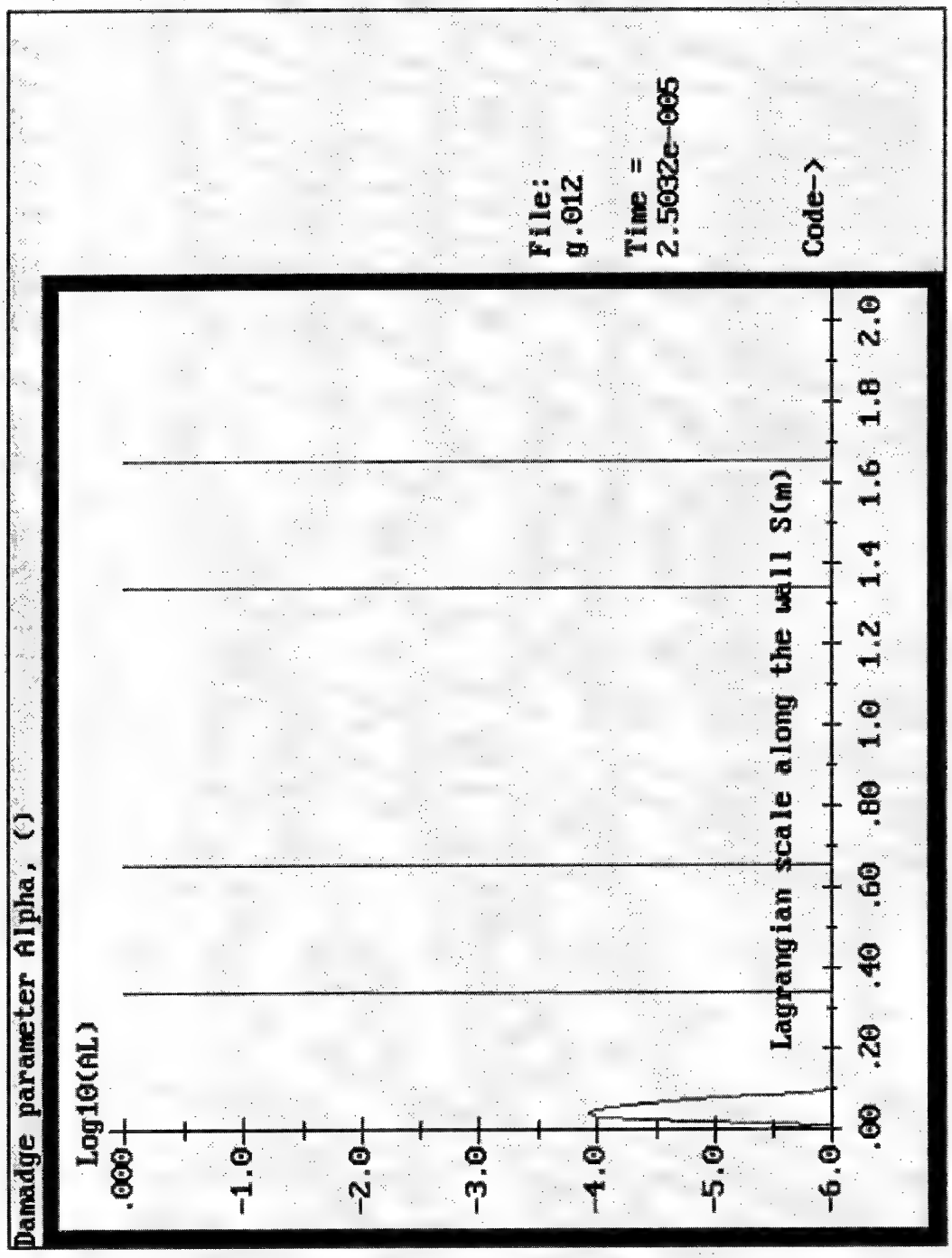
Damadge parameter Alpha, ()
Log10(AL)
.000
-1.0
-2.0
-3.0
-4.0
-5.0
-6.0
.00
.20
.40
.60
.80
1.0
1.2
1.4
1.6
1.8
2.0
Lagrangian scale along the wall S(m)
File:
g.012
Time =
2.5032e-005
Code->

Fig. 36.a

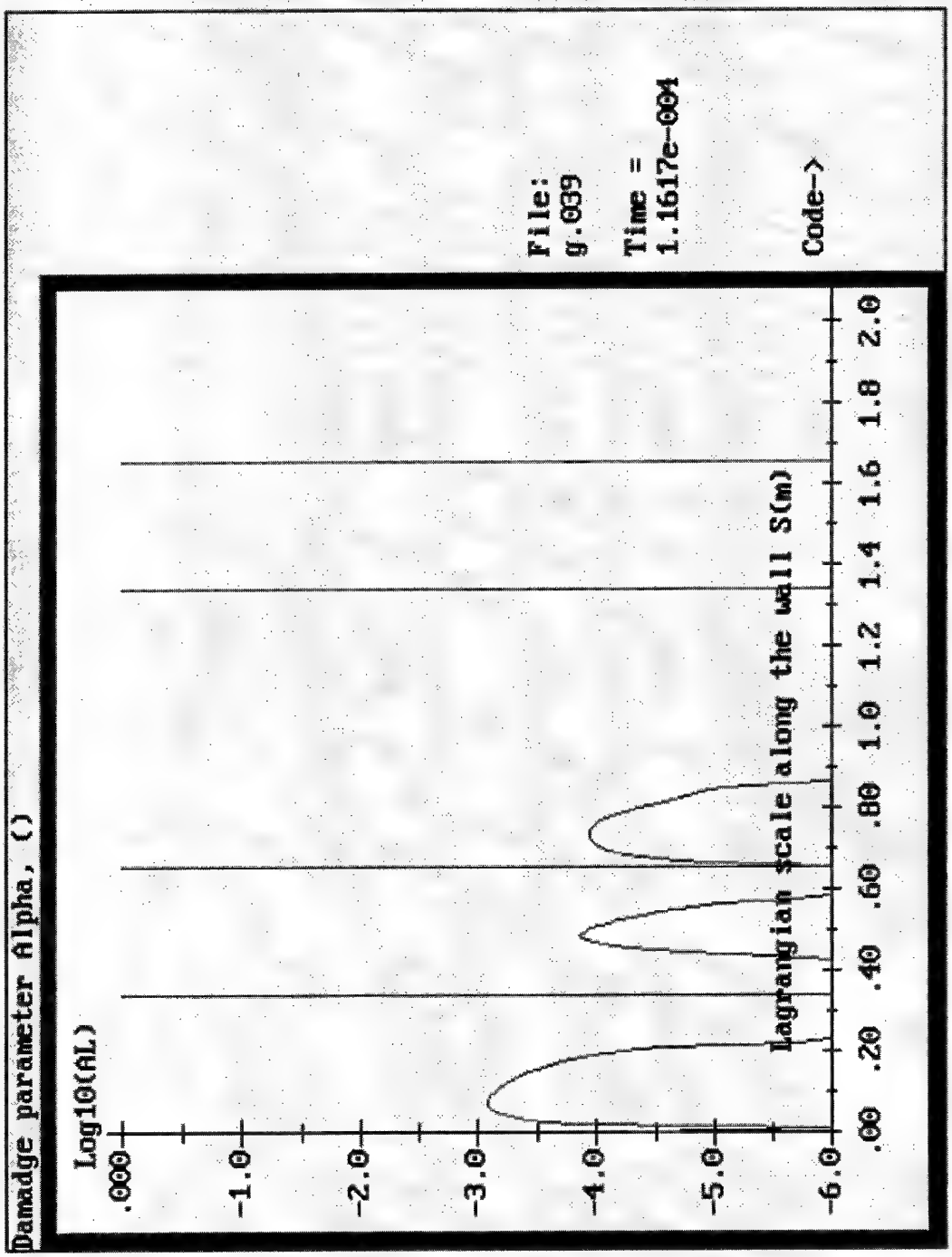
Damadge parameter Alpha, ()
Log10(AL)
.000
-1.0
-2.0
-3.0
-4.0
-5.0
-6.0
.00
.20
.40
.60
.80
1.0
1.2
1.4
1.6
1.8
2.0
Lagrangian scale along the wall S(m)
File:
g.039
Time =
1.1617e-004
Code->

Fig. 36.b.

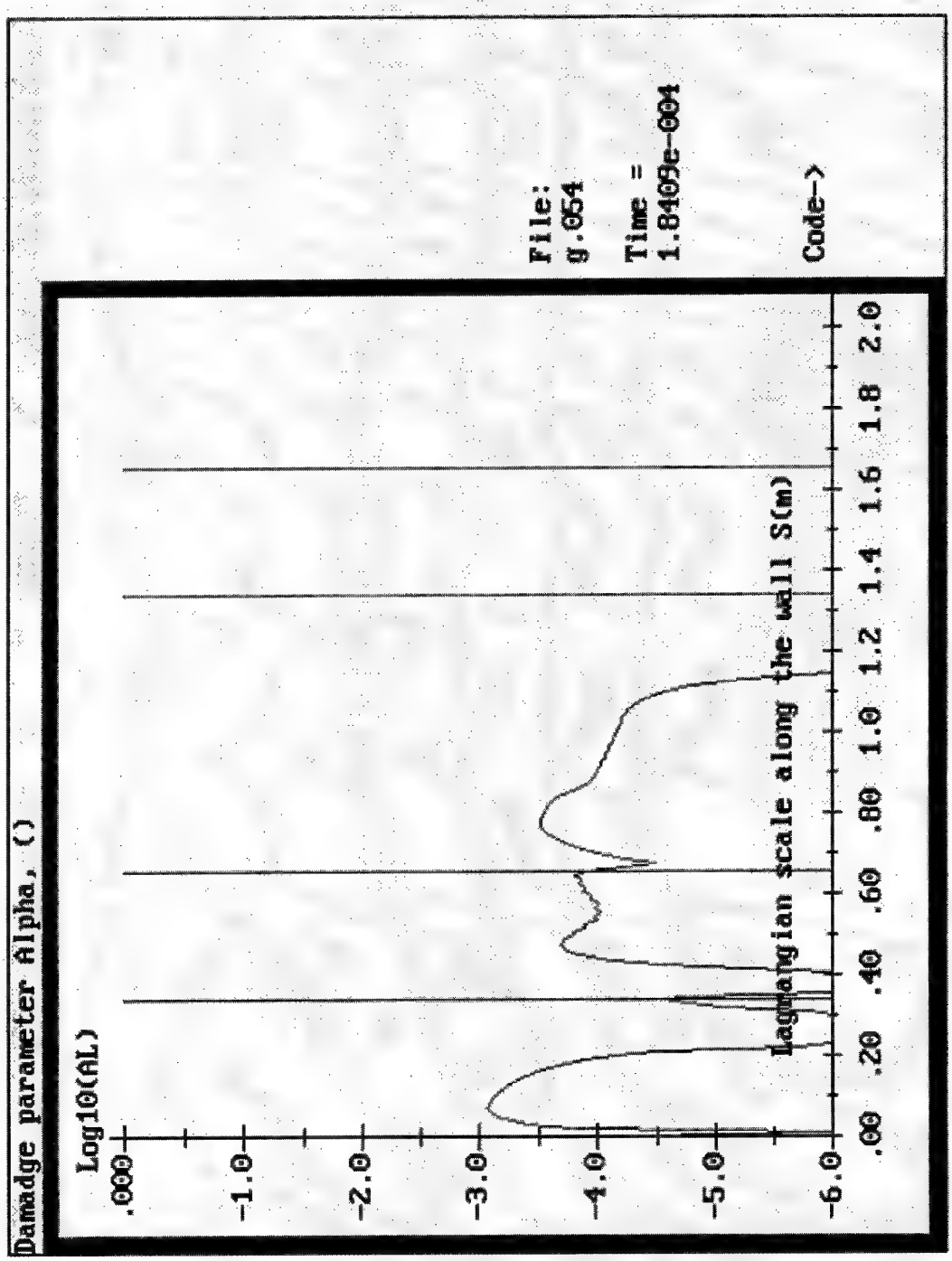
Damadge parameter Alpha, ()
Log10(AL)
.000
-1.0
-2.0
-3.0
-4.0
-5.0
-6.0
.00
.20
.40
.60
.80
1.0
1.2
1.4
1.6
1.8
2.0
Lagrangian scale along the wall S(m)
File:
g.054
Time =
1.8403e-004
Code->

Fig. 36.c.

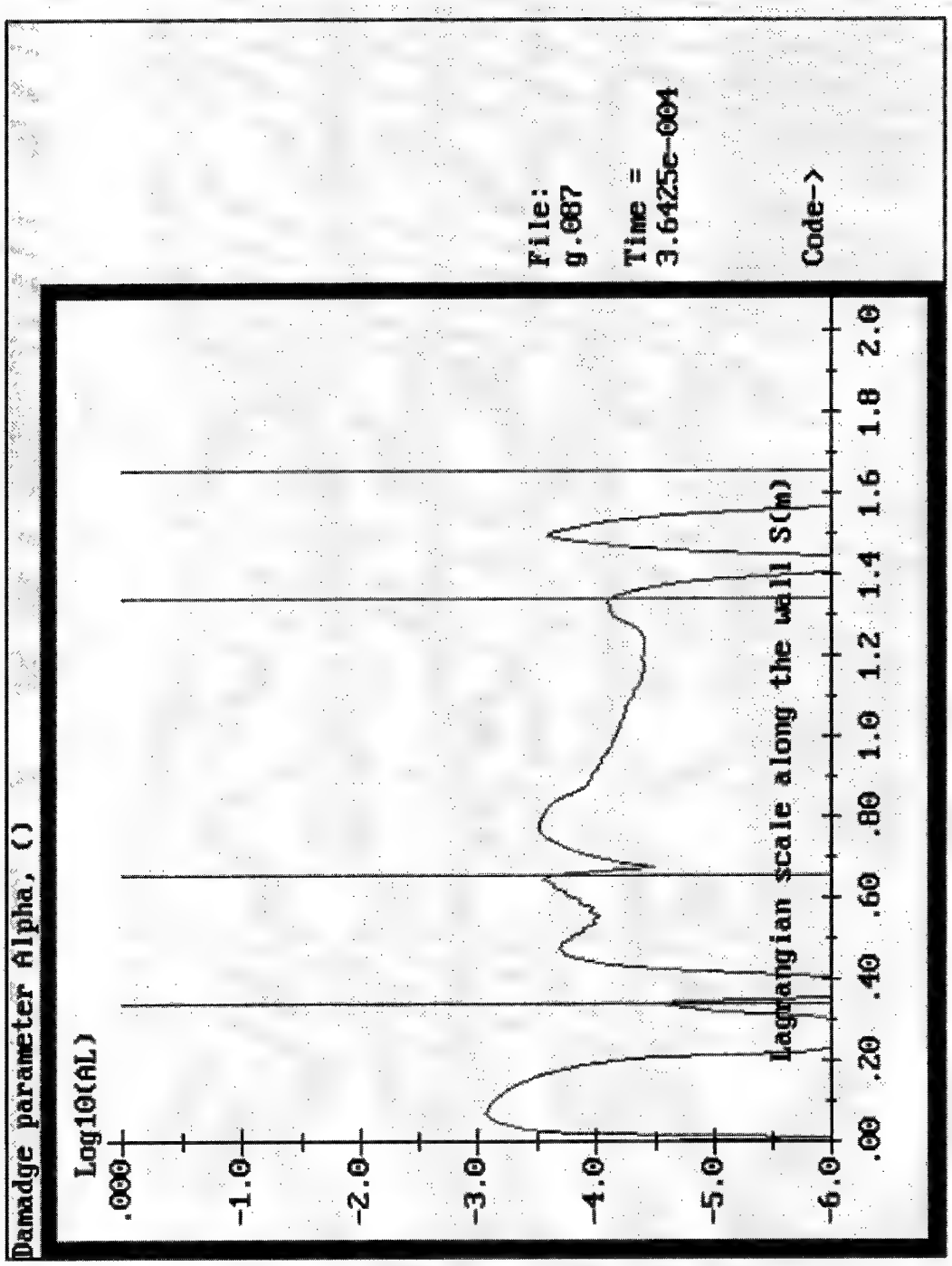
Damadge parameter Alpha, ()
Log10(AL)
.000
-1.0
-2.0
-3.0
-4.0
-5.0
-6.0
.00
.20
.40
.60
.80
1.0
1.2
1.4
1.6
1.8
2.0
Lagrangian scale along the wall S(m)
File:
g.087
Time =
3.6425e-004
Code->

Fig. 36. d.

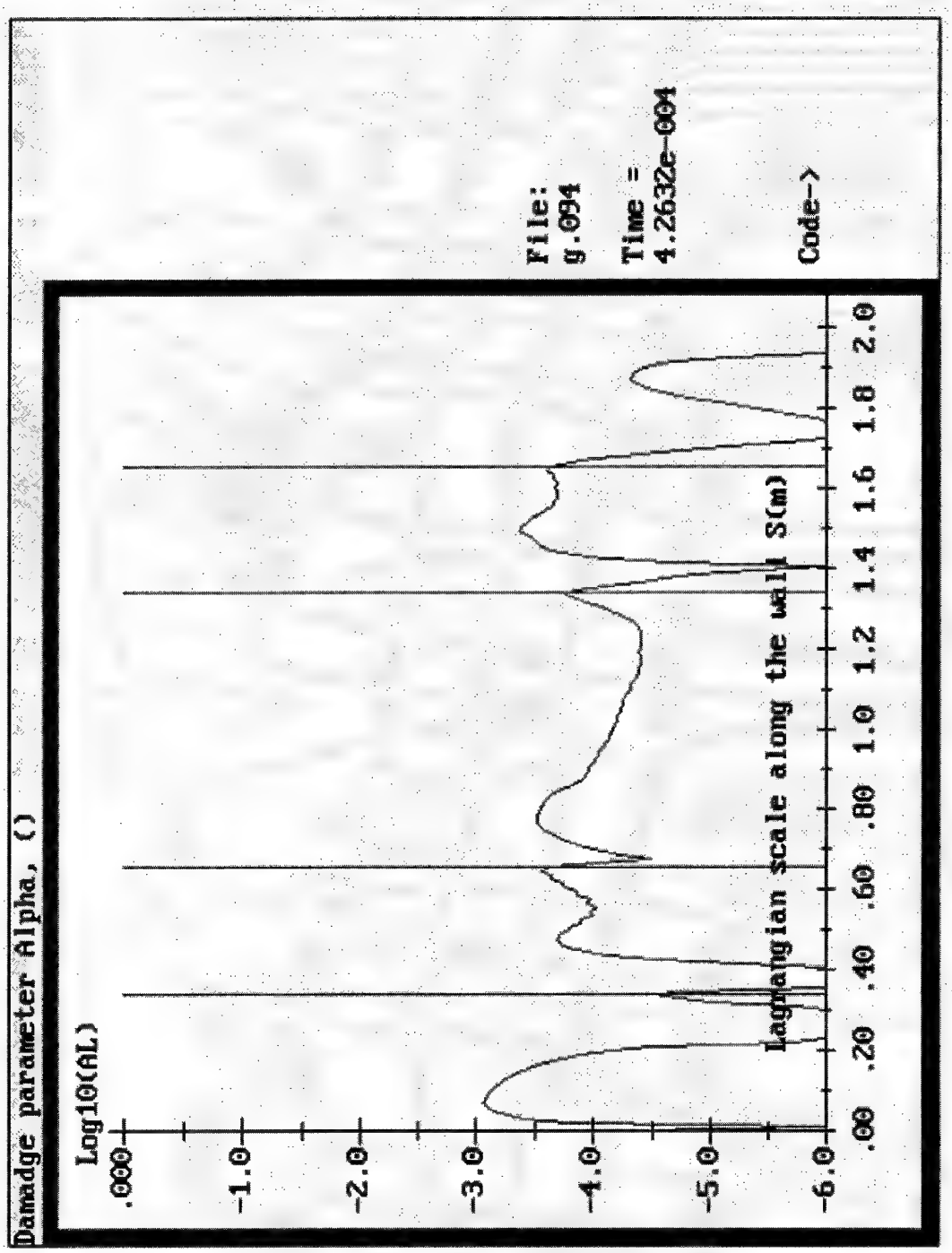
Damadge parameter Alpha, ()
Log10(AL)
.000
-1.0
-2.0
-3.0
-4.0
-5.0
-6.0
.00
.20
.40
.60
.80
1.0
1.2
1.4
1.6
1.8
2.0
Lagrangian scale along the wall S(m)
File:
g.094
Time =
4.2632e-004
Code->

Fig. 36. e.

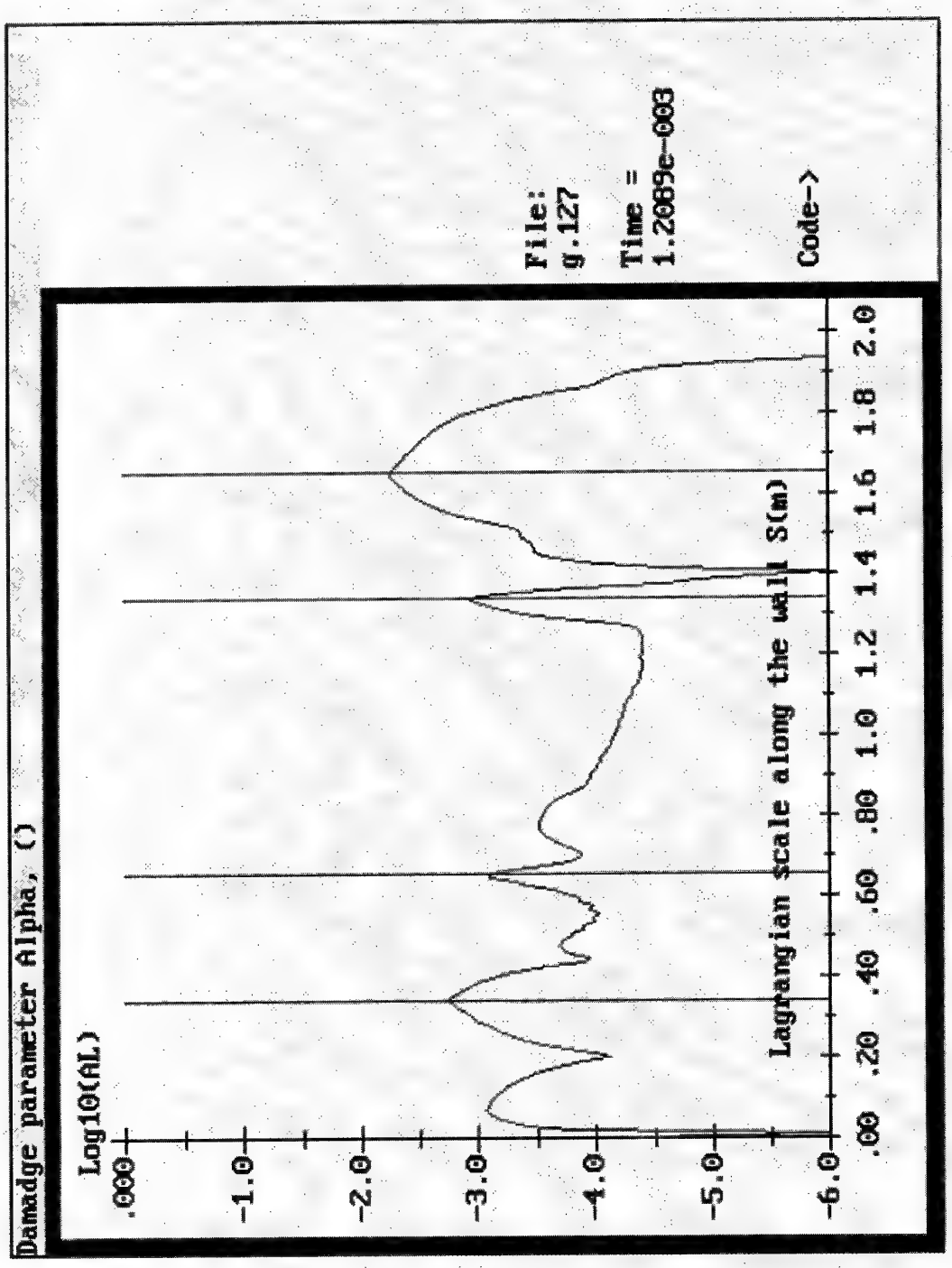
Damadge parameter Alpha, ()
Log10(AL)
.000
-1.0
-2.0
-3.0
-4.0
-5.0
-6.0
.00
.20
.40
.60
.80
1.0
1.2
1.4
1.6
1.8
2.0
Lagrangian scale along the wall S(m)
File:
g.127
Time =
1.2089e-003
Code->

Fig. 36. f.

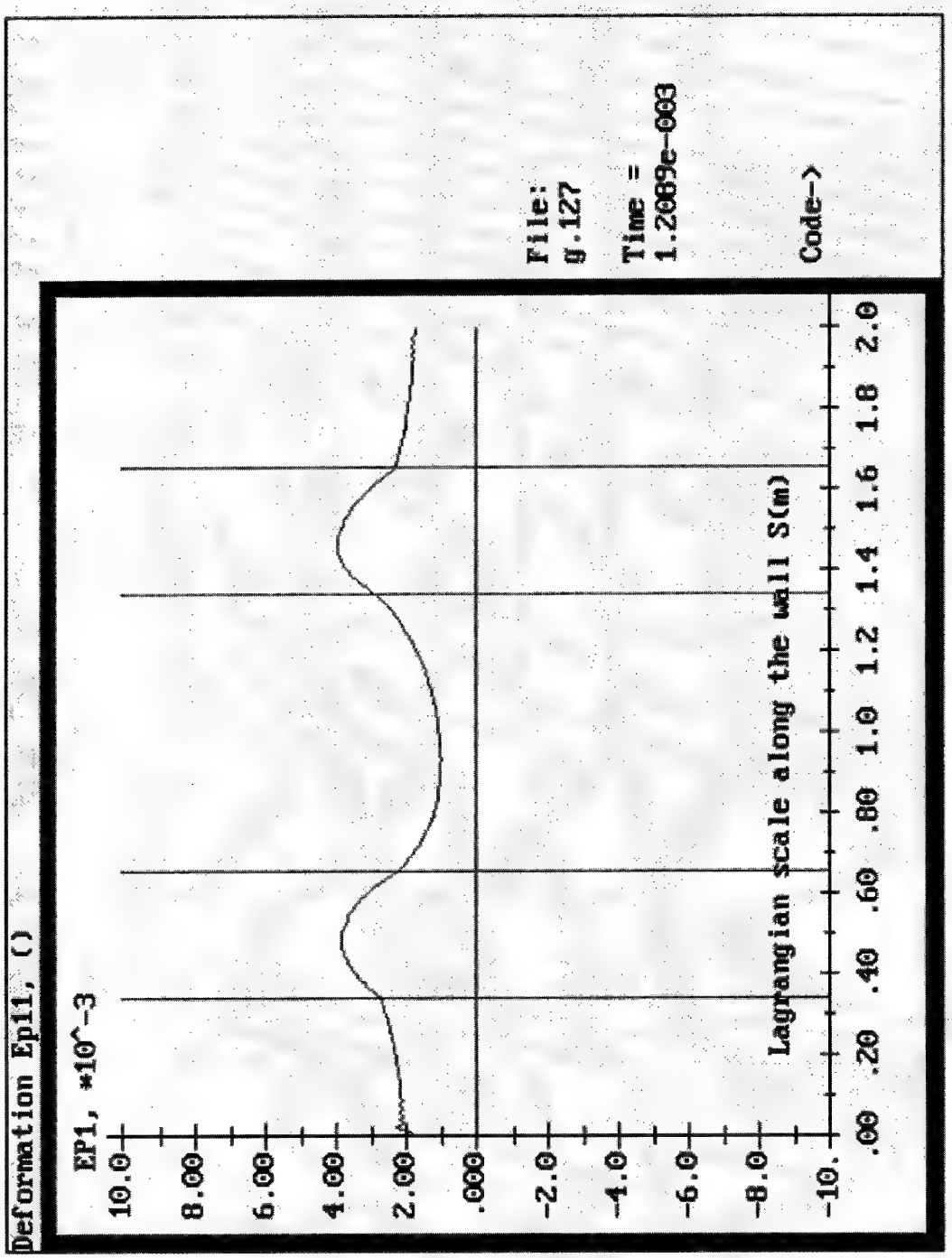
Deformation Ep11, ()
EP1, *10^-3
10.0
8.00
6.00
4.00
2.00
.000
-2.0
-4.0
-6.0
-8.0
-10.
.00
.20
.40
.60
.80
1.0
1.2
1.4
1.6
1.8
2.0
Lagrangian scale along the wall S(m)
File:
g.127
Time =
1.2089e-003
Code->

Fig. 37.

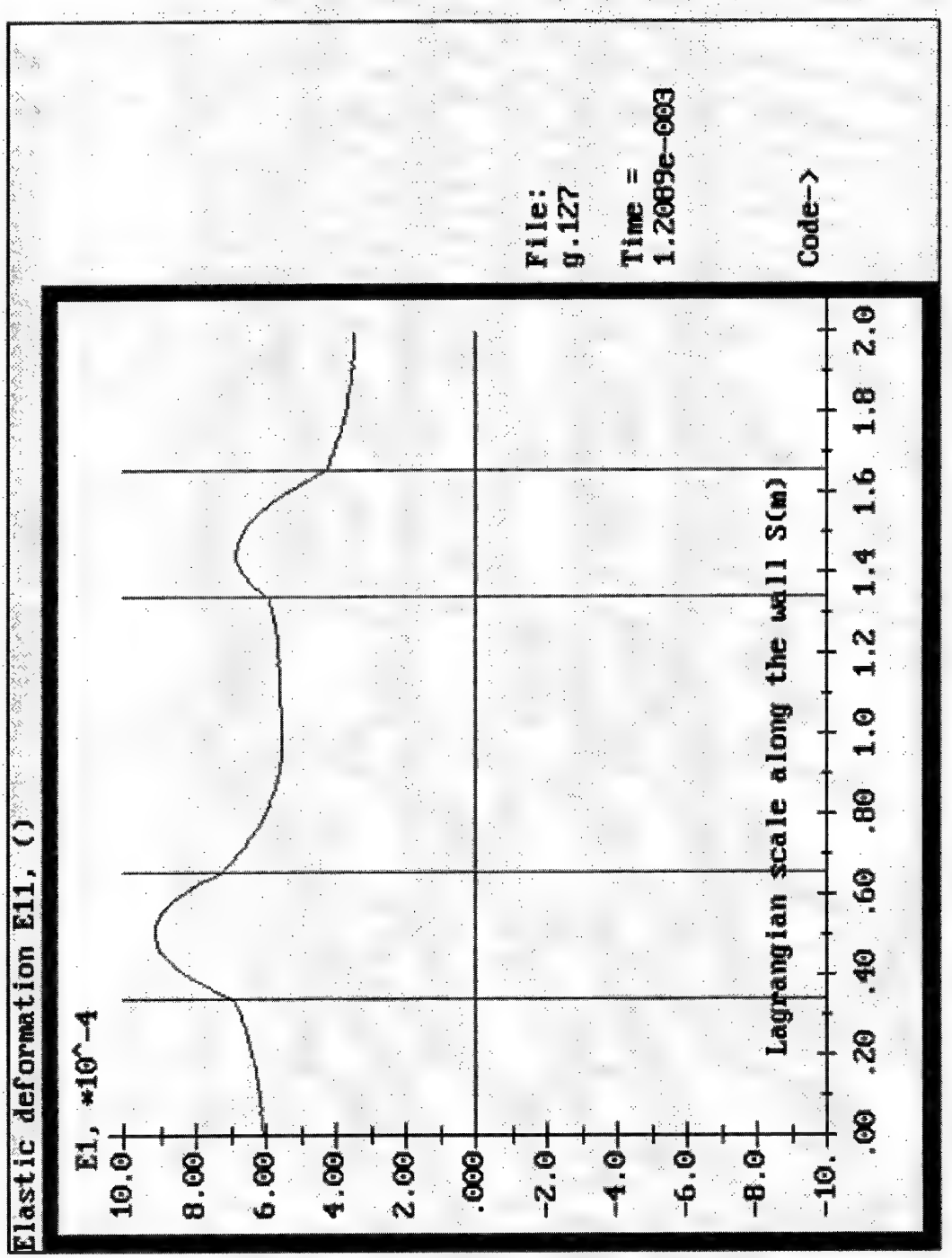
Elastic deformation E11, ()
E1, *10^-4
10.0
8.00
6.00
4.00
2.00
.000
-2.0
-4.0
-6.0
-8.0
-10.
.00
.20
.40
.60
.80
1.0
1.2
1.4
1.6
1.8
2.0
Lagrangian scale along the wall S(m)
File:
g.127
Time =
1.2089e-003
Code->

Fig. 38.

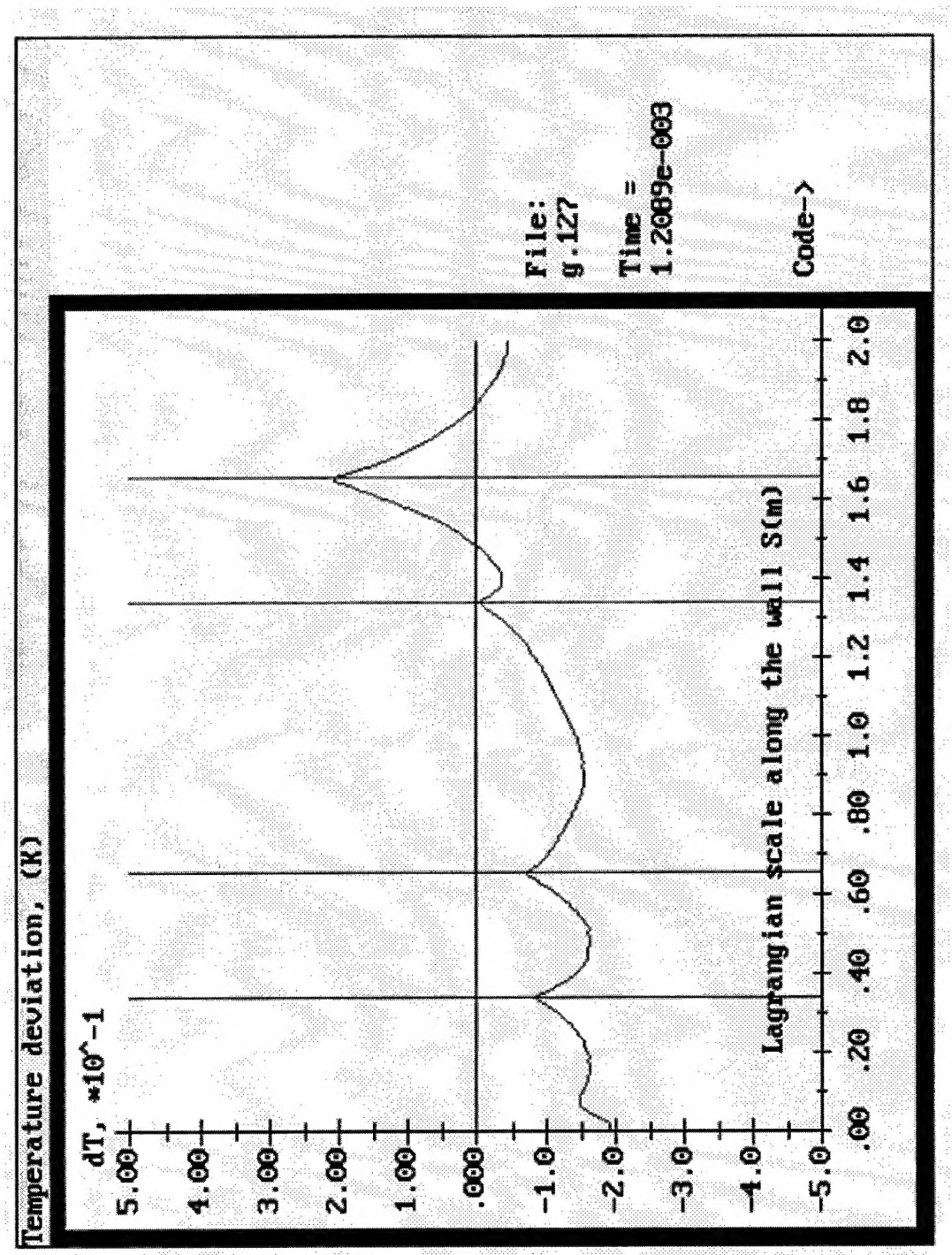
Temperature deviation, (K)
dT, *10^-1
5.00
4.00
3.00
2.00
1.00
.000
-1.0
-2.0
-3.0
-4.0
-5.0
.00
.20
.40
.60
.80
1.0
1.2
1.4
1.6
1.8
2.0
Lagrangian scale along the wall S(m)
File:
g.127
Time =
1.2089e-003
Code->

Fig. 39.

References.

1. N.N.Smirnov, A.B.Kiselev, I.D.Dimitrienko, V.R.Dushin, V.F.Nikitin. Computational damage model for composite materials. Mathematical Model of Dynamical Deforming and Fracture of Damageable Fibrous Thermoviscoelastic Composites. First Quaterly Report on SPC 96-4012. Brussels, 1994.

2. N.N.Smirnov, A.B.Kiselev, I.D.Dimitrienko, V.R.Dushin, V.F.Nikitin. Mathematical modelling of dynamical deforming and fracture of two-phase composites with laminated and fibrous structure. Second Quaterly Report on SPC 96-4012. Brussels, 1994.

3. N.N.Smirnov, A.B.Kiselev, I.D.Dimitrienko, V.R.Dushin, V.F.Nikitin. Experimental method of determining rheological parameters of the model for damaged thermoviscoelastic two-phase composites with laminated structure. Third Quaterly Report on SPC 96-4012. Brussels, 1994.

4. O.Pironeau, B.Mohammadi. Analysis of the K-Epsilon turbulence model. Mason Editeur, Paris, 1994.

5. D.A.Anderson, J.C.Tannehill, R.H.Pletcher. Computational Fluid Mechanics and Heat Transfer. Hemisphere Publ.Co., 1984.

6. E.S.Oran, J.P.Boris. Numerical simulation of reactive flow. Elsevier Publ.Co.,New York-Amsterdam- London, 1987.

7. A.R.Mitchell, R.Wait. The finite element method in partial differential equations. John Wiley & Sons Inc., Chichester-New York-Brisbane-Toronto, 1977.

CONCLUSIONS

The model of damageable thermoviscoelastic composite material was worked out during the contract period incorporating the thermodynamic breakup criterion based on the critical value of the total dissipation being the sum of mechanical dissipation, thermal dissipation and dissipation in continuous destruction causing accumulation of damages in tension, shear and delamination. The detailed description of the general mathematical model and methods to determine the critical dissipation can be found in the interim reports.

The present report contains the results of numerical investigations of behaviour of a composite shell of a containment under the influence of internal dynamical loading incorporating the worked out model for a damageable laminate. To demonstrate the utility of the mathematical model it was incorporated into a hydrocode and applied for the solution of the problem of dynamical deforming of a composite shell in a uniform and nonuniform loading caused by the internal explosion.

The model makes it possible to determine the formation and growth of potentially damaged zones taking into account nonuniformities of shell's parameters distribution due to loading and/or curvature nonuniformities. The material constants for the model had been taken arbitrary. Thus the results of the described numerical experiments are mostly qualitative. Analysis of the results shows the utility of the worked out mathematical model.

Table 1.

Problem parameters file
Thick membrane of composite materials under loading

50	Gas: grid points along OX
50	Gas: grid points along OR
3.00000e+000	Gas: total domain length
1.00000e+000	Gas: total domain radius
1.00000e+005	Gas: initial pressure
3.00000e+002	Gas: initial temperature
2.90000e-002	Gas: molar weight
1.40000e+000	Gas: adhiabatic ratio
1.00000e+007	Pressure behavior constants: amplitude
1.00000e+001	charact.radius
1.00000e-004	charact.time
601	Wall: number of nodes
1.00000e+000	Radius
2.00000e+000	Main section length
2.00000e-001	Corners' radius
1.00000e-002	Membrane thickness
6.10000e-001	Volume fraction of component 1
9.40000e+010	Comp1: Lamé coefficient La
5.30000e+010	Comp1: Lamé coefficient Mu
2.00000e-005	Comp1: Volume thermal extendibility
1.00000e+003	Comp1: Spec. heat capacity at constant deformations
1.60000e+003	Comp1: Density
1.00000e-004	Comp1: Relaxation time
7.54000e+009	Comp2: Lamé coefficient La
1.89000e+009	Comp2: Lamé coefficient Mu
1.50000e-004	Comp2: Volume thermal extendibility
2.00000e+003	Comp2: Spec. heat capacity at constant deformations
1.30000e+003	Comp2: Density
1.00000e-002	Comp2: Relaxation time
2.73000e+002	Initial temperature
1.00000e+000	Unknown damadge constant Big Lambda
1.00000e+000	Unknown damadge constant Big Lambda-Delta
1.00000e+004	Unknown damadge constant Big Omega
1.00000e+000	Unknown damadge constant Big A
1.00000e+004	Unknown damadge constant Big C
1.00000e+004	Unknown damadge constant Big D
1.00000e-002	Comp1: damadge constant E_*
7.00000e-003	Comp1: damadge constant E^t_*
3.00000e-003	Comp2: damadge constant E_*
2.00000e-003	Comp2: damadge constant E^t_*
5.00000e-003	Damadge constant Delta_*
1.00000e+007	Maximal dissipated energy

11296
□